Instituto de Física de Cantabria
(CSIC-Universidad de Cantabria)
y
Departamento de Física Moderna
(Universidad de Cantabria)

Desarrollo y aplicación de algoritmos de alineamiento para la optimización de la detección de muones en el experimento CMS del LHC

Memoria presentada por
Pablo Martínez Ruiz del Árbol
para optar al grado de Doctor
por la Universidad de Cantabria,
y dirigida por **Dr. Francisco Matorras Weinig**

Santander, Abril 2010

Instituto de Física de Cantabria
(CSIC-Universidad de Cantabria)
y
Departamento de Física Moderna
(Universidad de Cantabria)

Development and application of alignment algorithms for optimization of the muon detection at the CMS experiment at the LHC

Submitted by
Pablo Martínez Ruiz del Árbol
to the University of Cantabria,
for the Degree of
DOCTOR OF PHILOSOPHY
and supervised by **Dr. Francisco Matorras Weinig**

Santander, April 2010

A mis padres, mi hermana, Ali y Tito.

Contents

List of Figures

List of Tables

Chapter 1

Introduction

Particle physics studies the properties of the most fundamental components of matter and their interactions. The Standard Model of particles has been able to correctly describe particle dynamics up to the scales of energy achieved so far in the laboratory. All the particles postulated by the model have been observed, with the exception of the Higgs boson, a particle responsible for the electroweak symmetry breaking phenomenon for which particles acquire mass. On the other hand, it is known that the Standard Model is not consistent for energy scales far beyond the TeV, suggesting the existence of a different new model that overcomes it.

In order to test the correctness of the Standard Model and to find evidences of new physics, large particle accelerators are built. The Large Hadron Collider (LHC) located at CERN next to the city of Geneva, is the latest and most powerful accelerator. Bunches of protons will collide in this accelerator at energies close to 7 TeV per beam (1.18 TeV at the present date), allowing to explore the TeV energy scale. Large particle detectors are installed at the collision points, to identify and measure the properties of the particles emerging from the collisions.

Particle detectors must be able to determine the properties of the particles crossing them. The Compact Muon Solenoid (CMS) is a general purpose detector located at the LHC. In order to measure the momentum of charged particles, detectors must record their trajectory. To this end, CMS has been designed to have two tracking detectors: the central sillicon tracker and the muon system. The latter is a tracking device dedicated to the identification of muons and the measurement of their momentum, by determining the curvature of their trajectory in a magnetic field. The bending of muons with energies of several hundreds of GeV, is close to a few hundreds of microns in magnetic fields of the order of 2-3 Tesla. For this reason, the position of the subdetectors integrating the muon system must be known to a precision of about 100-200 microns, in order not to degrade the momentum measurement. The process of measuring the position of subdetectors is called alignment.

The work presented in this thesis is related to the alignment of the barrel of the muon system of CMS, using techniques such as photogrammetry and track based alignment. As a result of this thesis, corrected geometries of the barrel muon system of CMS has been produced, and has been used in the official CMS reconstruction, resulting in a clear improvement of the muon reconstruction.

The thesis is structured in 10 chapters, as follows:

- **Chapter 1. Introduction.** This introduction.
- **Chapter 2. The Large Hadron Collider and the Compact Muon Solenoid.** A description of the LHC accelerator and the CMS detector will be provided, with special emphasis in the expected physics processes. Emphasis will be made to those aspects related to the work of this thesis, like the muon reconstruction or the computing infrastructure in CMS.
- **Chapter 3. Alignment of the CMS muon system.** This chapter will be divided in two different parts. The first will be related to some general aspects of the muon alignment in CMS. The second part of the chapter is more specific and will describe several developments performed for this thesis, and used in the rest of the chapters.
- **Chapter 4. Muon alignment scenarios for Monte Carlo simulations.** Simulations are needed in order to study the actual impact of misalignments in the physics analysis, using fake, misaligned detectors. This chapter explains how this is implemented, and which misalignment scenarios were produced for the several simulation campaigns of CMS.
- **Chapter 5. Internal alignment of drift tube chambers.** The barrel muon system is composed of drift tube chambers. The alignment of the internal structure of these devices is performed using a combination of photogrammetry measurements and track-based alignment. A description of the internal algorithm and the produced results will be provided.
- **Chapter 6. Alignment of drift tube chambers using photogrammetry measurements.** The photogrammetry measurements of targets attached to the chambers are processed to convert them into real alignment corrections for the chambers. In this chapter, this procedure will be described, and the results obtained will be shown.
- **Chapter 7. Standalone alignment of the muon system.** A track-based alignment algorithm was used to align barrel chambers with respect to themselves. A compilation of results in several commissioning and simulation campaigns of CMS will be given.
- **Chapter 8. Alignment of the drift tube chambers with respect to the tracker.** A description of a track-based alignment algorithm, aligning drift tube chambers with respect to the tracker will be provided. The performance of the algorithm will be shown in both simulated and real data.
- **Chapter 9. Full muon alignment geometries.** The geometries calculated along this work must be combined in order to produce a complete alignment description. This chapter describes how this combinations is performed.
- **Chapter 10. Conclusions.**

Chapter 2

The Large Hadron Collider and the Compact Muon Solenoid

The atomic origin of matter was established in the 18th century by John Dalton, who discovered that matter was composed of atoms of different species that could be classified according to their chemical properties. In the last decades of the 19th century, the atomic model was well established, and the different atomic species had been classified in the periodic table of the elements.

In the year 1896, Henri Becquerel observed how photographic plates were being affected by an unknown radiation emanating from uranium atoms. This phenomenon was extensively investigated in the following years by Pierre and Marie Curie, and by Ernest Rutherford and it was established that there were three different types of radiation involved: α, β and γ rays.

In parallel with these investigations, J.J. Thomson was extending the work on the radiation that had been observed when electric fields were applied between electrodes in vacuum glass tubes. Thomson was able to finally measure the properties of these 'cathode rays', currently known as electrons, and determined their mass and charge. Thomson proposed an atomic model in which the atoms were composed by a region of positive charge filling the entire volume of the atom, with some electrons embedded.

In 1911, Rutherford and his collaborators performed a series of experiments, consisting in the scattering of α-particles by thin gold foils. It was observed that sometimes the α-particles scattered with a very large deflection angle (> 90 deg). This experimental result could only be explained if the positive charge of the atom was confined in a very small region of the total volume of the atom. Rutherford suggested a planetary model of the atom, in which electrons orbited a positively-charged nucleus. In the case of hydrogen, the nucleus was composed by a proton, a particle with electric charge opposite to electrons. Heavier atoms were considered to have nuclei consisting of several protons.

During the first decades of the 19th century, Quantum Mechanics and Relativity were developed. Quantum Mechanics was formulated on the basis of Max Plank's work on the black body radiation, where it was established that the energy transported by radiation was a discrete variable, and only multiples of a basic 'quantum' energy (called photons) were permitted. Bohr, in 1913, used the quantization idea to propose an atomic model that explained the spectral line emission of atoms. Schr"odinger and Heisenberg, independently developed a mathematical framework describing the dynamics of quantum systems. Relativity, on the contrary, was developed by Albert Einstein in the year 1915 setting a new dynamic framework over-seeding the classical framework based on Newton dynamics.

In the decade of 1930, the study of isotopic nucleus leaded Chadwick to the discovery of the neutron as one of the components of nuclei. Enrico Fermi, to explain the apparent non-conservation of the energy in β-decays, postulated the existence of a new particle, that was called neutrino. In the same years Quantum Mechanics and Relativity were successfully applied to several subatomic systems. In particular, theoretical developments, based on the application of Quantum Mechanics to relativistic systems, yielded Dirac to a dynamic description of electrons in which physical observables like the spin were contained. This description predicted as well the existence of antimatter, that was confirmed by Anderson's discovery of the positron in 1932. During the same decade, studies on the Cosmic Ray radiation, revealed the existence of a new unstable particle called muon. In the 1940s Richard Feynman stated the basis of quantum electrodynamics, model which explains the interactions between photons and electrons.

Technological developments, starting from 1950 enabled the possibility of producing high-energy particle beams in the laboratory, and hence a wide range of scattering experiments could be performed. By the 1960s this had resulted in the discovery of a very large number of unstable particles with very short lifetimes. Murray Gell-Mann and George Zweig suggested the quark model, that established that the new particles were bound states of three families of more fundamental physical particles, called quarks. Bound states of quarks, were named Hadrons.

In the 1960s Sheldon Glasgow, Steven Weinberg and Abdus Salam proposed a model of particle physics, currently known as the Standard Model [1, 2, 3, 4], in which the fundamental components of matter were composed by two different types of particles: leptons and quarks. There are three leptonic families: the electron, the muon and the tau particles, with their counterpart neutrinos. There are as well three families of quarks with different 'flavors': up and down, strange and charm, and top and bottom. Forces in nature are transmitted through the interchange of particles: the photon for the electromagnetic force, the Z and W bosons for the weak force, and gluons (G) for the strong force. In addition, a new particle, known as Higgs bosons was predicted as part of the mechanism that allows the rest of the particles to acquire mass. As modern particle colliders were increasing their accelerating power most of the particles predicted by the Standard Model were observed. It is remarkable the discovery of the electroweak bosons W and Z in 1981, and the observation in 1995 of the latest and heaviest quark, the Top quark.

Nowadays the Standard Model is considered as a successful theory up to the energies achieved in modern colliders so far $\simeq$ TeV. Nevertheless a further investigation is still required in order to understand the nature of the electroweak symmetry breaking phenomena, in which particles acquire mass and for which the Higgs Mechanism [5, 6, 7, 8, 9, 10, 11], not observed yet, is presumed to be responsible. The latest particle collider, the Large Hadron Collider [12] was designed and constructed with the main motivation of seeking the TeV scale to find an experimental explanation of this electroweak symmetry breaking phenomena, that could be the Higgs Mechanism as expected by the Standard Model, some of the known alternatives to the Standard Model like SuperSymmetry [13] or Technicolor [14], or even some unknown mechanism.

Hadron colliders are suitable machines to explore new domains of energy. In particular, the LHC was originally designed to provide proton beams with an energy of 7 TeV yielding an energy of 14 TeV in the center of mass reference and with a luminosity of $10^{34}\mathrm{s}^{-1}\mathrm{cm}^{-2}$ which guarantees the possibility of producing extremely unusual events. The LHC has also the functionality of accelerating heavy-ions instead of protons, producing collisions with a center-of-mass energy 30 times higher than in the current experiments. This feature allows the LHC to have a complete program in heavy-ion collisions to include studies about the hot nuclear matter.

To detect and measure the properties of the products of the collision, large detectors are built around the four collision points of the accelerator. This task involves several technologies, ranging from detection techniques, to the computational framework in charge of the selection, processing and storage of the registered information. The Compact Muon Solenoid (CMS) [15] is a general-purpose particle detector installed at the LHC and designed specifically to be a very powerful and precise muon spectrometer.

In this chapter a brief introduction to both the LHC accelerator and the CMS detector will be given, with the aim of setting the context of the work presented in this thesis.

2.1 The LHC machine

The LHC is a circular proton-proton collider with a length of 27 Km, located 100 m underground across the Swiss and French borderline near the city of Geneva. The total length of the accelerator is formed by 8 circular sectors of 2460 m length, connected through 4 straight regions of 540 m, where the experiments are located. The machine comprises 1232 dipole magnets, with radio frequency cavities providing a kick that produces an increase in the proton energy of 0.5 MeV/turn.

Two different beams are accelerated in opposite directions colliding at 4 points where the 4 experiments are built: ALICE [16], CMS, LHC-b [17] and ATLAS [18]. A schematic view of the LHC accelerator is shown in figure 2.1.

The number of events produced per second in a collider is given by the product of the specific probability of that event (given as a cross section) and a magnitude known as the luminosity. The luminosity of a circular collider like the LHC is given by:

$$L = \frac{\gamma f k_B N_p^2}{4\pi\epsilon_n \beta\star} F \tag{2.1}$$

where γ is the Lorentz factor, f is the revolution frequency, k_B is the number of bunches, N_p is the number of protons/bunch, ϵ_n is the normalized transverse emittance, $\beta^\star$ is the betatron function at the interaction point (IP), and F is the reduction factor due to the crossing angle (beams collide with a relative inclination).

The nominal energy of each proton beam is 7 TeV and the design luminosity of L=10^{34} $\mathrm{cm}^{-2}\mathrm{s}^{-1}$ leads to around 1 billion proton-proton interactions per second. The values for some of the

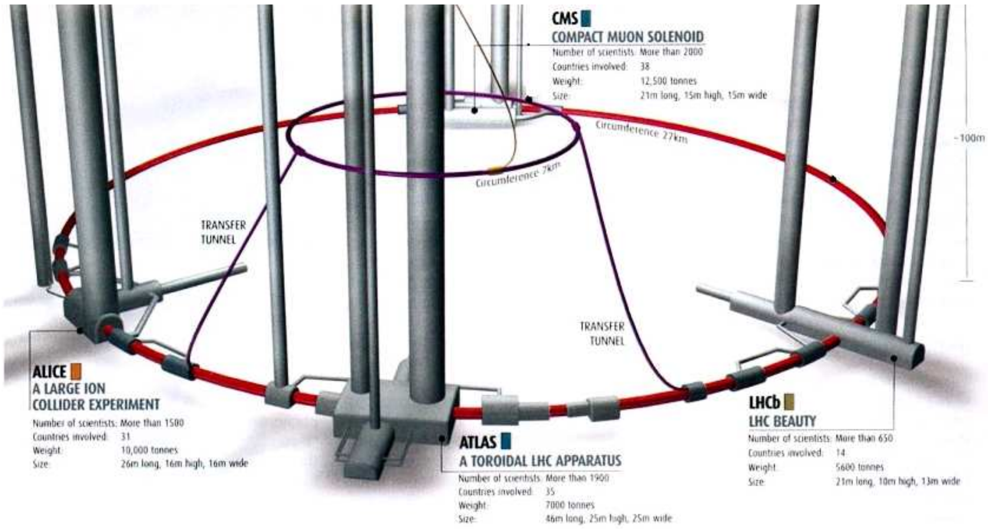

Figure 2.1: Schematic view of the LHC accelerator including the location of the four experiments.

		pp	HI
Energy per nucleon	E	7 TeV	2.76 TeV
Dipole field at 7 TeV	B	8.33 T	8.33 T
Design Luminosity	L	10^{34} cm^{-2}s^{-1}	10^{27}cm^{-2}s^{-1}
Bunch separation	k_B	25 ns	100 ns
No. of bunches	k_B	2808	592
No. particles per bunch	N_p	1.15×10^{11}	7.0×10^{7}
Collisions			
β -value at IP	$\beta^\star$	0.55 m	0.5 m
RMS beam radius at IP	$\sigma^\star$	16.7μm	15.9μm
Luminosity lifetime	τ_L	15 hr	6 hr
Number of collisions/crossing	n_c	$\simeq 20$	-

Table 2.1: Operation parameters of the LHC machine. All the numbers in the table correspond to design values.

most significant parameters of the LHC can be found at the table 2.1.

These parameters ensure the capability of the LHC to seek into the TeV region producing a sufficient number of interesting events. The LHC collides protons with protons instead of protons and antiprotons as previous hadron colliders. This allows to achieve a higher luminosity avoiding the large effort needed to produce a bunch of antiprotons. At this high energy, most of the momentum of a proton is carried by gluons, and the gluon content is similar in protons and antiprotons.

The LHC is the last step of a complex of accelerators as can be seen in figure 2.2. From the first linear accelerators, to the LHC, the protons obtain the proper energy and then are injected in successive phases into the next accelerator. This process configures the bunch structure of the beam through the injection scheme and the properties of the dump system. In particular, the bunches are formed in the 26 GeV Proton-Synchrotron (PS) with an spacing of 25 ns, and then are accelerated to 450 GeV in the Super Proton Synchrotron (SPS) before being injected into the LHC.

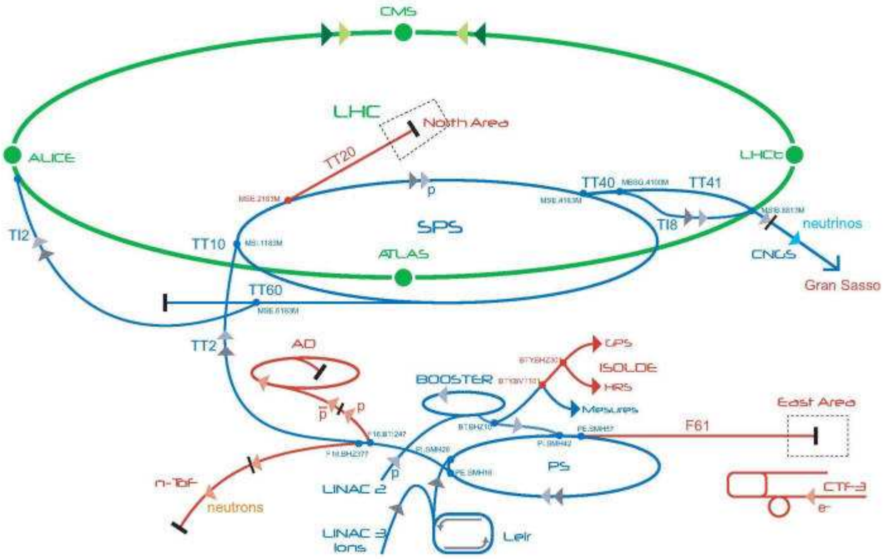

Figure 2.2: General view of the CERN accelerator complex. The properties of the beam are configured through the different acceleration steps in the chain.

In December 2009, the LHC started to produce the first proton-proton collisions. The energy of the beams was fixed to 450 GeV, yielding to a center of mass energy of $\sqrt{s}$ =0.9 TeV. The luminosity for these first runs was kept several orders of magnitude below the nominal value 10^{34}cm^{2}s^{-1}. The energy of the beams was increased along December until a center of mass energy of $\sqrt{s}$ =2.2 TeV was reached, becoming the most powerful hadron accelerator ever built. The four particle detectors installed at the LHC were able to record the products of the collisions. Figure 2.3 shows the first proton-proton collision recorded by the Compact Muon Solenoid (CMS) detector. At the end of March 2010, the LHC started to produce collisions with $\sqrt{s}$ =7 TeV.

2.2 Physics at the LHC

A wide range of physics is potentially possible with the seven–fold increase in energy and 2 hundred–fold increase in integrated luminosity over the previous hadron collider. The approximate total proton–proton cross section at the design energy, $\sqrt{s}$ = 14 TeV, is roughly 100 mb. Figure 2.4 shows the cross section and production rates associated to some of the most interesting potential processes expected in the LHC. Channels with hadronic decays are difficult to use for discovery due to large QCD backgrounds and the limited energy resolution available for hadronic jets. Decays into lepton or photons are preferable, despite the smaller branching ratios.

The Physics program for the two general purpose detectors is the following:

- Study of the the electroweak symmetry breaking mechanism through the detection of one or more Higgs bosons, or through some alternative or new mechanism.

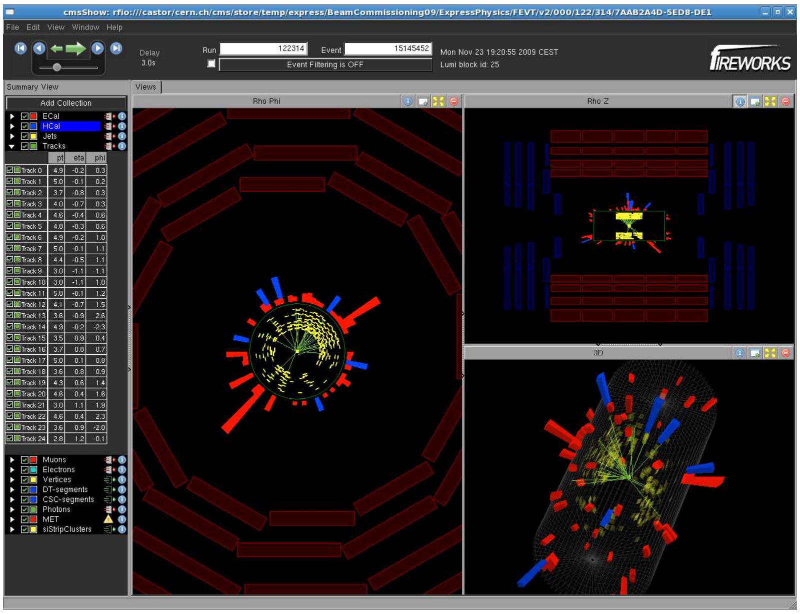

Figure 2.3: Minimum bias event from the first proton-proton collision recorded in CMS. Yellow points represent hits in the central sillicon tracker, while red and blue bars represent the energy deposited in the hadronic and electromagnetic calorimeters respectively.

- Search for new physics beyond the Standard Model: SuperSymmetry, extra-dimensions [19], Technicolor, etc.
- Detailed studies of the Standard Model physics, especially regarding multi-jet QCD and physics of the top quark.
- CP violation on the B-sector in order to perform precise measurements of the Cabibbo-Kobayashi-Maskawa (CKM) mixing matrix [20].
- Properties of the quark-gluon plasma in heavy ion collisions.

The other two experiments are more restrictive and dedicated to more specific studies. The LHC-b detector has been designed to study the physics of the B-mesons and hence the origin of the matter and antimatter asymmetry, while ALICE is dedicated to the study of quark-gluon plasma produced in heavy ion collisions.

2.3 Physics goals for the Compact Muon Solenoid

The Compact Muon Solenoid is a general purpose detector installed at P5 (point 5) in the proximity of the village of Cessy in the France countryside. The main distinguishing features of CMS are a high-field solenoid, a full silicon-based inner tracking system, a fully active scintillating crystals-based electromagnetic calorimeter, and a muon system installed in the return yoke.

The detector requirements for CMS to meet the goals of the LHC physics program can be summarized as follows:

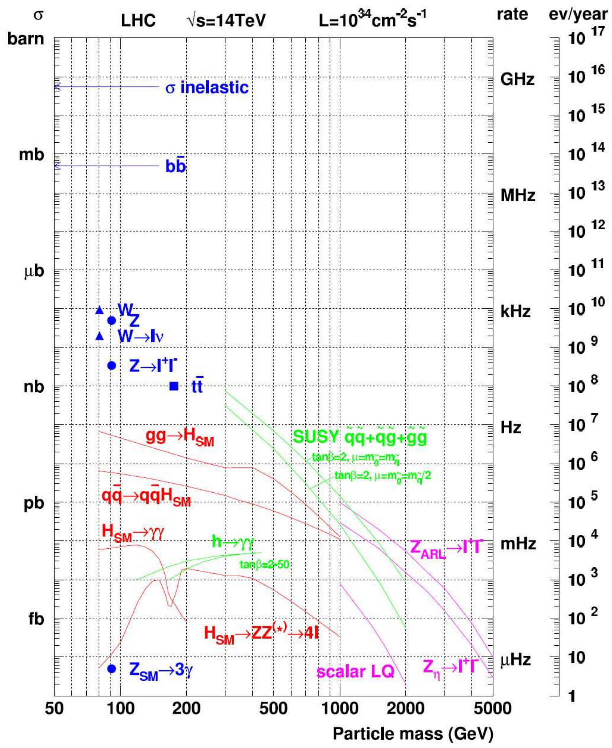

Figure 2.4: Expected cross section for some of the most interesting processes at the LHC.

- Good muon identification and momentum resolution over a wide range of momenta in the region $|\eta| < 2.5$, good di-muon mass resolution $\simeq 1\%$ at 100 GeV/c^2, and the ability to determine unambiguously the charge of muons with p $<$ 1 TeV/c.

- Good charged particle momentum resolution and reconstruction efficiency in the inner tracker. Efficient triggering and offline tagging of taus and b-jets, requiring pixel detectors close to the interaction region.

- Good electromagnetic energy resolution, good di-photon and di-electron mass resolution ($\simeq 1\%$ at 100 GeV/c^2), wide geometric coverage ($|\eta| < 2.5$), measurement of the direction of photons and/or correct localization of the primary interaction vertex, π^0 rejection and efficient photon and lepton isolation at high luminosity.

- Good E_T and di-jet mass resolution, requiring hadron calorimeters with a large hermetic geometric coverage ($|\eta|$ <5) and with fine lateral segmentation ($\Delta\eta \times \Delta\phi < 0.1{\times}0.1$).

The Compact Muon Solenoid, has been designed to give answers on the most important questions in high energy physics. The different subdetectors have been designed and optimized to best measure the physical signatures of these processes [21]. The understanding of the origin of mass will be a central issue but CMS will also cover a much wider high energy physics spectra. If SuperSymmetry (SUSY) is a true symmetry of Nature, and it is realized at the TeV scale, it will almost certainly be seen in CMS. CMS will also study subjects as B–physics, heavy ions with interesting phenomena of gluon plasma production, top physics, electro–weak precision tests and measurements of parton distribution functions. In the following subsections some interesting examples of physics process accessible to LHC and CMS are given.

2.3.1 Higgs physics

A key feature of the Standard Model of particle physics is the existence of the Higgs boson. The detection of this particle was a primary design consideration for CMS. The Higgs boson couples to the rest of the particles giving place to mass terms. The theory does not predict the mass of the Higgs, but it does predict its production rate and decay modes for each possible mass. However it is possible to set mass limits attending to current measurements. Indirect bounds based on precision electroweak measurements [22] and direct searches favor low Higgs masses, in the range of 100–200 GeV. LEP direct search [23] set a lower mass limit at 114 GeV. The latest analysis of data [24] from the CDF [25] and D0 [26] experiments at Fermilab excludes the range between 160 and 170 GeV, at a confidence level of 95%. The CMS detector can probe the entire mass range up to m_{Higgs} ∼1 TeV with a signal significance well above 5σ.

According to the SM, Higgs boson production will take place via four main processes at the LHC: gluon fusion ($gg \rightarrow$H), top–quark fusion ($gg \rightarrow$H$t\bar{t}$), weak boson fusion ($qq \rightarrow$Hqq) and weak boson bremsstrahlung ($q\bar{q'} \rightarrow$HW). Fig. 2.5(a) shows the SM Higgs production cross section. Gluon fusion is dominant for Higgs boson masses up to about 700 GeV. Weak boson fusion becomes significant for a higher Higgs mass. This process involves central, high p_T hadronic jets in the final state, a distinct feature that can be used to suppress backgrounds.

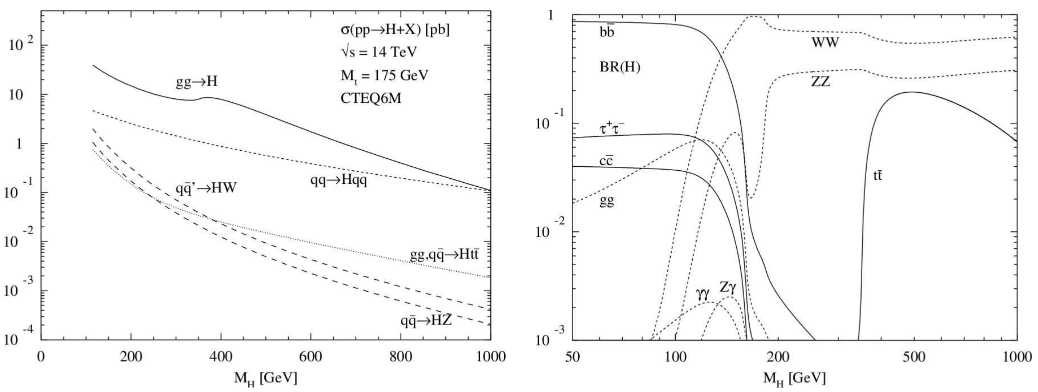

(a) (b)

Figure 2.5: Higgs boson production channel cross sections (a) and decay branching ratios ratios as a function of mass (b)

The branching ratios of the most likely Higgs boson decay channels are shown in figure 2.5(b). In the low mass range (m_H < 120 GeV), hadronic decays dominate. These channels are difficult to use for discovery due to large QCD backgrounds and the poor energy resolution available for hadronic jets. Instead, decays into lepton or photons are preferable, despite the smaller branching ratios. In the intermediate and high mass range (120 GeV <m_H), the signal resolution will be dominated by decays to W and Z. Here, the two photon or ZZ* decay modes are the most promising and the detection of the decay products, muons and photons in particular, will become crucial at this mass ranges.

Depending on the Higgs mass, different experimental signatures will arise. The three most promising channels are H→ $\gamma\gamma$, H→WW*→2$l^{\pm}$, and H→ZZ*→4$l^{\pm}$, specially the 4μ channel is considered the golden channel for Higgs masses above the ZZ threshold.

2.3.2 SuperSymmetry

Even though the SM describes existing data very precisely, it is known that this model is incomplete. One problem of the SM is the instability of the Higgs boson mass under radiative corrections in the Planck scale ($\sim 10^{19}$ GeV). This divergence disappears in SuperSymmetry, because of cancellations between the virtual effects of SM particles and their supersymmetryc partners.

Extrapolating the coupling strength of the fundamental forces measured at mass scales of a few 100 GeV to energy scales relevant for cosmology (about 10^{15} to 10^{19} GeV) does not lead to unification in the SM. However unification of the electromagnetic, weak and strong forces at the GUT scale ($\sim 10^{15}$ GeV) is predicted in SuperSymmetry.

SuperSymmetry (often abbreviated as SUSY) is a symmetry that interchanges bosons and fermions. In supersymmetryc theories, every fundamental fermion has a bosonic super–partner and vice versa. If SUSY exists at the electroweak scale, then its discovery at the LHC should be straightforward. The SUSY cross section is dominated by gluinos and squarks production, which are strongly produced with large cross sections. Gluinos and squarks then decay via a series of steps into the Lightest SUSY Particles (LSP). These decay chains lead to a variety of signatures involving multiple jets, leptons, photons, heavy flavors, W and Z bosons, and missing energy. The combination of a large production cross section and distinctive signatures makes it easy to separate SUSY from the Standard Model background. Therefore, the main challenge is not only to discover SUSY, but to separate the many SUSY processes that occur and to measure the masses and other properties of the SUSY particles.

2.3.3 New Heavy Gauge Bosons

Additional heavy gauge bosons (W' and Z') are predicted in many superstring-inspired models and grand unified theories (GUTs), as well as in dynamical symmetry breaking and little Higgs models. There are no reliable theoretical predictions however of their mass scale. Because its striking experimental signature $Z' \to \mu\mu$ is considered a benchmark process. Current lower limits on the Z' mass are (depending on the model) of the order of 600-900 GeV. The mass region up to about 1 TeV is expected to be explored at the Tevatron in Fermilab. The LHC offers the opportunity to search for Z' bosons in a mass range significantly larger than 1 TeV.

2.4 The morphology of the Compact Muon Solenoid

The overall layout of CMS can be seen in figure 2.7. The inner part of CMS is occupied by a fully silicon tracker with a length of 5.8 m and a diameter of 2.9 m. In the region close to the beam pipe three layers of silicon pixel detectors were placed to improve the measurement of the vertex of the collision and the secondary vertices. The EM calorimeter (ECAL) was installed outermost to the tracker and increasing in radius from the interaction point in order to measure photons and electrons. The ECAL is surrounded by a brass/scintillator sampling hadron calorimeter (HCAL) able to measure the energy of hadronic particles. The solenoid of the superconducting magnet is located surrounding the HCAL. This magnet is able to produce a 3.8 T magnetic field in the inner region of CMS, curving the charged particles and

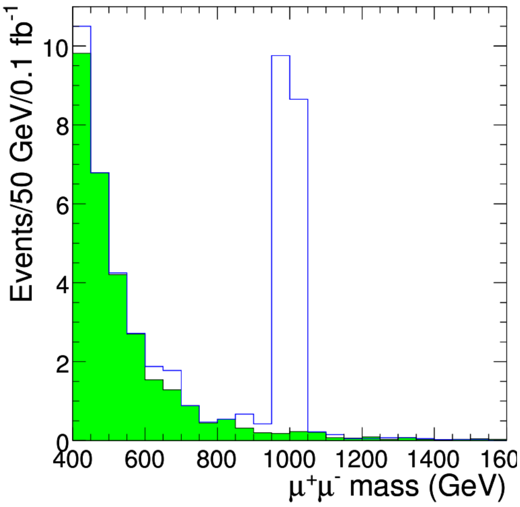

Figure 2.6: Di-muon invariant mass showing the Z' resonance.

allowing the measurement of the momentum. The field lines of the solenoid return through the iron wheels surrounding it. A muon system is installed in the return yoke to produce a precise and fast muon identification and muon momentum measurement.

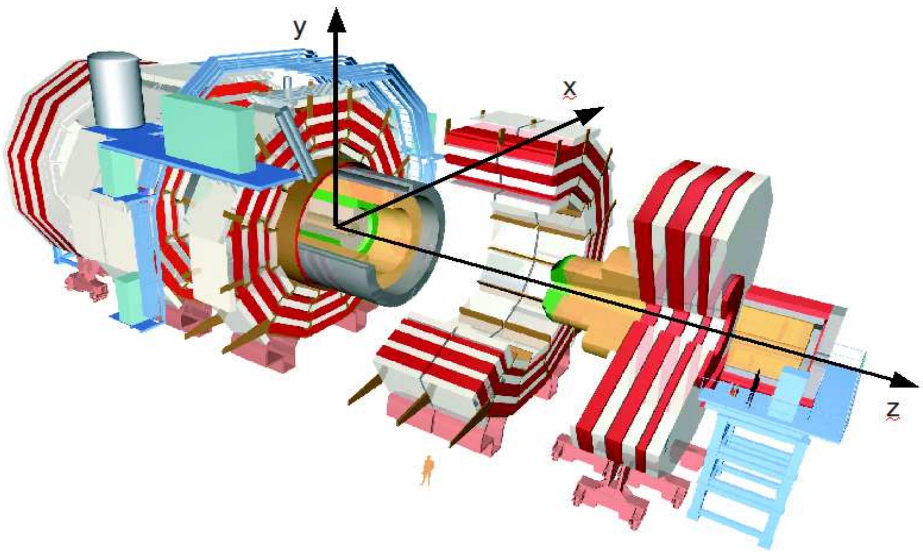

Figure 2.7: Schematic view of the Compact Muon Solenoid. From the innermost region to the outermost, the central silicon tracker, electromagnetic and hadronic calorimeters, the solenoid and the muon system can be found.

All the different subsystems of CMS share a common spatial system of coordinates. The Z axis of this system is defined to be coincident with the beam line, while the X axis is pointing to the geometric center of the LHC ring, and the Y axis is orthogonal to the ground, as sketched in figure 2.7. This system will be referred to as the global CMS system of coordinates.

2.4.1 The magnet system

The design of CMS is driven by the configuration of the magnetic field. The bending power experienced by charged particles in CMS is achieved through a very strong central magnetic field of 3.8 T parallel to the beam line. This selection forces CMS to have a compact and dense structure allowing the return of the magnetic flux.

The CMS magnet system [15, 27] is the conjunction of a superconducting coil embedded within a vacuum tank, surrounded by the return iron yoke. The magnet coil is a 13 m long, 6 m inner diameter, 3.8 T superconducting solenoid (19.5 kA) providing a large bending power. The distinctive feature of the 220 tones cold mass is the four–layer winding made from a established reinforced NbTi conductors. The ratio between stored energy and cold mass is high, 11.6 KJ/Kg, causing a large mechanical deformation (0.15%) during energizing, well beyond the values of previous solenoidal detector magnets.

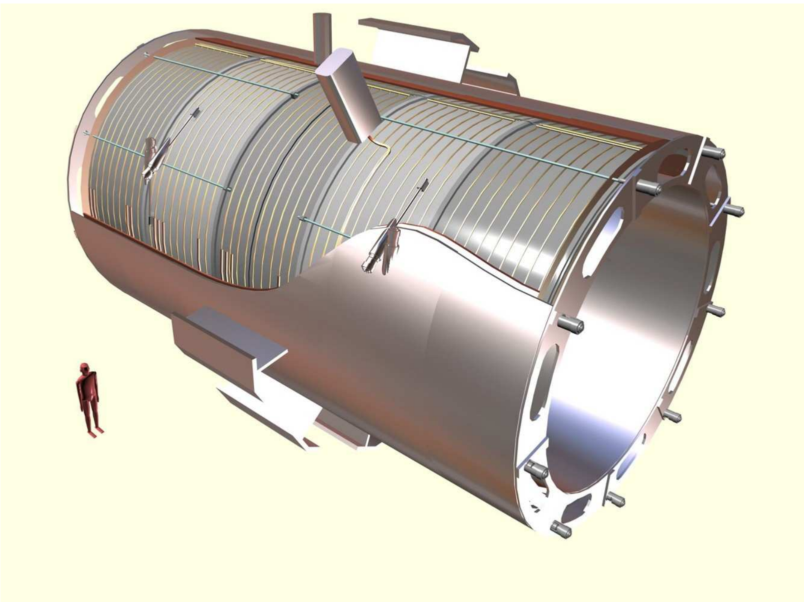

Figure 2.8: Vacuum tank in which the superconducting solenoid is contained. This structure is inserted in the central wheel of CMS.

The magnet flux is returned through the yoke comprising 5 wheels and 2 endcaps, composed of three disks each. The barrel part is formed by 5 vertical rings. The central one (YB0) supports the vacuum tank, within which, the coil is housed (see 2.8). The forward endcap disks are independent from each other, allowing thus access to CSC chambers. The weight of the wheels and disks goes from 400 tones for the lightest up to 1920 tones for the central wheel, which includes the coil and its cryostat.

2.4.2 The CMS central tracker

The central tracking system of CMS [15, 28] is designed to provide an efficient measurement of the trajectories of charged particles emerging from the LHC collisions, as well as a precise reconstruction of secondary vertices. It is placed around the interaction point, very close to the beam pipe, and its length and diameter are 5.8 m and 2.4 m respectively. The design of the tracker is mainly driven by the features of the LHC accelerator. At the design luminosity there will be on average $\sim$ 1000 charged particles from more than 20 overlapping proton–proton interactions traversing the tracker at each bunch crossing. A very high granularity is needed to identify the different trajectories and a very fast response in order to assign them to the correct bunch crossing. However, these features imply a high power density of the on–detector electronics which in turn requires efficient cooling. This is in direct conflict with the aim of keeping to the minimum the amount of material in order to limit multiple scattering, bremsstrahlung, photon conversion and nuclear interactions. A compromise had to be found in this respect. The intense particle flux will also cause severe radiation damage to the tracking system. The main challenge in the design of the tracking system was to develop detector components able to operate in this hard environment for an expected lifetime of 10 years. These requirements on granularity, speed and radiation hardness lead to a tracker design entirely based on silicon detector technology. Together with the electromagnetic calorimeter and the muon system the tracker has to identify electrons and muons. In order to reduce the event rate from the LHC bunch crossing, tracking information will be heavily used in the high level trigger of CMS.

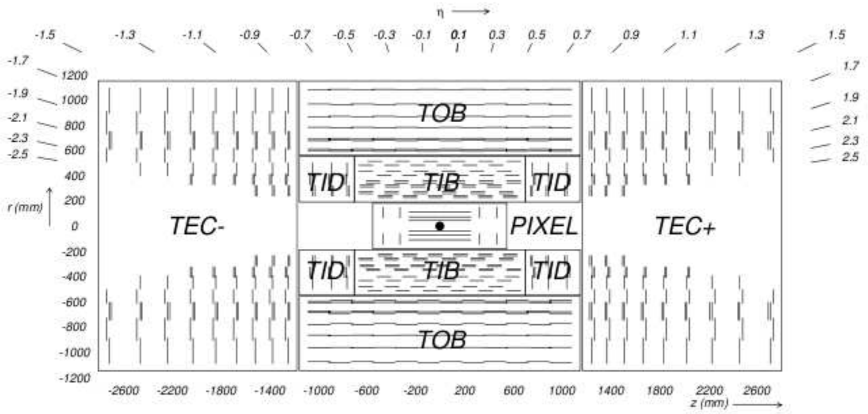

Figure 2.9: General layout of the silicon tracker.

Figure 2.9 shows an schematic view of the central tracking system. At a radius between 4.4 and 10.2 cm, three cylindrical layers of pixel detector modules surround the interaction point. They are complemented by two disks of pixel modules on each side. The silicon strip tracker is at the radial region between 20 cm and 116 cm. It is composed of three different subsystems: the Tracker Inner Barrel (TIB) and the Tracker Inner Disks (TID) which are composed of 4 barrel layers up to R = 55 cm, supplemented by 3 disks at each end. The TIB/TID is surrounded by the Tracker Outer Barrel (TOB). It has an outer radius of 116 cm and consists of 6 barrel layers, it extends until Z = $\pm$118 cm. Beyond this Z range the Tracker EndCaps (TEC+ and TEC-) cover the region 124 cm $<| Z |<$ 282 cm and 22.5 cm $<| R |<$ 113.5 cm. Each TEC is composed of 9 disks.

The Pixel detector

The pixel system is the part of the tracking system that is closest to the interaction region. It contributes precise tracking points in $r\phi$ and z and therefore is responsible for a small impact parameter resolution that is important for a good secondary vertex reconstruction. The size of the pixel cells is 100 μm$\times$150 μm resulting in a similar resolution for both the $r\phi$ and z projections, which allows an effective 3D reconstruction of the secondary vertices. The pixel detector covers a pseudorapidity range -2.5$< \eta <$2.5, matching the acceptance of the central tracker.

The Silicon Strip Tracker

The Silicon strip tracker surrounds the pixel system. In order to equip all regions in the CMS tracker, 15 different sensor geometries are needed: two rectangular sensor types each for TIB and TOB, and 11 wedge-shaped sensor types for TEC and TID. They have either 512 or 768 strips, reflecting the read-out modularity of 256 channels (two 128-channel front-end chips multiplexed to one read-out channel). Since the sensors are fabricated on 6 inch wafers, they can be made rather large. Typical dimensions are for instance about 6$\times$12 cm^2 and 10$\times$9 cm^2 in the inner and outer barrel, respectively. The total number of silicon sensors in the strip tracker is 24244, making up a total active area of 198 m^2, with about 9.3 million of strips.

2.4.3 The CMS Electromagnetic Calorimeter

The electromagnetic calorimeter of CMS (ECAL) [15, 29] is a hermetic homogeneous calorimeter made of 61200 lead tungstate (PbWO4) crystals mounted in the central barrel part, closed by 7324 crystals in each of the two endcaps. A preshower detector is placed in front of the endcap crystals. Avalanche photodiodes (APDs) are used as photodetectors in the barrel and vacuum phototriodes (VPTs) in the endcap. The use of high density crystals has allowed the design of a calorimeter which is fast, has fine granularity and is radiation resistant, all important characteristics in the LHC environment. One of the driving criteria in the design was the capability to detect the decay to two photons of the postulated Higgs boson. This capability is enhanced by the good energy resolution provided by a homogeneous crystal calorimeter.

Figure 2.10 is a 3D schema view of the ECAL detector, which can be subdivided into barrel, endcap and preshower. The barrel part of the ECAL (EB) covers the pseudorapidity range $\mid \eta \mid < 1.479$. The crystal cross-section corresponds to 22$\times$22 mm^2 at the front face of crystal, and 26$\times$26 mm^2 at the rear face. The crystal length is 230 mm corresponding to 25.8 X_0. The barrel crystal volume is 8.14 m^3 and the weight is 67.4 t. The centers of the front faces of the crystals are at a radius 1.29 m.

The endcaps (EE) cover the pseudorapidity range $1.479 < \mid \eta \mid < 3.0$. The longitudinal distance between the interaction point and the endcap is 315.4 cm. Each endcap is divided into 2 halves, or Dees. Each Dee holds 3662 crystals. The crystals are arranged in a rectangular X–Y grid, with the crystals pointing at a focus 1300 mm beyond the interaction point, giving off–pointing angles ranging from 2 to 8 degrees. The crystals have a rear face cross section 30$\times$30 mm^2, a front face cross section 28.62$\times$28.62 mm^2 and a length of 220 mm (24.7 X_0). The endcaps crystal volume is 2.90 m^3 and the weight is 24.0 tones.

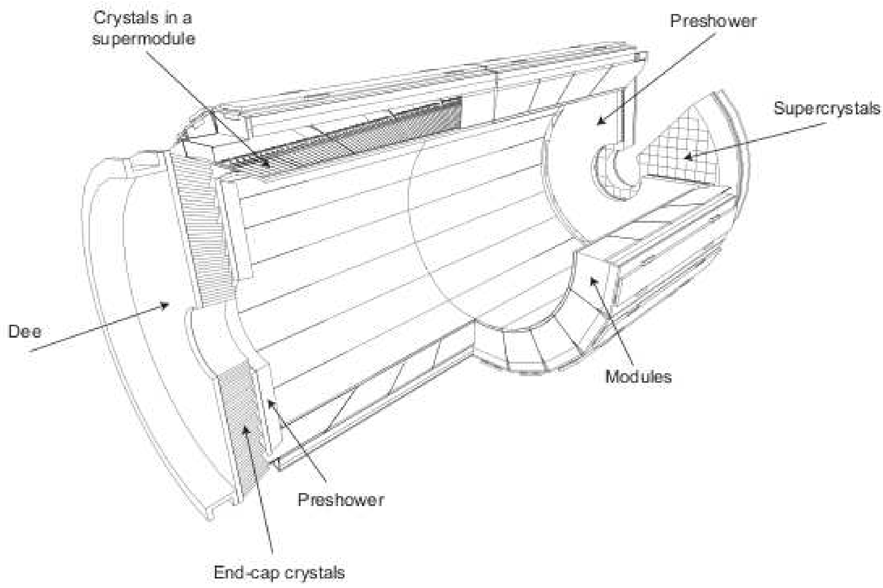

Figure 2.10: Schematic view of the electromagnetic calorimeter. The barrel, endcap and preshower components can be distinguished clearly.

The aim of the preshower detector is to identify neutral pions in the endcaps at the region $1.653 <| \eta |< 2.6$. It also helps the identification of electrons against minimum ionizing particles, and improves the position determination of electrons and photons with high granularity. The preshower is a sampling calorimeter with two layers: lead radiators initiate electromagnetic showers from incoming photons/electrons while silicon strip sensors placed after each radiator measure the deposited energy and the transverse shower profiles. The total thickness of the preshower is 20 cm.

2.4.4 The CMS hadronic Calorimeter

The Hadronic Calorimeter (HCAL)[15, 30] will play a role in the identification and measurement of quarks, gluons and neutrinos by measuring the energy and direction of jets and missing transverse energy flow in events. The design of the hadron calorimeter requires good hermeticity, good transverse granularity, moderate energy resolution and sufficient depth for hadron shower containment. The hadron calorimeter is made of copper layers interleaved with scintillator material.

Figure 2.11 is a longitudinal cut of a quarter of CMS plane with the hadron calorimeter mark on it. As seen from the interaction point, the hadron calorimeter barrel (HB) and endcaps (HE) are behind the tracker and the electromagnetic calorimeter. The barrel is radially restricted between the outer part of the electromagnetic calorimeter (R = 1.77 m) and the inner part of the magnet coil (R = 2.95 m). This constrains the total amount of material which can be put in to absorb the hadronic shower. Therefore, an outer hadron calorimeter (HO) or tail catcher is placed on the central wheel, YB0, outside the solenoid complementing the barrel calorimeter. The forward hadron calorimeters (HF) placed at 11.2 m from the interaction point extend the pseudorapidity coverage down to $| \eta | \approx 5.2$ using a Čerenkov–based radiation–hard technology.

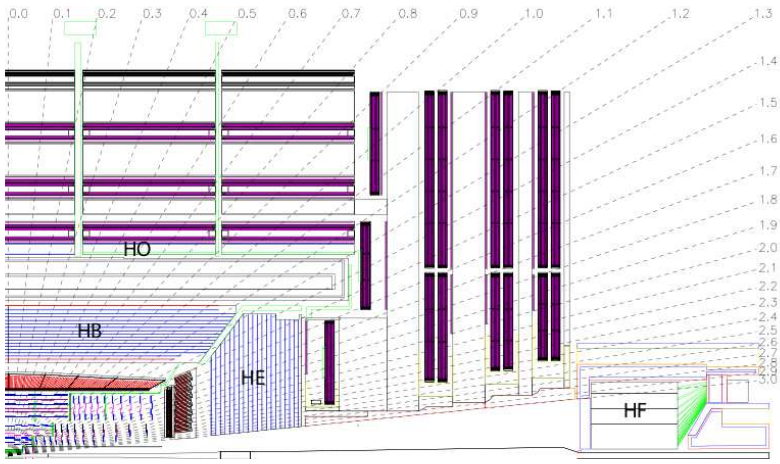

Figure 2.11: Longitudinal cut of a quarter of CMS. The HB and HE components are surrounding the ECAL calorimeter, while the HO is located at the central wheel and outside the solenoid, and the HF behind the last station of the muon system.

The HB is mounted inside the 3.8 T field. The plastic scintillator is divided into 16 η sectors, resulting in a segmentation $(\Delta\eta, \Delta\phi) = (0.087, 0.087)$, covering $\eta <$ 1.3. It consists of 36 identical azimuthal wedges which form the two half–barrels (HB+ and HB-). Each wedge is a 20 degree stack.

The endcap calorimeters, HEs, are attached to the muon endcaps and have about 10 interaction lengths. They are about 1.8 m thick, with an inner radius of 40 cm and outer radius of about 3 m. The η–ϕ segmentation matches the central barrel, except near the $\mid \eta \mid = 3$ region, where the segment size is 0.17×0.17. There are 19 layers of scintillator.

The HF, at $3 <\mid \eta \mid< 5.2$, is made of iron and quartz fibers as active media. It resides in a very high radiation area and therefore cannot be constructed of conventional scintillator and waveshifter materials. Hadronic showers are sampled at various depths by the quartz fibers, of selected lengths, which are inserted into the absorber plates. The energy of jets is measured from the Čerenkov light signals produced as charged particles pass through the quartz fibers. These signals result mainly from the electromagnetic component of showers, which results in excellent directional information for jet reconstruction. Fiber optics transport the Čerenkov signals to photomultiplier tubes located in radiation shielded zones to the side and behind each calorimeter. For the very forward detectors, conventional photomultiplier tubes are used.

2.4.5 The Muon System

Muon detection is a powerful tool to recognize signatures of interesting processes over the very high background rate expected at the LHC with full luminosity. For example, the predicted decay of the Standard Model Higgs boson into ZZ or ZZ*, which in turn decay into 4 leptons, has been called "gold plated" for the case in which all the leptons are muons. This example, and others from SUSY models, emphasize the discovery potential of muon final states and the necessity for wide angular coverage for muon detection.

The muon system has three purposes: muon identification, momentum measurement, and triggering. The system is designed [15, 31] to have the capability of reconstructing the momentum and charge of muons over the entire kinematic range of the LHC.

The structure of the muon system is composed by two different regions: the barrel, cylindrically shaped around the beam line, and the two planar endcaps closing the detector at the two sides.

In the barrel region, where the neutron–induced background is small, the muon rate is low and the 3.8 T magnetic field is mostly contained in the steel yoke, drift chambers with standard rectangular drift cells are used. The barrel drift tube (DT) chambers cover the pseudorapidity region $|\ \eta\ | < 1.2$ and are organized into 4 stations interleaved among the layers of the flux return plates.

In the two endcap regions of CMS, where the muon rates and background levels are high and the magnetic field is large and non–uniform, the muon system uses cathode strip chambers (CSC). With their fast response time, fine segmentation, and radiation resistance, the CSCs identify muons between $0.9 <|\ \eta\ |< 2.4$. There are 4 stations of CSCs in each endcap, with chambers positioned perpendicular to the beam line and interleaved between the flux return plates.

The trigger capabilities of both types of detectors is complemented with the use of gaseous parallel–plate chambers (Resistive Plate Chambers, RPC). They combine a moderated spatial resolution with excellent time resolution. RPCs provide a fast, independent, and highly–segmented trigger. Trigger signals coming from the DT, CSCs and the RPCs will proceed in parallel to the Global Trigger in order to perform efficient rejection of background, track identification and selection over the transverse momentum of muons.

Muon barrel system: Drift Tube Chambers

The CMS barrel muon detector consists of 4 stations forming concentric cylinders around the beam line (see figure 2.12). The three inner cylinders have 60 drift chambers each and the outer cylinder has 70. There are about 172000 sensitive wires. In each of the 12 sectors of the yoke there are 4 muon stations per wheel, labeled MB1, MB2, MB3 and MB4. The yoke–iron supports between the chambers of a station generate 12 unavoidable dead zones in ϕ coverage. To reduce dead zones, the geometry is designed to overlap in ϕ.

A drift tube (DT) chamber is made of 3 superlayers (SL) or 2 in the case of chambers in station 4. Each superlayer is made of 4 layers of rectangular drift cells. Figure 2.13 left is a view of a chamber in the (Rϕ) plane. The wires in the 2 outer SLs are parallel to the beam line and provide a track measurement in the magnetic bending plane (Rϕ). In the inner SL, the wires are orthogonal to the beam line and measure the Z position along the beam. This third, Z–measuring, SL is not present in the fourth layer of chambers, which therefore measures only the ϕ coordinate. In order to create a solid and light frame while increasing the angular resolution, an aluminum honeycomb spacer, $\sim$ 128 mm thick, separates the Z and outer ϕ SLs. The chamber design ensures redundancy, since the muon crosses more cells than geometrically needed to define the track. A muon coming from the interaction point first encounters a ϕ–measuring SL, passes through the honeycomb plate, then crosses the Z–measuring SL and the second ϕ–measuring SL.

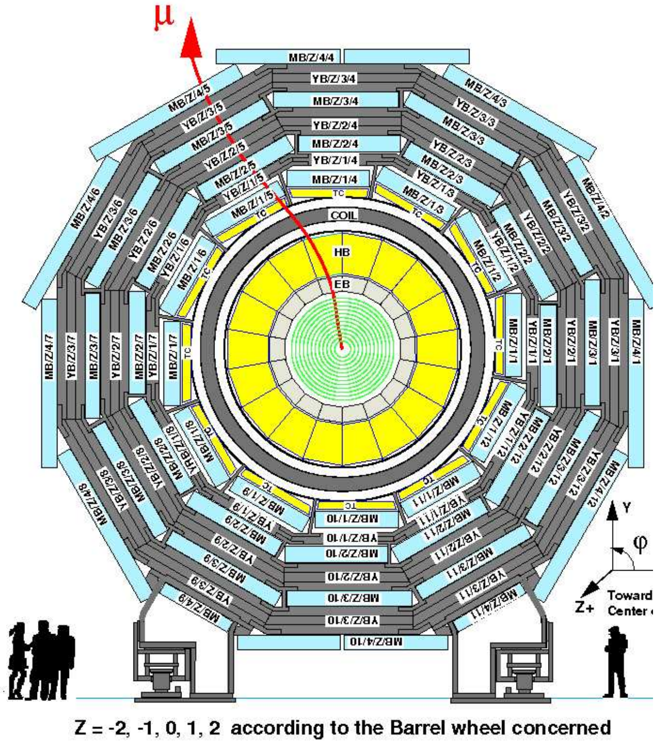

Figure 2.12: Transversal view of the DT system, with the corresponding labeling of the chambers.

The drift cell mechanism is based in the constant drift velocity of electrons for certain gas mixtures, independently of the reduced electric field E/P (E is the magnitude of the electric field, P the gas pressure). If the value of the drift velocity is constant, the drift time of the electron can be measured and thus the passage of a muon is calculated from a linear relationship. Maximum drift times are about 400 ns. The cell design includes 5 electrodes, 1 anode wire, 2 field shaping strips, and 2 cathode strips. Five electrodes shape the electric field inside the cell. The wire itself, which collects the electrons, two electrodes on the inner sides of the I beams and finally two in the inner sides of the aluminum plates. The latter improve the time–position linear relationship. Both, *aluminum plates* and *I beams* are grounded. Therefore, the electrodes are sticked to them, and electrically isolated. Cell dimensions are 42 mm width and 13 mm height with 50 μm diameter anode wire. The wire length varies from about 2 to 4 m, from the smallest (inner) to the largest (outer) chambers. As active gas, a mixture of Ar/CO_2 85%/15% is used.

In order to ensure an efficient muon momentum measurement, the target chamber resolution must be 100 μm in the Rϕ plane and 150 μm in the Z direction. This is achieved by 8 track points measured in the two (Rϕ) SL, provided the maximum deviation from linearity of the cell space–time relation be less than 100–150 μm and the wire resolution be better than 250 μm. In order to reach the cited performance, the position placement precision of the electrodes is 300 μm. The wire pitch tolerance inside one layer and the misalignment between layers in the same SL has to stay within 100 μm. Misalignment between SLs of a chamber should be less than 500 μm and be measured better than 100 μm, in order to be

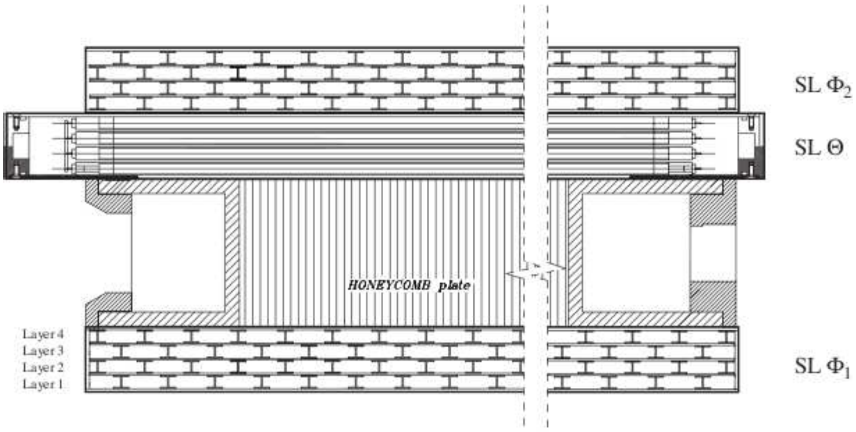

Figure 2.13: Longitudinal view of the internal structure of a DT chamber. The three Superlayers containing 4 planes of wires each are identified.

bellow the intrinsic resolution of the chamber.

Muon endcap system: Cathode Strip Chambers

CSC chambers are arranged to form four disks, called stations ME1, ME2, ME3, ME4. The station ME1 has three rings of chambers (ME1/1, ME1/2, ME1/3), while the other two stations are composed from two rings of chambers (MEn/1 and MEn/2). The CMS endcap muon system consist of 468 cathode strip chambers (CSC) arranged as drawn in figure 2.14. The chambers are trapezoidal and cover either 10° or 20° in ϕ. All chambers, except for the ME1/3 ring, overlap and provide continuous ϕ–coverage. A muon in the pseudorapidity range $1.2 <| \eta |< 2.4$ crosses 3 or 4 CSCs. In the endcap–barrel overlap range, $0.9 <| \eta |< 1.2$, muons are detected by both the barrel DTs and endcap CSCs.

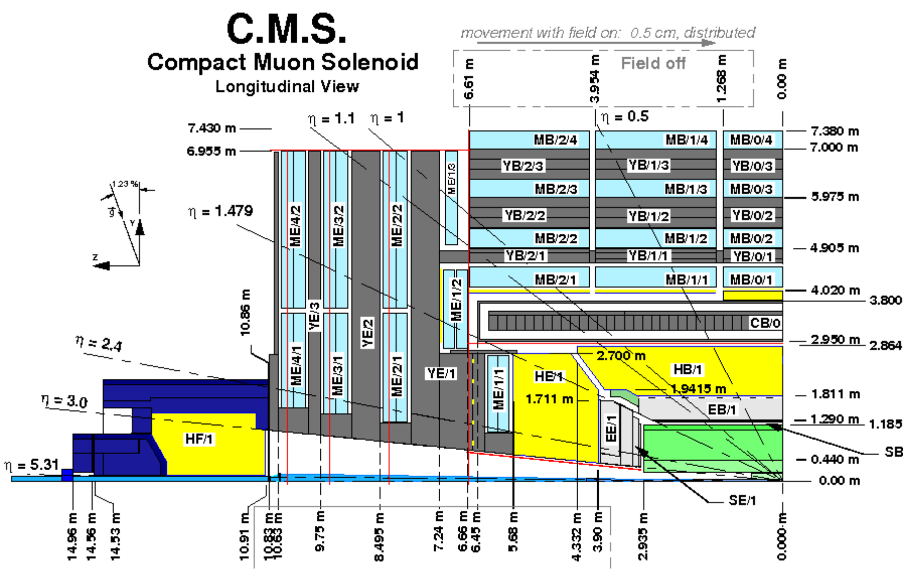

Figure 2.14: Longitudinal view of the CSC system layout. Four stations/disks of chambers are disposed orthogonal to the beam line.

The CSCs are multiwire proportional chambers composed of 6 anode wire planes interleaved among 7 cathode panels. The panels form 6 gas gaps planes of sensitive anode wires. Wires run azimuthally and define the track radial coordinate. Strips are milled on cathode panels and run lengthwise at constant $\Delta\phi$ width. The muon coordinate along the wires (ϕ in the CMS coordinate system) is obtained by interpolating charges induced on strips. An avalanche developed on a wire induces on the cathode plane a distributed charge of well known shape. Their orthogonal segmentation allows the calculation of two coordinates from a single plane.

The CSCs chambers have different sizes, the 144 largest CSCs, ME2/2 and ME3/2, are 3.4 m long along the strip direction and up to 1.5 m wide along the wire direction. The overall area covered by the sensitive planes of all chambers is about 5000 m^2, the gas volume is $\sim$50 m^3, and the number of wires is about 2 million. The nominal gas mixture is 40%Ar + 50%CO_2 + 10%CF_4. The CO_2 component is a non–flammable quencher needed to achieve large gas gains, while the main function of the CF_4 is to prevent polymerization on wires.

The CSCs provide the functions of precision muon measurement and muon trigger in one device. The chamber position resolution varies from 75 to 200 μm from the first to the last station to cope with the CMS goal for momentum resolution.

Resistive Plate Chambers

Resistive Plate Chambers (RPC) are gaseous parallel–plate detectors combining moderated spatial resolution with a time resolution comparable to that of scintillators. They are suited for fast space–time tracking as required for the muon trigger, and serve as dedicated muon trigger detector, complementing the high precision muon chambers DTs and CSCs. Time tagging capabilities of RPCs is better than 25 ns (LHC bunch crossing time).

A total of 6 layers of RPCs are embedded in the barrel muon system. In the first and second muon stations there are 2 arrays of RPC chambers located internally and externally with respect to the DT chambers. In the third and fourth stations there is one layer of RPC located on the inner side of the DT.

The redundancy in the first 2 stations allows the trigger algorithm to work even for low p_T tracks that may stop before reaching the outer 2 stations. In the endcap region, there is a plane of RPCs in each of the first 3 stations. They overlap in ϕ as to avoid dead space at chamber edges.

The CMS RPC basic double–gap module consists of 2 gaps, referred as up and down gaps, operated in avalanche mode with common pick–up readout strips in between. The total induced signal is the sum of the 2 single–gap signals. When an ionizing particle traverses a RPC, a cluster of electrons starts an avalanche multiplication. The drift of the charge towards the anode induces on the pick–up electrode a fast charge which represents the useful signal of the RPC. The two–gaps configuration allows the single–gaps to operate at lower gas gain (lower high voltage) with an effective detector efficiency higher than for a single–gap.

2.4.6 The Trigger system

The LHC provides proton-proton and heavy-ion collisions at high interaction rates. For protons, the beam crossing is 25 ns, corresponding to a crossing frequency of 40 MHz. The number of collisions at each crossing of the proton bunches is approximately 20 at the nominal design luminosity. Since it is impossible to store and process the large amount of data associated with the resulting high number of events, a drastic rate reduction has to be achieved to reach 100 Hz, which is the rate limit for the current storage systems. This task is performed by the trigger system, which is the start of the physics event selection process. This reduction is achieved in two steps, the Level-1 (L1) Trigger and the High-Level Trigger (HLT) [15, 32], respectively.

The Level-1 Trigger consists of custom-designed, largely programmable electronics, whereas the HLT is a software system implemented in a filter farm of about one thousand commercial processors. The rate reduction capability is designed to be at least a factor of 10^6 for the combined L1 Trigger and HLT. The design output rate limit of the L1 Trigger is 100 kHz. The L1 Trigger uses coarsely segmented data from the calorimeters and the muon system, while holding the high-resolution data in pipelined memories in the front-end electronics. The HLT, however, has access to complete read-out data an can therefore perform complex calculations similar to those made in the analysis off-line software if required for specially interesting events.

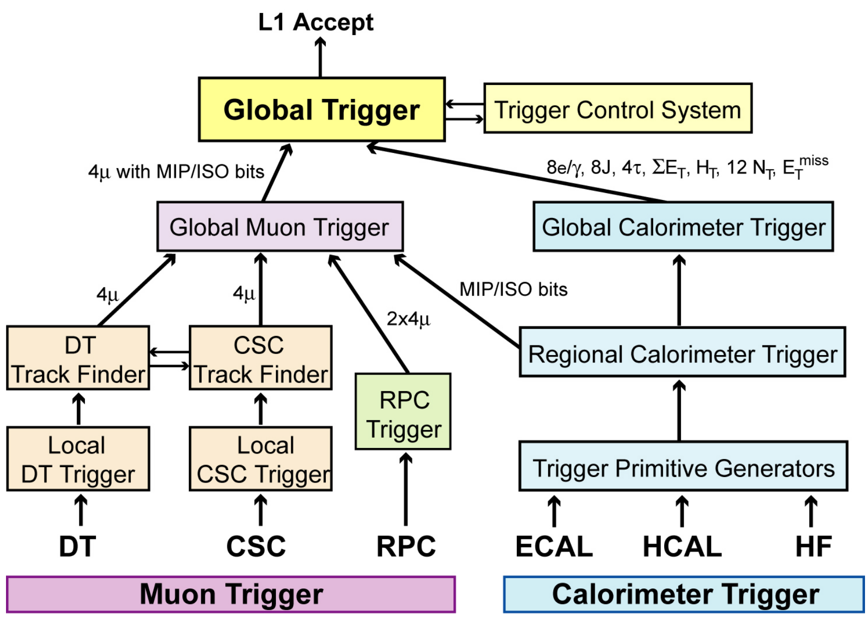

Figure 2.15: Architecture of the L1 Trigger.

The L1 trigger decision has to be taken within 3.2 μs, that is, after 128 bunch crossings. In order to avoid any data loss, readings must be buffered in pipelined memories. The L1 trigger electronics is housed partly on the detectors, partly in the underground control room located at a distance of approximately 90 m from the experimental cavern. Trigger decisions are based on the output of algorithms performed on Trigger objects, namely candidate electrons, jets or muons. In turn, these objects are determined by calorimeter and muon specific triggers.

The L1 trigger system of CMS works in several steps (see 2.15). It has local, regional and global components. At the bottom end, the local triggers, also called Trigger Primitive Generators (TPG), are based on energy depositions in calorimeter trigger towers and track segments or hit patterns in muon chambers, respectively. Regional Triggers combine their information and use pattern logic to determine ranked and sorted trigger objects such as electron or muon candidates in limited spatial regions. The rank is determined as a function of energy or momentum and quality, which reflects the level of confidence attributed to the L1 parameter measurements, based on detailed knowledge of the detectors and trigger electronics and on the amount of information available. The Global Calorimeter and Global Muon Triggers determine the highest–rank calorimeter and muon objects across the entire experiment and transfer them to the Global Trigger, the top entity of the L1 hierarchy. The latter takes the decision to reject an event or to accept it for further evaluation by the HLT. The decision is based on algorithm calculations and on the readiness of the subdetectors and the DAQ, which is determined by the Trigger Control System (TCS). The Level–1 Accept (L1A) decision is communicated to the subdetectors through the Timing Trigger and Control (TTC) system.

2.4.7 Computing at CMS

The CMS offline computing system [15, 33] must support the storage, transfer and manipulation of the recorded data for the lifetime of the experiment. These tasks start with the acceptance of the data coming from the detector and the posterior processing: pattern recognition, event filtering, track reconstruction, etc. Then, it must support the different physics analysis of the collaboration, which implies as well the production and distribution of simulated data, and the access to conditions and calibration information.

The basic elements of the offline computing system include:

- A software framework for event process and analysis.
- Distributed database systems.
- A set of computing services, providing tools to transfer, locate and process large collections of events.
- Underlying generic Grid services giving access to distributed computing resources.
- Computer centers, managing and providing access to storage and CPU at a local level.

The software framework

The CMS application software (CMSSW)[34] must perform a variety of event processing, selection and analysis tasks, and is used in both offline and online contexts. The software must be sufficiently modular that it can be developed and maintained by a large group of geographically dispersed collaborators.

The central concept of the CMS data model is the *Event*. The *Event* provides access to the recorded data from a single triggered bunch crossing, and to new data derived from it. This may include raw digitized data, reconstructed products, or high-level analysis objects.

The *Event* is used by a variety of physics modules, which may read data from it, or add new data. Each module performs a well-defined function related to the selection, reconstruction or analysis of the *Event*.

Modules are isolated from the computing environment, execute independently from one another, and communicate only through the *Event*. A complete CMS application is constructed by specifying to the Framework one or more ordered sequences of modules through which each *Event* must flow.

Distributed database systems allowing access to non-event data

In order to set up the detector configuration a large number of constants like the geometry description, voltages, constants of the gas systems, etc are needed. This makes the database system an essential service for CMS to run. The two most important requirements identified by CMS are:

- CMS has to be able to operate without network connection between its location (P5) and the outside world. Therefore CMS must own an independent database structure based at P5.
- The offline condition data work-flow has to fit a multi-tier distributed structure.

A system [35] based on 3 different databases, using ORACLE technology [36], was designed to fit the requirements above:

- Online Master Database System (ODMS). It is the online master database located at P5 on the CMS online network. It stores the configuration of the detector and the non event data, produced by the sub-systems like slow control, electronics, data acquisition (DAQ) and trigger data.
- Offline Reconstruction Condition database for Online use (ORCON). It stores all the non-event data required for the High Level Trigger (HLT) and for the offline reconstruction. It also contains conditions needed for data quality indicators.
- Offline Reconstruction Condition database for Offline use (ORCOFF). It is the master offline database located at the CERN site, and it contains a copy of ORCON.

The data access is controlled only by an external interface called POOL-ORA. In the offline databases, only a subset of configuration data and condition data, as well as all calibration data, must be stored. All these data need a tag, labeling their version and an interval of validity for describing their time information, as meta-data. The matching with the raw data from the collision events is indeed possible via these meta-data.

Computing centers and services

The scale of the computing system is such that it could not be hosted entirely at one site. The system is built using computing resources at different size computing centers, provided by collaborating institutes around the world. CMS proposes to use a hierarchical architecture of Tiered centers, with a single Tier-0 center at CERN, a few Tier-1 centers at national computing facilities, and several Tier-2 centers at institutes.

The Tier-0 receives raw data from the detector and produces a first-pass reconstruction. Raw and reconstructed data are then transferred to the Tier-1 centers, where they are stored as a safe and independent copy. Additionally, Tier-1 centers develop a second pass reconstruction, including improved calibrations, and serve it to the Tier-2 centers. Physics analysis and simulated data production are finally performed in the Tier-2 centers.

In addition to the Tier-0 center, CERN also hosts an Analysis Facility known as CAF, which combines flexible CPU resources with rapid access to the entire CMS dataset. This center supports fast turn-around analysis when required, and a variety of other specialized functions (calibration, performance monitoring) related to the operations of the CMS detector.

The integration of the resources at CMS computing centers into a single coherent system relies upon Grid middleware [37] which presents a standard interface to storage and CPU facilities at each WLCG (Worldwide LHC Computing Grid) site. The Grid allows remote job submission and data access with robust security and accounting. As an example, most of the work presented in this thesis was carried out in the Tier-2 centre at the Instituto de Fisica de Cantabria, and the CAF at CERN.

2.5 Muon Reconstruction in CMS

The strategy for physics analysis in CMS is based on the reconstruction of high-level physics objects which correspond to particles traveling through the detector. The detector components record the signal of a particle as it travels through the material of the detectors, and this signal is reconstructed as individual points in space known as *recHits* [38]. To reconstruct a physical particle traveling through the detector, the *recHits* are associated together to determine points on the particle trajectory. The characteristics of the trajectory as it travels through the detector are then used to define its momentum, charge, and particle identification.

2.5.1 Track Parameters

Measuring the full trajectory in space of a charged particle in a magnetic field provides a method to determine the momentum p and charge, q. The Lorentz force provides a relation between the momentum and its motion in a magnetic field, and allows the determination of the equation of motion for the trajectory of the charged particle. Parameterizing the Lorentz force as a function of the distance along the trajectory, s(t), the trajectory in the absence of electric field is given by the differential equation:

$$\frac{d^2\vec{r}}{ds^2} = \frac{q}{p}\frac{d\vec{r}}{ds}B(r) \tag{2.2}$$

where $\frac{d\vec{r}}{ds}$ is the unit length tangent to the trajectory, and $\frac{d\vec{r}^2}{ds^2}$ is a measurement of the trajectory's curvature. Thus, for a known B, the momentum at a point (x, y, z) is determined by measuring the tangent to the trajectory and the curvature of the trajectory. The tangent to the trajectory makes an angle λ with respect to the magnetic field. Solving equation 2.2, for known, homogeneous B, yields three relations for x(s), y(s), and z(s) that describe a helix in space parameterized by x, y, z, λ, q/p. The projection in the xy plane follows a circle with fixed radius of curvature $R_T = |p|cos(\lambda)/qB$, while the z coordinate measures the stretch of the helix in the direction parallel to B.

The above parameterization does not take into account three important factors caused by the real CMS detector:

- Inhomogeneous B field.
- Energy loss as the particle travels through the detector.
- Multiple scattering which deflects the trajectory in a stochastic manner.

Therefore, a failure to include these effects biases the most important parameters that are extracted from the trajectory: the momentum and its direction. An accurate measurement of direction is critical in determining whether the particle came from the interaction point or a detached vertex. In order to take into account these effects we use a different set of parameters capable to deal with the changes mentioned.

The magnetic field is a function of the coordinates B(x, y, z), therefore to correctly describe the trajectory it is necessary to incorporate the magnetic field changes into the parameterization. The set of parameters (x, y, $\frac{dx}{dz}$, $\frac{dy}{dz}$, $\frac{q}{|p|}$), at reference surfaces $z = z_r$ provides the change from the ideal, constant field trajectory. This new parameterization also deals with the effects of multiple scattering and localizes the trajectory to a plane region where the B field can be expanded as a perturbation to a good approximation. Thus, a solution to the trajectory in an inhomogeneous B field field can be found by using a recursive method of Runge-Kutta.

2.5.2 Tracking Algorithm

The hits from the position sensitive detectors are analyzed using a pattern recognition algorithm to associate the measurements with trajectories. Independent of the sub detector information used the procedure from hits to tracks follows the same sequence and reconstructing and parameterizing a track occurs in four stages: seeding, trajectory building, trajectory cleaning, and trajectory smoothing.

Trajectory Seeding

The initial point for the track reconstruction is determined using an estimated trajectory state or set of hits that are compatible with the assumed physics process. The most common types of trajectory seeds in CMS are based on the information of a set of hits (hit-based seed), or in a previous estimation of the track parameters (state-based seeds). It is assumed that the trajectories, and therefore the trajectory seeds, are compatible with the beam spot. Hit-based seeds require a hit-pair or hit-triplet compatible with the beam spot to provide the initial vector (except for cosmic muons). Additional options are that the seed direction meets certain criteria, or that the hits are located in a certain geometric region of the detector. State-based seeds do not require any hits and are specified by an initial momentum and direction.

Trajectory Building

Trajectory building starts at the position specified by the trajectory seed, and the building then proceeds in the direction specified by the seed to locate compatible hits on the subsequent detector layers. The track finding and fitting is accomplished using a combinatorial Kalman filter where the full knowledge of the track parameters at each detector layer is used to find compatible measurements in the next detector layer, forming combinatorial trees of track candidates. The Kalman filter method uses an iterative approach to update the trajectory estimate and its covariance matrix by incorporating material effects. The method starts with track parameters $\hat{p}_i$ and covariance $\hat{C}_i$ at a known surface, and propagates them ($\hat{p}_{i+1}$) to the next surface with the known equation of motion by incorporating scattering effects and also uses information from the subset of the measurement vector at the propagated surface $c_{i+1} = f_{i+1}(p_{i+1}) + \epsilon_{i+1}$. In this process, the trajectory state which is propagated to the next detector layer is then updated with the information of a compatible hit. The final trajectory estimate is properly weighted with information from the measurement m_{i+1} and the information with predicted state based in all preceding detectors. The propagation of a trajectory state to another position must take into account the detailed knowledge of the B field and the effects of propagating through the detector material in order to properly evaluate the position and momentum vectors.

Trajectory Cleaning

Trajectory building produces a large number of trajectories, many of which share a large fraction of their hits. In the cleaning stage, ambiguities among the possible trajectories are resolved and a maximum number of track candidates are kept.

Trajectory Smoothing

A backward fitting allows the use of all covariance matrices to be applied to all the intermediate points based on all measurements used so far. Thus, the Kalman filter provides a good method in track finding/fitting since it is linear in the measurements, and its backward complement makes use of the full information, protecting the algorithm from bad seeding estimates.

2.5.3 Propagators

The propagators provide a solution for the muon transport in the detector accounting for magnetic field and energy loss in detector material. It predicts the mean expected path as well as provide a propagation of initial state errors (covariance matrix) to the final point including material effects like multiple scattering and energy loss fluctuations. Several propagators are used during the muon track reconstruction to perform a function of predicting the state of a muon given its initial state vector.

Three propagators are used at different stages of muon reconstruction: the analytic with material propagator, the Runge-Kutta propagator, and the stepping-helix propagator. The first two propagators are used extensively inside the silicon tracker volume, while the latter is predominantly used to propagate muons outside the tracker volume. The first two propagators are used in the standard tracking software, and the stepping helix propagator is predominantly used for muon reconstruction only. In a typical muon reconstruction application when the propagated trajectory crosses into the tracker volume the analytic with material or the Runge-Kutta propagators are coupled with the stepping helix propagator into the smart propagator which internally selects which propagator is to be used depending where the initial propagation state is: the stepping helix propagator is chosen if the state is outside the silicon tracker volume.

The analytical propagator assumes a constant and perfectly aligned magnetic field, while the Runge-Kutta propagator is able to deal, through a Runge-Kutta numerical method, with inhomogeneous magnetic field. In both cases, material effects are added at the end of the propagation process. On the contrary, the stepping helix propagator applies numerical methods to calculate the trajectory in an inhomogeneous magnetic field, and implements material effects internally while performing the propagation.

2.5.4 Local Reconstruction in the Drift Tube Chambers

Drift tube chambers have the capability of producing a local reconstruction of the track, which is used for trigger purposes and to make pattern recognition of the global track easier. It is useful in order to illustrate some of the following chapters, to describe the process of the local reconstruction in the drift tube chambers.

In the first stage of the local reconstruction, the drift time associated to each cell activated by a muon, is converted through the parameterized drift velocity into a *hit* containing the position of the muon.

Hits with drift time t_d <-3 ns are discarded, while hits having -3 ns $< t_d <$ 0 ns are retained and assigned the position x = 0 in the local reference frame of the cell, corresponding to the anode wire position. The conversion from time measurements to hit positions in a DT cell, leading to one-dimensional reconstructed hits, or rechits, is performed assuming a constant effective drift velocity in the whole chamber volume, independent of track position and inclination. This assumption is justified for all chambers except the innermost stations, MB1n (n = 1...12), of those mounted on the YB2 and YB-2 wheels. More sophisticated algorithms based on a detailed parameterization of the DT cell behavior, developed using simulated data, are currently under study.

For each signal there are two possible rechits due to the left-right ambiguity on the position with respect to the anode wire inside the cell. This ambiguity is resolved at the track segment building stage by the local pattern recognition algorithm [39] that takes the rechits as input, thanks to the staggered structure of the cells in the chamber SLs as shown in figure 2.13.

The pattern recognition is initiated by considering all possible pairs of hits (seeds) in different layers, starting from the most separate hits in the chamber. For each seed, additional hits are searched for in all layers and included in the segment candidate if they are compatible with the extrapolation from the seed within a loose requirement (2 mm). Segment candidates are built by performing a straight-line fit to the associated hits and sorted on the basis of their total number of hits and χ^2, defined as the sum of the squares of the hit residuals divided by the hit position error, normalized to the number of degrees of freedom. The sagitta of the muon track in the (generally small) residual magnetic field in the chamber volume is negligible. For each seed, only the segment candidate with the maximum number of hits is considered; among the candidates with the same number of hits, the one with best χ^2 is selected. Segments with at least three hits and $\chi^2/\mathrm{NDOF} < 20$ are finally retained.

The pattern recognition is performed independently in the $r\phi$ and rz SLs of each chamber to deliver the so-called 2-dimensional (2D) track segments in both views. The 2D segments are then paired using all possible combinations to form 4-dimensional (4D) segments in the chamber, carrying 3-dimensional spatial information and the fitted value of the arrival time of the muon in the chamber. This process is performed in a reference frame attached to the drift tube chamber, which is usually referred to as the local system of reference. Figure 2.16 shows the definition of this frame: the x coordinate is coincident with the $r\phi$ direction, although the sense depends on the cabling of the chambers. The y coordinate is parallel to the beam line, with the sense again depending on the cabling. Finally the z coordinate is orthogonal to the chamber and points always to the center of CMS.

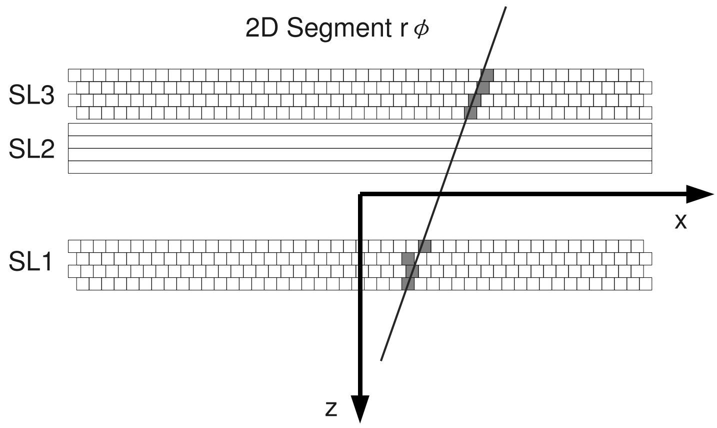

(a)

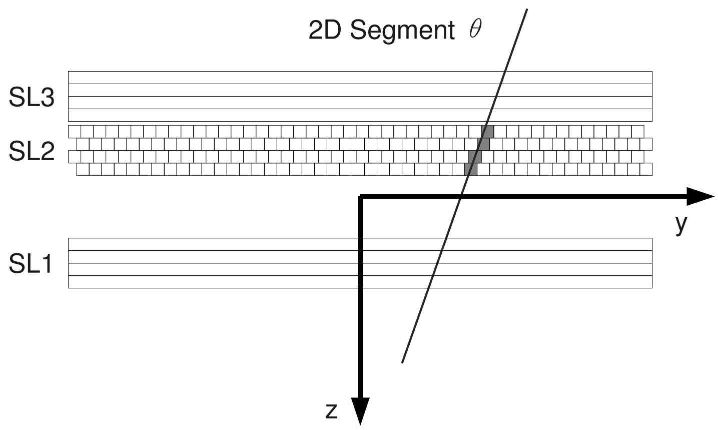

(b)

Figure 2.16: Segment definition in a DT chamber using both projections and a local system of reference common for all the layers.

Chapter 3

Alignment of the CMS Muon System

For optimal performance of the CMS muon spectrometer over the entire momentum range up to the TeV region, the different muon chambers must be aligned with respect to each other and to the central tracking system within a few hundred microns in the $r\phi$ plane [40].

Muon chambers are installed over very large and heavy iron structures that cannot be assumed to be stable nor perfectly rigid. Deformations may occur because of different processes such as the own weight of the structures. In general, there are several potential sources of misalignment in the muon spectrometer, from chamber production to final detector operating conditions, including:

- **Chamber construction tolerances.** These are unavoidable geometrical tolerances in the production of the chamber components. The relative positioning of the different internal components of a chamber was measured during construction to be within the required tolerances.

- **Detector assembly and closing tolerances**. Gravitational distortions of the return yoke lead to static deformations of the iron support. This effect, together with the installation tolerances, results in displacements of the chambers in the different barrel wheels and endcap disks of up to several millimeters with respect to their nominal detector positions.

- **Solenoid effects.** Magnetic forces generated by the 3.8 T solenoid field lead to displacements and deformations of the return yoke which is at the same time the support structure of the muon chambers. This results in further displacements of the chambers with respect to their nominal positions.

- **Time-dependent effects.** During operation, thermal instabilities and other time-dependent factors can cause dynamic misalignments at the sub-millimeter level.

The required alignment precision for the endcap chambers is 75-200 μm, while for the barrel the precision varies from 100 μm for the inner station to 350 μm for the outer station. To this end, after following strict chamber construction specifications, CMS combines precise survey and photogrammetry measurements, measurements from an opto-mechanical system, and the results of alignment algorithms based on muon tracks (both from cosmic rays and from pp collisions) crossing the spectrometer. In addition to the measurement methods and techniques, a software infrastructure has been developed in order to properly store and manage the alignment corrections, and apply them to the reconstruction algorithms.

During the development of this thesis, contributions to the three alignment procedures: opto-mechanical system, photogrammetry measurements and track based alignment have been produced. Nevertheless, the core of the work presented here is related to the two last techniques, and to the development of a software infrastructure for the muon system alignment. As a consequence, this chapter is divided in three separated sections. The first part will describe, in a very general way, the three different alignment techniques used in CMS. The second part will be dedicated to explain some of the mathematical tools developed for this thesis specially regarding track-based alignment. Finally, the last part will describe the software alignment infrastructure for the muon system of CMS.

3.1 Alignment techniques for the muon system of CMS

The muon system of CMS is aligned using three different techniques in order to reduce the systematic errors of the final alignment, and to allow cross-checks among the different methods, guaranteeing a good and consistent alignment.

3.1.1 The Optical Alignment System

The CMS alignment system is made of four independent parts: internal alignment of the tracker, DT, and CSC systems, and a Link system which locks them together, allows simultaneous monitoring of the barrel and endcap, and monitors he displacements of heavy structures during the critical closing phase and during normal operation.

The internal alignment of tracker elements is described elsewhere [41]. The alignment process can begin only after CMS is closed. The system is designed to provide continuous monitoring of the muon chamber positions in the entire magnetic field range between 0 T and 3.8 T, and to meet the challenging constraints of large radiation and magnetic field tolerance, wide dynamic range, high precision, and tight spatial confinement. The system [31, 42] is based on a number of precise rigid structures independently supported by the tracker and by each yoke element. These structures contain optical sensors that look at the relative positions of chambers within the same yoke element. The connection among the structures located on the various yoke elements is possible only when CMS is closed, and is obtained through a network of laser beams, local distance sensors, and digital cameras.

The aim of the optical muon alignment system is to provide position information of the detector elements with a precision comparable to the intrinsic chamber resolution.

Optical Muon Alignment Layout

The basic geometrical layout of the muon alignment system consists of three r–z alignment planes with 60° staggering in ϕ. This segmentation is based on the 12-fold geometry of the barrel muon detector. Within each plane, distributed networks of optical sensors attached directly to muon chambers or to rigid local structures are connected by laser or LED lines. The optical alignment network is complemented by different types of analog sensors: electrolytic clinometers, optical and mechanical proximity sensors, probes for magnetic field measurement, temperature and humidity sensors.

Figure 3.1 shows schematic longitudinal and transverse views of CMS, with the light paths indicated.

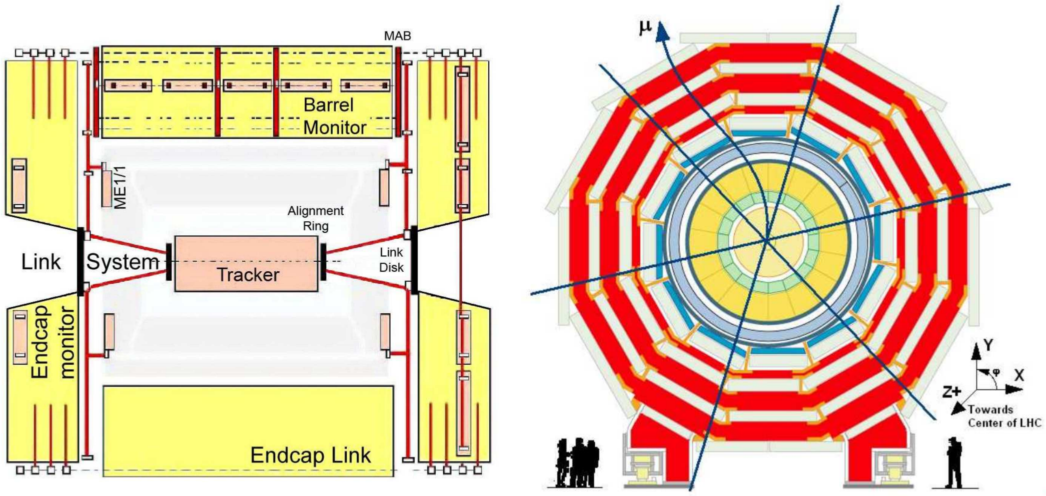

Figure 3.1: Schematic view of the CMS alignment system. *Left:* longitudinal view of CMS showing one of the three r_{CMS}–z_{CMS} alignment planes. The continuous and dashed lines show different optical light paths. *Right:* transverse view of the barrel muon detector. The crossing lines indicate the r_{CMS}–z_{CMS} alignment planes with 60° staggering in ϕ.

Each muon endcap station is monitored through three radial straight line monitors running along the full diameter of the supporting disks. Each straight line monitor consists of laser beams detected by two optical sensors in each of the four crossed chambers. Approximately one sixth of the chambers are directly monitored; the rest are aligned with respect to these monitored chambers using tracks that pass through their overlapping regions.

In the barrel, the positions of the 250 DT chambers are monitored by a network of 36 rigid carbon fiber structures called Modules for the Alignment of the Barrel (MAB), supported by the yoke wheels, and optically connected together once the detector is closed. Two groups of six MABs are on the outer faces of the external wheels and six MABs are inside each gap between the wheels. The external MABs contain link and endcap elements used to refer the three alignment subsystems to each other.

The Link system simultaneously monitors the twelve external MABs and twenty four CSC chambers located in the first endcap muon station, in YE±1 (twelve per side), and relates them to the tracker volume using laser beams emitted from two rigid carbon fiber structures, called alignment rings, attached to the tracker endcaps. Other sources and optics housed in MABs and link disks complete the light path layout. The link disks are floating structures suspended inside the innermost endcap iron disks (YE±1). Each subsystem performs an independent reconstruction, with the link providing a common reference frame.

Offline geometry reconstruction

The muon alignment system uses a dedicated reconstruction program called CMS Object-oriented Code for Optical Alignment (COCOA) [43, 44, 45] to transform the various measurements into a reconstructed DT and CSC aligned geometry. The software reconstructs the position and orientation of the optical system objects and chambers, and performs a full propagation of errors to take into account the correlations between different measurements.

For the entire muon alignment system, COCOA handles about 30 000 parameters: ≈ 3000 for the link, ≈ 6500 for the endcap, and $\approx 20\,000$ for the barrel. The alignment geometry of the chambers and all alignment objects within the system are organized in a hierarchical order using a system description which must be provided in addition to the measurements themselves.

This description includes the interconnection of elements, e.g., laser – sensor association, and the system hierarchy, e.g., system elements association to mechanical structures, together with an approximation of the geometry obtained from other measurements (calibrations or photogrammetry). Supplying a good estimate of the initial geometry is not necessary, but speeds up the convergence, ensures good quality of the fit results, and helps to avoid falling into local minima.

The geometry reconstruction proceeds independently for each alignment subsystem, each having a completely different set of measurements and geometry description and thus requiring a different fit strategy implemented in COCOA. The output of COCOA contains the best geometrical description of the system compatible with the measurements and with the information from structure calibrations. Propagated uncertainties for all aligned objects are also provided.

One of the most important sources of uncertainty in the optical alignment is related to the fact that usually the monitored elements are not the detecting planes themselves, but other structures attached to the external covers of the detectors. In the reconstruction process only the detecting planes are important and the transfer of alignment information from the external references to the active elements is not always trivial.

3.1.2 Photogrammetry

During the building and assembly stages, the position of most of the CMS components was measured using photogrammetry techniques. In this procedure a collection of bright targets is distributed over the structure under study (see 3.2). A set of references is fixed, and pictures of the targets are taken from different angles and positions. The position of the targets is calculated using triangularization algorithms. In CMS the quoted precision in the position of a single target is 300 μm.

Photogrammetry is applied hierarchically to most of the elements of CMS ranging from large structures like muon yoke wheels, or disks, to small components like chambers, or sensors of the optical alignment system.

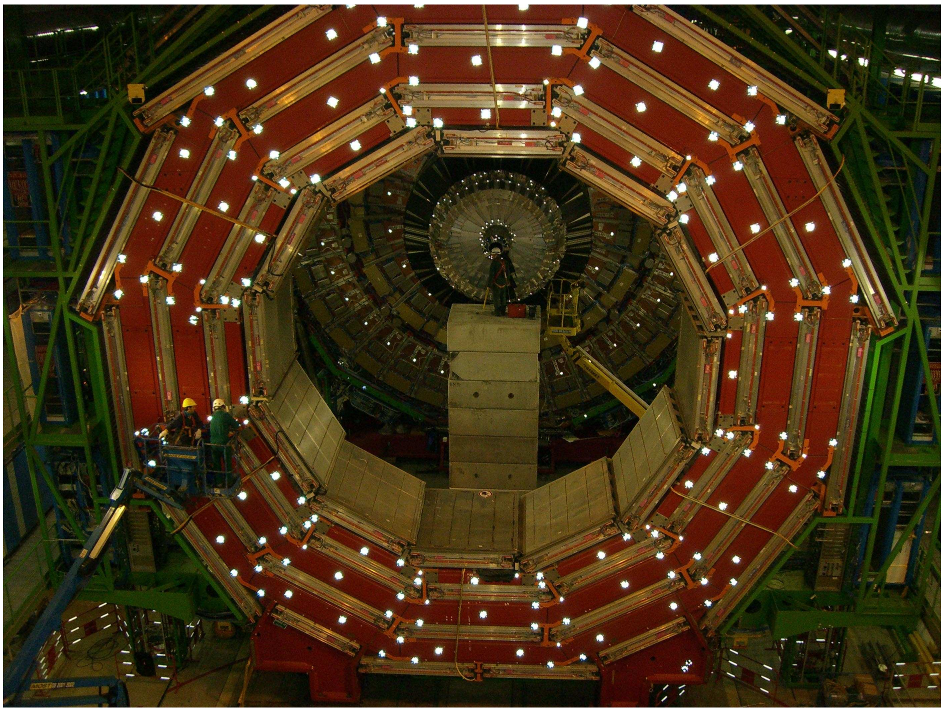

Figure 3.2: This picture shows the distribution of the photogrammetry bright targets over one of the barrel wheels.

In general, geometries based on photogrammetry are used as a first order geometry (as it will be shown in chapter 5), usually precise enough to guarantee the correct operation of the trigger system. It is also useful to provide a first estimation of the position of the components of the optical alignment system, making easier the convergence of the reconstructing algorithm.

There are several drawbacks associated to photogrammetry. The measurements can only be taken before and after the running of the experiment, because the detectors must be open in order to expose its internal components. For this reason, photogrammetry cannot account for motions produced in the closing process, being specially critical in the relative position of large structures such as wheels or disks. In addition, photogrammetry can only be taken during shutdown periods, and therefore cannot monitor geometry changes during operation. Other drawback concerns the location of the targets, since they are always placed over external surfaces, and not directly over the detecting components. As it was previously addressed in the case of the optical system, the reference of the external instruments to the internal active detectors might be complicated in many cases adding systematic errors.

3.1.3 Alignment with Tracks

The optical alignment system is able to operate in a very fast way, allowing the detection of misalignments very precisely in a quasi-online time scale. However, there are some limitations for this system as quoted in the previous section. Track-based alignment optimizes component positions for a given set of tracks, directly relating the active elements of the detectors traversed by the charged particles in a shared coordinate frame. The latency and systematic errors associated to this procedure are different than in the optical or survey alignment methods.

The working principle of track-based alignment algorithms is based in the bias produced in the track reconstruction by the differences between the actual, unknown geometry and the geometry used to reconstruct the tracks. The diagram in figure 3.3 illustrates the procedure. A particle crosses a region of the detector producing signals in a collection of misaligned detecting planes. The reconstruction algorithms use a design geometry and therefore the positions of the track at the detecting planes differ from the actual positions. The difference between the track and the actual measurement, called residual, is an observable sensitive to the misalignments.

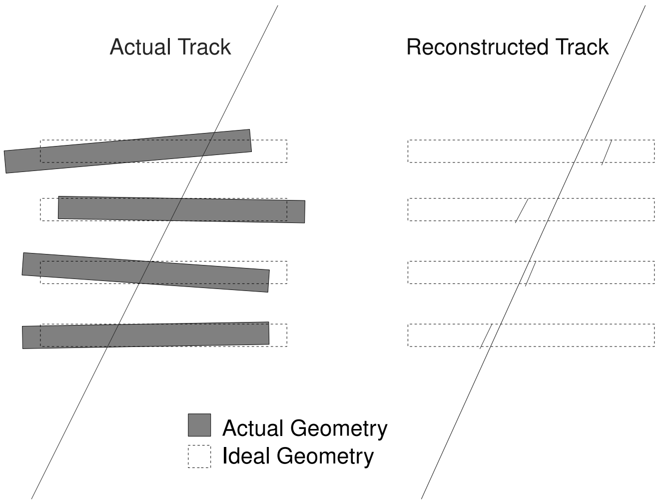

Figure 3.3: Sketch of a track crossing a misaligned detector. The same track is reconstructed by the software using the design geometry and therefore the position of the hits is not well estimated.

Residuals are geometrically related to the alignment parameters of a given object. This connection is used in linear models which establish a matrix relation between the residuals and the alignment parameters. One of the most popular parameterization is called the Karimaki parameterization [46]. In the following subsections an extension of these parameterization will be provided.

There are many different track-based alignment algorithms using different statistical techniques. Among the most widely-used it is possible to find HIP (Hit Impact Point [47, 48]), Kalman Filter alignment [49], and Millepede [50, 51, 52]. In spite of using different statistical techniques, they all share some common systematic errors related to systematic errors in the tracking procedure.

3.2 Implementation of the MBAA algorithm: mathematical basis

The core of this thesis is dedicated to the implementation and application of the MBAA algorithm (Modified Blobel Alignment Algorithm) for the barrel muon system of CMS. This algorithm is based in the original work by V. Blobel in the University of Hamburg (Millepede algorithm [52]). Nevertheless, the algorithm has been implemented in an independent way in order to adapt it to the barrel muon system. The first point covered in the following subsections is the geometrical model that relates residuals and alignment parameters for stereo detectors that not only measure the position but also the direction of the track (like drift tube chambers). Then, the MBAA algorithm will be described using a different notation (more convenient for practical purposes of the implementation) than in Blobel's papers. Afterwards, the different systematics affecting the algorithm will be discussed, and finally the techniques used to implement external constraints to the algorithm will be described.

3.2.1 Derivation of alignment parameters as a function of the residuals

Misalignments of a detecting plane or object produce a bias in the associated residual distributions. There is a pure geometric relation between the alignment parameters and the residuals, which allows to express the residuals as a function of the alignment parameters [53].

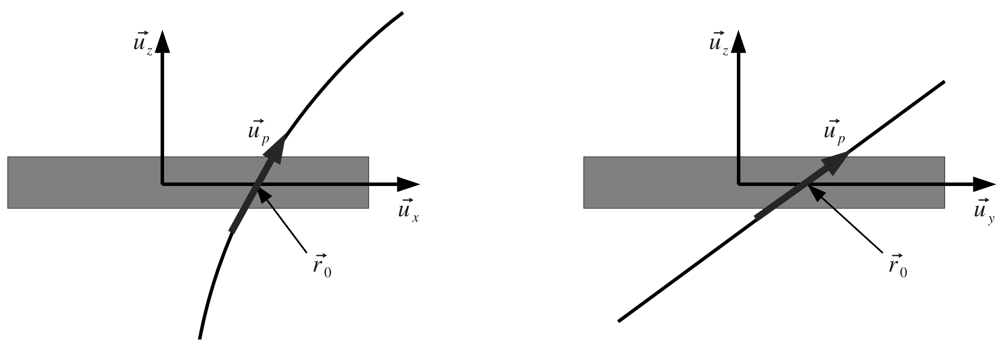

(a) (b)

Figure 3.4: Definition of the MBAA components: the track is parameterized as a straight line in the vicinity of the chamber. It is defined by the position of its intersection with the chamber $\vec{r}_0$ and its direction vector $\vec{u}_p$.

The object under consideration in this derivation will be a stereo, tracking detector, which measures four coordinates: the position x and the direction $\frac{dx}{dz}$ in the XZ plane, and the position z and the direction $\frac{dy}{dz}$ in the YZ plane. Figure 3.4 shows a diagram in which a particle is crossing such a detector in the two projections. A local system of reference has been defined in the center of this object. The unitary vectors of the axis are denoted as $\vec{u}_x$, $\vec{u}_y$ and $\vec{u}_z$ respectively. Measured in this local reference system, in the neighborhood of the station, the trajectory can be considered as a straight line defined by the equation

$$\vec{r} = \vec{r}_0 + \epsilon\vec{u}_p \tag{3.1}$$

where $\vec{r}$ represents the coordinates of any spacial point of the track, $\vec{r}_0 = x\vec{u}_x + y\vec{u}_y$ the intersection of the plane and the track in the local system of coordinates, $\vec{u}_p = sin(\Phi)cos(\Theta)\vec{u}_x + sin(\Phi)cos(\Theta)\vec{u}_y + cos(\Theta)\vec{u}_z$ the unitary vector along the momentum direction expressed in conventional spherical coordinates, and ϵ any real (small) number.

It is conventional in stereo detectors to measure separately both projections, in the XZ plane and in the YZ plane in this case. By defining the slopes in each of the projections as

$$\frac{dx}{dz} = \frac{\vec{u}_p\vec{u}_x}{\vec{u}_p\vec{u}_z} = cos(\Phi)tg(\Theta) \tag{3.2}$$

$$\frac{dy}{dz} = \frac{\vec{u}_p\vec{u}_y}{\vec{u}_p\vec{u}_z} = sin(\Phi)tg(\Theta) \tag{3.3}$$

it is possible to express the unitary vector as

$$\vec{u}_p = cos(\Theta)(\frac{dx}{dz}\vec{u}_x + \frac{dy}{dz}\vec{u}_y + \vec{u}_z) \tag{3.4}$$

If the detector behaves as a rigid body, misalignments can be described by degrees of freedom usually chosen as the displacements along the x, y and z position of its center and the three Euler rotation angles. Displacements are represented by a three component vector $\vec{\delta}$. Installation tolerances guarantee that misalignments are small in comparison to the dimension of the chamber. In this case, rotations can be considered infinitesimal and the rotation matrix can be linearized as

$$\mathbf{R} = \begin{pmatrix} 1 & \phi_z & -\phi_y \\ -\phi_z & 1 & \phi_x \\ \phi_y & -\phi_x & 1 \end{pmatrix} \tag{3.5}$$

where ϕ_x, ϕ_y and ϕ_z are the rotation angles with respect to each of the axis respectively. Considering the local system of reference attached to the detector plane (as shown in figure 3.5), the unitary vectors associated to the new axis can be written in terms of the previous vectors simply by applying the rotation matrix:

$$\vec{u}_x^* = \vec{u}_x - \phi_z\vec{u}_y + \phi_y\vec{u}_z \tag{3.6}$$

$$\vec{u}_y^* = \phi_z\vec{u}_x + \vec{u}_y + \phi_x\vec{u}_z \tag{3.7}$$

$$\vec{u}_z^* = -\phi_y\vec{u}_x + \phi_x\vec{u}_y + \vec{u}_z \tag{3.8}$$

The detector plane after it is moved is described by the equation

$$\vec{r} = \vec{\delta} + \lambda_x^*\vec{u}_x^* + \lambda_y^*\vec{u}_y^* \tag{3.9}$$

where λ_x^* and λ_y^* are real numbers. In particular, at the point of crossing between the track and the plane $\lambda_x^* = x^*$ and $\lambda_y^* = y^*$, the local coordinates in the new system of measurement.

The problem is reduced to obtain x and z from the following three equation system:

$$\vec{\delta} + \lambda_x^*\vec{u}_x^* + \lambda_y^*\vec{u}_y^* = \vec{r}_0 + \epsilon\vec{u}_p \tag{3.10}$$

multiplying this equation by $\vec{u}_x$, $\vec{u}_y$ and $\vec{u}_z$ respectively, it yields

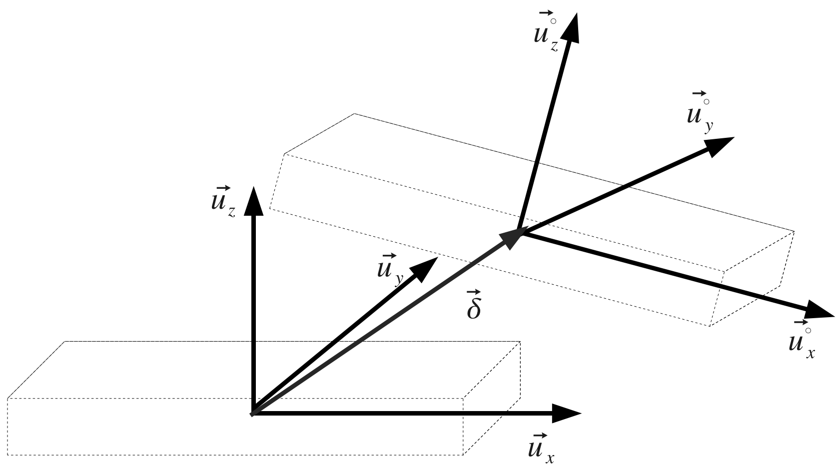

Figure 3.5: Sketch of a misaligned chamber. The misalignments can be described as a displacement, represented by vector $\vec{\delta}$ and a rotation, represented by a new set of orientations for the axis.

$$(\vec{\delta} - \vec{r}_0)\vec{u}^*_z = \epsilon(\vec{u}_p\vec{u}^*_z) \quad (3.11)$$

$$(\vec{\delta} - \vec{r}_0)\vec{u}^*_x + x^* = \epsilon(\vec{u}_p\vec{u}^*_x) \quad (3.12)$$

$$(\vec{\delta} - \vec{r}_0)\vec{u}^*_y + y^* = \epsilon(\vec{u}_p\vec{u}^*_y) \quad (3.13)$$

If $\vec{u}_p$ and $\vec{u}_z$ are orthogonal there is no solution, the track direction is parallel to the chamber and therefore there is no crossing track coming from the central region. If they are not orthogonal ϵ, x* and y* can be obtained directly:

$$\epsilon = \frac{(\vec{\delta} - \vec{r}_0)\vec{u}^*_z}{(\vec{u}_p\vec{u}^*_z)} \quad (3.14)$$

$$x^* = \frac{(\vec{\delta} - \vec{r}_0)\vec{u}^*_z}{(\vec{u}_p\vec{u}^*_z)}(\vec{u}_p\vec{u}^*_x) - (\vec{\delta} - \vec{r}_0)\vec{u}^*_x \quad (3.15)$$

$$y^* = \frac{(\vec{\delta} - \vec{r}_0)\vec{u}^*_z}{(\vec{u}_p\vec{u}^*_z)}(\vec{u}_p\vec{u}^*_y) - (\vec{\delta} - \vec{r}_0)\vec{u}^*_y \quad (3.16)$$

After replacing the vectors $\vec{u}^*_x$, $\vec{u}^*_y$ and $\vec{u}^*_z$, operating the scalar products, and neglecting all the infinitesimal quadratic terms, these expressions yield:

$$\Delta\ x = x^* - x = \delta_x - \frac{dx}{dz}\delta_z - y\frac{dx}{dz}\phi_x + x\frac{dx}{dz}\phi_y - y\phi_z \quad (3.17)$$

$$\Delta\ y = y^* - y = \delta_y - \frac{dy}{dz}\delta_z - y\frac{dy}{dz}\phi_x + x\frac{dy}{dz}\phi_y + x\phi_z \quad (3.18)$$

where $\Delta\ x$ and $\Delta\ y$ denote the residuals for the x and y coordinates.

The same treatment can be applied to the angular coordinates. The slopes in the misaligned system of reference can be expressed as

$$\frac{dx}{dz}^* = \frac{\vec{u}_p\vec{u}_x^*}{\vec{u}_p\vec{u}_z^*} \quad (3.19)$$

$$\frac{dy}{dz}^* = \frac{\vec{u}_p\vec{u}_y^*}{\vec{u}_p\vec{u}_z^*} \quad (3.20)$$

replacing the vectors and operating to first order (neglecting again quadratic terms in the alignment parameters), these expressions give place to

$$\Delta\frac{dx}{dz} = \frac{dx}{dz}^* - \frac{dx}{dz} = -\frac{dx}{dz}\frac{dy}{dz}\phi_x + (1+\frac{dx}{dz}^2)\phi_y - \frac{dy}{dz}\phi_z \quad (3.21)$$

$$\Delta\frac{dx}{dz} = \frac{dx}{dz}^* - \frac{dx}{dz} = (-1-\frac{dy}{dz}^2)\phi_x + \frac{dx}{dz}\frac{dy}{dz}\phi_y + \frac{dx}{dz}\phi_z \quad (3.22)$$

It is useful for further calculations and implementation in algorithms, to combine equations 3.18, 3.22 in matrix form:

$$\begin{pmatrix} \Delta\, x \\ \Delta\, \frac{dx}{dz} \\ \Delta\, y \\ \Delta\, \frac{dy}{dz} \end{pmatrix} = \begin{pmatrix} 1 & 0 & -\frac{dx}{dz} & -y\frac{dx}{dz} & x\frac{dx}{dz} & -y \\ 0 & 0 & 0 & -\frac{dx}{dz}\frac{dy}{dz} & 1+\frac{dx}{dz}^2 & -\frac{dy}{dz} \\ 0 & 1 & -\frac{dy}{dz} & -y\frac{dy}{dz} & x\frac{dy}{dz} & x \\ 0 & 0 & 0 & -1-\frac{dy}{dz}^2 & \frac{dx}{dz}\frac{dy}{dz} & \frac{dx}{dz} \end{pmatrix} \begin{pmatrix} \delta_x \\ \delta_y \\ \delta_z \\ \phi_x \\ \phi_y \\ \phi_z \end{pmatrix} \quad (3.23)$$

3.2.2 The Blobel approach and the MBAA algorithm

An official implementation of this algorithm exists and it is known as the Millepede algorithm available at the following reference [52]. The basic idea behind this algorithm is to minimize the residual distribution in a global and unique χ^2 fit which involves track and alignment parameters at the same time.

Consider a collection of high momentum muons crossing the detector. Let $\vec{p}_j$ denote a vector which contains the N track parameters for the muon j, and $\vec{\delta}$ denote a vector containing the total number of alignment parameters M. This number can be factorized in the number of objects to be aligned O, and the number of alignment parameters per object D, so that $M = O \times D$. The vector containing the alignment parameters for a particular detector i will be referred to as $\vec{\delta}_i$. The detected generalized positions of a muon j at the different object are denoted as $\vec{x}_j$, a vector containing one entry for each of the coordinates measured by the subdetectors. The number of coordinates measured by each subdetector is denoted as S.

In the case of a misaligned detector, the position $\vec{x}_j$ is a function of the real track parameters $\vec{p} + \Delta\vec{p}$ and the alignment parameters $\vec{x}_j = \vec{x}_j(\vec{p} + \Delta\vec{p}, \vec{\delta})$. If the actual misalignments are assumed to be small, the position can be expanded as a Taylor's series of the form

$$\vec{x}_j(\vec{p} + \Delta\vec{p}_j, \vec{\delta}) \simeq \vec{x}_j(\vec{p}, 0) + \mathbf{B_j}\Delta\vec{p}_j + \mathbf{A_j}\vec{q} \quad (3.24)$$

where $\vec{x}_j(\vec{p},0)$ is the estimation of the positions provided by the reconstruction, with parameters $\vec{p}$ and no misalignments, and $\mathbf{B_j}$ and $\mathbf{A_j}$ are $S \times N$ and $S \times D$ matrices respectively, containing the derivatives of the generalized position with respect to the track and alignment parameters. In case the system is not linear, a second or a third iterations can be performed although in all the applications shown in this thesis one iteration was enough.

As previously defined, the quantity called residual is the difference between the real measurement in the detector, and the estimation provided by the track reconstruction process

$$\vec{R}_j = \vec{x}_j(\vec{p} + \Delta\vec{\ } p_j, \vec{\delta}) - \vec{x}_j(\vec{p}, 0) \tag{3.25}$$

and therefore,

$$\vec{R}_j \simeq \mathbf{B_j}\Delta\vec{\ } p_j + \mathbf{A_j}\vec{q} \tag{3.26}$$

This relation allows to define the following χ^2

$$\chi^2 = \sum_j (\vec{R}_j - \mathbf{B_j}\Delta\vec{p}_j - \mathbf{A_j}\vec{q})^T \mathbf{E_j} (\vec{R}_j - \mathbf{B_j}\Delta\vec{p}_j - \mathbf{A_j}\vec{q}) \tag{3.27}$$

where E_j is the error matrix associated to the residual $\vec{R}_j$ and j is running over the number of muons.

Usually track parameters $\Delta\vec{p}_j$ are referred to as local parameters because they depend on the track, while alignment parameters are referred to as global parameters because they don't have dependency on a given track.

The minimization of the χ^2 yields to the following system of linear equations of dimension $N \times N_{muons} + M$

$$\begin{aligned} \nabla_{\Delta\vec{p}_j}\chi^2 &= 0, j = 1, N_{muons} && (3.28) \\ \nabla_{\vec{\delta}}\chi^2 &= 0 && (3.29) \end{aligned}$$

The expansion of the derivatives in the previous equations yield to the following expressions

$$\begin{aligned} \mathbf{B_j^T E_j B_j}\Delta\vec{p}_j + \mathbf{B_j^T E_j A_j}\vec{\delta} &= \mathbf{B_j^T E_j}\vec{R}_j && (3.30) \\ \sum_j \mathbf{A_j^T E_j B_j \Delta p_j} + \sum_j \mathbf{A_j^T E_j A_j}\vec{\delta} &= \sum_j \mathbf{A_j^T E_j}\vec{R}_j && (3.31) \end{aligned}$$

The number of equations and free parameters in the previous linear system might be very high, as a new entry is added with every new track. The matrix associated to this system has a block structure. One of the blocks is related to the alignment parameters component of the fit, while the others are related to the track component for each of the muons. It is possible to decouple these two components in order to reduce the dimension of the system to the number of alignment parameters. As a consequence the track parameters component is not calculated explicitly. To this end, consider equations 3.31, from where it is possible to compute $\Delta\vec{p}_j$ as

$$\Delta\vec{p}_j = (\mathbf{B_j^T E_j B_j})^{-1}(\mathbf{B_j^T E_j}\vec{R}_j - \mathbf{B_j^T E_j A_j}\vec{\delta}) \tag{3.32}$$

Once this expression is substituted in the other equation 3.31, the system transforms into

$$\sum_j \mathbf{A_j^T E_j}(\mathbf{A_j} - \mathbf{B_j}(\mathbf{B_j^T E_j B_j})^{-1}\mathbf{B_j^T E_j A_j})\vec{\delta} = \sum_j \mathbf{A_j^T E_j}(\vec{R}_j - \mathbf{B_j}(\mathbf{B_j^T E_j B_j})^{-1}\mathbf{B_j^T E_j}\vec{R}_j) \tag{3.33}$$

whose dimension is M the number of alignment parameters. This linear system is intrinsically non-regular due to invariances of the χ^2 (misalignment patterns that leave the χ^2 invariant). In order to get a solution of the system two alternatives are available: the first one consists in the calculation of a pseudo-inverse matrix in which invariances are detected and fixed to 0, and the other consists in the addition of external information that makes the system regular. These invariances are usually known as weak modes of the system. It is important to remark that many track-based algorithms ignore these weak modes, and apply iterative methods to find a solution of their corresponding linear systems. In that case the magnitude of the weak modes might be out of control.

Weak modes in track-based alignment algorithms

Track-based alignment algorithms are limited due to the entanglement between track and alignment parameters. In some occasions it is possible to disentangle this relation and discern which contribution in the track parameter determination is due to alignment effects. On the contrary, sometimes it is not possible to correctly separate both because some specific configurations of misalignments could be perfectly absorbed as fake track parameters.

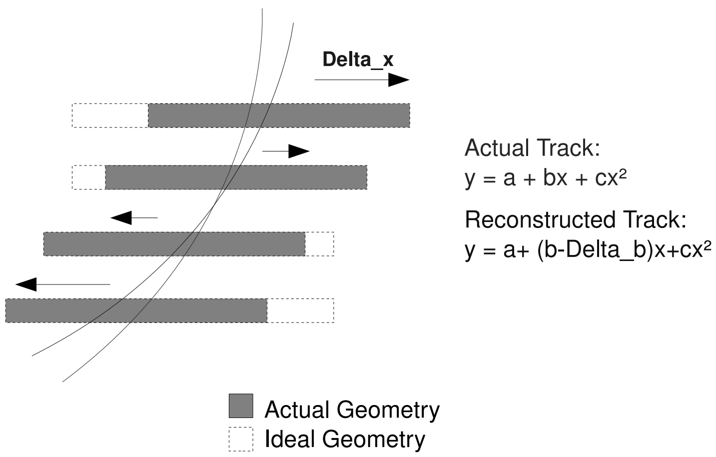

Figure 3.6: Displacement proportional to the radial position of the detectors. In this configuration, misalignments are absorbed as a different slope parameter.

Figure 3.6 illustrates an example of a very simple weak mode for a detector with four detecting planes. If the four planes displace by an amount proportional to their radial position, the muon will be reconstructed perfectly but with a different slope parameter than the actual track. No alignment information can be extracted for this particular configuration of the misalignments. Nor the residuals, nor the χ^2 of the track are sensitive to this kind of movement. These configurations, say $\vec{\Lambda}$, leave invariant the χ^2 of the tracks: $\chi^2(\vec{\delta}+\vec{\Lambda}) = \chi^2(\vec{\delta})$. It is important to clarify that this effect is common to most of the track-based algorithms, and not an specific problem of the MBAA.

The number and structure of weak modes depends on the topology of the tracks and on the geometry of the detector. Regarding the topology of the track, there are two different aspects: the number of parameters needed to parameterize the track, and the geometrical distribution of the tracks over the detector. The more degrees of freedom required to describe the trajectory the less redundancy in the determination of the parameters and therefore the more misalignment configurations that keep invariant the χ^2 of the fit. This effect is illustrated in figures 3.7(a) and 3.7(b). The trajectory can be described with three parameters: an intercept to locate the track in the horizontal direction, a slope to account for the direction of the track, and the curvature term. There are three weak modes associated to this system, a translation proportional to the radial distance of the layers like in 3.6, a constant translation of all the layers like in 3.7(a) and a displacements of the chambers proportional to the square of their radial position, as sketched in 3.7(b).

The geometrical distribution is also important in the characterization of weak modes. The relation between the residuals and the alignment parameters (summarized in equation 3.23) includes correlation terms depending on the track parameters. For instance, δ_z is measured through the correlation between the Δ_x residual and the direction of the track $\frac{dx}{dz}$. A constant distribution of $\frac{dx}{dz}$ centered at 0 (all the tracks being perpendicular to the chamber) will not allow a measurement of the δ_z as shown in figure 3.8(a).

Finally, the geometry of the detector can favor some weak modes due to a poor connection, in terms of track occupancy between different regions of the detector. For example, the alignment of neighboring sectors using tracks coming from the interaction point (like those in figure 3.8(b)) is a weak mode of the system, cause most of the tracks are crossing different chambers in the same sector, but not both. This is not technically an intrinsic weak mode, related to overlap between track and alignment parameters. This kind of weak modes are due to the fact that some alignment configurations are measured with a very much lower precision than the others, because not enough tracks are contributing to it. If the precision is really very poor, they are treated as intrinsic weak modes.

Calculation of the pseudo-inverse matrix

The matrix associated to the linear system 3.33, denoted as $\mathbf{C}$, can be made diagonal by applying an orthogonal transformation V, $\mathbf{D} = \mathbf{VCV^T}$. The elements of the diagonal are the eigenvalues of $\mathbf{C}$ and are denoted as λ_k. We assume that the eigenvalues are sorted in such a way that $\lambda_k > \lambda_{k+1}$. As the matrix $\mathbf{C}$ is non regular, its eigenvalues are 0 for k $> M$. A matrix $\mathbf{D^{-1\star}}$ can be defined as the diagonal matrix:

$$\mathbf{D}_{kk}^{-1\star} = \frac{1}{\lambda_k}, (k <= M) \tag{3.34}$$

$$\mathbf{D}_{kk}^{-1\star} = 0, (k > M) \tag{3.35}$$

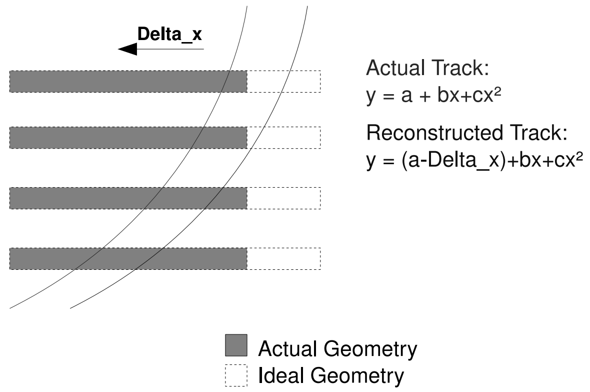

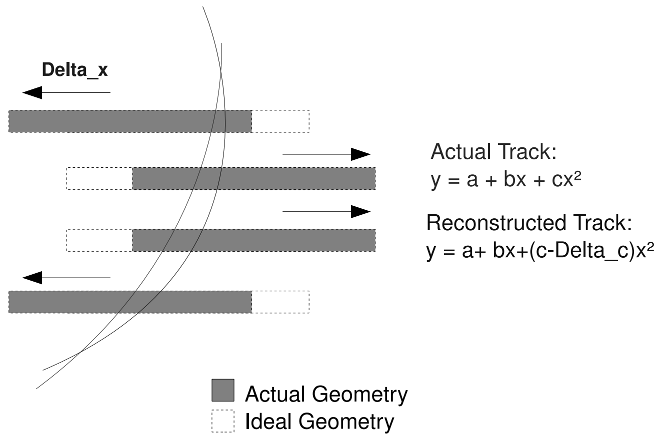

(b)

Figure 3.7: Floating weak mode 3.7(a) and quadratic weak mode 3.7(b)

in such a way that $\mathbf{D}\mathbf{D}^{-1\star} = \mathbf{I}^\star$, where $\mathbf{I}^\star$ is the unit matrix with zeros, instead of the unit in the diagonal for $k > M$. The pseudo-inverse matrix of $\mathbf{C}$ is defined as:

$$\mathbf{C}^{-1\star} = \mathbf{V}^{\mathbf{T}}\mathbf{D}^{-1\star}\mathbf{V} \tag{3.36}$$

and by construction accomplishes as well the relation $\mathbf{C}\mathbf{C}^{-1\star} = \mathbf{I}^\star$. This matrix provides a solution of the system 3.33 of the form

$$\vec{\delta} = \mathbf{C}^{-1\star} \sum_j \mathbf{A}_\mathbf{j}^\mathbf{T}\mathbf{E}_\mathbf{j}(\vec{R}_j - \mathbf{B}_\mathbf{j}(\mathbf{B}_\mathbf{j}^\mathbf{T}\mathbf{E}_\mathbf{j}\mathbf{B}_\mathbf{j})^{-1}\mathbf{B}_\mathbf{j}^\mathbf{T}\mathbf{E}_\mathbf{j}\vec{R}_j) \tag{3.37}$$

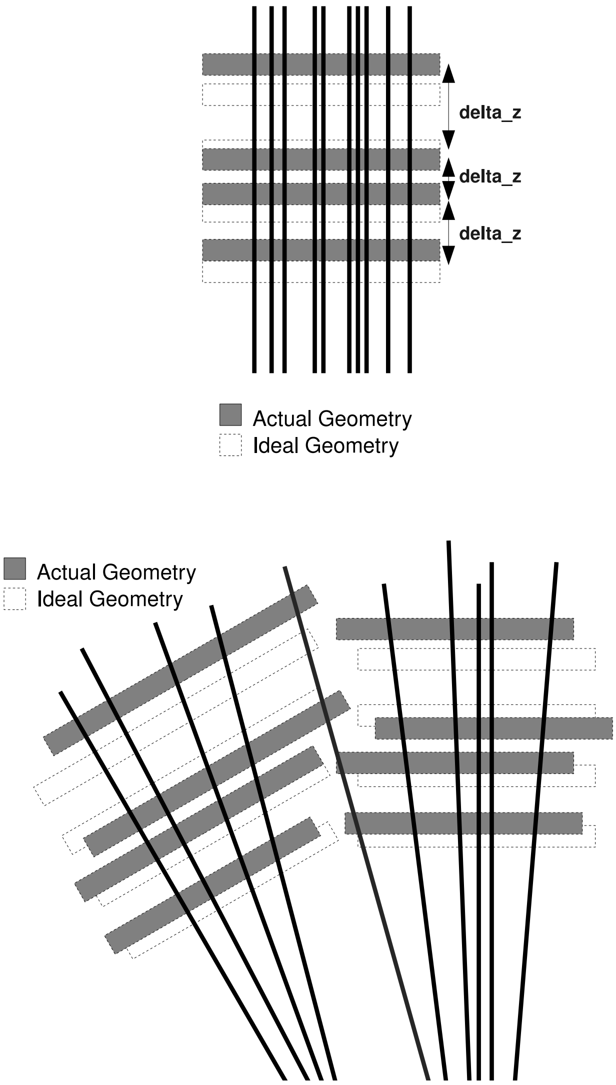

(b)

Figure 3.8: A set of orthogonal tracks crosses a four-layered detector (a) and a set of tracks crosses two sectors of layers, with only one track of overlap (b). In the first case the δ_z displacements cannot be measured, while in the second the relative alignment between sectors is too poor to connect them

in which weak modes are fixed to 0, and the rest of the space of misalignments is inverted normally.

Constraints in the MBAA algorithm

Sometimes it is possible to use external information to constraint 3.27 in such a way that the resulting linear matrix system is regular. This is usually performed by adding new terms to the χ^2 implementing constraints. These new terms can be of two different types: measurement-like and Lagrangian-like.

Measurement-like terms use information from other sources (like survey or the optical alignment) to constraint the fit. These measurements are added to the χ^2, weighted by their corresponding errors. In this way, weak modes are fixed by the external constraints while the rest of the fit is dominated by the more precise track-based component.

Lagrangian-like terms are used to artificially fix some of the weak modes to a given value. This kind of constraint is equivalent to the pseudo-matrix inversion. For instance, sometimes the global position of a detector it is not as interesting as the relative alignment of its components. The weak mode shown in 3.7(a), which is a global displacement of the whole structure could be irrelevant for reconstruction purposes, and hence it is convenient to fix it to some value (0 for example) just to make the system regular, without taking care of this particular configuration. This kind of constraint is performed using Lagrangian multipliers, which become new free parameters of the system.

The general form of the χ^2 is then

$$\chi^2 = \chi^2_{tr} + (\vec{m} - \mathbf{C}\vec{\delta})^T \mathbf{E}_{ex}(\vec{m} - \mathbf{C}\vec{\delta}) + \sum_i \lambda_i(\vec{\delta} - \vec{l}) \tag{3.38}$$

where χ^2_{tr} is 3.27, and $\vec{m}$ represents the external measurements, C is the matrix relating the measurements to the alignment parameters, $\mathbf{E}_{ex}$ is the inverse of the covariance matrix, and λ_i are the Lagrangian multipliers, and $\vec{l}$ the fixation vector in the Lagrange constraint.

3.2.3 Systematics in Track-Based Alignment

The systematic errors affecting track-based alignment algorithms can be divided in two different groups: systematic errors coming from systematics in the track reconstruction, and systematic errors coming from the intrinsic limitations of the algorithms (the weak modes explained in the previous section).

Systematic errors in the tracks are provoked by any kind of bias in the reconstruction process. A wrongly reconstructed track will produce biased residuals, resulting in a bad estimation of the alignment parameters. In general residuals have a dependency on the following effects:

- Misalignments (purely geometric effects usually distributed as δ functions).
- Intrinsic hit resolution (Negligible in most of the cases).
- Statistical uncertainty in the fitted track parameters (following a Gaussian distribution).
- Hard Coulomb scattering of nuclei (which has non-Gaussian tails).
- Multiple Coulomb scattering (Gaussian in the limit of many interactions).
- Calibration parameters.
- Background from pattern-recognition errors and noisy channels (non-Gaussian).

- Systematic errors in magnetic field (proportional to q/p_T).
- Material budget for average energy loss (proportional to q/p^2).

Bias produced by misalignments are the target of alignment algorithms. Sometimes alignment algorithms use tracks which are partially reconstructed outside the detector under consideration (for instance, using tracker tracks to align the muon system). In this case, misalignments of the reference volume are propagated producing large deviations in the residual distributions.

The intrinsic hit resolution is negligible in most of the cases, but may become important in the case of miscalibrated detectors (for example, in a drift tube chamber, a bad estimation of the T_0 [54] time makes the hit resolution worse).

Scattering effects make residual distributions wider and can introduce non-gaussian tails due to hard coulomb scattering or even δ-ray emission [55]. The scattering probability depends inversely on the momentum of the particle, being the effect less important with increasing momentum. In the range of very high momentum, particles can shower producing several signals in the detectors [55]. Pattern recognition algorithms can introduce bias when dealing with high multiplicities in the events.

The trajectory description of a particle is usually dramatically affected by a wrong estimation of the magnetic field which changes the real bending power experienced by the particle. Similarly a bad description of the material budget affects to the energy of the particle and therefore to the momentum [55].

3.3 The CMS Muon Alignment framework

Muon alignment corrections must be incorporated to the reconstruction process in order to improve the physics performance of the detector. A software framework has been developed in CMS to implement the full alignment chain, with special emphasis in the integration with the other CMS subsystems and the use of common tools. In particular, the framework must be able to:

- Store and manage alignment constants.
- Apply constants to the reconstruction process.
- Provide common methods and tools for the track-based alignment algorithms.

Most of these functionalities are encoded in several packages within the *Alignment* package of CMSSW. During the development of this thesis several contributions have been performed in the design, implementation and testing of the muon alignment framework.

3.3.1 Management and storage of alignment databases

The treatment of alignment objects is done in CMSSW [34] through a C++ class called *Alignable* defined in the *Alignment/CommonAlignment* package, and it is common for all the tracking detectors. This class is intended for representing an alignment object, and therefore it contains information about the position and orientation of the object with their corresponding errors, methods to interact with this data, and links to other *Alignable* objects. In addition, when the object is a real CMSSW detector object (*Det*), with a real CMSSW identifier, *Alignable* contains a link to it.

There are dedicated classes defined for the muon system, inheriting from *Alignable* and contained in the *Alignment/MuonAlignment* package. These classes form a hierarchical structure describing the whole muon system, as represented in figure 3.9.

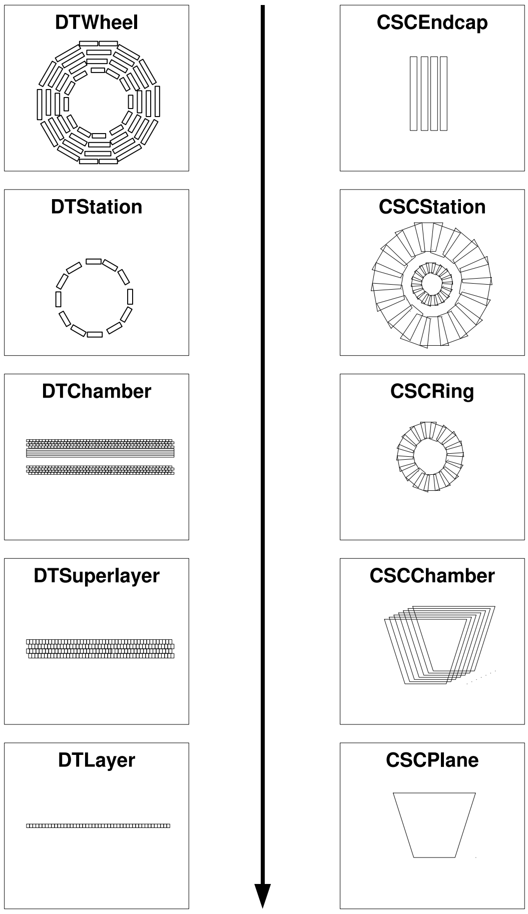

Figure 3.9: Hierarchy of alignables in the muon system.

Most of the methods included in the *Alignable* classes have two functionalities: change the location of the object, propagating down the changes to their child alignables, and retrieving or putting information into a CMS geometry database.

The geometry database for the muon system is divided in four alignment records: *DTAlignmentRcd*, *CSCAlignmentRcd*, *DTAlignmentErrorRcd* and *CSCAlignmentErrorRcd*. These records or tables, store the identifiers, position, orientation, and errors of the objects in the barrel and endcaps, respectively.

The identifiers always refer to the official identifiers of the objects defined in CMSSW, and the position and the three rotation Euler angles are absolute and given in the CMS reference frame. Only *Alignables* referring to a real CMSSW detector are written to the database. In the case of the drift tube chambers, these *Alignables* are, the DTChamber, the DTSuperLayer and the DTLayer. Respectively, for the cathode strip chambers, the CSCChamber and CSCLayer.

In addition to the records, the databases store metadata information used for bookkeeping. Each record is identified by a tag containing a record tag name, and an interval of validity (IOV) containing the range of CMS runs where the record is valid.

The *MuonAlignment* package is able to produce these records in several database formats. Nevertheless a standard procedure has been defined in CMS, in such a way that private records are always stored as SQLite files. Once a geometry has been properly tested the SQLite [56] files are transferred to the ORACLE-based ORCON (see previous chapter) through the so called drop-box mechanism.

3.3.2 Application of constants to the reconstruction

All tracking components have a local system of reference in which intrinsically they measure. In order to perform the reconstruction, it is needed to convert the measurements from each individual local system to a common frame (for instance, the CMS global system of coordinates). This conversion requires a displacement $\vec{r}$ and a rotation matrix $\mathbf{M}$ (obtained from the geometry database) which redefines the center and orientation of the object.

$$\vec{x}^{global} = \mathbf{M}(\vec{x}^{local} + \vec{r}) \tag{3.39}$$

The strategy followed in CMS in order to apply alignment corrections was based on the update of this pair of displacement and rotation matrix to correctly adapt the conversion from the local system of coordinates to the global frame. The old $\vec{r}$ and $\mathbf{M}$ are converted in $\vec{r}'$ and $\mathbf{M}'$ in such a way that the global position of the hit is the correct place. It is important to notice that if the alignment parameters are expressed as a displacement $\vec{\delta}$ and a linear rotation matrix R, then

$$\vec{r}' = \vec{r} + \vec{\delta} \tag{3.40}$$

$$\mathbf{M}' = \mathbf{RMR^T} \tag{3.41}$$

One of the advantages of this method is that all the products of the local reconstruction remain unchanged and only their global position is updated. This allows to perform the reconstruction over many different geometries having only to repeat the last step in the reconstruction chain.

This procedure is not only valid for corrected geometries, it is used as well to produce fake misaligned geometries, in which objects are misaligned on purpose to study the performance of the reconstruction under several misalignment environments. These fake geometries are usually called alignment scenarios.

3.3.3 Common methods for alignment algorithms

The CMS alignment framework has to provide common methods for the different alignment algorithms running over the different subsystems. This is a strong requirement in an environment like CMS where the flux of new developers may be high and an easy maintenance of the code is needed.

In particular from the point of view of the track-based alignment algorithms, this unification was performed through a collection of common classes mainly contained in the packages *Alignment/CommonAlignment* and *Alignment/CommonAlignmentAlgorithm*. The core of this framework is the class *AlignmentProducer*, a generic class which controls the workflow of the track-based alignment procedures. Specific alignment algorithms are invoked as plugins from *AlignmentProducer*, receiving a unified data format to perform the calculations. All the alignment algorithms must inherit from *CommonAlignmentAlgorithms*, a very generic class which defines the standard methods and data formats used by all the algorithms. In addition, *AlignmentProducer* has the functionality of writing to a database the output of the algorithms, and using the tools explained in the previous section.

3.3.4 Integration in the CMS alignment and calibration workflow

The CMS alignment and calibration workflow [57, 58, 59] has to ensure that the prompt offline event reconstruction can apply alignment and calibration constants that are already updated for possibly rapidly changing data taking conditions. In addition, the framework has to support longer latency workflows for constants that change less rapidly and require more data than can be accumulated. These constants can then be applied in a later re-reconstruction.

The key components of the alignment and calibration workflows are the online processing at the CMS detector site (P5), including the software based High Level Trigger (HLT), and the offline processing at the Tier 0 (T0) and the CERN Analysis Facility (CAF)[60], both located at the CERN Meyrin site.

Special alignment and calibration datasets are called *AlCaReco* (see appendix A). The interplay between the key components and the data streams is sketched in figure 3.10 and detailed in the following.

- **P5**. The HLT machines select events and feed them to the Storage Manager. Here, the events are buffered and transferred to the T0 in a special streamer format. According to the HLT decision, different data streams are processed: one for the bulk data for physics analysis and a subset as an express stream for the prompt alignment and calibration as well as for physics data quality monitoring. In addition, some calibration tasks require such a high data rate that special calibration streams (AlCaRaw) are created where the content of selected events is already reduced before sending the data.
- **T0**. The data is first repacked from the streamer format into the ROOT [61] based CMS Event Data Model (EDM), and primary datasets are built based on HLT decisions. The physics data is cached on disk for about 24 hours until the prompt alignment and calibration constants are available for reconstruction. Express and calibration streams

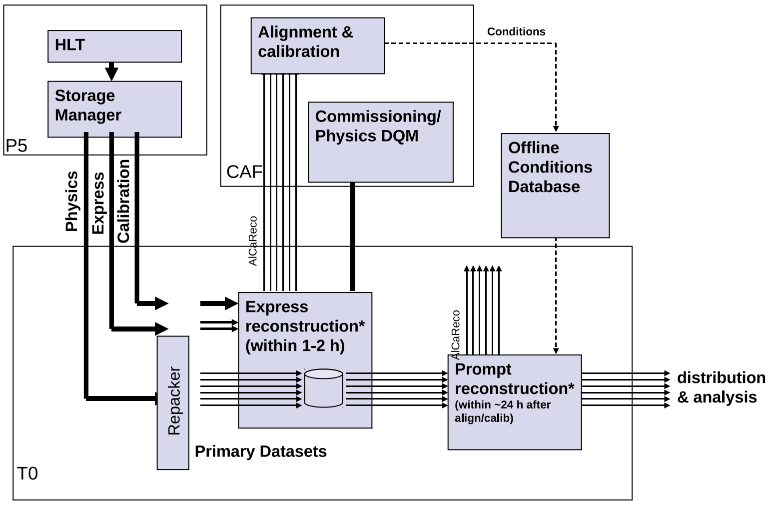

Figure 3.10: Diagram showing the different steps of the alignment and calibration workflow of CMS.

are reconstructed with lower latency. AlCaReco datasets are created both from the calibration streams and normal data. The number of events and the event content for these datasets are reduced to exactly match the requirements of the different alignment and calibration tasks. In that way I/O latencies can be avoided.

- **CAF**. The CAF is the prime platform for offline alignment and calibration algorithms. The AlCaReco datasets are stored on a dedicated CAF disk pool. This ensures fast access by the algorithms that run on CAF farm queues to compute and validate their constants.

- **Databases**. Alignment and calibration constants derived at the CAF are transferred to the online environment at P5. There they are uploaded to the online database (ORCON) from where they are automatically streamed to the offline counterpart (ORCOFF). The prompt reconstruction at T0 reads the constants, similarly to analysis jobs, via intermediate caching layers, called Frontier [62].

Muon Alignment workflows are integrated in this general scheme. In particular, the hardware alignment system whom raw data is not event-like, participates through the calibration stream to move data to the T0 and then to the CAF, where COCOA analysis are run. Track-based alignment algorithms use dedicated AlCaReco samples: *MuAlGlobalMuon*, *MuIsolatedMuon*. A detailed description can be found in appendix A.

Chapter 4

Muon Alignment Scenarios for Monte Carlo Simulations

The software, reconstruction and analysis machinery of CMS was extensively tested in parallel with the construction and commissioning of the detector (see appendix B for a detailed description). The CMS software was used to generate Monte Carlo-based samples emulating the detector response. These samples were reconstructed using the standard procedures and several relevant physics analysis were performed.

Special emphasis was put in the preparation for the LHC start-up, in order to understand the impact of the misalignments and miscalibrations of the detector in the different steps of the reconstruction and analysis chain. For this reason, different sets of realistic alignment and calibration conditions were designed and populated into the official databases of CMS.

In particular, for the alignment of the muon system, several fake geometries, known as alignment scenarios, were produced to resemble the expected alignment accuracy of the muon system. As muon alignment was evolving in parallel with the development of the detector, the correctness and realism of these scenarios were based in the current knowledge at the moment of the scenario definition.

This chapter covers a description of the tools used to generate muon fake geometries, and a description of the most important alignment scenarios used by the collaboration in the large-scale simulation campaigns.

4.1 Simulation of fake alignment conditions in the muon system

In chapter 3, it was shown, how a misaligned geometry could be corrected, by updating the geometrical transformations between the reference systems of the specific subdetectors and the CMS official frame. This procedure can be applied as well to produce a fake, misaligned geometry. In this case, the nominal geometry is modified according to a set of misalignments depending on the scenario definition.

Monte Carlo samples are generated using different particle generators like Pythia [63] or Alpgen [64]. The propagation and electronic response produced by the particles through the different subdetectors of CMS is simulated using the Geant4 software [65]. It is important to remark, due to its relevance in the alignment, that simulation is always performed with the nominal geometry. Finally, the reconstruction algorithms calculate the trajectory of the particles using a task-defined geometry; it can be the ideal geometry, a corrected geometry or even a misaligned geometry for estimation purposes. As it was pointed out in chapter 3, this procedure allows to reduce drastically the required computational resources, provided a full generation or simulation is not required to test and check different geometries.

In general, muon misalignment scenarios are able to take into account two different effects:

- **Permanent effects.** These are unavoidable misalignment effects whose shape and magnitude are known to some level of accuracy (i.e. magnetic compression of the CMS endcaps [66]), and which are represented by single-fixed valued misalignments.

- **Accuracy effects.** The different alignment mechanisms of CMS are able to provide an alignment within a given precision. This is modeled in the scenario production through a random smearing, based on normal distributions with a spread equal to the reference accuracy.

The first implementations of the muon alignment scenarios were included in the previous version of the CMS software called ORCA [67]. Those scenarios [68] made extensive use of both kind of misalignments. In particular permanent effects were utilized to describe the magnetic compression of CMS [66]. Nevertheless, the new implementations of the alignment scenarios, in the era of CMSSW, include only accuracy effects. The argument given to support this decision is related to the fact that the actual geometry of the detector is irrelevant to the reconstruction process and only the uncertainty in the determination of this geometry is important. This assumption works whenever misalignments are small enough to not affect considerably the efficiency of the detectors, which is guaranteed by the construction tolerances.

4.1.1 Software implementation

The software used to produce muon alignment scenarios is contained within the *Alignment/MuonAlignment* package of CMSSW and it is based in the previous implementation in ORCA [68, 69]. Besides the tools and functionalities pointed out in chapter 3, this package contains a module called *MuonScenarioBuilder* which performs the following tasks:

- Interpretation of the muon scenario configuration files.

- Calculation of fake misalignment constants.

- Application of the constants to the muon geometry.

- Production of muon alignment records with the scenario geometry.

The workflow associated to the production of a muon alignment scenario starts with a formatted configuration file in which the scenario is coded. *MuonScenarioBuilder* establishes a connection between the muon *Alignable* objects and the tags specified in the file, and uses random engines with the specified parameters to produce the real misalignment values. These

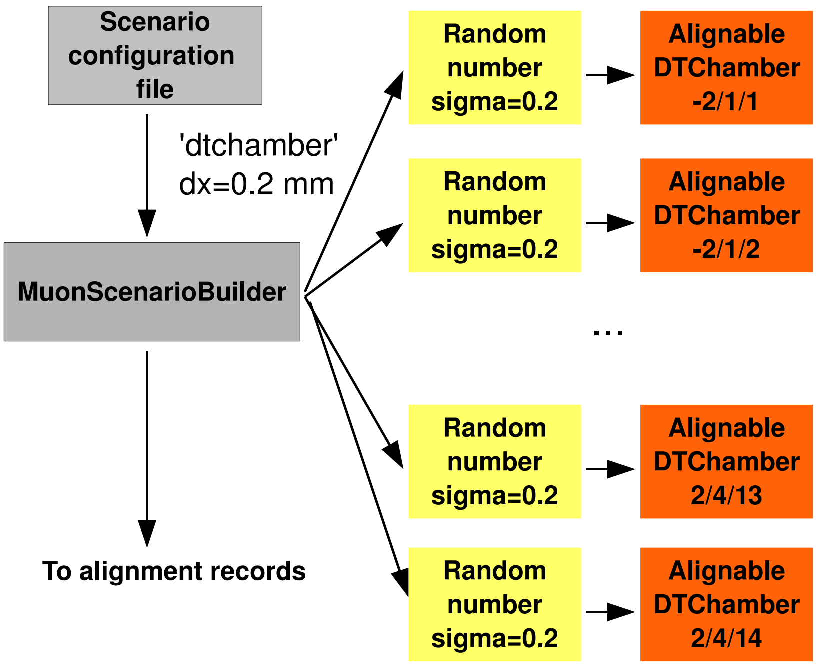

Figure 4.1: Workflow associated to the generation of a misalignment scenario.

numbers are properly updated in the *Alignable* object, and finally using the standard machinery it is dumped to alignment records. This process is sketched in figure 4.1.

The *MuonAlignment* package in CMSSW was based in the same-named package in the previous CMS software ORCA. Part of this thesis consisted in the implementation of this package [68, 69], and the collaboration in the porting to CMSSW. The administration, management and further developments in the modern *MuonAlignment* package constitute as well part of this thesis.

Muon scenario configuration files

Muon alignment scenarios are defined trough a formated text file usually called scenario configuration file. The syntax of these files was initially based in the *PSet* format defined in CMSSW. After the migration to the PYTHON [70] configuration files, the scenarios were defined as well using the PYTHON syntax.

In these configuration files, each scenario is represented by a block labeled with the name of the scenario. Each of these blocks is a nested structure of sub-blocks referring to the different *Alignable* objects. Within each sub-block, single parameters can be found in order to specify the type of random distribution used for the generation of the values, the spreads associated to the *Alignable* (for all the position and rotation coordinates, and both in local and global) and the factor scales for the errors and for the alignment parameters. Additionally, in the root block some parameters common to all the structures are defined, as the seed for the random engines. Figure 4.2 shows an snapshot of a muon alignment scenario configuration file directly from the CVS browser.

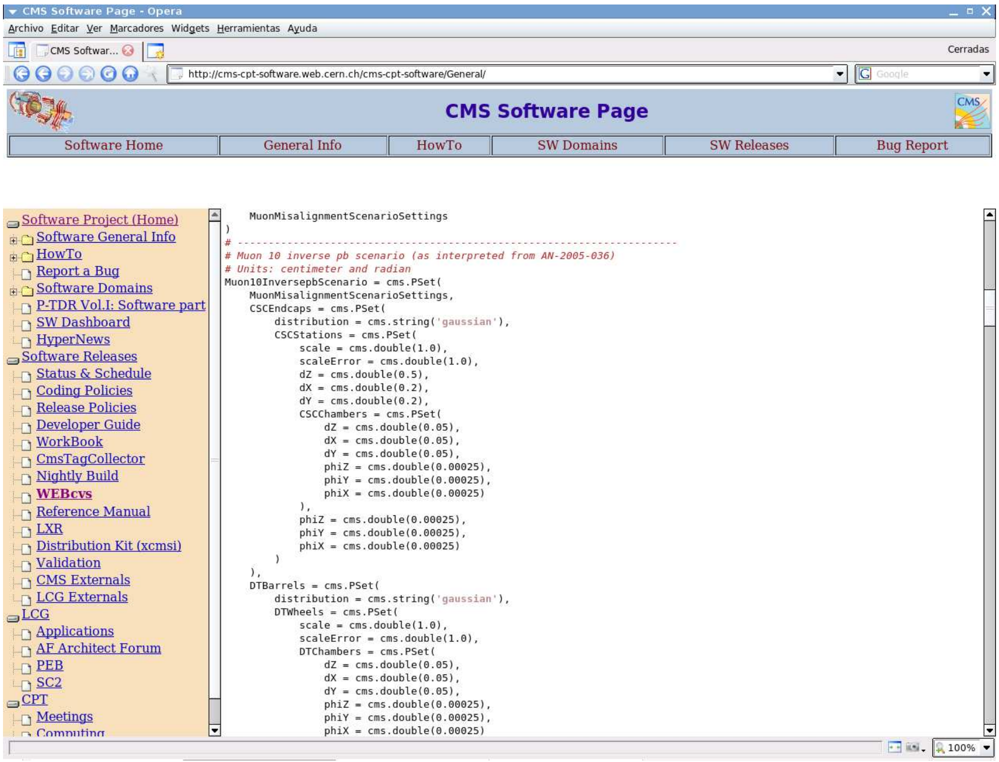

Figure 4.2: Snapshot of a scenario configuration file from the CVS web navigator.

In chapter 3, it was established that *Alignable* objects contains references to its children *Alignable* producing a hierarchical structure of the *Alignable* objects, in such a way, that misalignments in a parent object were propagated down to their children. The nested block syntax in the configuration files benefits from this functionality to recursively apply the alignments to the whole hierarchical structure.

4.1.2 Updates and further development in the MuonAlignment package

Blocks used in the definition of the scenarios were restricted to the Alignable objects implemented in the MuonAlignment package. This turned out to be insufficient in order to properly describe all the expected misalignments in the muon system. In particular there were two important misalignment configurations that could not be applied:

- Global misalignment of the muon system. A rigid, unique, misalignment of all the muon system to simulate possible misalignments between the tracker-muon system.

- Correlated misalignment of sectors. These configurations of misalignments are important weak modes of the track-based algorithms (a detailed explanation was provided in chapter 3). A proper simulation of this effect was needed in order to test and evaluate the response and performance of the algorithms.

Global misalignments were not allowed in the first implementation of the code because the Barrel and the Endcap structures were not depending on any other upper structure from which the misalignments could be propagated down. Additionally, the correlated misalignments of sectors were not possible because sectors were not *Alignable* objects and therefore were not included in the hierarchy associated to the muon structures. Some new methods were added to the *MuonScenarioBuilder* class to produce these misalignments.

In particular three new specific categories were created: *Muons*, *dtsectors* and *cscsectors*. The corresponding blocks had to be added to the scenario definition block, without belonging to any other structure. These blocks are parsed by the *MuonScenarioBuilder*, which calls to the corresponding associated methods, in charge of getting the corresponding random numbers, and apply them properly to the *Alignable*.

For the global movement of the muon system, a loop is performed over all the *DTChamber* and *CSCChamber* objects using a same set of random misalignments. In the case of the sectors, misalignments are applied to all the chambers within a sector. The definition of sector in the barrel region is quite intuitive because the chambers are well separated in the ϕ coordinate, however in the endcap there is a certain overlap between chambers, making the classification in sectors not so clear. To this end, the trigger sector convention was used.

Figure 4.3 shows the hierarchy of *Alignable* objects (from the point of view of the functionality) after these improvements.

4.2 Alignment Scenarios for CSA06

During October 2006, a Computing and Software Analysis (CSA) exercise took place at CERN. The target of this exercise was to simulate 25% of the computational load expected for the LHC startup. A detailed description of the main features of this exercise can be found in appendix B.

Alignment and calibration scenarios were prepared for the different subdetectors and applied to the reconstruction process. In particular, concerning the alignment of the muon system, three scenarios were designed: Survey Only, Short Term and Long Term.

These scenarios were inspired in the scenarios developed for alignment studies in the Physics Technical Design Report [21]. The main difference is related to the removal of permanents movements in the endcap region. Only accuracy effects are taken into account, using in all the cases normal distributions centered at 0.

4.2.1 The Survey Only alignment scenario

The Survey Only scenario is intended to emulate the alignment status of the detector when the only available information is provided by construction and closing tolerances and the first survey information. In this scenario, neither the hardware-optical alignment system, nor the track-based alignment have started to produce constants. It is divided in two different kinds of effects: misalignments of large structures, accounting for effects as the closing tolerances and individual movements of the chambers.

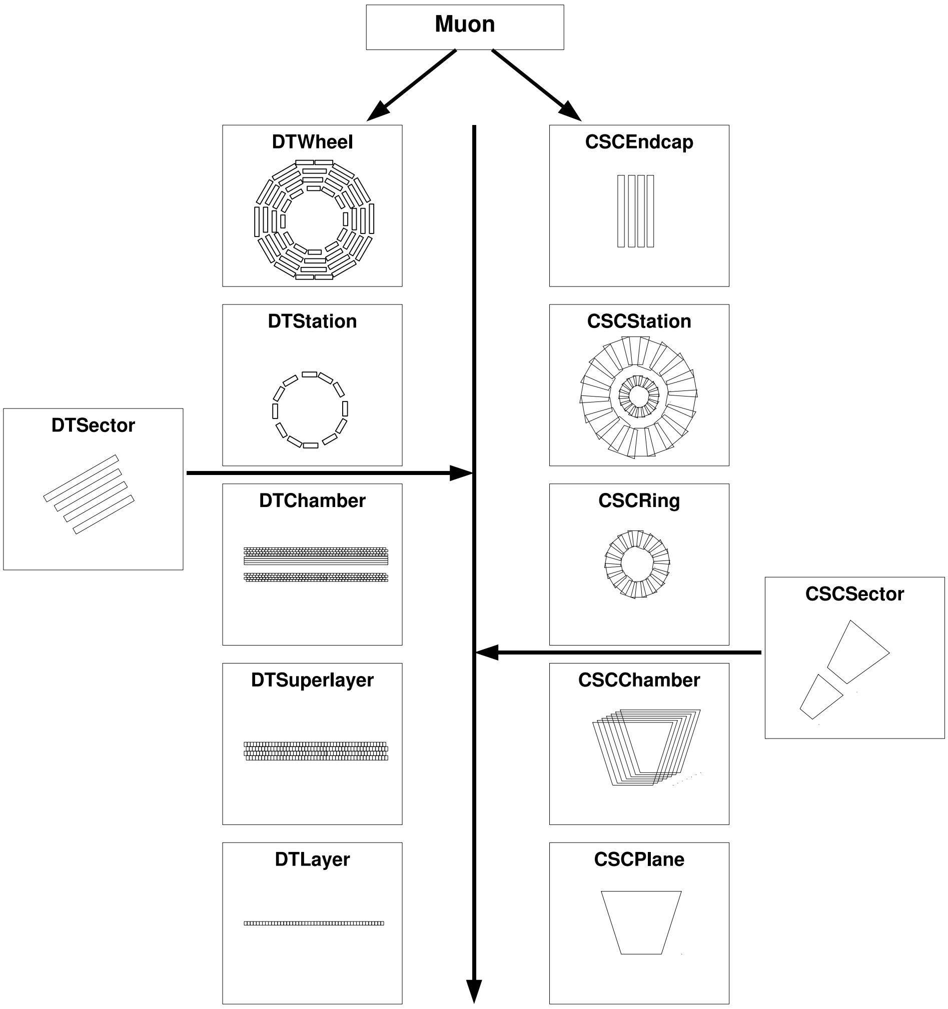

Figure 4.3: Functional hierarchy of *Alignables* for the scenario definition.

Endcap disks are displaced with a $\sigma = 0.25$ cm in the global X and global Y coordinates, and $\sigma = 0.55$ cm in the Z global coordinate, because of the magnetic compression expected for the endcaps of CMS. Rotations were only implemented around the global Z axis with $\sigma = 0.25$ mrad. This corresponds to displacements of about 0.2 cm in the outermost chambers, and therefore is consistent with the translational precisions. Barrel wheels have the same uncertainty in global X, Y and Z coordinates, $\sigma = 0.25$ cm, because the photogrammetry precision is the same in all the coordinates. Rotations are the same as in the endcap disks $\sigma = 0.25$ mrad. Individual misalignments for both endcap and barrel chambers have a spread of $\sigma = 0.1$ cm, according to the photogrammetry precision, for all the coordinates, and a rotation with $\sigma = 0.05$ mrad around the Z axis. This value corresponds approximately to differences of about 2 mm between both sides of the chambers.

Alignable	X/cm	Y/cm	Z/cm	$\Phi_X/mrad$	$\Phi_Y/mrad$	$\Phi_Z/mrad$
Endcap Station	0.25	0.25	0.55	0	0	0.25
Endcap Chamber	0.1	0.1	0.1	0	0	0.05
Barrel Wheel	0.25	0.25	0.25	0	0	0.25
Barrel Chamber	0.1	0.1	0.1	0	0	0.05

Table 4.1: Resolution for the position and orientation of the different structures and chambers in the Survey Only alignment scenario

4.2.2 The Short Term alignment Scenario

The Short Term scenario was designed to reproduce the status of the alignment once the hardware alignment has started to operate and is producing the first results. This scenario keeps the division between structure and individual movements, although the accuracy of the structure misalignments is much better due to the hardware alignment preliminary measurements. In particular, large effects as the magnetic compression were expected to be measured [66] and hence the spread of the translational misalignments for wheels and disks is the same for all the coordinates, $\sigma = 1$ mm. Rotations around the Z axis are roughly improved $\sigma = 0.2$ mrad. Measurements of the individual movements of the chambers were not expected to improve significantly at this stage and therefore the spread of the misalignments is the same as in the previous scenario: $\sigma = 0.1$ cm for displacements and $\sigma = 0.05$ mrad for the rotation around Z.

Alignable	X/cm	Y/cm	Z/cm	$\Phi_X/mrad$	$\Phi_Y/mrad$	$\Phi_Z/mrad$
Endcap Station	0.1	0.1	0.1	0	0	0.2
Endcap Chamber	0.1	0.1	0.1	0	0	0.05
Barrel Wheel	0.1	0.1	0.1	0	0	0.2
Barrel Chamber	0.1	0.1	0.1	0	0	0.05

Table 4.2: Resolution for the position and orientation of the different structures and chambers in the Short Term alignment scenario

4.2.3 The Long Term alignment Scenario

The Long Term scenario emulates the situation of the detector after sufficient data are collected and the hardware alignment is understood and reaches its nominal precision. Typically this might take a few months of data taking. The structure of the movements is kept similar to the previous scenarios, but there are significant reductions in the spreads of the distributions. Misalignments of wheels and disks have a spread of $\sigma = 0.02$ cm for all the coordinates, and $\sigma = 0.04$ mrad for the rotation with respect to the Z axis for the wheels and $\sigma = 0.05$ mrad for the disks. These numbers come from the final precision of the optical alignment and track based alignment systems. Individual movements on the contrary have a spread of $\sigma = 0.02$ cm for all the coordinates except for the Z of the CSC chambers where it is kept slightly higher $\sigma = 0.04$ mrad, to be conservative provided the Z is measured with a lower resolution by both the optical and track-based alignment systems. The rotations for the individual chambers are smeared with spread $\sigma = 0.1$ mrad and $\sigma = 0.5$ mrad respectively for the cathode strip and drift tube chambers, being consistent with the individual displacements performed.

Alignable	X/cm	Y/cm	Z/cm	$\Phi_X/mrad$	$\Phi_Y/mrad$	$\Phi_Z/mrad$
Endcap Station	0.02	0.02	0.02	0	0	0.04
Endcap Chamber	0.02	0.02	0.04	0	0	0.1
Barrel Wheel	0.02	0.02	0.02	0	0	0.5
Barrel Chamber	0.02	0.02	0.02	0	0	0.5

Table 4.3: Resolution for the position and orientation of the different structures and chambers in the Long Term alignment scenario

4.2.4 Validation of the CSA06 alignment scenarios

The scenarios explained in the previous section were produced and stored into SQLite private databases, and then populated to the official databases of CMS. During the CSA06 exercise, the scenarios were widely used for the different workflows and analysis tested. In particular, the muon alignment scenarios were of great relevance, for the muon alignment workflow [71] and for all the analysis depending strongly on the muon system (see [72] for detailed description of these analysis).

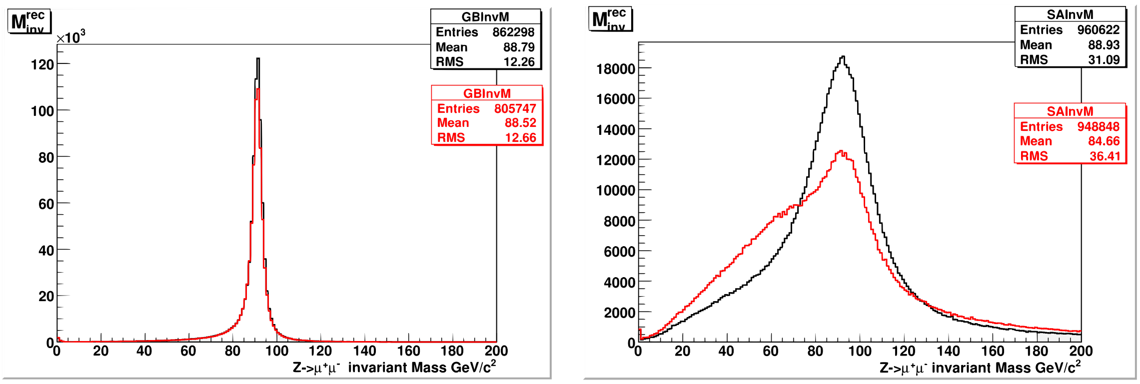

(a) (b)

Figure 4.4: Di-muon invariant mass for Z boson decay using a perfect alignment and the ShortTerm scenario, for global muons (a) and standalone muons (b).

The first available samples produced at the CSA06 were used to validate and study the alignment scenarios. In particular, figures 4.4 show the di-muon invariant mass for the decay Z→ $\mu^+\mu^-$ using the design geometry and the short term scenario, and for the global and standalone reconstruction. The distortion provoked in the mass peak is small in the global reconstruction as it is dominated by the tracker (assumed perfect in this exercise) in this range of energies [75]. The standalone reconstruction however is strongly affected.

Figures 4.5 show the global reconstruction efficiency and momentum resolution with respect to the pseudorapidity and the momentum respectively. The plot is repeated for the design geometry, the Short Term scenario and the longterm scenario. The efficiency plot clearly shows a degradation of the efficiency of almost 0.1% for the ShortTerm scenario, which is recovered by the longterm. The same trend can be observed in the momentum resolution plot. The Short Term scenario produces a significant degradation of the resolution, which is almost recovered by the long term scenario, exhibiting still an appreciable deviation for high momentum tracks.

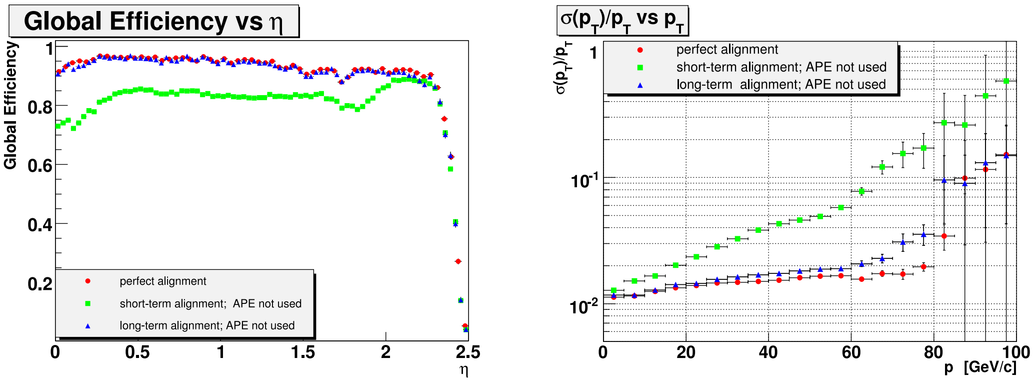

(a) (b)

Figure 4.5: Efficiency (a) and momentum resolution (b) of the global reconstruction using a perfect geometry and the Short Term and Long Term scenarios. Alignment Position Errors (APE) were not used.

4.3 Alignment Scenarios for CSA07

During the Computing and Software Analysis challenge in 2007 (CSA07) all the computational chain of CMS was tested again using Monte Carlo samples. The target was to simulate the 50% of the expected load for the start-up of the LHC.

Two new alignment scenarios were designed and deployed for this exercise. The quality of the alignment has a component depending on the time, because of the number of high momentum tracks that can be collected to feed the track based algorithms. For that reason the names of the scenarios corresponds to the integrated luminosity that the detector has collected. This must be interpreted as the expectation of the state of the alignment with the given integrated luminosity.

In particular for the CSA07 campaign the two scenarios were the $10\,pb^{-1}$ and $100\,pb^{-1}$ respectively.

4.3.1 The $10\,pb^{-1}$ alignment scenario

This scenario was inspired in the previous Survey Only scenario, under the conservative assumption, that the first data will not improve it considerably. Nevertheless, some improvements and corrections were made incorporating the experience from the Magnet Test and Cosmic Challenge (see appendix B and [74]), which basically establishes that the relative alignment of objects within large structures would be improved.

Displacements of endcap stations are slightly reduced to $\sigma = 0.2$ cm and 0.5 cm respectively for x and y, and z. Rotations are added to the ϕ_x and ϕ_y angles with magnitude

σ =0.25 mrad, the same as ϕ_z. The trend is the same for barrel wheels. These numbers are very similar to those in the Survey Only scenario. Rotations were extended to coordinates ϕ_x and ϕ_y as a conservative approach.

The alignment of individual chambers is improved by a factor 2 with respect to Survey Only in what respects to displacements, with a spread of σ =0.05 cm. Rotations are set to σ =0.25 mrad. This improvement comes from the knowledge acquired during the MTCC in which even with a relatively small sample of tracks, it was possible to align the muon chambers relative to each other with a precision better than the precision of photogrammetry (see chapter 7).

Alignable	X/cm	Y/cm	Z/cm	$\Phi_X/mrad$	$\Phi_Y/mrad$	$\Phi_Z/mrad$
Endcap Station	0.2	0.2	0.5	0.25	0.25	0.25
Endcap Chamber	0.05	0.05	0.05	0.25	0.25	0.25
Barrel Station	0.25	0.25	0.3	0.25	0.25	0.25
Barrel Chamber	0.05	0.05	0.05	0.25	0.25	0.25

Table 4.4: Resolution for the position and orientation of the different structures and chambers in the 10 pb^{-1} alignment scenario

4.3.2 The $100\,pb^{-1}$ alignment scenario

In consonance with the $10\,pb^{-1}$ scenario, the $100\,pb^{-1}$ scenario was based in the previous Short Term scenario. The basis of the scenario is to reduce slightly the magnitude of the individual misalignments of chambers and disks under the assumption that the hardware alignment system and the track-based alignment will measure it with good precision. In addition some new effects not present in the previous scenarios were added.

In particular, a global misalignment of the muon system with respect to the tracker was implemented, mimicking the expected error for the link system. The spreads were $\sigma = 0.1$ cm for displacements and σ =0.25 mrad for rotations. Individual misalignments of the sectors, using the same spread σ =0.1 cm were included to study the performance of the track-based algorithms. Individual misalignments of chambers were reduced to $\sigma = 0.02$ cm and $\sigma = 0.1$ mrad.

Alignable	X/cm	Y/cm	Z/cm	$\Phi_X/mrad$	$\Phi_Y/mrad$	$\Phi_Z/mrad$
Muon	0.1	0.1	0.1	0.25	0.25	0.25
Endcap Chamber	0.02	0.02	0.02	0.1	0.1	0.1
Endcap Sectors	0.1	0.1	0.1	0.25	0.25	0.25
Barrel Chamber	0.02	0.02	0.02	0.1	0.1	0.1
Barrel Sectors	0.1	0.1	0.1	0.25	0.25	0.25

Table 4.5: Resolution for the position and orientation of the different structures and chambers in the 100 pb^{-1} alignment scenario

4.3.3 Validation of the CSA07 alignment scenarios

A first validation of the muon alignment scenarios was performed in order to spot problems before the large scale CSA07 production started. Two variables were studied: the efficiency of the reconstruction and the momentum resolution. The study used the first single muon samples that where available at the moment of creation of the scenarios. The generated P_t of the muons was $100\,GeV$.

Figures 4.6(a) and 4.6(b) show the reconstruction efficiency as a function of the pseudorapidity η for both the standalone and global reconstruction. As can be expected the drop in efficiency is not too important, except for the case of the $10\,pb^{-1}$ and for $\eta > 2.1$. That value of the pseudorapidity is the boundary between the barrel and endcap systems. In this region of pseudorapidity, tracks have a very small bending path, what makes the process of the reconstruction much more difficult, and much more sensible to misalignments.

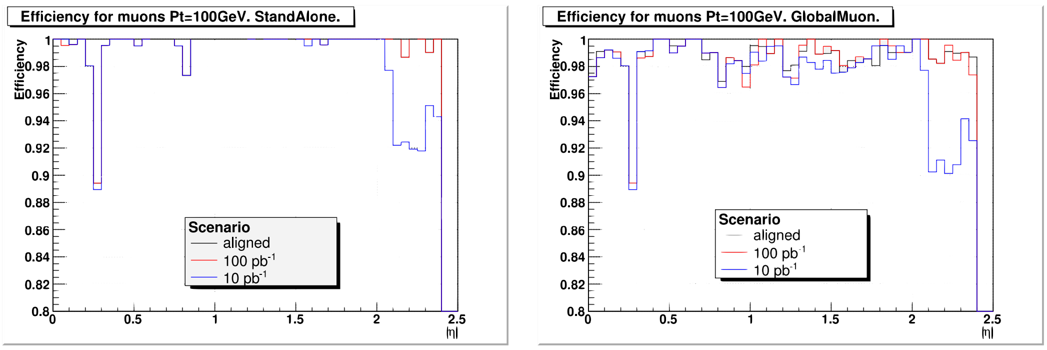

(a) (b)

Figure 4.6: Reconstruction efficiency for the CSA07 scenarios and for the 4.6(a) standalone and global 4.6(b) reconstruction.

On the contrary, figures 4.7(a) and 4.7(b) show the momentum resolution for both reconstructions. Degradation of the resolution in the barrel is not too much appreciable in none of the cases. Once the endcap chambers start to enter in the reconstruction fit ($|\eta| > 1.0$), the resolution degrades, provided the bending path is smaller, and therefor more sensible to misalignments. This trend is specially significant for the $10\,pb^{-1}$ scenario and the standalone reconstruction. The momentum resolution using the global reconstruction is more similar to the nominal geometry. This is an indication that the tracker (which is assumed to be perfectly aligned in this study) dominates the momentum measurement at this momentum range.

4.3.4 Inconsistencies at the TeV scale

The collection of test samples available for studying the performance of the scenarios before the large-scale production started was limited because of time constraints and overloaded resources. For that reason a full-range momentum evaluation was not possible until the official samples of CSA07 were produced.

Once the analysis started, an unexpected behavior of the 100 pb^{-1} scenario was reported by the group in charge of the Z' studies [82, 83]. Momentum resolution studies of the global

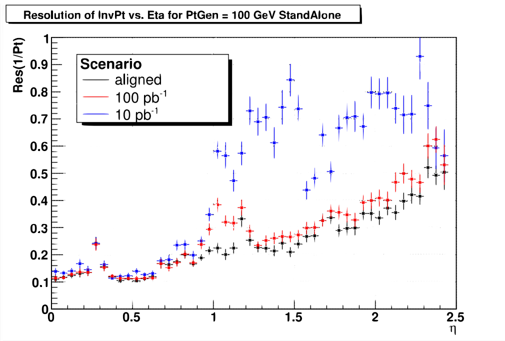

(a)

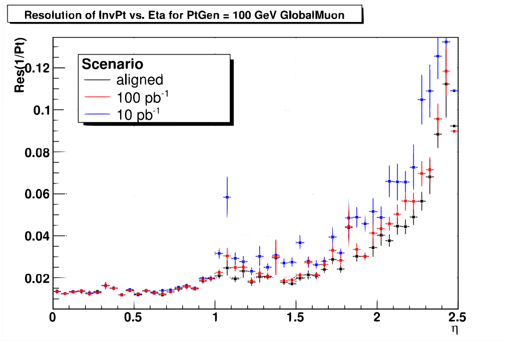

(b)

Figure 4.7: Momentum resolution for the CSA07 scenarios and for the standalone (a) and global (b) reconstruction.

reconstruction at the TeV scale showed a better performance of the 10 pb^{-1} scenario than the 100 pb^{-1}, as it can be observed in figure 4.8. This effect did not show a consistent picture of the alignment procedures, because new geometries are not published unless it was demonstrated they are an improvement of the geometries already in use. In this sense, the 100 pb^{-1} situation, should be at least as good as the 10 pb^{-1} situation.

The degradation of the momentum resolution was not observed however for the standalone reconstruction. As it only appeared when the tracker and the muon system were combined, the effect pointed to some mismatching between the tracker and the muon system. In view of the scenario definition in table 4.5, the problem was the global misalignment of the muon system with respect to the tracker, provided it leaves invariant the muon system reconstruction, but introduces a large bias in the matching of tracker and muon tracks.

The 100 pb^{-1} scenario was redefined without the relative misalignment between the tracker and the muon system in order to isolate the effect that was provoking that was degrading the momentum resolution. In figure 4.8 the momentum resolution for this case is shown as well. As can be observed the momentum resolution of the global reconstruction is recovered after this update of the scenario. It was concluded that the relative position between the tracker and the muon system plays a crucial role in the reconstruction process. Dedicated studies on this subject were performed afterwards and can be found in [38].

4.4 Alignment Scenarios for CSA08

A new computing exercise was performed during the year 2008. In this occasion the Computing, Software and Analysis challenge (CSA08) was focused in emulating the first data taking of CMS, and more in particular the first $10\,pb^{-1}$. Three different scenarios were requested for this exercise: the START-UP scenario, the $1\,pb^{-1}$ scenario and the $10\,pb^{-1}$ scenario.

In the case of the muon alignment the decision was to merge the START-UP and $1\,pb^{-1}$ in a single scenario, given the fact that not a big improvement in the alignment of the muon system was expected for the first $1\,pb^{-1}$ of integrated luminosity.

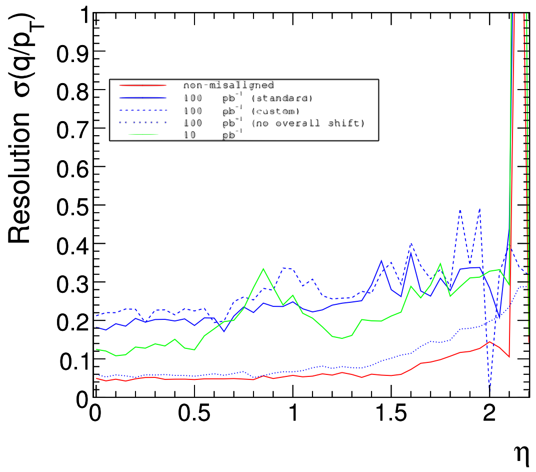

Figure 4.8: Global reconstruction momentum as a function of the pseudorapidity. Resolution for the 10 pb^{-1} scenario is better than the 100 pb^{-1} for very high momentum muons (1 TeV in this case). If the global misalignment of the muon system with respect to the tracker is removed this trend is corrected.

4.4.1 Startup and $1\,pb^{-1}$ alignment scenario

All the available information from the photogrammetry, and the experience with the local commissioning runs, was used to develop this scenario. The contribution expected from the hardware alignment and the track-based algorithms at this point was small, so the scenario was based on the photogrammetry precision. In particular the magnitude of the misalignments of wheels and stations was set to 1.5 mm which is the given survey precision for these large structures. Conservatively this value was slightly higher, 2 mm for the Z coordinate. Misalignments of individual chambers were set to 1 mm, which is the precision achieved by the photogrammetry (see chapter 5). In $r\phi$ it was slightly better under the assumption that some improvement in this coordinate could be achieved by applying the track-based alignment algorithms, to the commissioning runs, previous to the start up. Finally a misalignment of the sectors was added for training of the track based alignment algorithms.

Table 4.6 shows the detailed description of the algorithm.

Alignable	X/cm	Y/cm	Z/cm	$\Phi_X/mrad$	$\Phi_Y/mrad$	$\Phi_Z/mrad$
Endcap Stations	0.15	0.15	0.2	0.3	0.3	0.2
Endcap Rings	0.04	0.04	0.02	0.4	0.4	0.1
Endcap Chamber (local)	0.07	0.1	0.15	1	1	0.7
Endcap Sectors	0.05	0.05	0.05	0.05	0.05	0.05
Barrel Wheels	0.15	0.15	0.2	0.3	0.3	0.2
Barrel Chamber (local)	0.07	0.1	0.1	0.7	1	1
Barrel Sectors	0.05	0.05	0.1	0.05	0.05	0.1

Table 4.6: Resolution for the position and orientation of the different structures and chambers in the Startup alignment scenario.

4.4.2 The $10\,pb^{-1}$ alignment scenario

In order to avoid the inconsistencies found in the previous set of scenarios, this scenario respected the same configuration as the startup, but decreasing the magnitude of the misalignments. In this way, it is guaranteed that the $10\,pb^{-1}$ scenario has a better performance in all the momentum ranges.

The values used in this scenario assume that both the track based alignment and hardware alignment algorithms have produced the first results. The misalignments of the large structures are almost reduced by a factor 2 except for the Z coordinate which is measured with lower precision. The magnitude of the sector misalignments remains the same to serve for testing the algorithms.

Alignable	X/cm	Y/cm	Z/cm	$\Phi_X/mrad$	$\Phi_Y/mrad$	$\Phi_Z/mrad$
Endcap Stations	0.07	0.07	0.2	0.3	0.3	0.1
Endcap Rings	0.04	0.04	0.04	0.1	0.1	0.1
Endcap Chamber (local)	0.05	0.07	0.15	0.7	0.7	0.5
Endcap Sectors	0.05	0.05	0.05	0.05	0.05	0.05
Barrel Wheels	0.07	0.07	0.1	0.15	0.15	0.1
Barrel Chamber (local)	0.05	0.1	0.1	0.7	0.3	0.3
Barrel Sectors	0.05	0.05	0.1	0.05	0.05	0.1

Table 4.7: Resolution for the position and orientation of the different structures and chambers in the 10 pb^{-1} alignment scenario for the CSA08.

4.4.3 Validation of the CSA08 alignment scenarios

Performance studies for the CSA08 alignment scenarios were very limited because no testing samples were produced on time before the large scale production.

Nevertheless these scenarios were used for the official reconstruction of the CSA08 campaign. The most important analysis associated to these scenarios, were those related to the muon alignment workflows, that will be described in chapter 7 of this thesis. A detailed description of other analysis carried out during the CSA08, and with a strong dependency on the muon geometry can be seen at [76].

Chapter 5

Internal Alignment of the Drift Tube Chambers

The drift tube chambers of CMS are complex detectors composed by several layers of wires. The hits recorded in every layer are combined to reconstruct the trajectory of the muon. This reconstruction is performed individually by every chamber, or globally using information from several chambers (see chapter 2). In order to ensure the quality of the reconstructed objects, a good alignment of the layers is required. This process will be referred to as the internal alignment of the drift tube chambers.

A procedure based on the MBAA algorithm and constrained with construction meaurements was developed to align internally the chambers. The δ_z alignment parameter between the superlayers, was not measured precisely using this method. For this reason, in a second stage, a refinement of the measurement of this parameters was performed.

This chapter provides a detailed description of the alignment algorithm, its corresponding results, and the validation studies performed to ensure the correctness and quality of the alignment.

5.1 Application of the MBAA algorithm to the internal geometry of the chambers

The alignment of the internal structures of the drift tube chambers is a complicated task due to the complexity of the chamber construction and assembly procedures. Different sets of measurements were performed along these processes, providing heterogeneous and partial information. In many cases the measurements were performed over local structures (i.e. layers) that were afterwards assembled into larger structures, requiring additional information to be correctly referred to the whole object or to other assembled components.

These collection of measurements can be organized chronologically as follows:

- **Measurements at the construction sites**. During the construction and assembly of the chambers different measurements were performed in order to ensure the quality and to check that the design tolerances were accomplished. This information is usually referred to as Quality Control Information (QC), and it covers different aspects of the chambers, ranging from measurements of the tension of the wires to the use of photogrammetry techniques to calculate the position of wires and layers.

- **Calibration of the chambers: Survey information**. After the chamber construction a process of calibration were performed. Using photogrammetry the position of reference points in the chambers was measured and analyzed.
- **Muon tracks**. A large amount of cosmic muon tracks was recorded during the different commissioning phases of the drift tube chambers (see appendix B), allowing the application of track-based alignment methods, such as the MBAA algorithm.

None of these measurements was able to fully describe the internal geometry of the chambers. In order to provide the most complete description, it was decided to apply the MBAA method using the other two sets of measurements as constraints. This procedure was divided in four different steps: the compilation and analysis of all the available measurements, the crosschecks on their compatibility, the combination of the measurements and the geometry determination, and finally the validation of the results.

5.1.1 Compilation and analysis of all the available measurements

The sets of measurements referred to in the previous section were performed at different locations, and several teams were involved in the process. The information was usually stored at web pages belonging to the institutions in charge of a particular subset of the measurements. In addition, the formats and conventions used by the different sites were not unified, varying from one site to another.

The first part of the work presented in this chapter was related to the compilation and unification of all these measurements. Several scripts were developed in order to automate the process of extracting the information remotely from the local databases.

Once the measurements were obtained and centralized, different calculations were performed to convert the raw data into real alignment corrections. The complexity of these analysis ranges from simple average calculations, to the use of complex algorithms and mathematical techniques, for instance in the case of track-based alignment. These analysis are described in the following sections.

Quality Control Measurements

Quality Control Measurements were performed at the 4 chamber production sites: RWTH (Aachen, Germany), Legnaro National Laboratory (Legnaro, Italy), CIEMAT (Madrid, Spain) and the University of Torino (Torino, Italy) by the teams in charge of the chamber construction and assembly.

In order to ensure the correct working of a drift tube chamber a large set of parameters must be checked. QC measurements are not only related to the alignment of the wires or layers, but also to many other magnitudes as the study of the gas system, tension in the wires, electronics, etc. A complete overview of the Quality Control process of the chambers can be found in [84, 85].

From the point of view of the alignment, only the information related to the position of the layers in the local x direction was used. The assembly of the different superlayers was always performed in dedicated construction tables, where the 4 layers were mounted one on top of the other. After finishing the installation of all the wires of a given layer, and before starting the next one, the position of the wires was recorded using a camera, and then compared to the nominal values. An average of all the wire measurements was performed to get a single local x displacement per layer and with respect to a fixed reference on the construction table, different from superlayer to superlayer, but identical for all the layers in a same superlayer. This process was repeated in both sides of the chamber (known as front-end and high voltage side) and the numbers published in the web pages of the construction sites [86], [87], [88], [89].

In the case of the Madrid site, the measurements were copied to a centralized database at CERN [90] where the measurements appeared in relational tables. The other sites had a complex directory structure (depending on the site) where all the QC information was stored as text files with different formats. Figure 5.1 shows an example of a text file for a given superlayer at the site of Aachen.

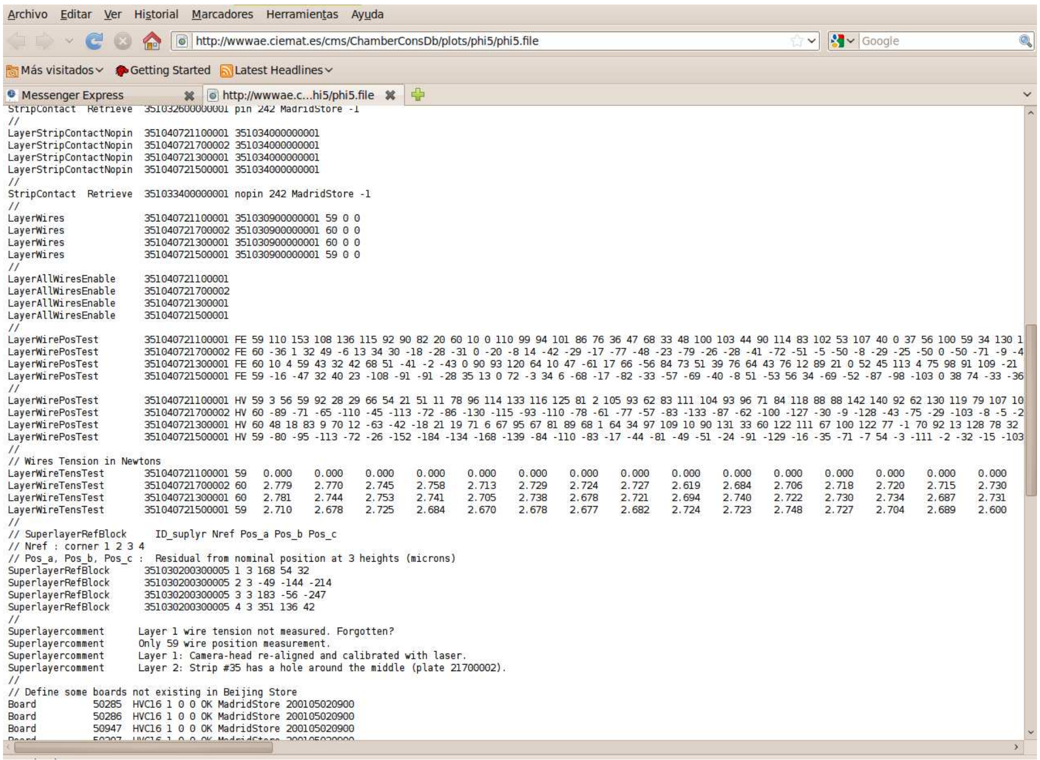

Figure 5.1: Capture of the file describing the layer position of a SL at Aachen.

Once the numbers were collected a single value was calculated for each layer, averaging the FE and HV sides. Figure 5.2(a) shows the result of this average for all the layers. As can be observed the measurements are spread with an RMS of 100 μm. The error associated to these measurements was taken as the highest between the statistical error (propagated from the single errors in each side) and half the difference between both sides measurements. Figure 5.2(b) shows the errors for each layer. The error for most of the chambers is contained within the range 20 to 50 μm. The peak is due to the fact that the error was fixed for one of the sites.

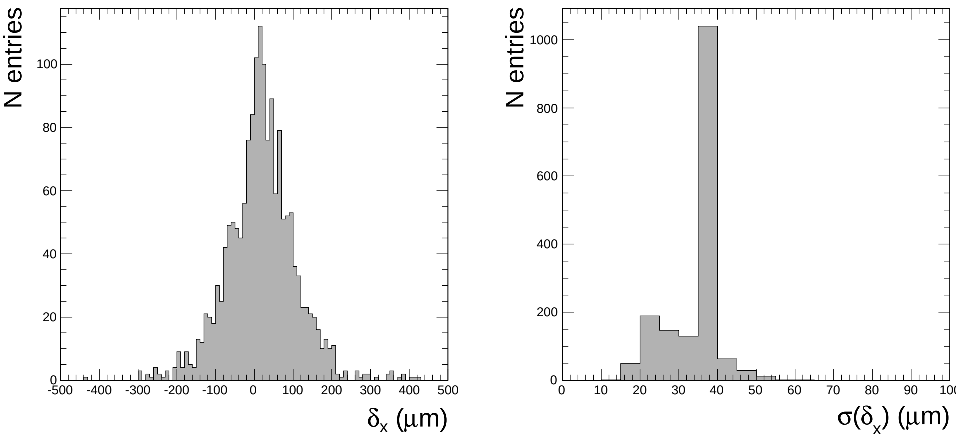

(a) (b)

Figure 5.2: QC δ_x displacements for all the layers (a) and errors associated to the δ_x displacement (b).

Calibration of the Chambers: survey measurements

After the construction, the chambers were calibrated and measured using photogrammetry techniques. Bright targets were placed in the corner blocks, in the proximity of the corners of each superlayer. A best fit calculation was performed in order to obtain the position and orientation of superlayers 2 and 3 with respect to superlayer 1. The measurements provided 3 position and 3 orientation coordinates expressing the absolute location of the superlayers in the superlayer 1 frame. These measurements were available through a web interface [91], in tables as shown in figure 5.3. A script was developed to automatically collect this information from the web and to extract the nominal values of the distances and orientations, resulting finally in a set of three displacements and three rotations, that were easily translated into the CMSSW framework.

The corrections are distributed with a spread of about 200 μm for the δ_x and δ_y displacements, and 150 μrad for the rotations, as can be seen in figures 5.4. A different situation was found for the δ_z distance between both superlayers. The magnitude of these displacements was much larger (1-1.5 mm) due to the extra distance introduced by the glue used to assemble the chambers. Before understanding the problem there was a lack of confidence in these numbers, which lead to neglect them and motivated a further study and the development of an alternative and more precise algorithm for measuring this coordinate, as described later in this chapter.

5.1.2 The MBAA alignment algorithm applied to the internal geometry of the DT chambers

In addition to the QC and survey measurements, the internal structure of the chambers was measured using alignment with tracks methods. In particular, an implementation of the MBAA algorithm was used to calculate the corrections as explained in chapter 3.

Some of the particular needs and features of the application of the algorithm are:

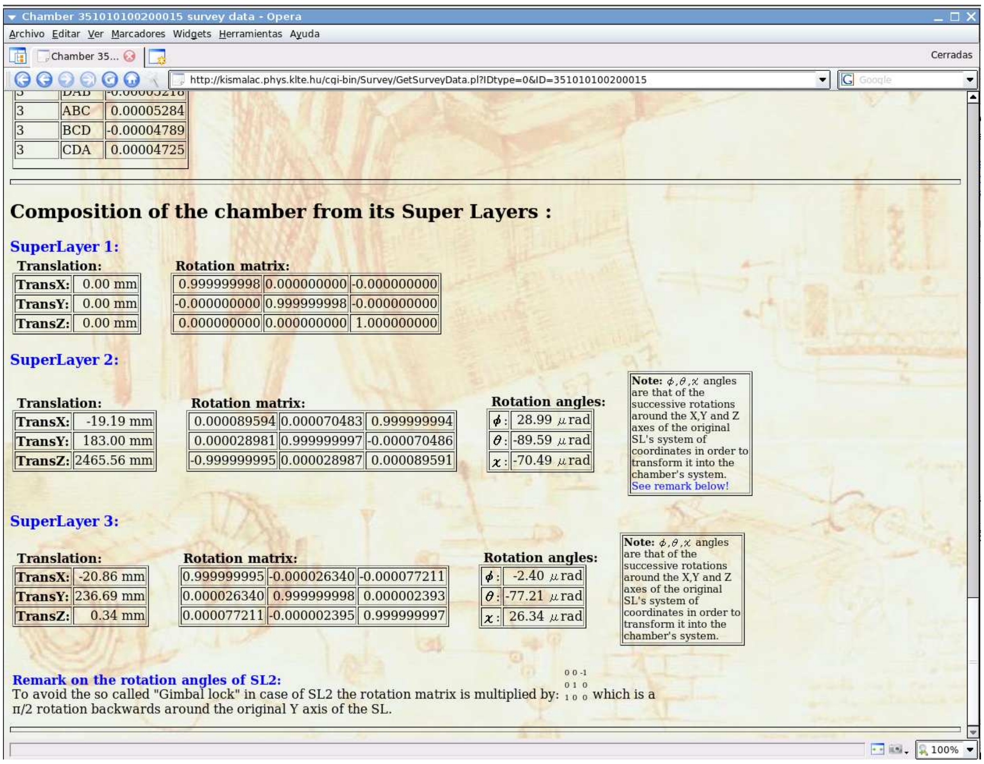

Figure 5.3: Capture of the web page containing survey measurements for a given chamber. The translations and rotations of the superlayers with respect to the previous one are presented in tables.

- The minimum alignable unit was the layer. The algorithm could be technically applied to the wire level, however no large misalignment were expected in the wires provided that the tolerances in its positioning were very tight. In addition, the dimension of the linear systems associated to the MBAA algorithm, was reduced by considering layers of wires.

- Layers only provide the position of the hit in the coordinate orthogonal to the wire direction, $r\phi$ in this case. This fact implied that only the Δ_x residuals could be used to calculate the alignment parameters.

- The track model was based in the DT local reconstruction process. Because of the small tracking volume, the trajectory of cosmic muons can be modelled as a straight line in the $r\phi$ plane, depending on two parameters: the intercept and the slope.

The MBAA alignment matrix **A** associated to this problem was defined by the two first items in the list above. As the layer only provides translational information along the local x direction, only the first row in equation 3.33 was used. In this application of the method, only the rϕ layers were measured, and hence there were 5 alignment parameters per layer: δ_x, δ_z, ϕ_x, ϕ_y and ϕ_z.

$$\mathbf{A} = \begin{pmatrix} -1 & \frac{dx}{dz} & -y\frac{dx}{dz} & x\frac{dx}{dz} & -y \end{pmatrix} \tag{5.1}$$

The rϕ layers are not able to measure the local y coordinate, for this reason the component associated to the θ of the segment is extrapolated to the position of the given layer in

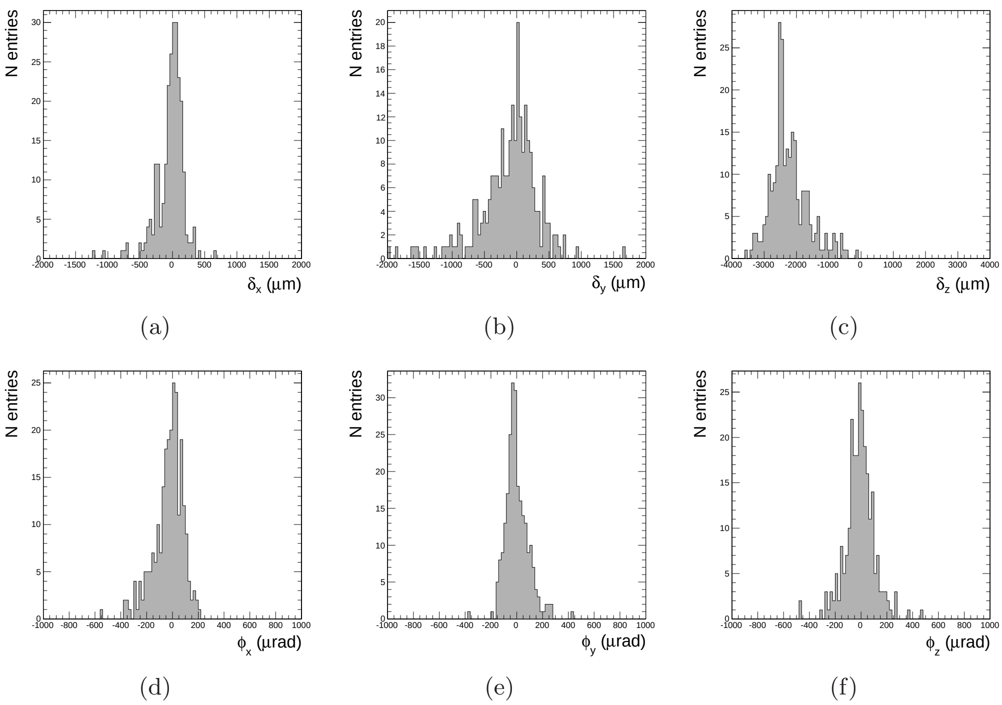

Figure 5.4: Values of the relative misalignments of SL 3 with respect SL 1 provided by the survey measurements.

order to get an estimation. In the case of the MB4 chambers, the matrix was restricted only to δ_x and ϕ_y which did not require to have an estimation of the y coordinate.

The matrix associated to the track parameters in the MBAA method, **B**, was defined by the track model, and has the form associated to a linear fit:

$$\mathbf{B} = \begin{pmatrix} -1 & z \end{pmatrix} \tag{5.2}$$

These matrices were used to generate a χ^2 function as in 3.27. This χ^2 had invariances or weak modes, easily identified by looking at the track model. In particular, for each of the alignment parameters two weak modes were found:

- Movement of all the layers by the same amount, as shown in figure 5.5(a). This configuration is absorbed by the intercept of the track.
- Movement proportional to the z coordinate of the layer, as shown in figure 5.5(b). In this case these misalignments are absorbed as a fake slope of the track.

In order to solve the linear system of equations, weak modes were fixed to zero, and a pseudo-inverse matrix was calculated as it was explained in chapter 3. This provided a partial alignment of the layers that did not include the weak modes. It is remarkable that the floating weak mode is actually irrelevant for the internal alignment of the chambers, provided their global position will be afterwards determined by other means.

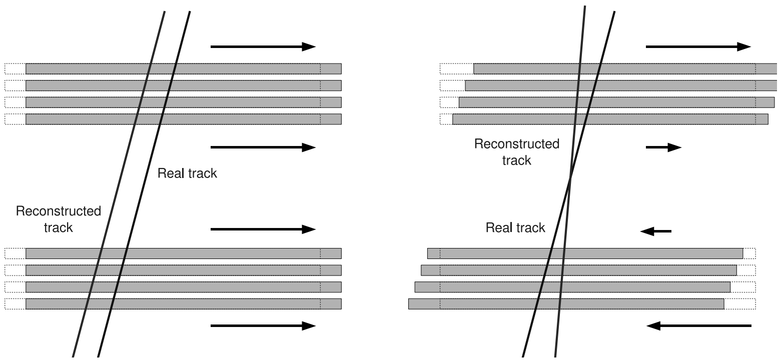

Figure 5.5: Weak modes affecting the track-based alignment of the internal geometry of the chamber

5.1.3 Consistency crosschecks

The different sets of measurements explained in the previous sections were not able to provide a full description of the internal geometry of the chambers, because of the following reasons:

- QC measurements only provided the relative alignment of layers within a superlayer. This alignment was relative because the external reference used to perform these measurements was lost once the superlayer was removed from the construction table.
- Survey measurements only contained information about the relative alignment of superlayers. No information about the layers could be extracted from these measurements.
- Track based alignment did not include any information about the weak modes.

QC and survey measurements were completely independent sets of measurements, because the former refers only to the internal alignment of a superlayer, and the latter to the relative alignment between superlayers. On the other hand, track-based alignment contains information that overlaps with the QC and survey measurements.

This redundancy is very useful to perform a crosscheck of the measurements. The common part can be extracted and compared. In order to do this, the respective solutions were projected in the space of the alignment parameters, to the common part. The results are shown and commented below, while a detailed explanation of the procedure can be found in appendix C.

Figure 5.6 shows a profile in which the common part of δ_x in the QC and survey measurements is drawn versus the track-based component (the straight line $y = x$ is shown for reference). In the profile there is an entry for every chamber. A remarkable agreement (about 100 μm) is observed.

This good agreement ensures the consistency of the measurements and gives confidence in the combination of results that will be explained in the following section.

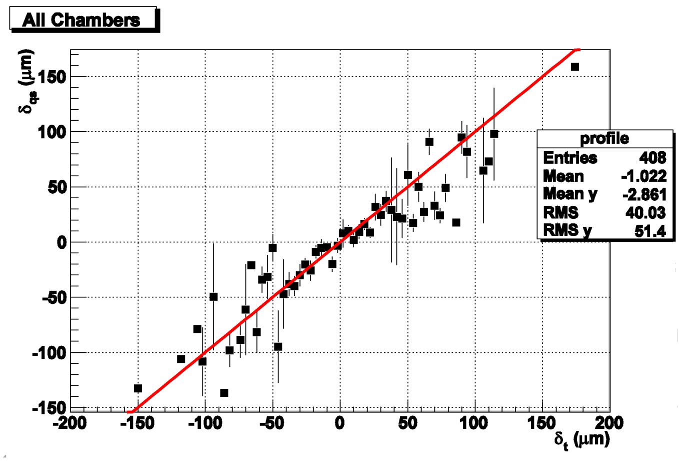

Figure 5.6: Redundant component of the QC and survey measurements and the track-based alignment results in the local x direction. The red line shows the straight line y=x.

5.1.4 Combination of measurements

In the same way that the redundant part of the measurements could be compared to perform crosschecks, the non redundant part could be combined to provide a complete solution. It is important to remark that even the combination of the three sets of measurements does not provide a full description of the chamber. The remaining degrees of freedom are related to the global positioning of the chamber. The first of the weak modes reported in the previous section, is not either present in the QC and survey descriptions. This weak mode is sometimes known as the floating degree of freedom. Equal and coordinated movements of all the chambers are in fact movements of the chamber itself and therefore cannot be accounted for using information related to the internal geometry. In any case, this kind of alignment is explained in the following chapters.

In order to perform a combination, the QC and survey measurements were used as a constraint in the track-based alignment algorithm, adding new terms to the original χ^2. In addition a function with a lambda multiplier was added to fix to zero, the floating degrees of freedom. These misalignments are absorbed afterwards when the chambers are aligned relatively to each other, or to the central sillicon tracker.

$$\chi^2 = \chi^2_{tracks} + \chi^2_{survey} + \chi^2_{QC} + f(\lambda) \tag{5.3}$$

In the following qcx_i will be used to denote the QC measurement for a given layer, while su_j will be used to denote the survey measurements for the degree of freedom j.

The term associated to the QC measurements only constrained the relative displacements of the layers with respect to the average displacement of all the layers, $\sum_j \delta_{xj}/4.0$ and $sum_j qcx_j/4.0$ respectively. This procedure was preferred instead of using one of the layers as the reference, because in this way no global movement of the superlayer is produced:

$$\chi^2_{QC} = \sum_i \frac{(\delta_{xi} - qcx_i - \sum_j(\delta_{xj} - qcx_j)/4.0)^2}{\sigma_i^2} \tag{5.4}$$

In this case, i denotes the layer being constrained and j is a blind index running over the layers belonging to the superlayer that contains the layer i and with the aim of calculating the average of all the layers.

On the other hand, survey measurements constrain only the relative alignment of the superlayers:

$$\chi^2_{survey} = \sum_j \frac{(su_j - (\sum_{i=SL3} \delta_i j - \sum_{i=SL1} \delta_{ij})/4.0)^2}{\sigma_j^2} \tag{5.5}$$

Finally the term $f(\lambda)$ represents the closure conditions that are needed to fix the global positioning and orientation of the chambers. Lagrangian multipliers are used in the fit, to keep the average displacements and rotations of all the layers to 0, in such a way that common misalignments are always absorbed by the global alignment methods that will be described in the following chapters. The form of this term is

$$f(\lambda) = \sum_i \lambda_i \sum_j \delta_{ji} \tag{5.6}$$

where i runs over degrees of freedom, and j over the layers.

5.1.5 Implementation of the algorithm

The analysis presented above was implemented in C++ as several ROOT [61] classes. From the point of view of the functionality, this software can be divided in three components: the interface to the QC and survey measurements, the commissioning raw data analyzer and the MBAA implementation. Figure 5.7 shows the general workflow of this algorithm, including the interconnections among the different components.

Interface to the QC and survey information

Once the QC and Survey measurements were extracted from their respective sources, they were centralized in a common ROOT file. The QC measurements for each chamber were stored as *TMatrixD* objects in which each row accounted for the information of each layer. The name of the *TMatrixD* was the hardware ID assigned to the chamber. Finally all the matrices were saved in a *TDirectory* object named QC. The same procedure was used to save the photogrammetry information. In this case the matrices contained one degree of freedom per row, and one superlayer per column. These matrices were saved in a *TDirectory* named *Survey*.

A class was defined in order to easily interact with the information in this root file and incorporate it into the rest of the programs. In particular the class included the following functionalities:

- Methods to translate into the different identifiers of the chambers (hardware ID, calibration ID, wheel-station-sector notation).

- Methods to get the measurements (both QC and survey) from a given identifier.

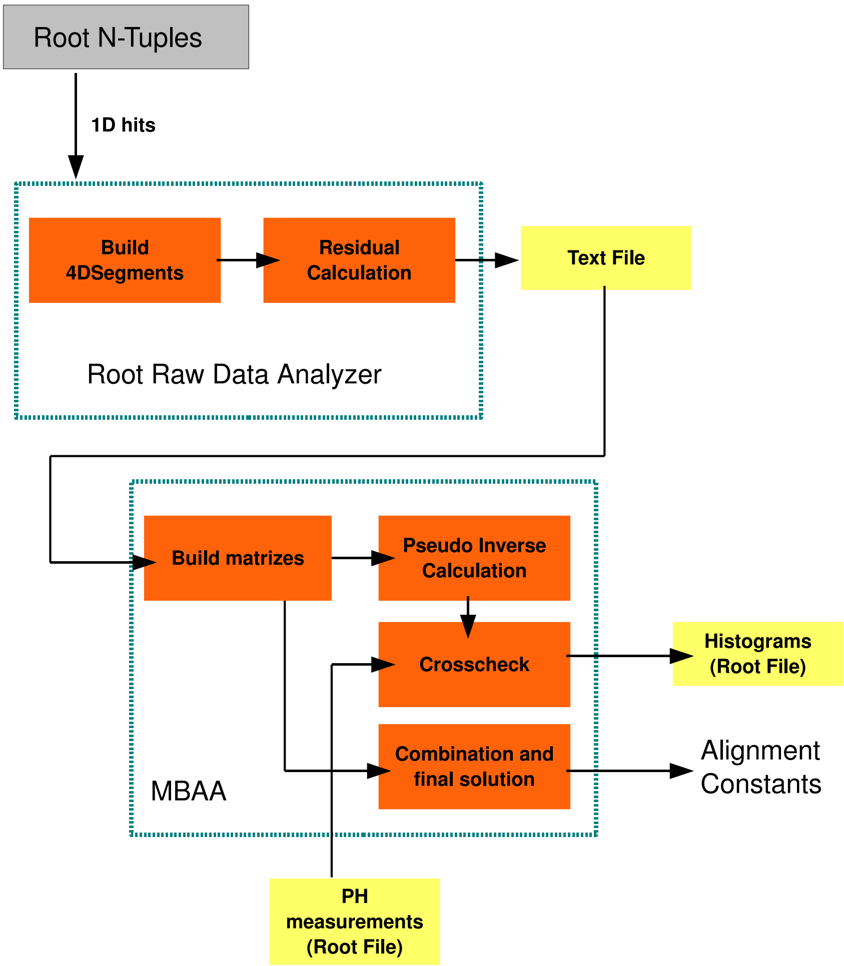

Figure 5.7: General workflow associated to the MBAA algorithm applied to the internal geometry of the chambers.

Commissioning raw data analyzer

The algorithm was applied over a sample of commissioning muon cosmics taken during the year 2005 and 2006 without magnetic field. These samples were encoded as ROOT n-tuple objects and a dedicated software was developed to extract the hits associated to the layers and produce the first processing. The tasks of this software are: to group the hits attending to the layers they belong to, calculate the 4D segments and the residuals, perform some quality selection and finally write the output.

There were two selection criteria applied over the sample, and in order to guarantee a good quality of the segments entering into the fit:

- The number of layers hit should be at least 7, because tracks with a low hit occupancy are suspicious of not being well reconstructed.
- The absolute value of the residuals must be smaller than 3 cm for every layer, in such

a way that very large residuals (usually not physical) are removed from the sample.

Finally the output is written in a text file, with blocks of 8 rows, 1 per layer, and containing in the columns: residuals, position components for the hits and the intersections with the 4D segment.

MBAA implementation

The last part of the code is the real core of the algorithm. Text files containing the information from the commissioning raw data analyzer are read and the different matrices related to the method are filled. In addition all the QC and survey information is read using the interface class explained before. At this point the algorithm calculates the pseudo-inverse of the MBAA associated matrix, performs the comparison with the QC and survey information, and finally calculates the combined solution. The output is written to text files which are converted into standard CMS databases afterwards.

This algorithm was ported in a second stage to CMSSW, in the package *MuonAlignmentAlgorithms*, although a description is not given in this thesis.

5.1.6 Results of the MBAA algorithm over the internal geometry

The algorithm was applied over a sample of commissioning muon cosmics, with approximately 60000 tracks per chamber. The resulting alignment parameters with respect to the nominal geometry are shown in figures 5.8, with the exception of the δ_z parameter. As it was already commented in the previous sections, the δ_z survey measurements were not used when the algorithm was applied, resulting on some very large errors for the estimation of this parameter ($1-2\,mm$). For this reason this parameter was not updated at this point (see following section for more information). Typical statistical errors for the other alignment parameters were 20-30 μm and 50 μrad.

It is important to remark that the closure conditions force the alignment parameters to be zero in average. Superlayer misalignments dominate against individual layer misalignments, and therefore in the distributions below layers belonging to a superlayer are mostly distributed symmetrically with respect to the layers of the other superlayer of the same chamber.

In view of figure 5.8 it is possible to conclude that in most of the cases the layers were built within their corresponding tolerances (most of the corrections are bellow the 100 μm and 50 μrad level). Nevertheless there are outliers in the distribution, which come mainly from effects between superlayers and whose misalignments are large (up to 1 mm in the δ_x parameter for example). In the final section of this chapter studies on the performance of the local reconstruction are presented as a proof of the improvement achieved with the calculated geometry.

5.2 Measurement of the thickness of the chambers

The glue used to keep the superlayers together changes the nominal width of the chamber. This effect is in fact a displacement of the superlayers in the local alignment parameter δ_z, and it is, in general, larger than the construction tolerances. The MBAA algorithm described

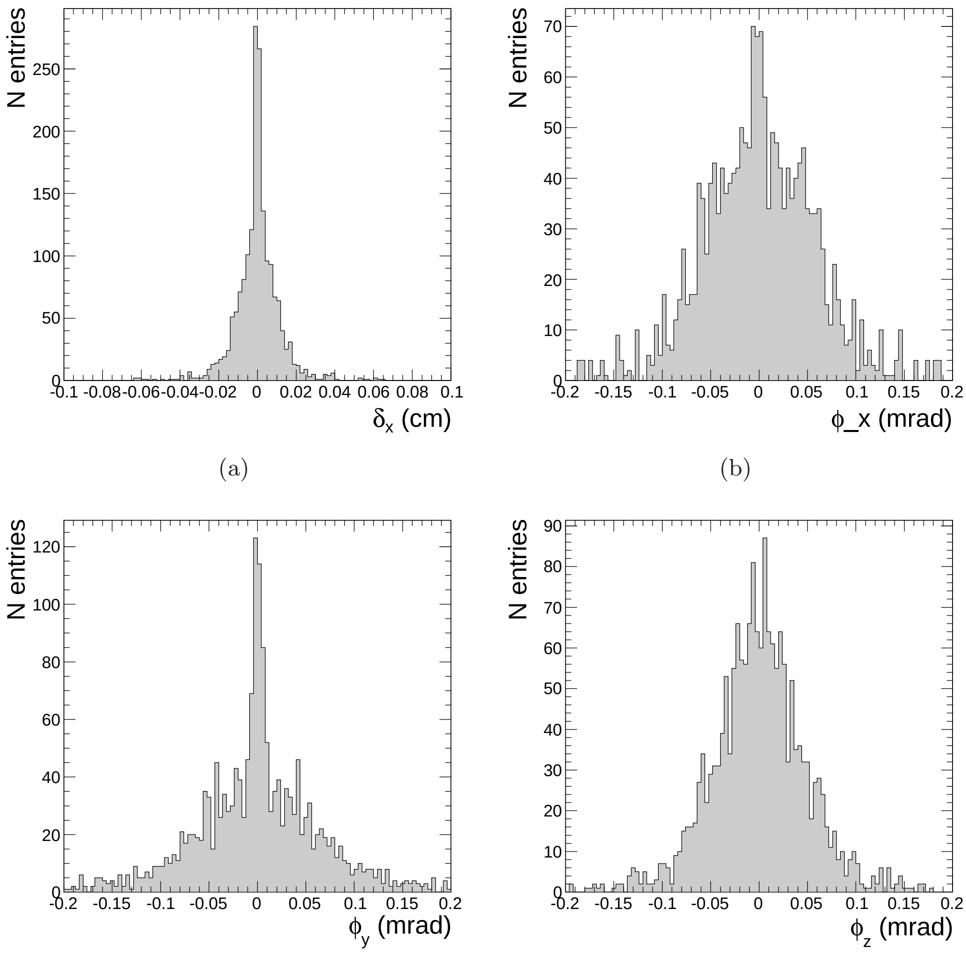

(a) (b) (c) (d)

Figure 5.8: Alignment parameters per layer and with respect to the nominal geometry. Figure (a) shows the δ_x displacement, while (b), (c) and (d) shows the three rotations ϕ_x, ϕ_y and ϕ_z respectively.

previously in this chapter did not update this information because the error in this parameter was too large.

5.2.1 The Superlayer to Superlayer Algorithm

A dedicated algorithm was designed in order to estimate the correct distance between superlayers. The algorithm is a particular case of the more general MBAA algorithm: instead of fitting the residual distribution as a function of the alignment and track parameters, only the latter are used. The estimation of the track parameters was calculated using one of the two $r\phi$ superlayers, and was assumed to be perfect, in such a way that the track-parameter part of the χ^2 3.27 could be dropped ($\vec{\Delta p} = 0$), yielding the following χ^2 which corresponds with the more intuitive idea of alignment:

$$\chi^2 = \sum_j (\overrightarrow{\Delta} - \mathbf{A}\overrightarrow{\delta})^T \mathbf{E} (\overrightarrow{\Delta} - \mathbf{A}\overrightarrow{\delta}) \tag{5.7}$$

Once the track was reconstructed in each of the superlayers it was extrapolated to the other superlayer as illustrated in figure 5.9. The residuals, defined as the difference between the track segment in the superlayer and the extrapolated segment were minimized against the δ_z parameter and the two correlated alignment parameters δ_x and ϕ_y. This correlation comes from the fact that a δ_z displacement is measured through the effect it produces in the Δ_x residual, highly correlated with the effect of δ_x. This correlation is present also with the ϕ_y parameter, provided both affect the Δ_x residual weighted by the slope of the segment. The **A** matrix, using the usual parameterization, had the form

$$\mathbf{A} = \begin{pmatrix} -1 & \frac{dx}{dz} & x\frac{dx}{dz} & -y \end{pmatrix} \tag{5.8}$$

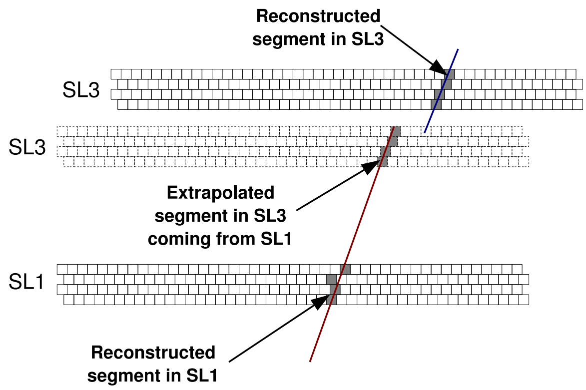

Figure 5.9: Sketch of the Superlayer-To-Superlayer method. A segment is reconstructed in one of the superlayers (SL1) and extrapolated to SL3. This extrapolation is compared with the segment reconstructed in SL3.

This method is not affected by weak modes, because the track parameters are fixed and no possible overlap between them and the alignment parameters is possible. On the other hand, individual misalignments of the layers are a source of systematic error, because of the distortion provoked in the estimation of the track parameters, which is propagated to the next superlayer. In order to control this systematic the procedure is repeated using the two $r\phi$ superlayers as reference. The error in the estimation of the alignment parameters was chosen to be the highest between the statistical error, and half the difference in the alignment parameters provided by the two estimations.

5.2.2 The Superlayer-To-Superlayer algorithm implementation

The algorithm was implemented as a CMSSW plugin included in the *MuonAlignmentAlgorithms* package, and it was prepared to read the collections of hits available in the AlCaReco stream *MuAlCalIsolatedMu* (see appendix A) and produced during CRAFT08 (Cosmic Run At Four Tesla 2008). The algorithm grouped 1D hits for every superlayer within a chamber and performed a local reconstruction restricted to each of the superlayers. Each of the segments was extrapolated to the other superlayer, and residuals were calculated. Several selection criteria were applied to the segments, and finally they were included in the fit, giving place to the χ^2 minimization. A schematic view of the working of this algorithm can be found at 5.10.

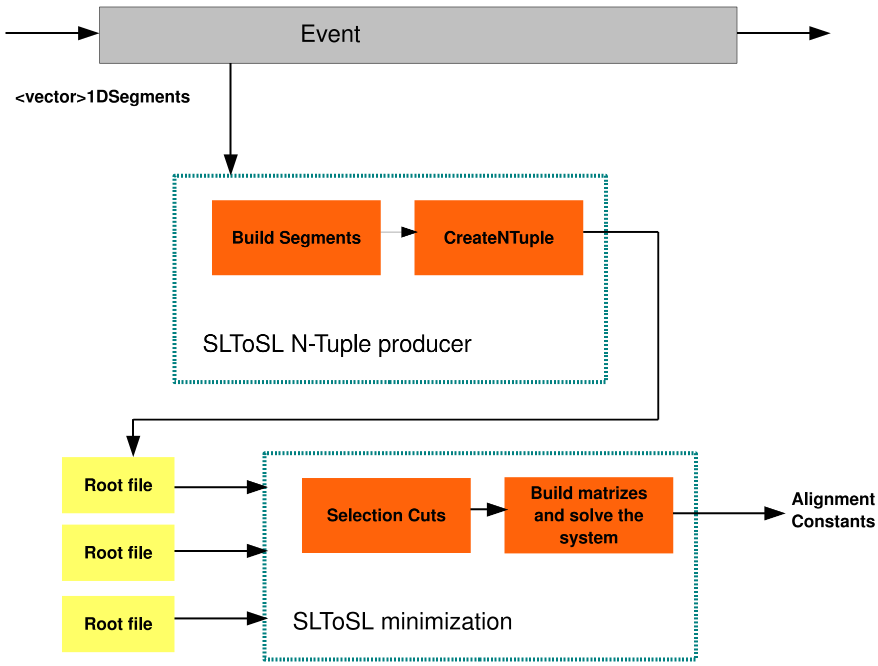

Figure 5.10: General workflow of the the Superlayer-To-Superlayer alignment algorithm.

The selection criteria applied over the segments and residuals were the following:

- The P_T of the associated standalone muon is required to be $P_T > 10$ GeV. Even if multiple scattering does not affect strongly this procedure because the material budget inside the chambers is not too large, by requiring the P_T of the muon to be greater than 10 GeV, many tracks which usually do not cross the whole muon system are eliminated.
- The number of $r\phi$ hits in the segment is required to be 8 (1 per layer). This selection cut was tighter than in the previous MBAA implementation because statistics in this case were higher.
- The residuals are always required to be smaller than 3 cm. This is to avoid unphysical tails to enter in the calculation.

5.2.3 Results of the Superlayer-To-Superlayer algorithm over the internal geometry

The final calculation of the constants followed a sequence in which the survey measurements δ_z were first introduced, and then the algorithm run on top of them. Nevertheless, in order to check the level of agreement between survey and tracks, a track-only estimation was also performed starting from the uncorrected geometry. Figures 5.11(a) and 5.11(b) show the magnitude of the measured δ_z by survey and the algorithm. The distribution of the differences in δ_z between survey and track based alignment is a gaussian with a sigma of 580

μm. The typical δ_z misalignments are of the order of 1 mm for stations 2, 3 and 4, and of the order of 1.5 mm for station 1, where the gluing procedure used in the assembly was different.

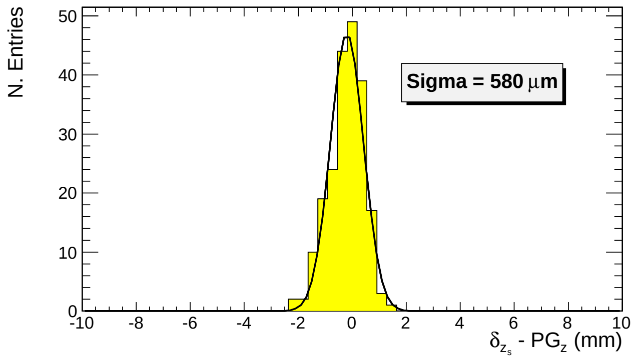

(a)

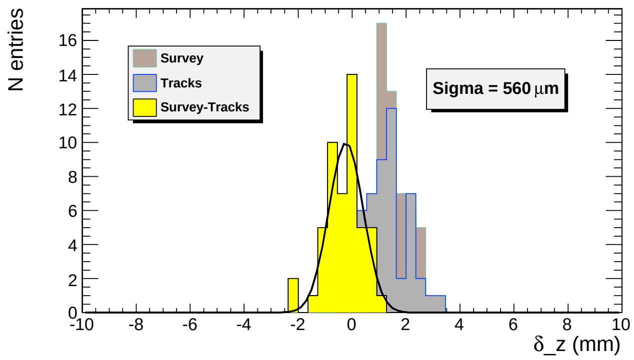

(b)

Figure 5.11: (a) Difference between the estimation of δ_z given by survey and by the track algorithm. (b) The measurements given by survey and the algorithm are plotted together with their differences for station 1, which had the largest δ_z misalignment due to the procedure used in the assembly

5.3 Validation of the geometries

The alignment constants calculated in the previous sections were introduced in databases compatible with the CMSSW format using the techniques and software described in chapter 3. During the first commissioning of CMS, from MTCC to the first CRAFT reprocessing only the constants coming from the MBAA method were taken into account. For the second CRAFT reprocessing, the geometry was updated to include the information related to the measurement of the thickness of the chambers.

Once the corrections were introduced, their quality and correctness were checked along the different commissioning phases of the detector. The following tests were performed:

- Study of the residual distributions of the local reconstruction layer by layer.
- Study of the residual distributions superlayer to superlayer.

These geometries were included in the official databases of CMS, and therefore all the validation studies and analysis involving the standalone or global reconstruction measured as well the quality of this alignment. In the following chapters, these validations were extensively performed using not only the updated internal geometry of the chambers, but also the updated positions and orientations of the chambers themselves. Validation and crosschecks will be provided then.

5.3.1 Residual distributions of the local reconstruction

The residual distributions of the layers (the difference between the hit measurement in one layer and its intersection with the reconstructed 4D segment) can be studied as a confirmation of the quality of the internal alignment of the chambers. It is convenient to remark that with a very good level of approximation, tracks, or segments, within a DT chamber are straight lines. Residuals are a measurement of the deviation with respect to the segment. It is remarkable also that often the residuals are smaller than the alignment parameters, because a part is absorbed by the weak modes.

The mean values of all the residual distributions were calculated and plotted together in figure 5.12. It is clear that after applying the updated geometry, deviations of the hits with respect to the segment are minimized within a range of a few microns.

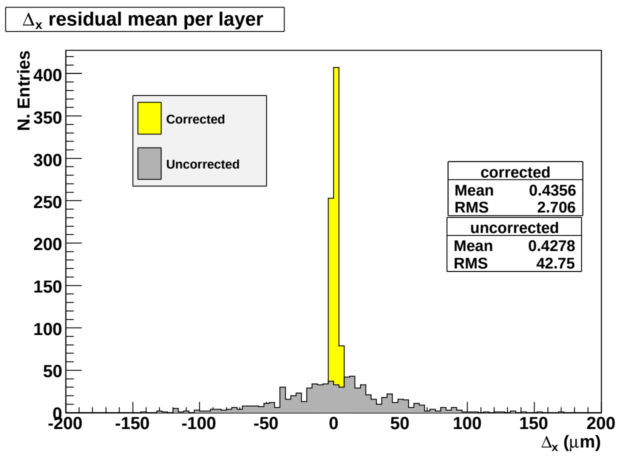

Figure 5.12: Mean of the residual distributions for all the layers after the corrections are applied.

This crosscheck was repeated for the different commissioning phases of CMS and a good stability of the measurements was observed, being the corrections still valid within the corresponding errors.

5.3.2 Residual distributions superlayer to superlayer

In order to check the relative alignment of superlayers, the superlayer to superlayer residual distributions were considered. The track was reconstructed individually in each superlayer and then extrapolated to the other superlayer. The residual distributions, defined as the difference between the track estimation in the superlayer and the extrapolation, were studied before and after applying the alignment corrections.

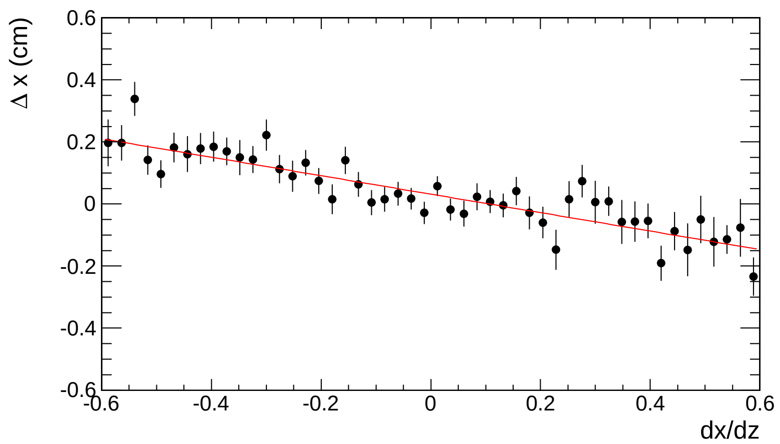

Figure 5.13: Dependence between the superlayer to superlayer residual and the direction of the track $\frac{dx}{dz}$

The δ_z misalignment introduces a correlation between the residuals (superlayer to superlayer) and the direction of the track $\frac{dx}{dz}$ (see an example in figure 5.13). In order to validate the geometry, the intercept and slope of these diagrams were drawn for the different wheels and for the nominal geometry (before alignment), and the finally corrected geometry. The results can be seen in figures 5.14 to 5.18. And a summary is contained in tables 5.1 and 5.2.

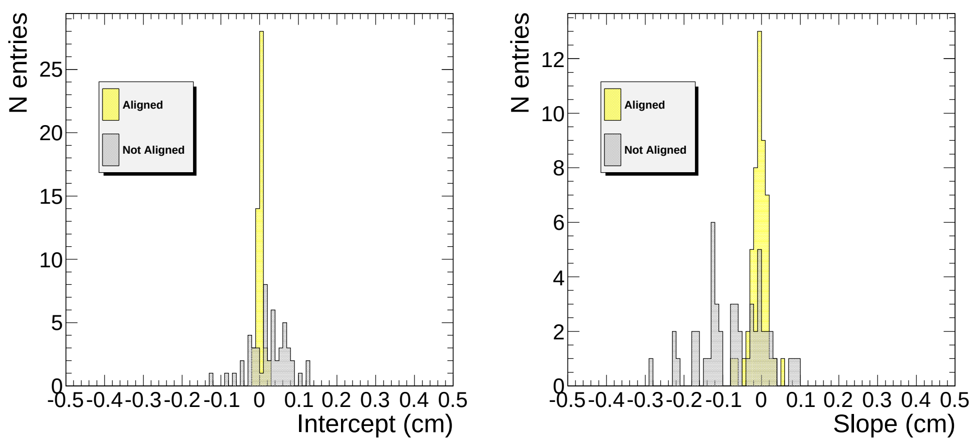

(a) (b)

Figure 5.14: Distribution of the intercepts (δ_x) and slopes (δ_z) before and after alignment for wheel -2.

All these results clearly show the significant improvement introduced by the corrected geometry. After the application of the constants the superlayer to superlayer residual distribution was centered at 0 with a RMS of the order of 100 μm. The distribution of the slopes is much centered at 0 as well, after the corrections are applied, with a typical RMS of 200 μm.

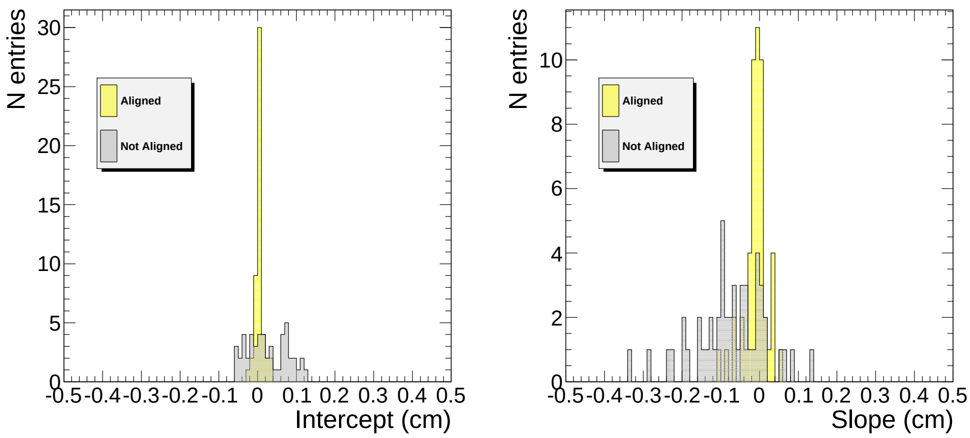

(a) (b)

Figure 5.15: Distribution of the intercepts (δ_x) and slopes (δ_z) before and after alignment for wheel -1.

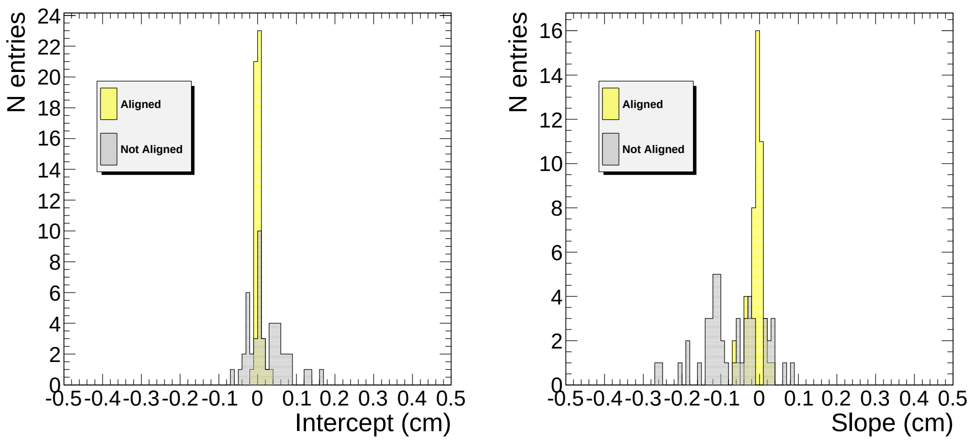

(a) (b)

Figure 5.16: Distribution of the intercepts (δ_x) and slopes (δ_z) before and after alignment for wheel 0.

Alignment	Wheel	Mean (mm)	RMS (mm)
corrected	-2	0.02	0.08
uncorrected	-2	0.5	0.2
corrected	-1	0.04	0.1
uncorrected	-1	0.3	0.5
corrected	0	0.02	0.08
uncorrected	0	0.2	0.5
corrected	1	-0.01	0.17
uncorrected	1	0.08	0.4
corrected	2	0.006	0.1
uncorrected	2	0.17	0.5

Table 5.1: Distribution of the intercept of the Δ_x vs. $\frac{dx}{dz}$ correlation with the uncorrected and corrected geometries.

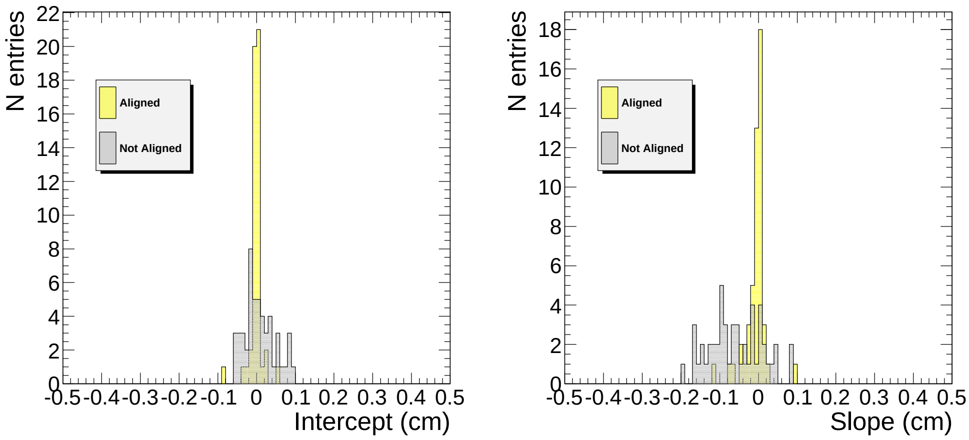

(a) (b)

Figure 5.17: Distribution of the intercepts (δ_x) and slopes (δ_z) before and after alignment for wheel 1.

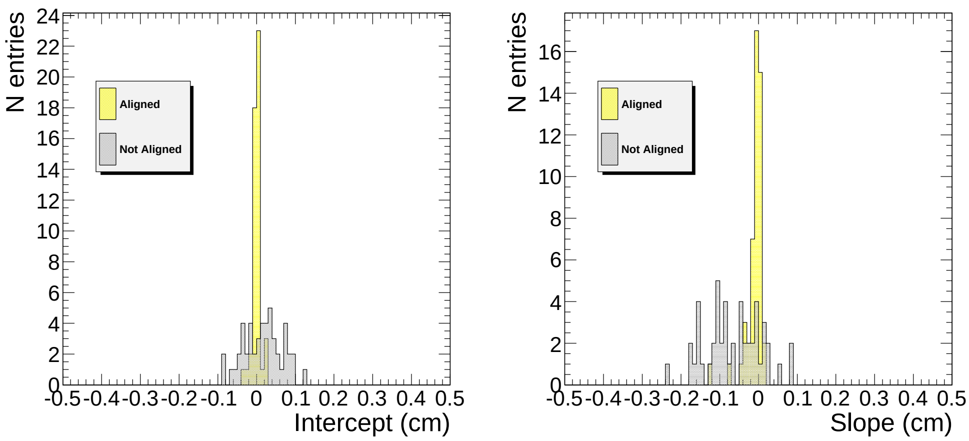

(a) (b)

Figure 5.18: Distribution of the intercepts (δ_x) and slopes (δ_z) before and after alignment for wheel 2.

Alignment	Wheel	Mean (mm)	RMS (mm)
corrected	-2	-0.06	0.2
uncorrected	-2	0.2	0.5
corrected	-1	-0.09	0.3
uncorrected	-1	0.3	0.5
corrected	0	-0.09	0.2
uncorrected	0	0.23	0.5
corrected	1	-0.007	0.3
uncorrected	1	0.08	0.4
corrected	2	-0.1	0.2
uncorrected	2	0.17	0.5

Table 5.2: Distribution of the slope of the Δ_x vs. $\frac{dx}{dz}$ correlation with the uncorrected and corrected geometries.

Chapter 6

Positioning of DT Chambers in the CMS frame: photogrammetry

After the installation of the DT chambers in their corresponding locations in the wheels, photogrammetry techniques were applied to both the iron and the chambers. At least three bright targets were located at the corner blocks of the DT chambers and its position was provided with an accuracy of 300 microns.

In this chapter the process of converting the raw position of the control points into real alignment corrections of the chambers will be described. The geometry of the barrel muon system was updated with these corrections and several crosschecks were performed in order to ensure the quality of this alignment. This geometry was used in the LHC start-up as a first order aligned geometry, enough from the point of view of the trigger, and was the starting point afterwards for the track-based algorithms.

6.1 Photogrammetry information

As defined in chapter 3, photogrammetry is a procedure which allows to calculate the position of some control points distributed over the space, by taking photographs of them from different angles and distances, and applying triangularization techniques.

In CMS the photogrammetry was applied to the different components of the detector, ranging from large structures as the yoke of the wheels and disks, to specific elements of the different subsystems.

There were four different kinds of photogrammetry information related to the barrel of the muon system:

- Photogrammetry of the iron yoke. Bright targets were disposed over the return yoke of CMS.
- Photogrammetry of the components of the optical alignment system. The MABs (Modules for Alignment of the Barrel) were instrumented with photogrammetry targets.
- Photogrammetry of the DT chambers. The control points were attached to the corner blocks of the chambers. This provided information to precisely define the location of the chambers in the CMS reference frame.

- Photogrammetry of the wheels. The position of each wheel is measured with respect to YB0.

Only the two last sets of information were used to provide an updated geometry of the barrel, for the position of the yoke itself is irrelevant (only the position of the chambers is important in the reconstruction process). The photogrammetry of the MABs was analyzed as well in order to provide a first geometry for the optical alignment system (see appendix E).

The team in charge of the photogrammetry performed the measurements and provided as output of its calculations, documents containing the position of the control points for the object under study, and their design positions. The positions of the points are shown in these documents as displacements from the design position of the control points. In particular, the general trend observed at this level for the barrel wheels, is a gravitational sag, due to the weight of the detector. This deformation was in good agreement with the expectations given by numerical calculations. All these photogrammetry documents were published in the edms server [92] at CERN. Examples of this deformation can be found in the references given below containing the raw photogrammetry measurements.

In this work these raw measurements are processed in order to be converted into useful alignment information of the muon chambers. In particular, concerning the Photogrammetry of the DT chambers, the following documents were used: YB0 Muon Chambers on SX5 [93], YB+1 Muon Chambers on SX5 [94], YB+2 Muon Chambers on SX5 [95], YB2 Muon Chambers on UX5 [96], YB0 Muon Chambers on UX5 [98], YB+1 Muon Chambers on UX5 [97], YB-1 Muon Chambers on UX5 [99] and YB-2 Muon Chambers on UX5 [100].

The tags *SX5* and *UX5* refers to the location of the detector: the photogrammetry was taken firstly at the surface of Point 5 *SX5*, and it was performed again once CMS was moved down into the pit, *UX5*.

The reference system in which the measurements in the documents above is defined to be coincident with the global CMS frame, except for the definition of the origin, which is displaced along the beam axis and fixed to the negative face of the wheel under consideration, as can be seen in figure 6.1.

Regarding the photogrammetry of the wheel with respect to the beam pipe, only the following document was considered, YB with respect to LHC beam axis on UX5 [101] .

6.2 Reconstruction algorithm

The photogrammetry measurements could not be directly implemented into CMSSW and a further processing was needed to implement them with the usual convention of the geometry files. A mathematical model was developed to perform this conversion. This model assumed the rigidity of the chambers, so that the observed position of the chambers could be modelled as a translation and a rotation of the nominal ones (resulting from the movement of the chamber as a rigid body).

In the following, $\vec{x} = (x, y, z)$ will denote the position of each photogrammetry point, while $\vec{x}^0 = (x^0, y^0, z^0)$ will denote its nominal position. The assumption of rigidity of the chamber implies the following relation

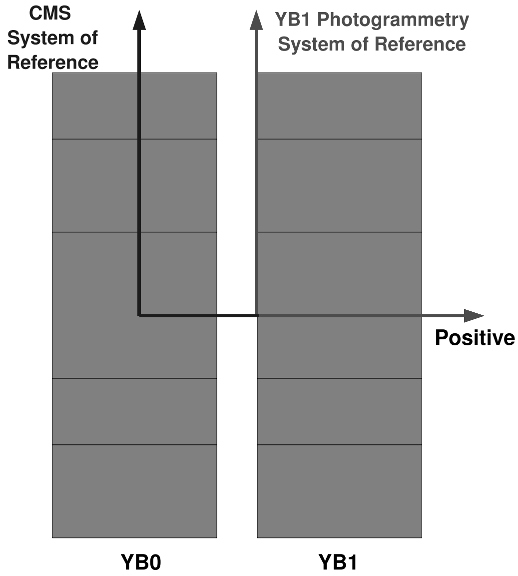

Figure 6.1: Sketch of the barrel wheels in the Y-Z plane. The reference system of the measurements of every wheel is fixed to its negative face.

$$\vec{x}_i = \mathbf{R}\vec{x}_i^0 + \vec{\delta} \tag{6.1}$$

where $\mathbf{R}$ and $\vec{\delta}$ are a rotation matrix and a displacement which transforms the nominal point $\vec{x}_i^0$ into the actual one $\vec{x}_i$. This relation must hold for all the points.

In order to calculate the rotation and displacement that best fit the actual measurements, the following χ^2 is defined

$$\chi^2 = \sum_i (\vec{x}_i - \mathbf{R}\vec{x}_i^0 - \vec{\delta})^T \mathbf{E} (\vec{x}_i - \mathbf{R}\vec{x}_i^0 - \vec{\delta}) \tag{6.2}$$

where $\mathbf{E}$ is the inverse of the covariance matrix of the measurements, in this case diagonal and single-valued because the error of the photogrammetry measurements is the same for all the points and all the coordinates, 300 μm.

The χ^2 above depends on six parameters: the three components of the displacement vector and the three Euler angles that define the rotation. For a general rotation, the dependency on the Euler angles should not be linear, however because of the construction and assembly tolerances, the expected rotation (and displacement) is small enough to consider only linear terms. The rotation matrix is then reduced to the following.

$$\mathbf{R} = \begin{pmatrix} 1 & \phi_z & -\phi_y \\ -\phi_z & 1 & \phi_x \\ \phi_y & -\phi_x & 1 \end{pmatrix} \tag{6.3}$$

The relation between the coordinates of the $\vec{r}_i$ and $\vec{r}_i^0$ can then be expanded as

$$\begin{aligned} \Delta_x = x - x^0 = -z^0\phi_y + y^0\phi_z + \delta_x \\ \Delta_y = y - y^0 = z^0\phi_x - x^0\phi_z + \delta_y \\ \Delta_z = z - z^0 = -y^0\phi_x + x^0\phi_y + \delta_z \end{aligned} \tag{6.4}$$

The equation above can be expressed in matrix form as

$$\vec{\Delta} = \mathbf{A}\vec{\delta} \tag{6.5}$$

where $\vec{\Delta}$ is the vector $(\Delta_x, \Delta_y, \Delta_z)$, $\mathbf{A}$ is the matrix

$$\mathbf{A} = \begin{pmatrix} 1 & 0 & 0 & 0 & -z^0 & y^0 \\ 0 & 1 & 0 & z^0 & 0 & -x^0 \\ 0 & 0 & 1 & -y^0 & x^0 & 0 \end{pmatrix} \tag{6.6}$$

and $\vec{\delta}$ is the vector of alignment parameters $(\delta_x, \delta_y, \delta_z, \phi_x, \phi_y, \phi_z)$. With these assumptions, the χ^2 above can be expressed as

$$\chi^2 = \sum_i (\vec{\Delta}_i - \mathbf{A}_i\vec{\delta})^T \mathbf{E}_i (\vec{\Delta}_i - \mathbf{A}_i\vec{\delta}) \tag{6.7}$$

The form of this χ^2 is formally very similar to the χ^2 in equation 3.27, and hence the solution is given by

$$\vec{\delta} = (\sum_i \mathbf{A}_i^T \mathbf{E}_i \mathbf{A}_i)^{-1} \sum \mathbf{A}_i^T \mathbf{E}_i \vec{\Delta}_i \tag{6.8}$$

The solution vector $\vec{\delta}$ is always well-defined provided there are at least three photogrammetry measurements which are not forming a straight line. In that case the information is rejected and the algorithm is not applied to that chamber (see following sections).

6.3 Implementation of the algorithm in CMSSW

The algorithm described above was implemented in CMSSW inside the package *SurveyAnalysis* and can be structured in three different parts:

- Data collecting. The input data is read and converted into the proper format.
- Fit analysis. The calculation of the constants is produced through the fit technique described in the previous section.
- Data output. Calculated alignment constants are stored in CMSSW readable format.

Figure 6.2 contains a diagram with the workflow associated to this algorithm.

Data collecting

The basic input information for the algorithm are the measurements and nominal positions of the raw photogrammetry measurements. As this data is usually provided in pdf or excel files, it was necessary to convert it into text files, and place them into the data/ directory of the *Alignment/SurveyAnalysis* package. The fields contained in these files are the following: the id of the point, the x, y, and z measurements, the error, and the displacements δx, δy

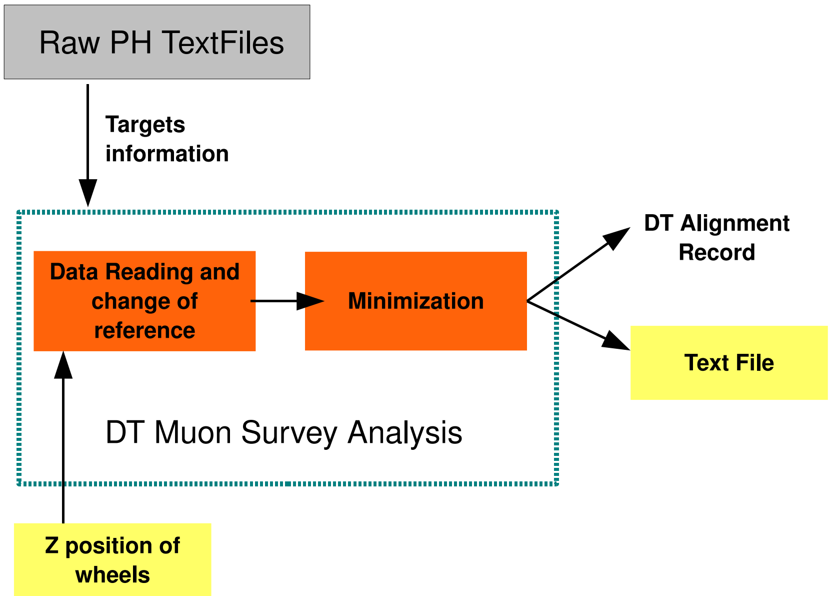

Figure 6.2: Workflow associated to the DT survey analysis algorithm.

and δz with respect to the nominal position.

The algorithm is designed to read this information, and to convert the measurements from the system of reference used by the PH team to the local system of coordinates of the DT chambers described in chapter 2. This is important to translate the alignment information into the natural system of the chamber defined by the direction of the wires.

Fit analysis

The fit described in the previous section was performed, requiring a minimum of three photogrammetry points per chamber, in such a way that the linear system resulting from the fit minimization is regular. Three non-aligned points is the minimum number of points that allow to reconstruct all the six degrees of freedom of a 3D object. The system was solved by inversion of the matrix, using standard algebra libraries from ROOT.

Data output

The algorithm is able to write the output in two different formats. The first one, very useful for further analysis of the constants is through plain text files where the following fields are expressed as columns: the wheel, station, sector and id of the chamber, the six alignment parameters and their errors, the χ^2 of the fit and the number of degrees of freedom.

The second format is the default in CMSSW: *DTAlignmentRcd* and *DTAlignmentErrorRcd* records exported into private sqlite files, that can be read by the reconstruction and uploaded into the official databases of CMS.

6.4 Analysis of the measurements at the surface

As it is explained in appendix B, CMS was initially mounted on the surface of P5. DT chambers were inserted in the yoke and the wheels were instrumented. In particular, during the MTCC (Magnet Test and Cosmic Challenge) sectors 10 and 11 of wheels YB+2 and sector 10 of YB+2 were fully instrumented and prepared for a cosmic muon data taking during the test of the magnet.

The photogrammetry of the wheels YB0, YB1 and YB2 was performed during this period, and the survey algorithm was applied in order to produce the first alignment corrections for the muon barrel of CMS.

6.4.1 Results

In this subsection the alignment constants calculated for the chambers in YB0, YB+1 and YB+2 at the surface are presented. To make easier the understanding of these results the local system of coordinates of the chambers (in which the constants are calculated) is slightly modified, in such a way that the sign convention has been unified, being always the local x direction identified with the rϕ direction (clockwise sense), the y direction identified with the global Z of CMS (along the beam) and the z direction identified with the radial coordinate, pointing always to the interaction point. It is important to remark that the official local system of coordinates defines the sense (the sign) of the axis depending on the orientation used to insert the chamber in its corresponding hole. This convention is used to store the geometry and to be properly uploaded into the CMS official database, although it is confusing for presentational purposes.

Figure 6.3 shows the alignment parameters for the six degrees of freedom as a function of the sector number and for wheel +2 (figures for all the wheels can be found in appendix D). This kind of representation is used to give a clear idea of the magnitude of the alignment corrections, which is very similar for all the wheels and is of the order of some millimeters for the position alignment parameters and a few mrads for the rotation parameters. A pattern can be distinguished also for the δ_x, δ_z, and ϕ_y alignment parameters.

To better understand these patterns a set of polar plots has been produced (figure 6.4 shows the plot for wheel 0, although a complete set of plots can be found in appendix D). The angular axis of these plots is related to the sector number, in such a way that it represents the real position of the chamber under consideration, in the wheel. The magnitude of the alignment constant is represented in the radial axis.

There are some conclusions that can be extracted from the figures:

- All the wheels show a similar behavior.
- There are not large differences for different chambers in a same sector (near-by chambers suffer a similar displacement).
- Large values for the alignment parameters δ_x, δ_z and ϕ_y (around 5 mm and 2-3 mrad), and some dependence versus the sector number.

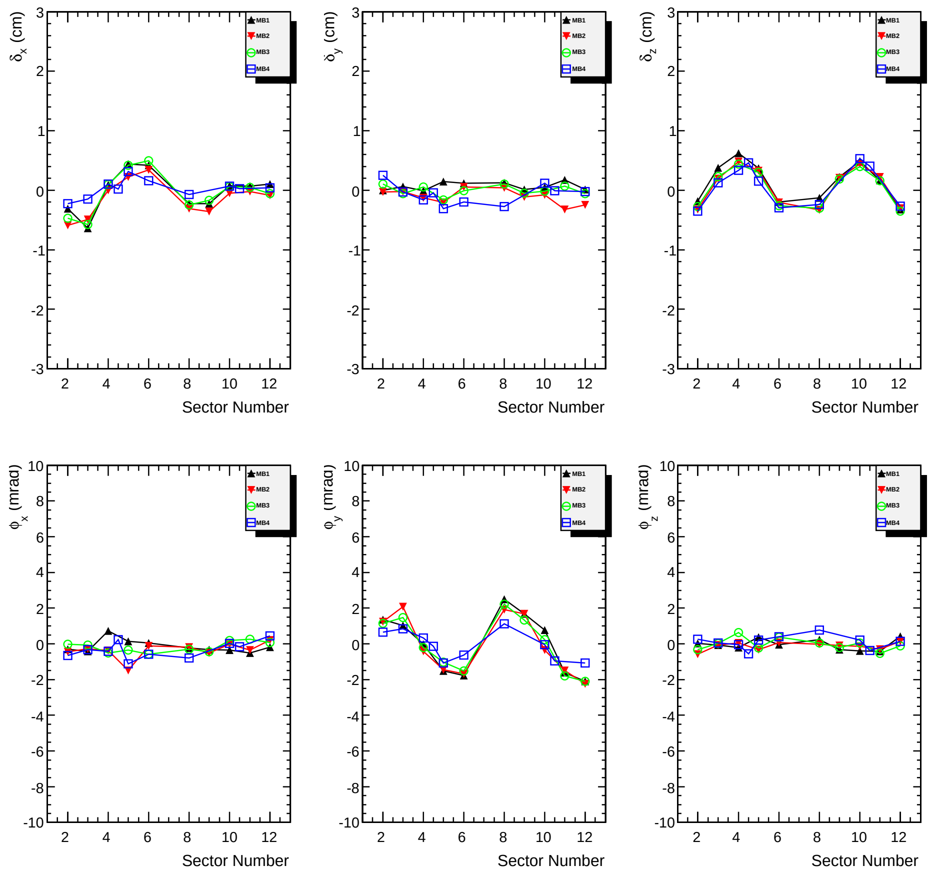

Figure 6.3: From top-left to bottom-right, δ_x, δ_y, δ_z, ϕ_x, ϕ_y and ϕ_z alignment parameters as a function of the sector number for wheel +2.

- The rest of the alignment parameters, are smaller and do not present any kind of structure, with the exception of the δ_y for YB0 where unexpectedly large values are present. This wheel was not instrumented in the MTCC and as it will be shown later, these strange values disappeared when the wheel was lowered into the pit.

The most significant correlation appears in the radial coordinate δ_z, where a butterfly-like shape can be observed. Horizontal sectors (sectors 4 and 10) have a very large positive displacement, while the vertical sectors (sectors 1 and 7) have a very large negative displacement. The sign of the displacements is defined to be positive if the displacement is towards the interaction point, and negative on the contrary. The butterfly-like shape can be interpreted therefore as a vertical compression and a horizontal expansion of the wheel.

The rotation with respect to the local y axis, ϕ_y, shows again a very characteristic shape. In this case, the butterfly-like shape is diagonally oriented. It is important to remark that this alignment parameter refers to the rotation in the $r\phi$ plane. Vertical and horizontal chambers do not suffer a large rotation, which is indeed more important in the intermediate sectors, including also a change of sign. This shape corresponds to a deformation in which the wheel changes its circular shape into an ellipse parallel to the ground.

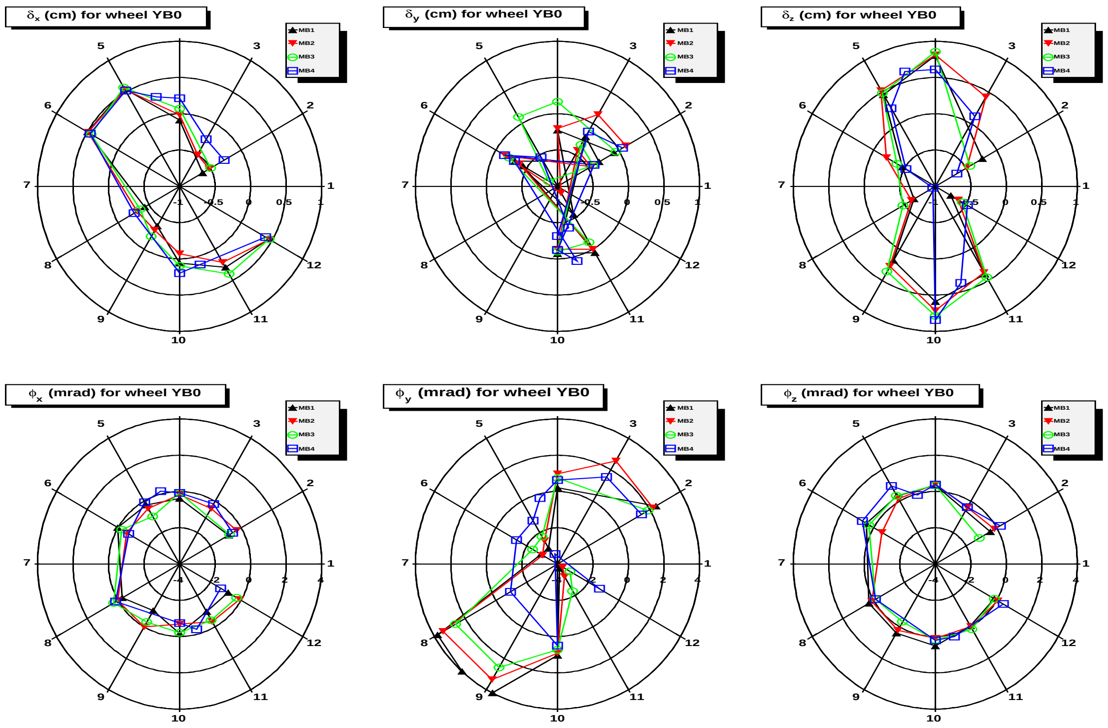

Figure 6.4: From top-left to bottom-right, δ_x, δ_y, δ_z, ϕ_x, ϕ_y and ϕ_z alignment parameters for wheel 0. The radius of these plots, represents the values of the plot 6.3, while the sector number is represented in the polar coordinate, mimicking their real position if the wheel is observed from the +Z side. It is important to remark that the 0 corresponds to the second inner circle.

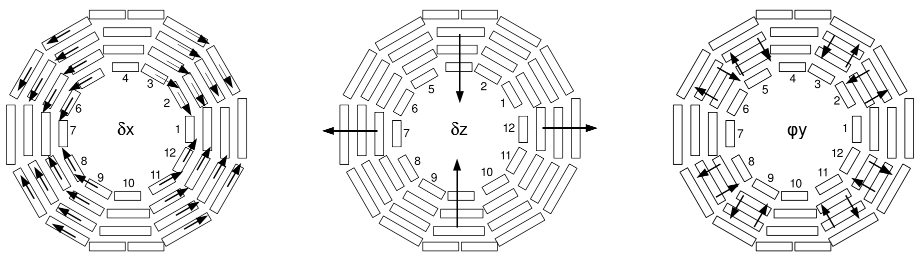

(a) (b) (c)

Figure 6.5: Sketch of the measured misalignments in δ_x (a), δ_z (b) and ϕ_y (c)

The last coordinate in which a characteristic shape is distinguished is the local x. This coordinate refers to the $r\phi$ direction. The behavior of this alignment parameter is very similar to the ϕ_y. The most important corrections do not appear in the vertical and horizontal chambers, but in the intermediate sectors.

All these effects can be interpreted as a gravitational sag due to the weight. Figures 6.5 show a diagram in which the kind of movements observed in the plots are drawn using arrows. This is in a good agreement with the expectations from finite element calculations, as can be seen in the magnet TDR report [27]. As an estimator of the deformation suffered by the wheels, the difference between the radial displacements δ_z for the horizontal sectors (4 and 10) is considered and averaged for the 4 stations, resulting in: $1.6\,cm$, $0.9\,cm$ and $1.0\,cm$ respectively for YB0, YB1 and YB2. The compression is much larger in YB0 were the weight of the magnet is contributing as well.

The rest of the alignment parameters do not present large values and in general the deviations from 0 are consistent with the mechanical tolerances in the installation process, or to possible deformations of the chambers.

6.5 Error analysis and goodness of the fit on surface data

The error matrix **E** in equation 6.7 is the inverse of the covariance matrix of the position of the photogrammetry points. The error associated to these measurements is 300 μm in all the coordinates, as can be extracted from the photogrammetry documents, and therefore the **E** matrix is $\frac{1}{(0.03\,cm)^2}$ times the identity matrix. The statistical errors obtained from the fit are of the order of a few micrometers and a few microrads.

In order to understand the quality of the error estimation, the normalized χ^2 distribution of the fits is studied. Figure 6.6 shows this distribution for all the chambers. As can be observed there are two different effects:

- There are some outliers with a very large value of the normalized χ^2 (about 30).
- The mean of the distribution is clearly displaced from 1.

The first statement can be justified by the presence of punctual mistakes in the position estimation of the photogrammetry points (problems in the location of the bright targets, unexpected movements). On the contrary, the second one is something affecting to all the chambers. This effect could be explained through deformations of the chambers, although not enough photogrammetry points were measured in order to check it. On the other hand, this effect is equivalent to the underestimation of the photogrammetry errors by a factor 3, from 300 μm to 900 μm approximately. Conservatively this last assumption was made.

6.6 Analysis of the measurements at the pit

After the Magnet Test and Cosmic Challenge, CMS was moved down into the pit. Barrel wheels were instrumented again and missing vertical chambers (sectors 1 and 7) were installed. The same procedure followed for the surface measurements in the previous sections, was followed for the photogrammetry measurements and for the data analysis in the pit.

6.6.1 Results

In figure 6.7 the alignment constants are shown for the different wheels and degrees of freedom as a function of the sector number and for wheel +2.

Similar conclusions to the surface measurements can be drawn from these results. The major difference is that the unexpectedly high δ_y for the wheel 0, observed in the surface measurements is not reproduced in the measurements at the pit.

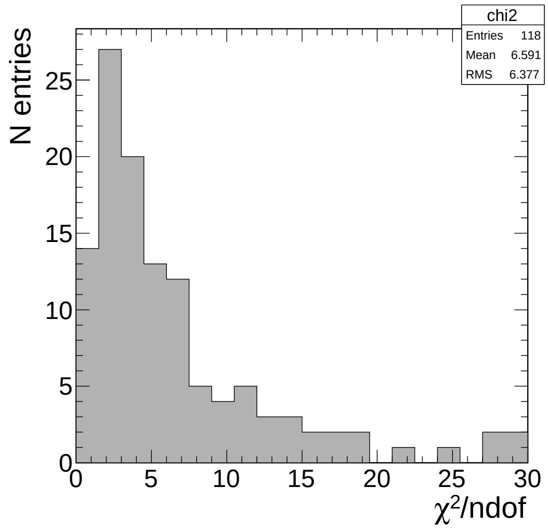

Figure 6.6: Normalized χ^2 of the fit, for all the chambers and using the photogrammetry on the surface.

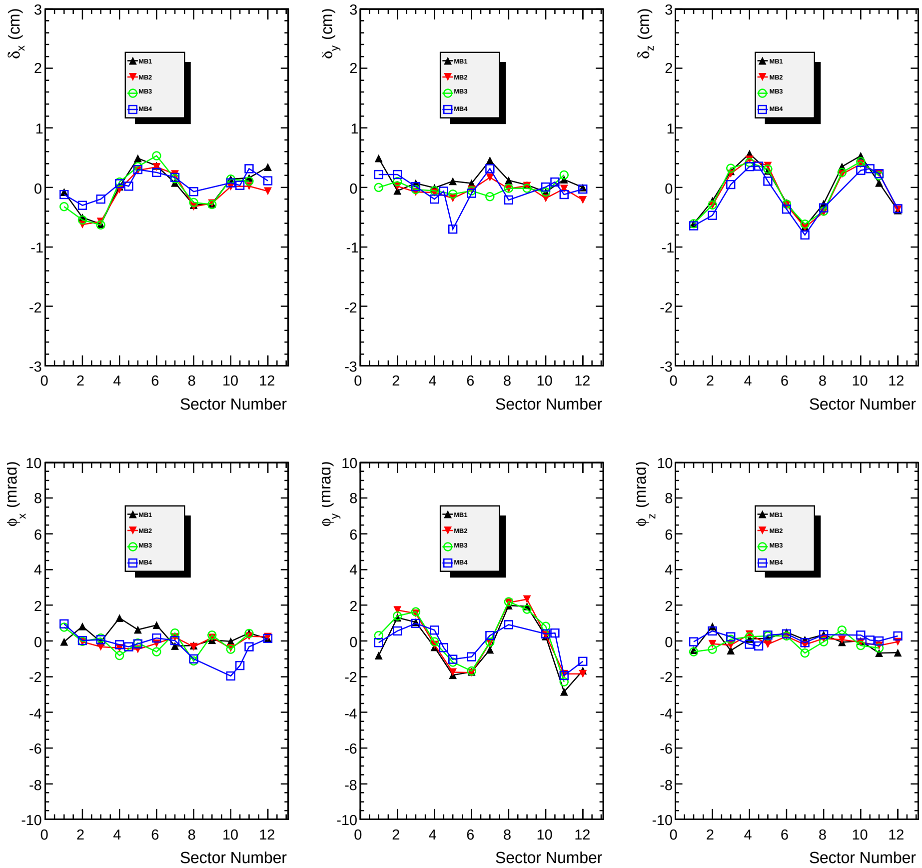

Figure 6.7: From top-left to bottom-right, δ_x, δ_y, δ_z, ϕ_x, ϕ_y and ϕ_z alignment parameters as a function of the sector number for wheel +2.

Using again the difference between the radial displacements δ_z for the horizontal sectors (4 and 10) as a measurement of the deformation of the wheel, the obtained values are: averaged for the 4 stations, resulting in: 1.0 cm, 1.0 cm and 1.5 cm, 0.8 cm and 0.9 cm respectively for YB-2, YB-1, YB0, YB1 and YB2. The largest compression is found in YB0, due to the extra-weight added by the magnet. Figure 6.8 shows the polar plot for the alignment parameters found in YB0. For a complete list of plots including all the wheels see appendix D.

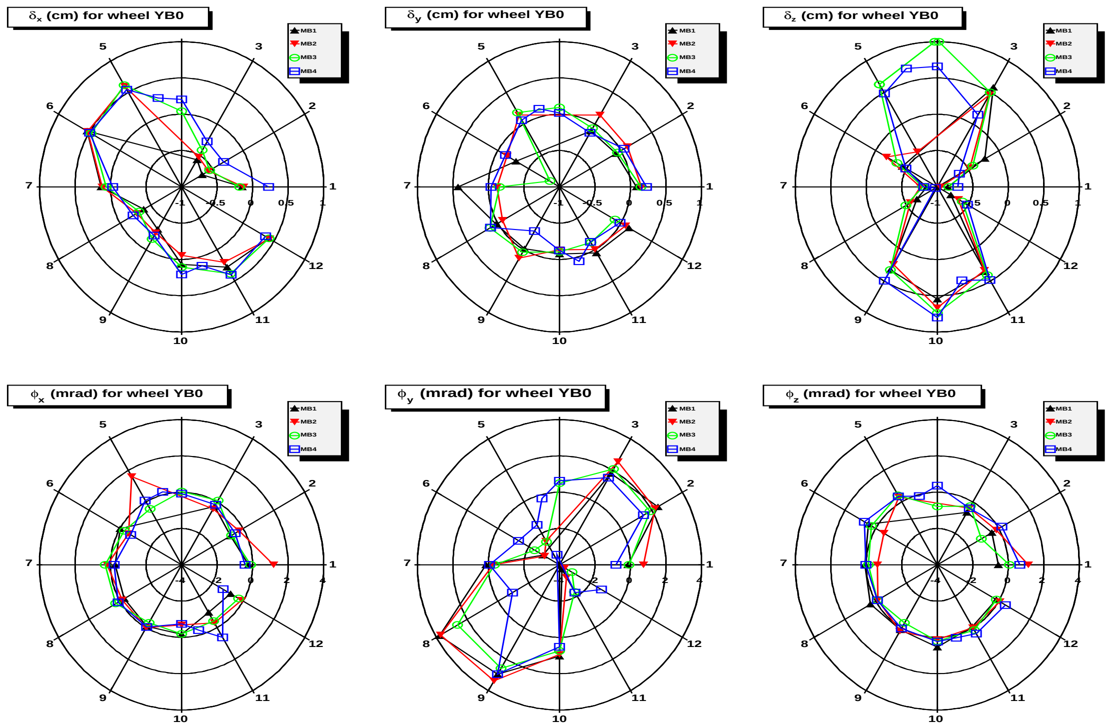

Figure 6.8: From top-left to bottom-right, δ_x, δ_y, δ_z, ϕ_x, ϕ_y and ϕ_z alignment parameters for wheel 0. The radius of these plots, represents the values of the plot 6.3, while the sector number is represented in the polar coordinate, mimicking their real position if the wheel is observed from the +Z side. It is important to remark that the 0 corresponds to the second inner circle.

The normalized χ^2 distribution is studied again for the measurements at the pit. Figure 6.9 shows the χ^2 distribution for these measurements with a similar behavior and identical conclusion to the surface case.

6.7 Surface vs. Pit comparison

The process of lowering down the wheels into the pit was a complicated task, that might have provoked deformations and misalignments with respect to the initial position at the surface of P5, due to the own weight of the detector. In particular, each of the wheels was lifted with the help of a crane and cables attached to both sides of the wheel. During this process the configuration of the tensions through the iron yoke changed, because the sustentation region was found at the sides instead of at the bottom. Once the wheels were placed again on the ground of the pit, the tension configuration was similar to the one on the surface of P5, but a complete reproducibility of the measurements was not expected.

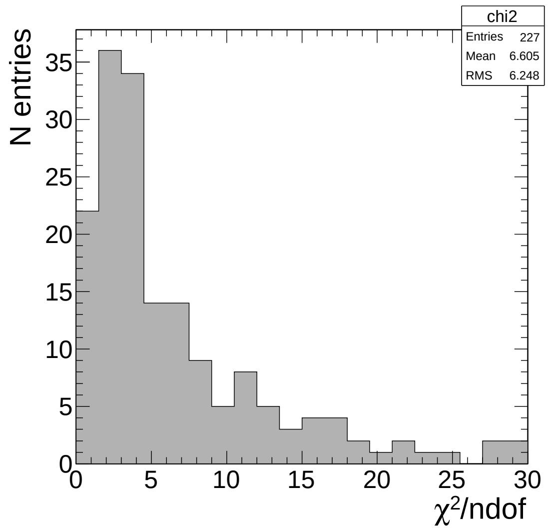

Figure 6.9: Normalized χ^2 of the fit, for all the chambers and using the photogrammetry on the pit.

Figures 6.10 show the differences between the alignment parameters calculated on the surface and on the pit. The level of agreement is of the order of 500 μm, 1.3 mm and 1 mm respectively for the positions, and of the order of 300-400 μrad for the angles. These values are slightly above the precision, once accounted for the factor 3 commented in the previous sections. Taking into account these considerations it is possible to affirm that the process of transportation of the wheels into the ground did not provoke large deviations in the alignment of the chambers. Nevertheless the CMS database was updated with the new information (which was important for some of the chambers were the differences were appreciable). The fact that after a complicated process as the lowering of the wheels, the results are compatible with the surface results within the expected precision, provides strong confidence in the relevance of these measurements.

6.8 Treatment of missing chambers

The distribution of bright targets over the chambers was not uniform, and sometimes the number of available photogrammetry points was not enough to allow the calculation of the alignment parameters. In the surface often the chambers had not been installed yet, while in the pit, some of the chambers were not accessible.

Figures E.1 and E.2 in appendix E show the chambers where the photogrammetry points could not be reconstructed. In the case of the surface measurements all the vertical sectors (1 and 7) were missing because the chambers were not installed yet.

Missing chambers were discovered to have a large impact in the muon reconstruction. If the position of a given chamber is not corrected, being corrected the position of its neighboring chambers, a strong and artificial relative misalignment appears in the system. The reconstruction is largely affected by this kind of misalignments. For this reason, the chambers which were initially not aligned were updated with an average of the misalignments found in

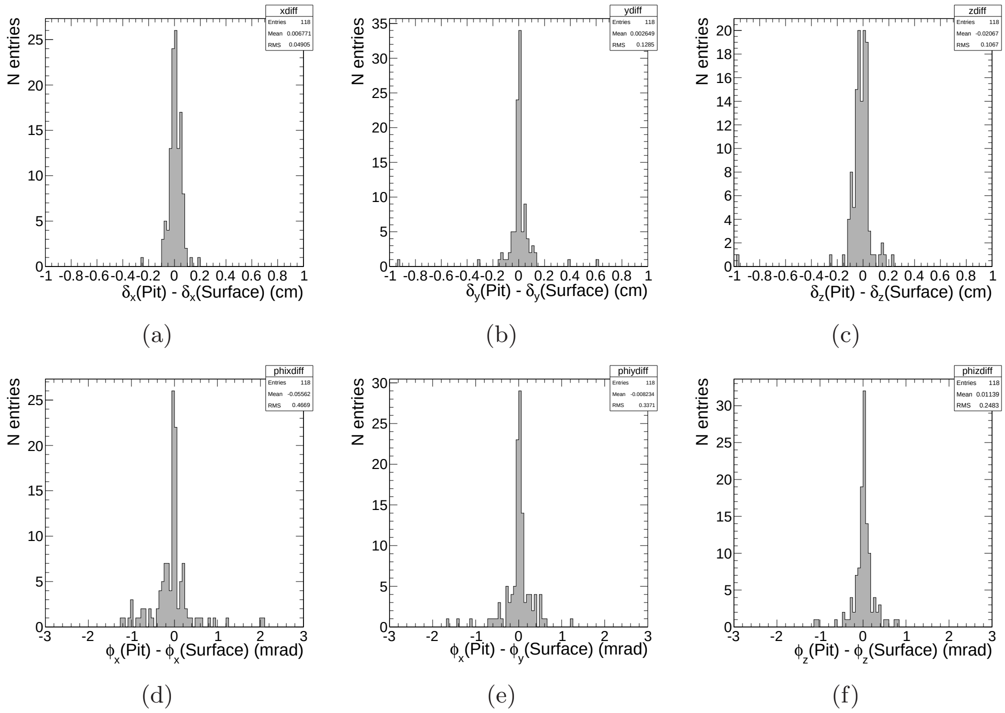

Figure 6.10: The difference in the alignment parameters between the surface and the pit. From (a) to (f), δ_x, δ_y, δ_z, ϕ_x, ϕ_y and ϕ_z alignment parameters.

the neighboring chambers in the same sector. This procedure reduced the alignment error of these chambers from up to 1 cm to the order of 2 mm, assuming a 1 mm error in the positioning of the updated chambers.

6.9 Photogrammetry of the wheels

It is important to remark that the measurements of the muon chambers are always referred to the center of the wheels. For this reason, these measurements do not contain any information about the position and orientation of each of the wheels.

To provide this information, the photogrammetry team measured the position of each wheel with respect to the LHC beam axis, using external references. The position of each wheel and two rotation angles ϕ_X and ϕ_Y were provided in the official CMS global system. The numbers are available at table 6.1.

wheel	x/cm	y/cm	z/cm	ϕ_x/mrad	ϕ_y/mrad
-2	-0.1	0.0	-535.8	0.2	0.3
-1	0.1	0.0	-269.7	0.5	0.3
0	0.0	0.1	0.2	0.2	0
1	-0.2	0.1	269.4	-0.1	-0.1
2	0.2	-0.1	535.8	-0.5	-0.4

Table 6.1: Global positioning of the wheels using photogrammetry information.

These measurements were introduced in *DTAlignmentRcd* records using the standard methods and on top of the alignment of the chambers with respect to the wheels, and the internal alignment. Finally it was exported to a private sqlite file.

6.10 Validation

The photogrammetry-based geometry described before was exported into the official database of CMS, and was used during most of the commissioning phases of CMS, including the start-up of the LHC in September 2008.

Before populating the constants for wide-use within the collaboration, a dedicated validation method (the segment-to-segment extrapolation method [102]) was run to ensure the quality and correctness of this geometry. Additionally the outcome of several analysis specially sensitive to the geometry were revised (see [103], [104]). In all the cases a significant improvement was observed.

6.10.1 The segment to segment extrapolation method

The segment to segment extrapolation method is a validation technique applied to the Drift Tube chambers of CMS, exploiting their local reconstruction functionality [102]. Tracks crossing the muon detector are reconstructed independently in every chamber giving place to the so called segments. This validation method proposes to extrapolate the segment in a given chamber to the chamber in the next station. And to compare the outcome of the extrapolation, with the segment of the targeted chamber. This comparison can be made not only in the position coordinate but also in the direction. In this context, two residuals are defined: the translational residual, which is the difference between the extrapolated and measured position, and the directional residual, which is the equivalent in the angular coordinate. The mean of the residual distributions defined in such a way are sensible to misalignments in the δ_x and ϕ_y coordinates, which are in fact the most important in the global reconstruction process.

In order to compare and quantify the improvement achieved, this procedure is applied for all the chambers (pairs of chambers) using the design geometry and using the updated one. The mean of the residual distributions as defined above are shown in figure 6.11, for the translational coordinate and in 6.12 for the angular component. Table 6.2 shows the RMS of the so called MRD (Mean of Residual Distribution) distribution, where each entry is the mean of the residual distribution associated to a pair of chambers in station N and station N+1. The reduction of this RMS indicates that the mean of the residual distributions is approaching to zero, as it should be in a perfectly aligned detector. From this table can be observed that the improvement is more important in the translational coordinate than in the angular. In the former, the improvement is about a factor 2, from the 2 mm level, to the 1 mm. The improvement in the latter, the angular part, is not so important, being more appreciable between stations 3 and 4, where there is a reduction of 0.4 mrad in the RMS.

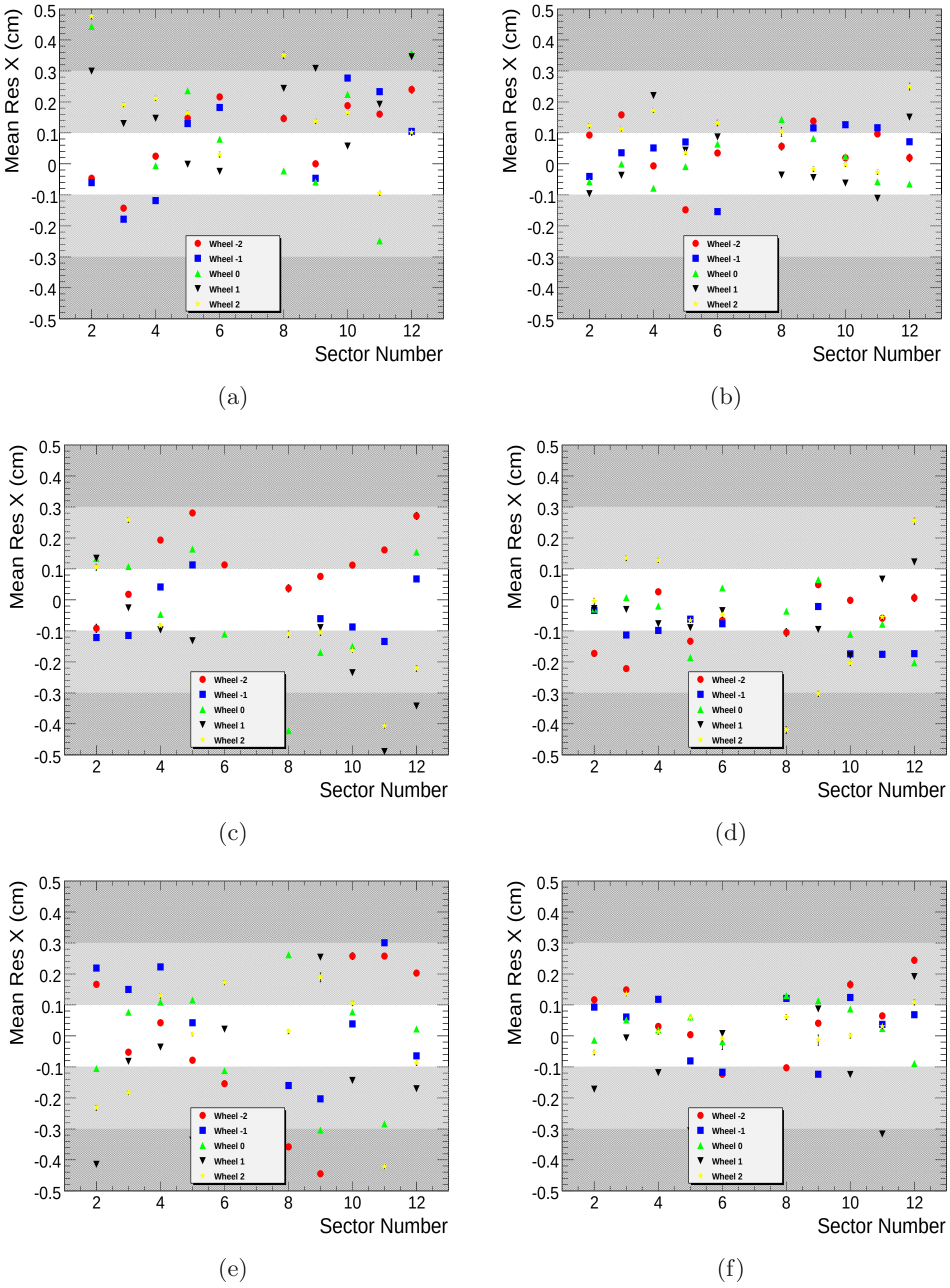

Figure 6.11: Mean of the segment-to-segment associated residual in the x position before applying the corrections (left column) and after applying the corrections (right column) for stations 1 and 2, 2 and 3, and 3 and 4 respectively in each of the rows.

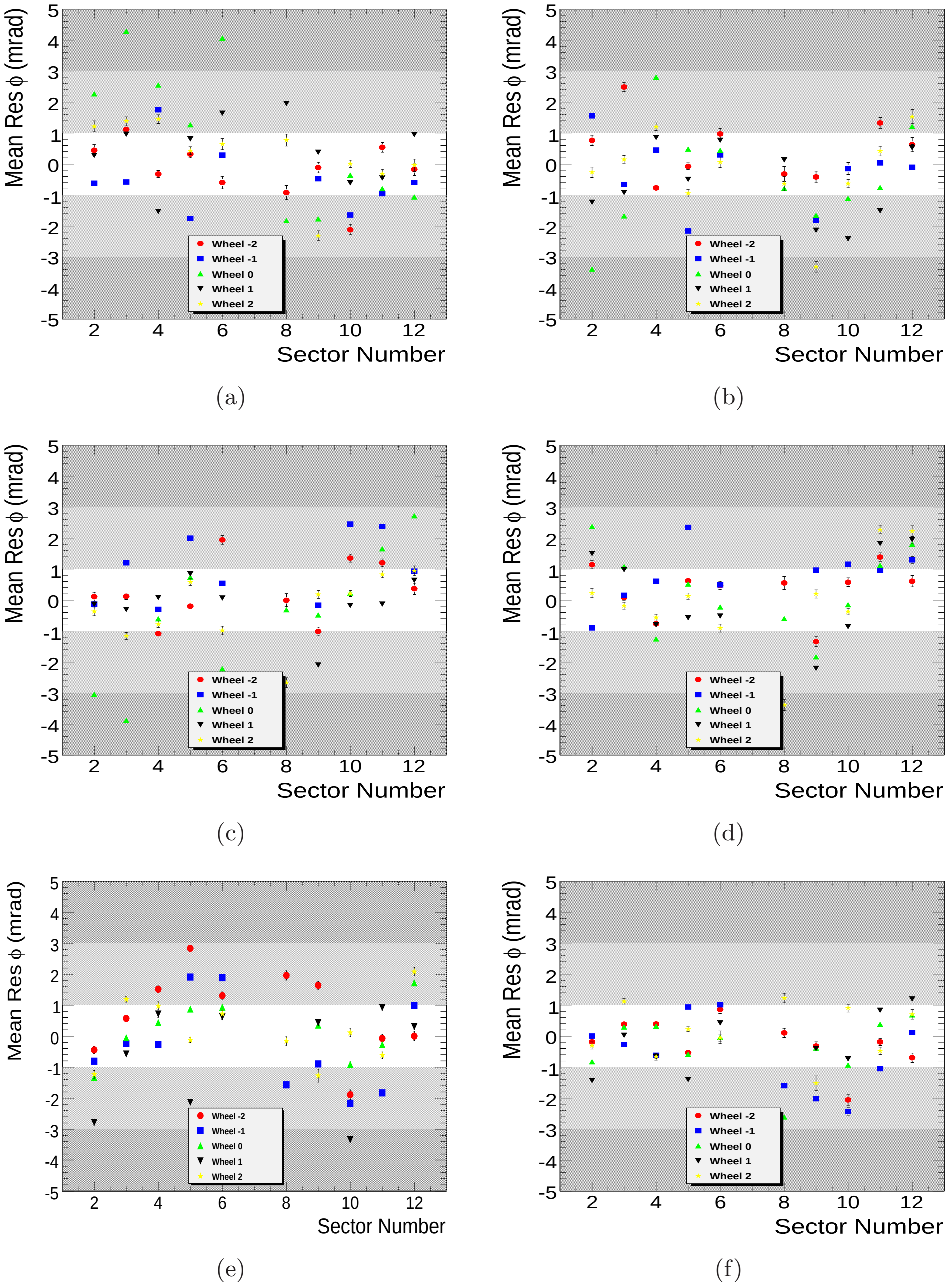

Figure 6.12: Mean of the segment-to-segment associated residual in the dx/dz direction before applying the corrections (left column) and after applying the corrections (right column) for stations 1 and 2, 2 and 3, and 3 and 4 respectively in each of the rows.

	Aligned	Not Aligned
	RMS MRD x/mm	RMS MRD x/mm
MB12	0.9	1.7
MB23	1.2	2.16
MB34	1.1	2.2
	RMS MRD $\frac{dx}{dz}$/mrad	RMS MRD $\frac{dx}{dz}$/mrad
MB12	1.3	1.4
MB23	1.2	1.3
MB34	0.9	1.3

Table 6.2: RMS of the Mean of the Residual Distribution (MRD) for both coordinates translational and directional and for both geometries: nominal and photogrammetry-based.

Chapter 7

Standalone track-based alignment of the muon system

During the Magnet Test and Cosmic Challenge (MTCC) and the different computing exercises of CMS (see appendix B), the MBAA algorithm was applied in order to get an alignment of the drift tube chambers.

The algorithm presented in this chapter (usually called the MBAA standalone algorithm, or simply the standalone algorithm) was intended to align the barrel of the muon system, using tracks reconstructed only in the muon chambers, and using photogrammetry information to constraint the weak modes associated to the track-based algorithms. This algorithm allows to provide a first corrected geometry of the muon spectrometer without the intervention of the central tracker system. It was particularly important before the year 2008, when the tracker was not operative.

7.1 The standalone alignment algorithm

The standalone alignment algorithm is a full implementation of the MBAA algorithm described in chapter 3, but specially adapted to fit the specific features of the drift tube chambers. The main characteristics of this application are listed bellow:

- The minimum alignable unit is the chamber which is considered a perfect rigid body. The algorithm is always applied over the already corrected internal geometry (see chapter 5).
- The 4 drift tube associated residuals (see chapter 3) ($\Delta\ x$, $\Delta\ \frac{dx}{dz}$, $\Delta\ y$, $\Delta\ \frac{dy}{dz}$) are used as observables.
- The track parameterization is based in the classical perigee parameterization. Eventually this parameterization can be simplified by removing the curvature parameter, in case the magnet is not switched on.
- Alignment derivatives are extracted from the usual parameterization 3.23, while track derivatives are calculated numerically.
- The photogrammetry information described in chapter 6 is used to constraint the fit and fix the weak modes.

The drift tube chamber was used as the minimum alignable unit. This is motivated by the correlations induced by the scattering processes that take place in the iron yoke between chambers, which deflect muons in a correlated pattern for all the hits in a same chamber. In practice, it implies that in many cases the statistical correlation between hits is above 99%, which implies an ill-conditioned system. To account for this correlation, single layer hits and the track intersections associated to them are combined in a linear fit producing four observables for each chamber: the position residuals Δx, Δy and the direction residuals $\Delta\frac{dx}{dz}$ and $\Delta\frac{dy}{dz}$. The chamber is treated as a rigid body, reducing the dimension of the associated system. The internal alignment of layers and superlayers is produced in a different procedure explained in chapter 5.

The algorithm takes three collections as inputs: the standalone reconstructed tracks, the segments associated to the DT chambers, and the photogrammetry measurements. From the logical point of view, the algorithm can be separated in 3 different steps: the calculation of the residuals, the calculation of the alignment and track derivatives and the application of the photogrammetry constraint and the χ^2 minimization. Finally the algorithm produces as output a list of alignment corrections.

7.1.1 Calculation of residuals

The residual calculation is performed by extrapolating states of the standalone track to the surfaces where the *DT4DSegments* are contained. The starting point for these extrapolations is the innermost point of the track in the muon system, which is usually the surface associated to the RPCs in the first station and very close to the first DT station. Then, the *SteppingHelixPropagator* is used to extrapolate the track to the surface associated to the segments as can be observed schematically in figure 7.1. The position and orientation of the extrapolated state and the *DT4DSegments* are compared to form the 4 residuals: (Δx, $\Delta\frac{dx}{dz}$, Δy, $\Delta\frac{dy}{dz}$). It is important to remark that these residuals are still correlated due to the scattering processes that take place in the iron of the muon system. These correlations are taken into account through the covariance matrix.

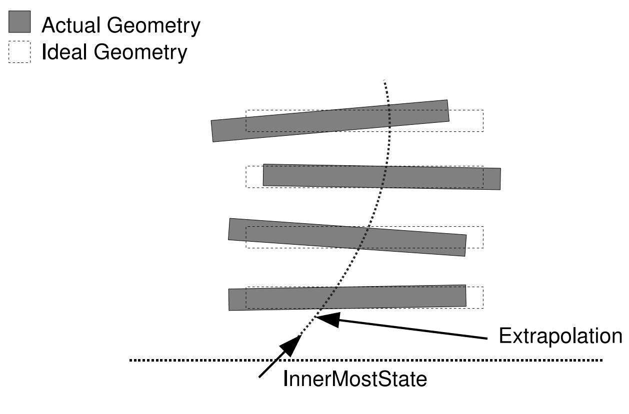

Figure 7.1: The inner most state is extrapolated to the plane of the chamber and the trajectory state is compared with the segment

7.1.2 Calculation of alignment and track derivatives

The calculation of the alignment derivatives is done analytically, using the parameterization given in chapter 3. On the contrary, track derivatives are calculated numerically, provided there is not a simple, analytical description of the trajectory path of a particle in a non-homogeneous magnetic field. The track-derivatives matrix takes the following form provided the perigee parameterization has 5 parameters d_0, z_0, ϕ, θ and k:

$$B = \begin{pmatrix} \frac{\partial \Delta x}{\partial d_0} & \frac{\partial \Delta x}{\partial z_0} & \frac{\partial \Delta x}{\partial \phi} & \frac{\partial \Delta x}{\partial \theta} & \frac{\partial \Delta x}{\partial k} \\ \frac{\partial \Delta dx/dz}{\partial d_0} & \frac{\partial \Delta dx/dz}{\partial z_0} & \frac{\partial \Delta dx/dz}{\partial \phi} & \frac{\partial \Delta dx/dz}{\partial \theta} & \frac{\partial \Delta dx/dz}{\partial k} \\ \frac{\partial \Delta y}{\partial d_0} & \frac{\partial \Delta y}{\partial z_0} & \frac{\partial \Delta y}{\partial \phi} & \frac{\partial \Delta y}{\partial \theta} & \frac{\partial \Delta y}{\partial k} \\ \frac{\partial \Delta dy/dz}{\partial d_0} & \frac{\partial \Delta dy/dz}{\partial z_0} & \frac{\partial \Delta dy/dz}{\partial \phi} & \frac{\partial \Delta dy/dz}{\partial \theta} & \frac{\partial \Delta dy/dz}{\partial k} \end{pmatrix} \tag{7.1}$$

In order to evaluate the partial derivative with respect to a given track parameter, say p_j, two new initial trajectory states are created, namely p_j^{left} and p_j^{right}. These states are a copy of the original trajectory state except for the track parameter under consideration which is modified symmetrically as $p_j - \Delta p_j$ and $p_j + \Delta p_j$ respectively for p_j^{left} and p_j^{right}. Both states are then extrapolated to the considered chamber and the associated residuals are calculated: $\vec{R}(p_j - \Delta p_j)$ and $\vec{R}(p_j + \Delta p_j)$. For a given residual, R_i, the partial derivative with respect to the parameter p_j is then calculated numerically as:

$$\frac{\partial R_i}{\partial p_j} = \frac{R_i(p_j + \Delta p_j) - R_i(p_j - \Delta p_j)}{2\Delta p_j} \tag{7.2}$$

This procedure is shown schematically in figure 7.2. It is important to remark that this calculation involves two extrapolations per track parameter and chamber, being the most CPU-consuming part of the algorithm.

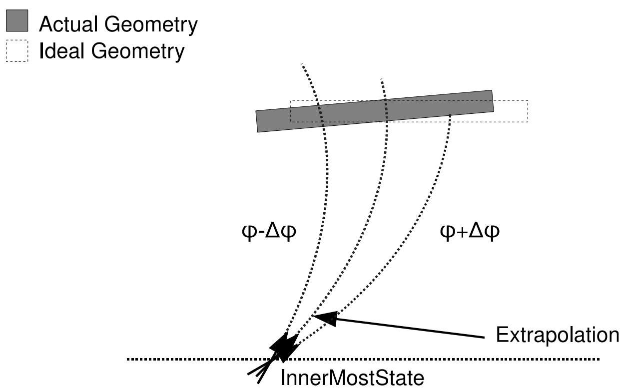

Figure 7.2: The track parameters of the initial state are modified symmetrically in order to calculate the track derivatives.

7.1.3 Photogrammetry constraint and χ^2 minimization

In order to fix weak modes, photogrammetry constraints are included in the MBAA fit. This is performed using equation 3.38 in which additional terms are incorporated to the χ^2. The form of the photogrammetry constraints contains terms such as $(\frac{\delta_i^{PH} - \delta_i}{\sigma_i^{PH}})^2$ where δ_i is the alignment parameter (a free parameter in the fit), δ_i^{PH} is the photogrammetry measurement for this alignment parameter and σ_i^{PH} its corresponding error.

Once the constraints are included, the linear system becomes regular and can be solved using standard linear algebra tools. In addition, as the problem is linear whenever misalignments are small, iterations are not needed. The dimension of the matrix is given by the product of the number of alignment parameters, 6 per chamber except for chambers in station 4, where only 5 alignment parameters are considered, and the number of chambers of each kind. This calculation yields to a dimension of 1430, which is acceptable for the current numerical techniques.

On the other hand, and complementary, the system can be solved by fixing the weak modes artificially. This is done by calculating the pseudo-inverse matrix, in which all the weak modes have been extracted.

7.2 Algorithm implementation

The algorithm described above was implemented in CMSSW under the name *MuonStandaloneAlignment* package. The general workflow of the algorithm is sketched in figure 7.3. As it was stated in the previous section, the algorithm takes the collection of standalone tracks and the collection of segments from the CMSSW event. First of all a matching between both collections takes place, and once every track has a set of associated segments, the calculation of residuals and matrices is performed, and introduced in objects called *TrackForAlignment* which are returned back to the event. This information is read again and used to produce the MBAA partial matrices, which are stored in root files. In a second phase, these root files are read, and all the partial matrices are merged, including as well the photogrammetry constraints. Finally the system is solved and the resulting alignment constants stored.

The workflow of the algorithm can be divided in two separated phases for practical purposes. The first phase involves the matching of segments and tracks, the calculation of residuals and derivatives, and the production of partial matrices. This is the most CPU-consuming part of the algorithm, and is usually parallelized in several hundred separated jobs. The second phase englobes the merging and solving of the system and is performed in a single job.

Segment to Track association

The reconstruction of CMS does not provide a matching between the segment and standalone track collections. This is usually not a problem when the event contains only one track, provided all the segments in the collection can be assumed to belong to that track (with caution regarding fake segments). However usually events contain more than one track, and it is needed to associate each of them to a subset of segments in the segment collection. This task is performed by the algorithm through the *TrackToSegmentAssociator* method.

This method exploits the fact that both the standalone track and the segments are built from the same collection of single hits (*RecHits*). The algorithm loops over the segments, and extracts their single hits, comparing them with the hits in the standalone track. If more

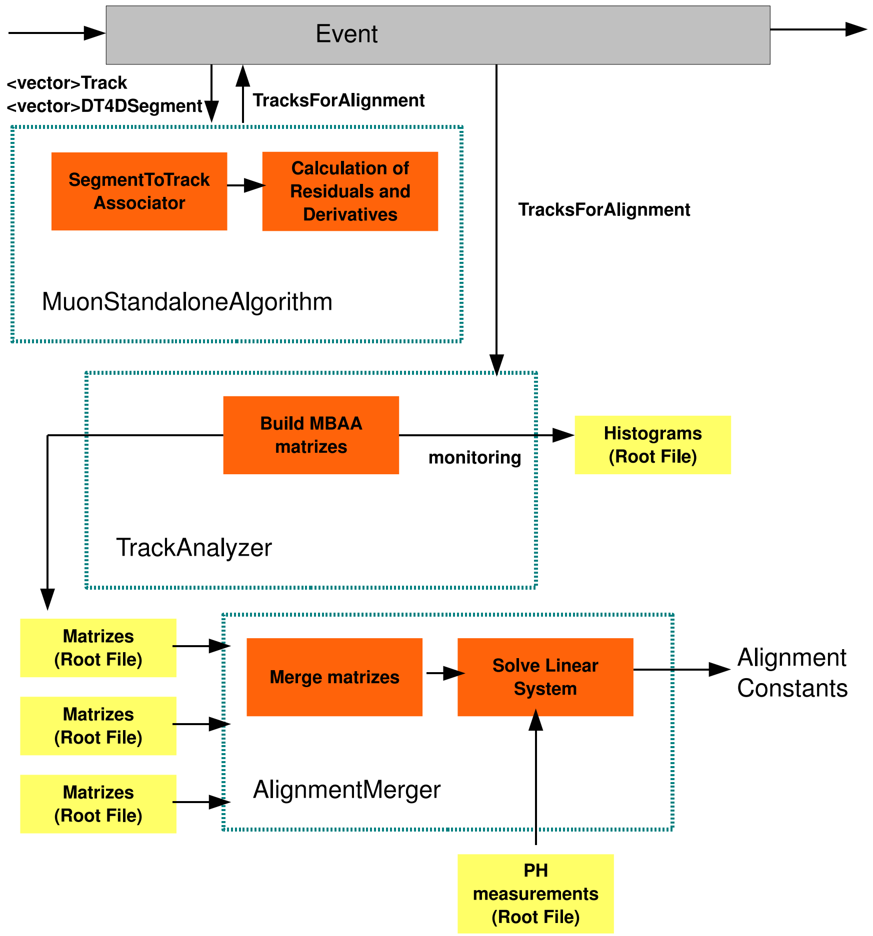

Figure 7.3: Workflow associated to the MBAA standalone algorithm.

than 4 hits are found in both the standalone track and the segment, then the segment is associated to that track. The efficiency of this algorithm is usually higher than 95%.

Production of AlignmentTrack objects and partial matrices

Once every track has a list of associated segments, the *innerMostState* is extracted, and the calculation of residuals starts, by extrapolating it to the surfaces associated to the segments. In addition, a method called *calculateJacobian* receives as input the perigee parameters of the inner most state, and the list of 4D segments, and calculates the track derivatives using the procedure explained in the previous section.

A selection criteria is then applied over the computed residuals and derivatives. The first selection is performed over the residuals. Only residuals below a given threshold in magnitude are accepted. This is generally a sanity check to avoid abnormally large residuals coming from pathological extrapolations, to enter in the fit. These extrapolations may occur because of a badly defined initial state, or because the extrapolation escapes the volume of the chamber. The second selection is other sanity check that concerns the track-derivatives. This selection prevents the algorithm to include bad-estimated derivatives. Even if the derivatives are computed numerically because of the non-homogeneity of the magnetic field, the trajectory of the particle still resembles an helix, and hence the derivatives must be close to the analytical derivatives. Derivatives with a value much larger than the analytical expectation are rejected. Finally, only standalone tracks with a segment per station are selected.

Tracks passing the selection criteria are stored in a C++ class called *TrackForAlignment*, which contains information referent to the track, as the P_T, ϕ, χ^2, etc. and a collection of *PointForAlignment* objects. These objects are defined in a C++ class with the same name, and contain the following information:

- Position and direction of the segments and the extrapolated track and their errors.
- Residuals associated to every chamber.
- Track derivatives matrix for every segment.

The *TrackForAlignment* object is made persistent and stored into the CMSSW event. This is done through a root dictionary [110] which allows CMSSW to dump objects of this type into root files.

Finally, the cumulative MBAA matrices are calculated for all the tracks in the sample. A system of indexes and tags was designed in order to allow these cumulative matrices to grow dynamically: if a track has information from a chamber not registered yet, the dimension of the cumulative matrices is adapted accordingly, and the chamber is included in the list of registered chambers. This mechanism allows to restrict the dimension of the problem when the algorithm is applied to a subset of chambers. At the end the matrices are stored in root files.

During the building of the matrices, histograms monitoring the different quantities are created and filled. This information is stored in a separated root file, and allows to quickly spot problems in the calculations.

Compilation Job

After the production of the alignment information and collections, a single job is in charge of reading all the partial matrices and the corresponding indexes and to build the final complete matrices. Survey constraints, when applied, are introduced at this stage. Finally the constants are calculated and stored in the official alignment records of CMSSW.

7.3 Application to the Magnet Test and Cosmic Challenge

During the summer of the year 2006, the magnet of CMS was tested for the first time, in the so called Magnet Test and Cosmic Challenge. In addition to the commissioning of the magnet, some chambers of the Muon System (both barrel and endcap) were instrumented and exposed to cosmic muons. More details about this commissioning step can be found in appendix B.

The cosmic muons recorded during this period provided the chance to perform a first alignment with tracks. In particular, the MBAA algorithm was applied to the three DT sectors instrumented, which corresponded to wheel +1, sector 10, and wheel +2, sectors 10 and 11. Each sector was aligned independently, and only the most important alignment parameter (δ_x) was considered for simplicity.

The algorithm was applied over the photogrammetry geometry calculated in chapter 6, and to solve the MBAA linear system, weak modes were extracted and a pseudo-inverse matrix was built. The solution in that case is analytical and given by equation 3.36. Developing the equation for this case, the solution can be expressed as the average $\vec{\delta} = 1/N \sum \vec{\delta}_j$, where $\vec{\delta}_j$ represents the contribution of a single track to the estimation of the alignment parameter, and has the form:

$$\vec{\delta}_j = N(\mathbf{A_j^T E_j}(\mathbf{A_j} - \mathbf{B_j}(\mathbf{B_j^T E_j B_j})^{-1}\mathbf{B_j^T E_j A_j}))^{-1}\mathbf{A_j^T E_j}(\vec{R}_j - \mathbf{B_j}(\mathbf{B_j^T E_j B_j})^{-1}\mathbf{B_j^T E_j}\vec{R}_j) \quad (7.3)$$

This formulation has the advantage that the δ_j can be represented graphically and abnormal contributions (δ-rays, bad extrapolations, badly reconstructed tracks) can be identified and removed.

This alignment estimator was studied (figure 7.4) for three different geometries. First of all, the alignment procedure was applied over the nominal geometry, which does not include any alignment information. In a second phase, the alignment was applied over the photogrammetry geometry calculated in chapter 6 and the results were used to produce a new track-based geometry. Finally the algorithm was applied over the new track-based geometry. Table 7.1 shows the mean value of the distributions for the three cases. The algorithm measures displacements of the order of almost 1 mm in the nominal geometry. Once the photogrammetry based geometry is considered, displacements go to the level of 200 μm. If these displacements are applied, the mean of the distributions is below 100 μm.

The calculated constants were introduced in alignment records and used in the first physics analysis of CMS, regarding the distribution of negative and positive muons. This analysis, including a discussion about the alignment was published under the name *Measurement of the muon cosmic charge ratio in the CMS detector*, and can be found at [103].

7.4 Application to the CSA06 exercise

The software tools, the computing infrastructure and the algorithms described in the previous sections, were tested during the Computing, Software and Analysis challenge of 2006 (CSA06, see appendix B) with different samples. Most of the tests were done with 2 million proton-proton simulated collisions, in which a Z^0 was produced and forced to decay to muon pairs. A simplified version of the MBAA standalone alignment algorithm was applied considering only the displacement in the more sensitive coordinate (rϕ). External constraints from photogrammetry were mimicked to avoid the problem of weak modes.

In order to quantify the impact of the inclusion of constraints in the algorithm, several Monte Carlo simulations were performed. In these studies, the algorithm was run using the same set of tracks and over the same alignment scenario (the Short Term scenario, see

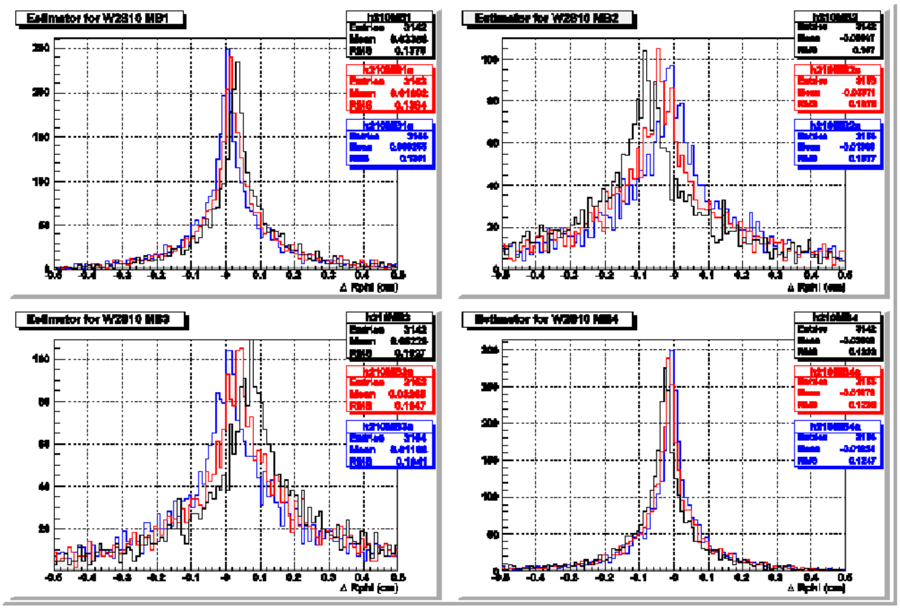

Figure 7.4: Alignment estimator for the 4 stations of wheel +2 and three different geometries (nominal, photogrammetry and track based). The averages of the distribution show a progressive improvement.

Station	Geometry	δ_x/mm
1	Nominal	0.3
1	Photogrammetry	0.19
1	Track-based	0.03
2	Nominal	-0.9
2	Photogrammetry	-0.4
2	Track-based	-0.13
3	Nominal	0.8
3	Photogrammetry	0.3
3	Track-based	0.1
4	Nominal	-0.3
4	Photogrammetry	-0.2
4	Track-based	-0.01

Table 7.1: Mean of the alignment estimator for the 4 stations and the 3 considered geometries.

chapter 5), but with different constraints, depending on the simulated precision. The achieved precision was quantified using the RMS of the differences between the calculated constants and the initial Monte Carlo misalignments. Figure 7.5 shows the achieved precision as a function of the precision of the photogrammetry constraints. The red line represents the spread of the Short Term scenario, and the green line is the spread of the solution achieved by the track-based algorithm without using external constraints. It is worth noting that the track-based when no constraints are applied does not improve significantly the geometry. Despite reducing the track residuals to the few 100 μm level, the weak modes avoid a precise measurement of the true positions. The track-based only solution cannot improve further the alignment because of the weak modes. On the other hand, the blue line represents the spread associated to the photogrammetry scenarios, which is by construction very close to the y=x straight line. Finally the black line represents the results of the track-based algorithm when the photogrammetry constraints are applied. It can be seen that even for a poorly precise constraint scenario, the performance of this algorithm is much better. The constraints provide a reference to the track based algorithm improving significantly the quality of the alignment.

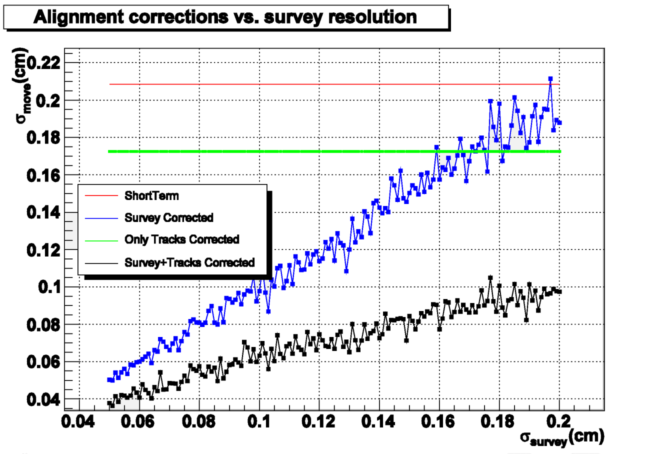

Figure 7.5: Alignment resolution achieved as a function of the resolution of the photogrammetry constraint.

This Monte Carlo study justified the use of photogrammetry constraints in the standalone MBAA algorithm. In order to produce a corrected geometry for the CSA06 exercise, a realistic constraint scenario with spread equal to 1 mm (see chapter 6) was used. This geometry was stored in a CMSSW standard database and a new reconstruction based on it was performed. The quality of the alignment was checked through the invariant Z^0 mass distribution. Figure 7.6 shows the distribution of the Z^0 mass for the nominal geometry, for the scenario geometry and for the geometry calculated with the standalone MBAA algorithm. For the nominal geometry the mean of the distribution was 94.11 GeV, with a spread of 20.51 GeV. When the misalignment scenario was introduced, the mean moved to 94.66 GeV, while the spread was degraded to 22.8 GeV. After correcting the misalignment scenario, the mean of the mass distribution recovered the nominal values, with a mean of 94.1 GeV and a spread of 20.59 GeV.

7.5 Application to the CSA08 exercise

The standalone MBAA algorithm was tested as well during the Computing, Software and Analysis challenge in 2008 (CSA08). This exercise was designed to emulate the first days of data taking (see appendix B for a detailed description). The produced Monte Carlo samples were composed mainly by minimum bias events. This was specially relevant for the standalone MBAA algorithm, because of the low P_T spectrum associated to this kind of events. Due to the energy loss most of the muons produced in these events were not able to reach the last stations of the muon system, resulting in a very limited statistics. Nevertheless, the scope of this exercise was more focused in the testing of the workflows, than in the performance of the algorithms themselves, that were already tested in previous exercises.

The CSA08 was divided in two independent cycles, according to the different luminosity and bunch configurations (see appendix B for details). They were called the S43 and S156

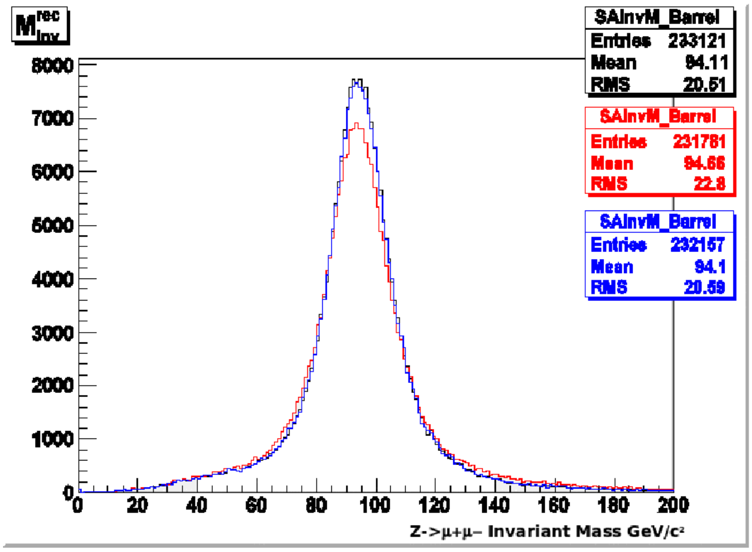

Figure 7.6: Di-muon invariant mass for muons contained in the region $|\eta| < 1.04$ (barrel), for the nominal geometry (black), using a simplified scenario (red) and after applying the corrections measured by the muon alignment algorithm (blue)

cycles. From the point of view of the muon alignment, the samples were reconstructed over the alignment scenarios detailed in chapter 5 of this thesis. In both cycles the full degree of complexity required for startup was considered. Workflows were carried out in real-time as needed in data taking mode: for both the S43 and S156 datasets, the target was to test the alignment and calibration infrastructure of CMS to obtain a complete set of calibration and alignment constants, to validate those constants and upload them to the conditions database ready for re-reconstruction within 1 week of the prompt reconstruction. The standalone MBAA algorithm successfully accomplished all these requirements.

The particular configuration for the algorithm was the following:

- Only three alignment parameters per chamber were measured for the CSA08, the local x, the local y and the local ϕ_y. Since the number of good tracks was small, it was decided to reduce the dimension of the problem, trying to align only the most critical alignment parameters.

- A set of photogrammetry measurements was mimicked for each scenario, in order to emulate the photogrammetry constraints. The photogrammetry scenario for the S43 exercise was optimistic and based in the accuracy observed for the real photogrammetry measurements (see chapter 6). On the contrary, the photogrammetry scenario for the S156 exercise was pessimistic and only provided the mechanical accuracy guaranteed by the closing procedure.

- The usual selection criteria are applied: the track must contain a segment in all the stations, and the derivatives, and residuals must be within their assigned acceptance region.

The number of good tracks is a crucial parameter for the standalone MBAA algorithm (and in general for every alignment with tracks algorithm) as the resolution of the algorithm (without taking into account systematic effects) scales with it as $1/\sqrt{N}$. This was not a problem in the previous exercises because there were enough good tracks, but it was not the case in the CSA08. For that reason an exhaustive analysis concerning the fraction of accepted tracks was performed for both the S43 and S156 exercises. A summary of the results is shown in table 7.2. The conclusions extracted were:

- The number of available good tracks was a very small fraction of the total. This determined the global performance of the algorithm as it is shown below.
- The main problem was related to standalone tracks that did not cross all the stations. This effect was expected provided most of the muons had a transverse momentum well below 10 GeV.
- A significant improvement in the acceptance of the residuals was observed in the S156 cycle and with respect to the S43. This effect was found to be related to the improvement in the DT calibration scenario used for both cycles. The set of calibration constants used in the S43 cycle was too pessimistic and produced a large amount of segments where the θ projection was not correctly estimated. These segments were not used by the algorithm. This effect was corrected in the S156 cycle, with a more realistic calibration scenario.

Cycle	Ev.	End.	No4Seg	No4Cham	BadR	BadD	Good
S43	970475	47.1%	36.2%	4.2%	46.8%	3.9%	2.0%
S156	3498228	46.4%	32.8&	4.0%	2.0%	5.0%	9.0%

Table 7.2: Summary of efficiencies for the standalone tracks analyzed by the standalone MBAA algorithm. The column labels stand for the cycle, the number of events (Ev.), the number of tracks crossing the endcap (End.), the number of tracks with less than 4 segments (No4Seg) or not hitting 4 different chambers (No4Cham), the number of tracks not passing the residuals cut (BadR), or the cut in the derivatives (BadD) and finally the number of good tracks.

As a consequence of the small number of good tracks, the expected errors for the alignment constants calculated by the algorithm were large. For this reason it was decided not to use the photogrammetry constraints, as their corresponding errors were expected to be lower than those of the tracks itself, and the target of the exercise was to test the track-based alignment component. A pseudo-inverse matrix was calculated for the MBAA liner system of equations, and a solution was calculated fixing the weak modes to 0.

In the S43 exercise, the number of good tracks available to perform the analysis was so small (less than 100 in many of the chambers) that the alignment precision was much higher than the magnitude of the misalignments of the scenario. The number of tracks in the S156 exercise increased almost by a factor 10 with respect to the S43. Even if the achieved precision was still bad, a good correlation between the measured alignment parameters and the Monte Carlo values was found. This is shown in figure 7.7. Chambers showing the largest deviations with respect to the MC truth have been identified as those containing a smaller number of tracks due to non-favorable track paths. The difference between measurements and MC truth is of about 1 mm and almost 0.7 mm once the low occupancy chambers are removed. These results were completely understood within the expected alignment precisions of the algorithm (for the available number of tracks). On the other hand, the CSA08 emphasized

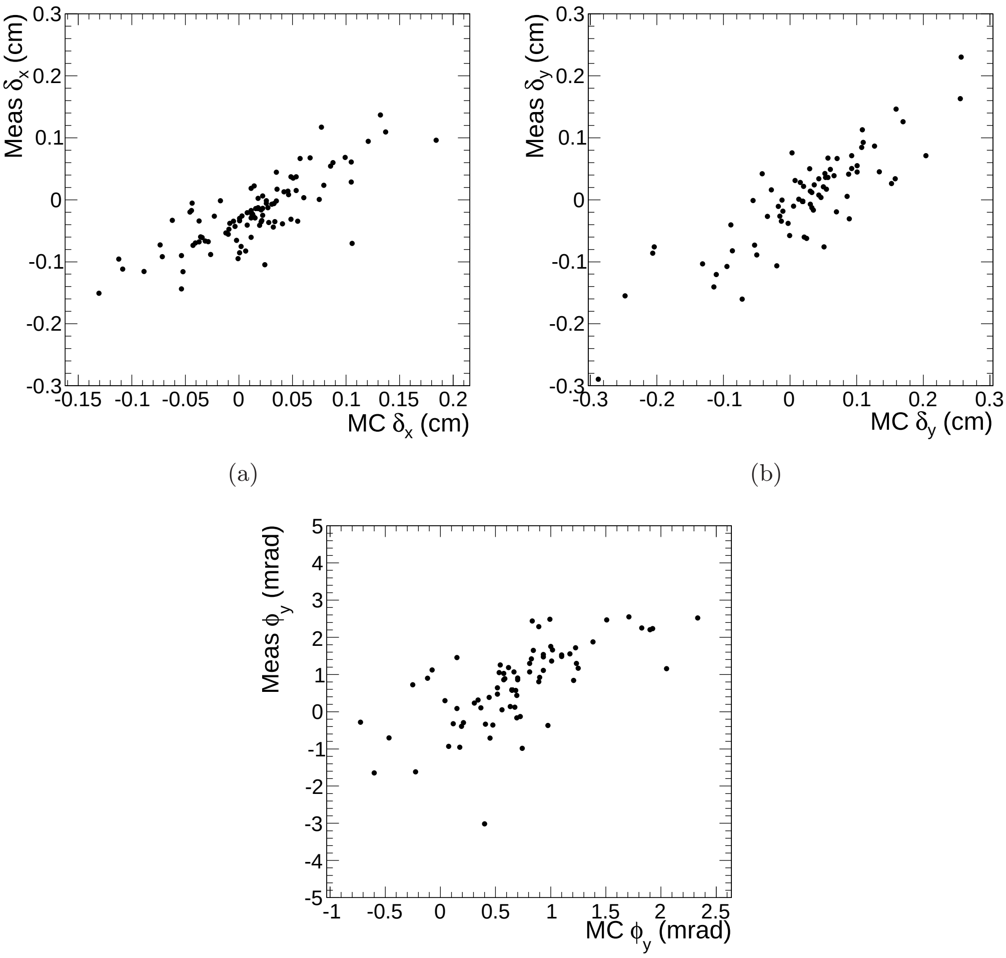

(c)

Figure 7.7: Comparison of the Monte Carlo and measured alignment parameters for the S156 exercise and for the local x coordinate 7.7(a), the local y 7.7(b) and the local ϕ_y 7.7(c).

the computational aspects of the workflows more than the performance of the algorithms. From this point of view the algorithm was declared as a success [76].

Chapter 8

Alignment of the barrel muon system with respect to the central tracker

The standard CMS muon reconstruction (global reconstruction) combines information from both the central silicon tracker and the muon system. This is the basis of an alternative alignment algorithm for the muon system which is able to align the muon chambers using the central silicon tracker as a reference. In addition to the relative alignment of the chambers, this algorithm aligns as well the chambers with respect to the tracker, correcting for the large degradations observed in the momentum resolution when relative misalignments between both subsystems were applied (see chapter 5). This algorithm has the advantage of not being affected by weak modes, although any distortion of the tracker is propagated to the muon system.

This chapter provides a description of the algorithm, and the specific features of its application to the cosmic run CRAFT08 (see appendix B). Results and validation plots are provided at the end of the chapter.

8.1 The global MBAA algorithm

The general MBAA algorithm was described in detail in chapter 3 and it is based in the minimization of the χ^2 described in 3.27, in which the residuals have been modelled as a function of both track and alignment parameters.

The global MBAA algorithm is a particular case of this algorithm, in which the track parameters are assumed to be perfectly determined by an external system (in this case, the silicon tracker). This condition is expressed mathematically as $\vec{\Delta p} = 0$, which yields to a new χ^2 where the contribution depending on track parameters is not present.

$$\chi^2 = \sum_j (\mathbf{R_j} - \mathbf{A_j}\vec{\delta})^T \mathbf{E_j} (\mathbf{R_j} - \mathbf{A_j}\vec{\delta}) \tag{8.1}$$

The first important consequence of this constraint is that intrinsic weak modes disappear, as the track parameters are determined externally and do not overlap with the alignment parameters. The linear system associated to the solution of the χ^2 is always regular and the solution is given by the expression:

$$\vec{\delta} = (\sum_j (\mathbf{A_j}^T \mathbf{E_j} \mathbf{A_j})^{-1} \sum_j \mathbf{A_j}^T \mathbf{E_j} \vec{R}_j \tag{8.2}$$

The second important consequence is related to the correlations among the chambers. The full MBAA algorithm refits track parameters in order to get a better estimation adapted to the measured misalignments. This introduces correlations among the chambers, and gives place to a single huge linear system. The tracker information could be included in the general MBAA method, by increasing the dimension of the problem. Nevertheless in the global MBAA algorithm, this is simplified assuming that the track estimation given by the tracker is perfect. This approach totally uncorrelates the different muon chambers, in such a way, that the associated linear system can be factorized in independent blocks corresponding to the chambers. In this sense, each of the chambers is aligned individually with respect to the tracker. The complexity of the problem is then reduced from a unique system of dimension ˜3000x3000, to 250 systems of dimension 6x6, that are better conditioned, and in general, easier to control. Nevertheless, this approach has the drawback that any bias in the tracker track (because of tracker misalignments or miscalibration) is amplified and propagated to the muon system. For instance, a bias of 100 μrads in the direction of the tracker track, provokes approximately a bias in the rϕ position measurement of about 300 μm, 400 μm, 500 μm, and 600 μm respectively for stations 1 to 4.

8.2 Application of the algorithm to the drift tube chambers

The global MBAA algorithm was used to align drift tube chambers with respect to the central silicon tracker. Tracker tracks were propagated into the muon system and residuals were defined as the difference between the extrapolated track and the real hits in the chambers. The covariance matrix of the residuals is calculated combining the error associated to the segment and the error associated to the extrapolation.

Quality criteria are applied over the tracks, to select those more suitable for alignment purposes. This selection was based in global parameters, such as track parameters, and in local parameters, such as the residuals themselves.

Calculation of residuals

Residuals were calculated by refitting global tracks without taking into account the muon chamber information (the error in the muon chambers is artificially set to a very large number). In this way, track parameters are calculated uniquely by the tracker. The track is then extrapolated to the surfaces of the muon chambers and compared with their corresponding hits.

The global MBAA algorithm took the drift tube chamber as the minimum alignable unit. This was motivated by the high correlation among the hits of a single chamber. To avoid this problem, hits were grouped in segments, exactly as it was done for the standalone MBAA algorithm in the previous chapter.

Calculation of the covariance matrix

Matrix E in equation 8.2 is the inverse of the covariance matrix associated to the residuals $\vec{R_j} = (\Delta x, \Delta\frac{dx}{dz}, \Delta y, \Delta\frac{dy}{dz})$. As explained above, residuals are calculated as the difference between the segment in the drift tube chamber, and the segment calculated from the intersections of the extrapolated track with the layers. The covariance matrix has two components, the covariance associated to the measured segment, and the component related to the extrapolated segment $C = C_{meas} + C_{ext}$.

Selection of tracks

Initial selection is performed over global parameters of the tracks. The most important are related to the transverse momentum of the muons, to the number of hits contained in the track, and its normalized χ^2, to ensure a good quality of the tracker tracks used in the calculation.

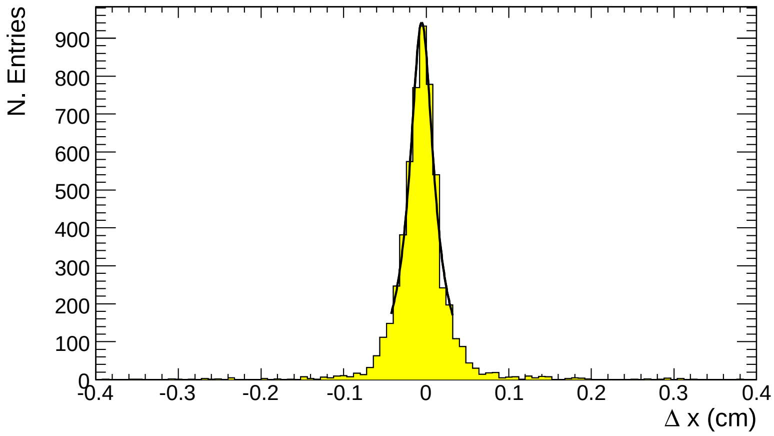

Figure 8.1: Δx distribution fitted by a Lorentz function.

The second selection is performed over the residual distributions in order to reduce the impact of unmodeled tails. Residuals are fitted using a Lorentz function, as it is shown in the central part of figure 8.1. An acceptance window is defined in terms of multiples of the Γ of the fitted Lorentz function.

8.3 Software implementation

The global MBAA algorithm is included in the *MuonAlignmentAlgorithms* package of CMSSW, and it is fully integrated into the CMSSW alignment framework. In this sense, the algorithm inherits from the more general *AlignmentAlgorithm* class, and it is centrally invoked from the common *AlignmentProducer* in CMSSW. The input to the algorithm is a *TrajToTrackAssociationMap* object which contains a collection of refitted tracks and trajectories. Then the algorithm takes pairs of measured and predicted hits in the muon system, groups them in blocks corresponding to individual chambers, and produces the 4D segments and the residuals. All the relevant information is stored in root N-Tuples for further processing. As the track refitting is the most CPU-consuming part of the algorithm, it is usually divided in several hundreds of jobs.

Once the N-Tuples are generated and properly stored, the algorithm is run again in a different working mode. In this case, the information of the N-Tuples is read, tracks useful for alignment are selected, and matrices $\mathbf{A_j}$, $\mathbf{E_j}$ and $\mathbf{R_j}$ are built and accumulated in order to calculate the solution vector in equation 8.2. The solution vector containing the alignment corrections is converted in a geometry database using the standard tools. The complete workflow is shown schematically in figure 8.2.

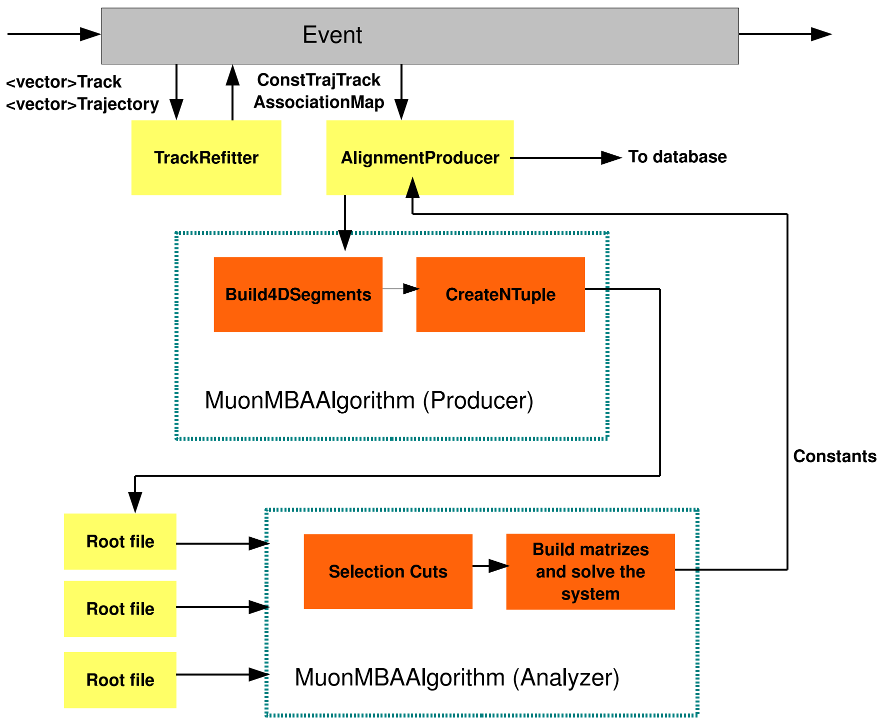

Figure 8.2: Worflow associated to the Global MBAA algorithm.

8.4 Application of the algorithm to CRAFT data

A simplified version of this algorithm was firstly applied over Monte Carlo data and the results were published in the Physics Technical Design Report [21]. Figure 8.3 shows the residual distribution in the rϕ coordinate before and after the alignment. Nevertheless, this work is focused in the recent implementations and their application to the Cosmic Run at Four Tesla 2008 (CRAFT08, see appendix B and [81]).

These samples of cosmic muons provided the opportunity to apply the global MBAA algorithm to real data, with the aim of producing a corrected geometry, to improve the quality of the first CMS physics analysis as the measurement of the cosmic muon charge ratio (CMS note in preparation).

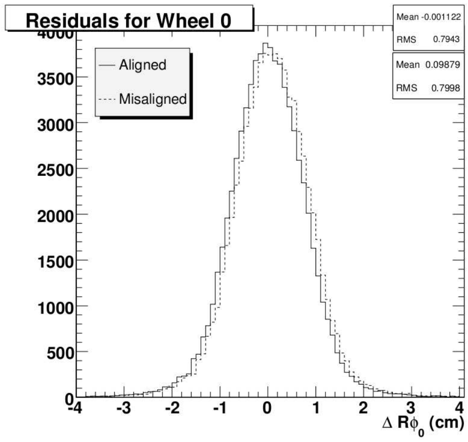

Figure 8.3: Residual distribution for the rϕ coordinate before and after the alignment. Figure extracted from the analysis prepared for the Physics Technical Design Report.

Cosmic muons cross the detector with a predominant vertical orientation with a $cos^2(\theta)$ dependence being θ the angle with respect to the vertical. This, together with the fact that the global MBAA method requires global tracks (reconstructed in both the tracker and the muon system) leaves very limited statistics in some of the muon chambers. This is the case for the external wheels YB+2 and YB-2 and for the vertical sectors in all the wheels (1 and 7). As not enough global tracks were collected for the chambers in these regions of the muon system, they were not included in the alignment (appendix E shows a detailed description of the chambers that were aligned during CRAFT08).

During this commissioning phase, the global MBAA algorithm was affected by a very relevant systematic error associated to the lack of knowledge of the magnetic field. In a perfect helix parameterization, the rϕ coordinate (local x) of the track depends as $x \propto \frac{qB}{p_T}$ with the magnetic field and the momentum. If the extrapolation is performed with a different magnetic field B', then the residual is given by $\Delta x = x - x_{ext} \propto \frac{q\Delta B}{p_T}$. In trajectories inside an inhomogeneous magnetic field, the quantity to be considered is not ΔB, but the difference between the integrated magnetic fields $\int \vec{B}\vec{dl}$ along the trajectory path. In any case the linear dependence of the residuals with q/p$_T$ is maintained.

This behavior was observed (see figure 8.4) in CRAFT08 data. Residuals showed differences of the order of 1 cm for low momentum, different charged muons. These studies were one of the first indications of the wrong field mapping that was readjusted using local propagation studies [111].

A procedure was derived to minimize the effect of this systematic error in the alignment: the observables were separated in bins of q/p$_T$, a linear fit was performed and the estimation given for q/p$_T$=0 (which corresponds to the limit of infinite momentum or straight track, insensitive to the momentum) was taken as the correct value (see 8.4). With this procedure the systematic error was reduced from almost 1 cm to the 1 mm level. At a second stage of the analysis, the field mapping was corrected and this dependence was negligible, hence the procedure was not longer applied. To reduce the impact of this and other sources of systematic errors, several quality selection criteria were applied. Scattering effects (with the

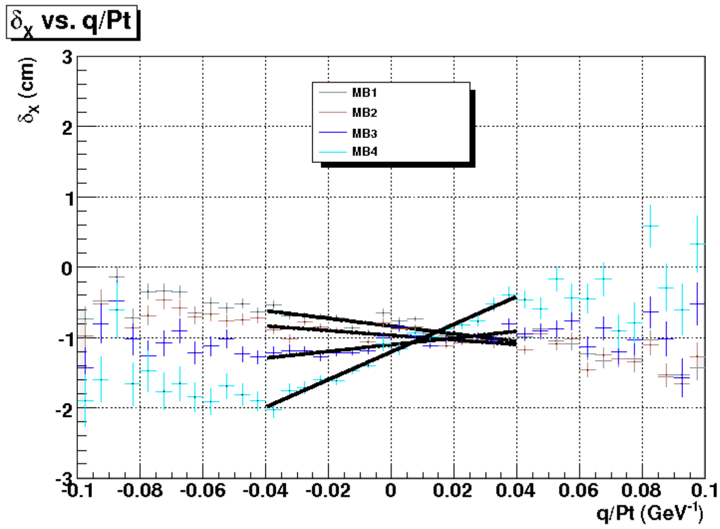

Figure 8.4: Δx residual as a function of q/p$_T$ for the four stations of a sector.

exception of δ ray production, and showering), and the magnetic bias decrease with the muon momentum. Selecting tracks with P$_T$ > 100 GeV these systematics are made negligible for the scope of this analysis. In addition, only tracks with P$_T$ < 200 GeV are considered. The reasons is that those high momentum tracks will be used as an independent sample for validation purposes.

The global MBAA algorithm used the tracker as a reference, and therefore the quality of the tracker tracks was important for the performance of the algorithm. In particular, tracks were required to have at least 15 hits, and a normalized $\chi^2/ndof$ lower than 10. To reduce the impact of the misalignments of the tracker, the MBAA algorithm is always run after the latest tracker geometry that has been released (for instance differences of the order of 1 mm where found in muon geometries calculated with the first and second CRAFT tracker geometries). The endcaps of the tracker (TEC and TID) were not aligned because the number of horizontal cosmic muons was small [41]. For this reason, tracker tracks containing hits in the TEC or the TID were rejected.

The latest T0 and TTrig calibrations of the drift tube chambers were used to run the global MBAA algorithm. In addition, the algorithm was run over the internal alignment of the chambers, described in chapter 5, and the photogrammetry-based geometry described in chapter 6.

The acceptance region for the residual distributions in order to reduce the impact of unmodeled tails, was twice the Γ associated to the Lorentz function used to fit them. A factor 2 was chosen as a best compromise between the resolution of the alignment parameter δ_x affected by the tails when the acceptance window is very wide, and δ_z, whom resolution deteriorates when the acceptance windows is very narrow.

The input to the algorithm was the AlCaReco stream called *MuAlGlobalCosmics AlCaReco* (see appendix A for more information), produced centrally at the Tier-0. The algorithm run on the CAF, and the produced geometry was stored in the databases. A process of validation of the geometry will be shown in the following sections.

8.4.1 Intrinsic resolution of the algorithm. Results on Monte Carlo samples.

The global MBAA algorithm was applied as well, to a Monte-Carlo sample. In that case, the value of the misalignments is known, and the intrinsic resolution of the algorithm can be calculated. As the algorithm was firstly applied over a sample of cosmic muons, a cosmic muon Monte Carlo sample was used for this study, trying to resemble as much as possible the conditions in which the algorithm run in the real data taking.

This cosmic muon Monte-Carlo sample was reconstructed using a totally random alignment scenario, with typical smearings of 4 mm and 4 mrad. The magnetic field and the tracker geometry were considered perfect, and their design values were used, in such a way, that no magnetic field, nor tracker misalignment biases are expected. The same quality selection of tracks than the used with real data was chosen for this exercise.

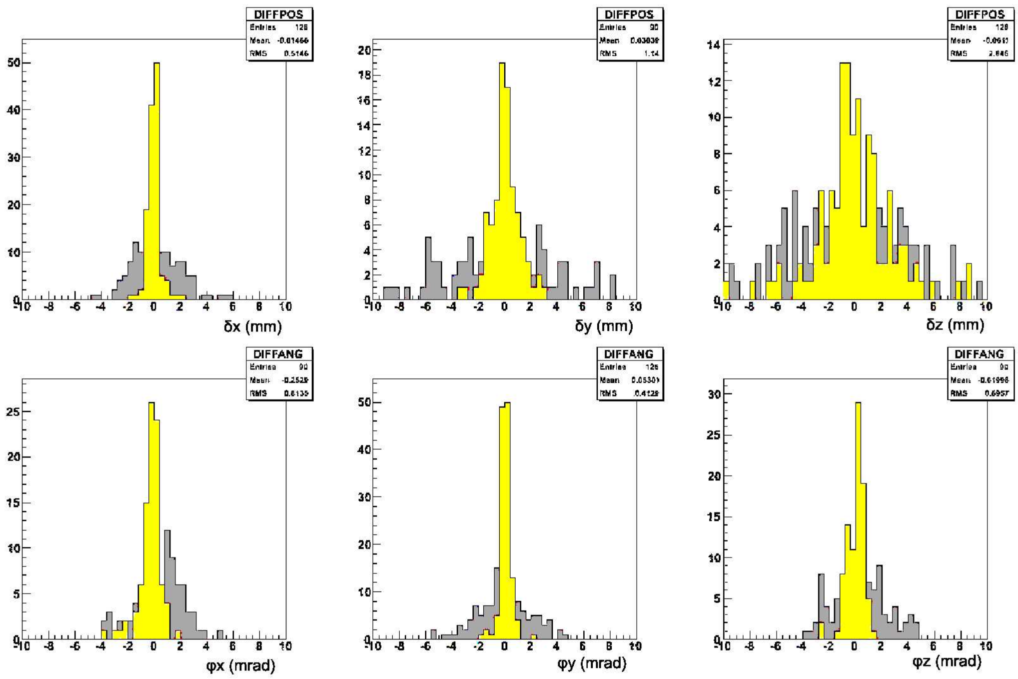

Figure 8.5: Misalignments with respect to the nominal geometry for the scenario before the alignment (grey) and after the alignment (yellow).

Figure 8.5 shows the difference between the real Monte-Carlo misalignment and the value measured by the algorithm. Table 8.1 shows the RMS of the distributions. The two most important alignment parameters δ_x and ϕ_y are measured with an intrinsic resolution of 500 μm and 400 μrad respectively. The δ_y parameter is less precisely measured, because of the worse resolution of drift tube chambers on that coordinate. It can be appreciated that the measurement of the δ_z is poor, induced by the quality selection performed over the residual distributions of the positions. Radial misalignments interact with the translational residuals through the slopes of the segments ($\frac{dx}{dz}$, $\frac{dy}{dz}$). If the angular distribution of tracks is wide, the spread of the translational residual distributions is wide as well. Selecting tracks very close to

	δ_x/mm	δ_y/mm	δ_z/mm	ϕ_x/mrad	ϕ_y/mrad	ϕ_z/mrad
RMS	0.5	1.1	2.8	0.8	0.4	0.7

Table 8.1: RMS of the difference between the Monte Carlo alignment parameters and the calculated alignment parameters.

the peak of the residual distribution deteriorates the measurement of δ_z. Nevertheless, if the acceptance window is opened, the tails of the distribution enter in the calculation producing instabilities in the fit, specially in the translational position. In general is preferable to ensure the good measurement of the $r\phi$ coordinate, than the δ_z, whose impact in the reconstruction is not so important.

8.4.2 Validation: Segment to Segment extrapolation

The segment-to-segment extrapolation method was used to validate the geometry produced by the algorithm. As it was explained in chapter 6, the resolution of this method (considering the intrinsic resolution of the drift tube chambers, and the errors coming from the extrapolation) is of about 700 μm in $r\phi$ and 1 mrad in ϕ.

Figures in 8.6 and 8.7 show for each chamber the estimate of its position and orientation given by the mean of all the track residuals in that chamber, using the nominal geometry and the track-based aligned geometry. Table 8.2 shows the width of these distributions of means for both geometries. The RMS of the mean of the distributions is only slightly larger than the resolution of the Segment-To-Segment extrapolation method, which implies an alignment resolution better than 700 μm and 1 mrad.

	Aligned	Not Aligned
	RMS MRD x/mm	RMS MRD x/mm
MB12	0.8	1.9
MB23	0.8	2.2
MB34	0.9	2.3
	RMS MRD $\frac{dx}{dz}$/mrad	RMS MRD $\frac{dx}{dz}$/mrad
MB12	0.8	1.7
MB23	0.8	1.5
MB34	0.7	1.7

Table 8.2: RMS of the Mean of the Residual Distribution (MRD) for both coordinates translational and directional and for both geometries: design and photogrammetry (aligned).

8.4.3 Validation: Split tracks momentum measurement

The performance of the global reconstruction was extensively studied as part of the commissioning program of CMS during CRAFT. The momentum resolution is one of the most interesting parameters as it is the magnitude which measures the quality of the momentum measurement. A method to estimate the momentum resolution of the CMS detector was proposed by the muon group, and applied over CRAFT data. This method benefits from the fact that most of the cosmic muons traverse both, the upper and the lower parts of CMS. This provides the possibility to reconstruct the cosmic muon as two different tracks (in the

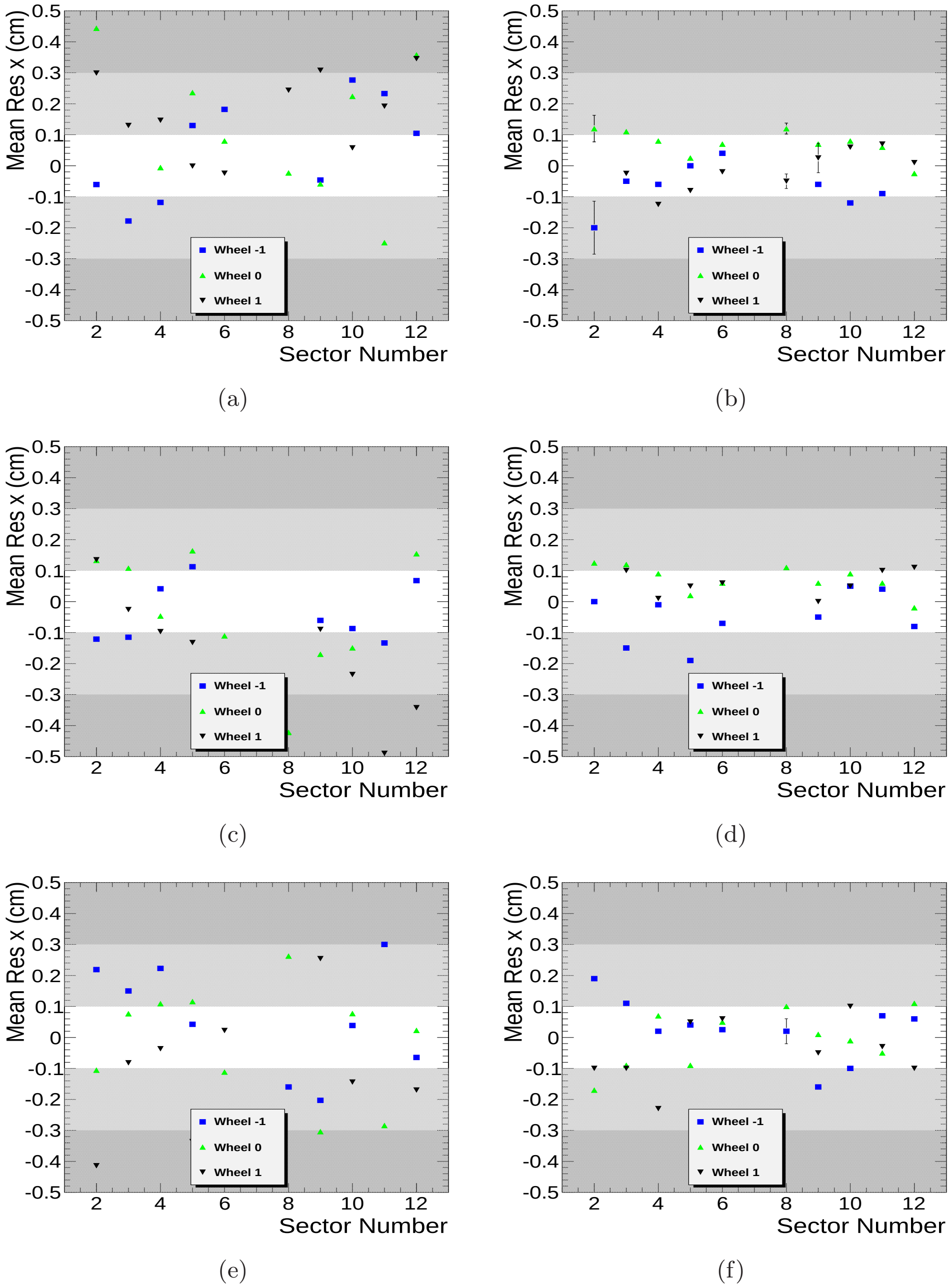

Figure 8.6: Mean of the residual in the local x position before (left column) and after (right column) the alignment, for stations 1 and 2, 2 and 3, and 3 and 4, respectively in each row.

regions $y < 0$ and $y > 0$). Each track has an independent estimation of the momentum of the muon. One of these estimations can be used as a reference and the momentum resolution is calculated as $(p_T^u - p_T^l)/p_T^l$.

This technique was called the split tracks momentum measurement, and was applied to different types of global reconstruction, using different conditions data of the detector. As it was shown in chapter 4, the momentum measurement is strongly affected by misalignments, and hence this technique was used as well to evaluate the quality of the alignment procedures.

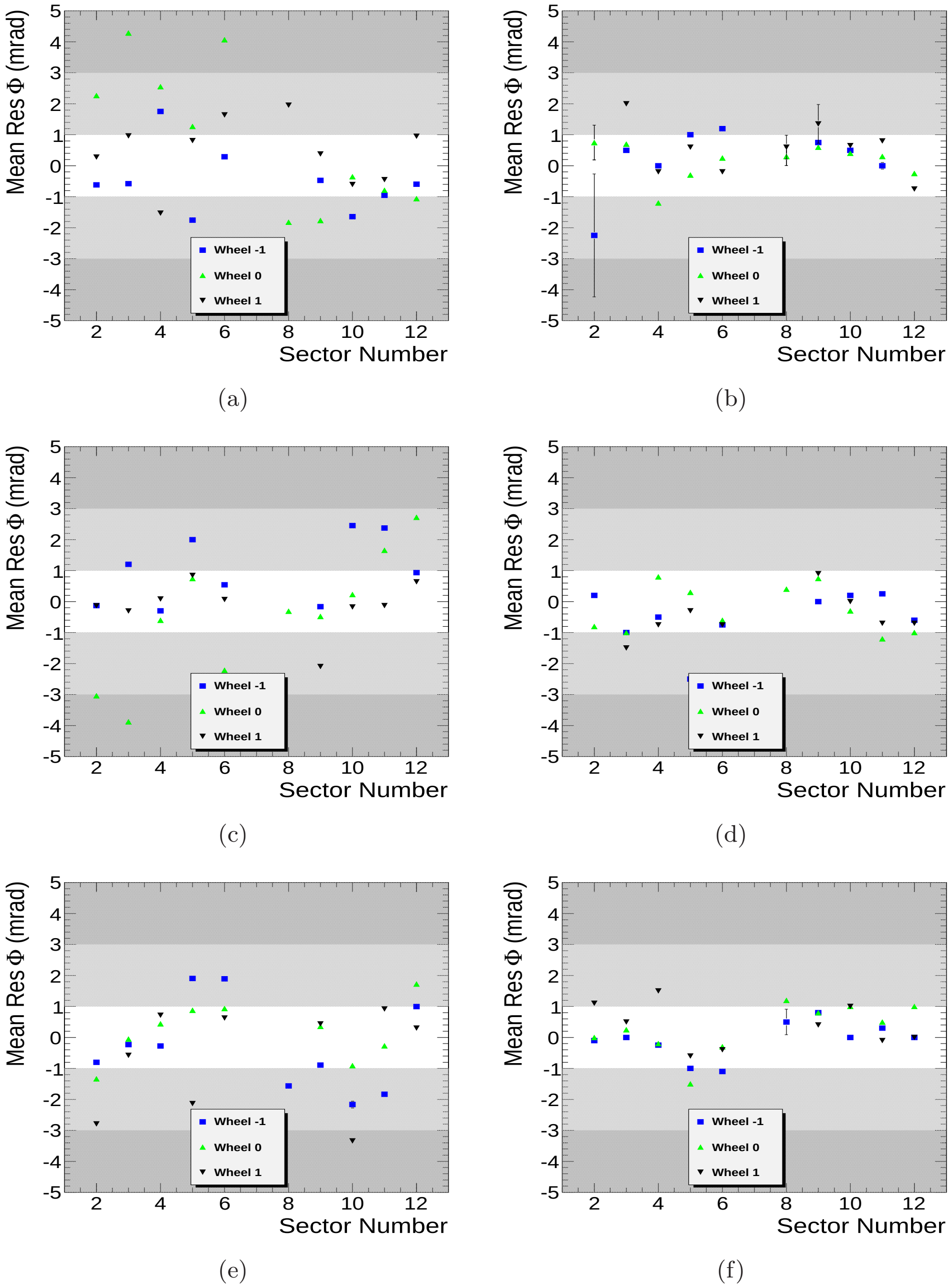

Figure 8.7: Mean of the residual in the local dx/dz direction before (left column) and after (right column) the alignment, for stations 1 and 2, 2 and 3, and 3 and 4, respectively in each row.

For this range of momentum, the momentum resolution of the global reconstruction depends mostly in the resolution of the tracker, the first station of muon chambers, and their relative alignment (in this range, the rest of stations are crucial for muon identification, but do not contribute significantly to the momentum measurement). A dedicated reconstruction was performed using only these two elements, the tracker and the first station of drift tube chambers. Figure 8.8 shows the estimated momentum resolution for the tracker-only recon-

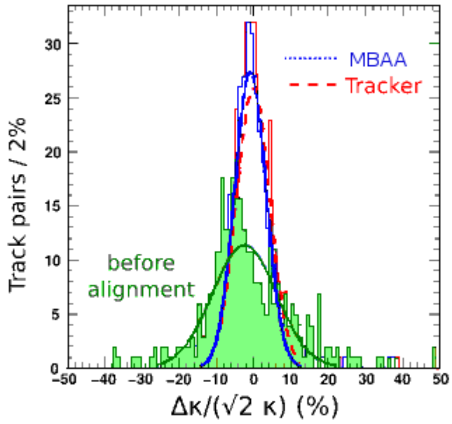

Figure 8.8: Fractional curvature resolution for tracks with $p_T > 200$ GeV. The curvature is related to the p_T through the formula $k = q/p_T$ and hence the fractional curvature is equivalent to the fractional momentum resolution.

struction (using the tracker exclusively), the momentum resolution using the tracker and the first station of DT chambers without the alignment, and finally the momentum resolution using the tracker and the first station of DT chambers after the alignment provided by the global MBAA algorithm. In table 8.3 the mean and spread of the histograms can be found. From those numbers, it can be concluded that after the inclusion of the alignment of the muon chambers, the momentum resolution was much better and to the level of the tracker reconstruction only (more details about this study can be found in [112]).

	Gaussian mean (%)	Gaussian RMS (%)
Before alignment	-2.5±0.6	8.6±0.5
Global MBAA	-0.9±0.2	4.2±0.2
Only Tracker	0.3±0.3	4.5±0.2

Table 8.3: Parameters for the fits in 8.8.

Chapter 9

Full muon alignment geometries

The ultimate goal of the muon alignment procedures is to provide an improved geometry description through the corresponding database records (*DTAlignmentRcd* and *CSCAlignmentRcd*), in order to be used by the reconstruction algorithms. Throughout this work, several algorithms and analysis regarding the alignment of the drift tube chambers were presented, without giving details of their interconnections, and the connections with other alignment workflows, as those of the optical alignment system.

The work of this thesis, in addition to the production of alignment constants for the muon drift tube system, as described in the previous chapters and utilized as official geometries of the CMS collaboration, consisted in the creation of the geometries, the population into the official databases, and the production and maintenance of documentation for the rest of the CMS users.

This chapter serves as a summary of the real geometries produced using the calculations explained along this work. In addition, the procedures used to combine the different components of the geometries, and to upload them to the official databases will be briefly described.

9.1 Produced barrel muon geometries

In order to produce full barrel muon geometries a connection between the internal and the global alignment of the chambers was needed. To this end, the software infrastructure described in chapter 3 was used to handle properly the *DTAlignmentRcd* records, in such a way that the internal alignment geometries (chapter 5) only changed the position of the layers and superlayers, while the remaining geometries (chapters 6, 7 and 8) changed exclusively the position of the drift tube chambers, propagating down the motions to their internal structure. To completely disentangle the internal and global alignments, the internal geometries were always constructed through a set of Lagrangian multipliers, that fixed the average misalignment of the layers to 0. In general, the procedure used to create a combined full muon geometry was divided in two steps: first, layers and superlayers were aligned according to the internal constants without changing the global position of the chambers, and second, the chambers were aligned according to the global constants, propagating down the motions to their internal structure.

In the case of the track-based algorithms explained in chapters 7 and 8, it is important to keep the consistency between both the internal and the global geometry. Even if the global track-based algorithms are intended for measuring the position of the chambers, they are sensible to the internal geometry. Different internal geometries distort the track-based algorithms producing different global geometries, and therefore, the algorithm must be run over the internal geometry that will be included in the final complete database.

The calculations carried out in this thesis were used to produce several barrel muon geometries, that were widely used for all the CMS collaboration. These geometries provided a complete description of the barrel, although connections with the optical alignment system are foreseen in the future (see following section). The geometries can be divided in three blocks:

- The combined internal-photogrammetry geometry developed with the MTCC information, that used the alignment constants calculated in chapters 5 (only the MBAA part), 6 and 7.
- The combined internal-photogrammetry geometry developed after the lowering of CMS to the pit, that used the alignment constants calculated in chapters 5 (only the MBAA part) and 6.
- The combined internal-global track based geometry developed with CRAFT information, that used the alignment constants calculated in chapters 5 (both MBAA and Superlayer-To-Superlayer information), and 8.

The first block of geometries were used in the physics and performance analysis carried out in the MTCC by the collaboration (see [74]). The second block of geometries was used during all the 2008 data taking (GRUMM [77] and CRUZET [78], and for the first LHC start-up. And finally, the third block of geometries was used all along the CRAFT08 analysis in the years 2008 and 2009.

Although the geometries can be divided in these three blocks, several versions of them were published. For instance, in the MTCC the combined internal-photogrammetry geometry, and the internal-photogrammetry-track-based geometry were deployed separately. There were as well two internal-photogrammetry geometries used at the pit. In the second one, all the chambers that were not aligned using the photogrammetry were filled following the procedure explained in chapter 6. Finally, in the geometries extracted from CRAFT there were several sets, intended for the different reprocessing of the samples. The differences among them were related to the internal alignment, that was updated to include the correction of the thickness of the chambers (see chapter 5), and to the different geometries produced by the global algorithms as long as the tracker geometry and the magnetic field description were improving.

9.2 Connection between track-based alignment, photogrammetry and the optical hardware alignment system

On top of the differences in the scope between the internal and global geometries, there are differences in the information sources of a given geometry. This is the case for example of the track-based, and quality control measurements in the case of the internal alignment, or the track-based algorithms and the photogrammetry measurements in the global alignment. In general track-based algorithms, photogrammetry and the optical alignment system are able to produce information about the same system, and procedures to combine them are needed in order to get the most accurate response.

The connection between the track-based algorithms and the photogrammetry (or quality control measurements) has been extensively treated along this document. Track-based algorithms allow to implement external constraints, which in fact are very useful to fix their weak modes. This was done to build the internal geometry of the drift tube chambers, and was implemented as well in the global alignment of the chambers in the MTCC. It is quite evident that the measurements of the optical alignment system can be treated in the same way, as external constraints in the track-based algorithms. In fact, it is possible to extract from COCOA the position, orientation and errors of the chambers, and introduced them in the fit, even taking into account the correlations. The advantage is that in this case the precision is much better than the photogrammetry and comparable to the track-based precision, producing a much better fixation of the weak modes.

The combination of track-based alignment algorithms and the optical system can be performed as well by implementing the track-based information as a constraint in the COCOA minimization (see chapter 3). Alternatively, it could happen that some of the alignment parameters are measured by the optical system, while others are measured using track-based. This was the case for example of the first geometry extracted from CRAFT data. In that occasion the global z measurement, very important because of the shifts due to the magnetic field, was provided by the optical system, while the rϕ plane was measured using track-based alignment algorithms.

9.3 Population of constants to the database and documentation

As it was described in chapter 2 the official databases of CMS are based in ORACLE technology. The access to them can be performed using a software interface integrated in CMSSW, POPCON access, or using dedicated tools (based on the POPCON tools) that allow the database access from local MySQL databases.

In the case of the muon alignment workflows, no specific software was developed, and the standard tools were used starting from a private MySQL database. In practice this was the best solution, provided the databases were firstly circulated privately for testing and validation.

The process of populating a database, required to login in one of the machines at the CMS environment (see chapter 3), with the private MySql geometry. At that point, two tools called *cmscond_iov_list* and *cmscond_iov_export*, where used to check, change and populate the different tags into the ORACLE records. The interval of validity was defined at this point when required.

Since the end of the year 2008, a security improvement was performed to the population mechanism. Individual access to the official databases was not allowed, and was centralized through the so called drop-box mechanism. This mechanism consist in a set of cron jobs that check periodically for new MySQL private files in a given repository. In this case, a text file has to be included with a specific format indicating the name of the tags, the IOV and the destination database.

Once a new record was introduced in the database it was documented in the alignment and calibration [113], and muon alignment [114] TWIKI pages, with a brief description of their content, in order to keep the CMS community informed.

Chapter 10

Conclusions

This thesis has been developed within the the context of the Compact Muon Solenoid experiment (CMS) at the Large Hadron Collider (LHC). In particular, this work is related to the process of alignment of the muon spectrometer of CMS, and more specifically to the alignment of the drift tube chambers which compose the barrel muon system of CMS. In this section, a compilation of the most significant achievements and results obtained are listed.

Development and maintenance of the muon alignment software infrastructure in CMSSW.
The alignment of the muon barrel system requires a software to permit the storage and handling of the alignment constants, in order to be properly incorporated into the reconstruction algorithms. Several contributions have been made in the development of this infrastructure, ranging from code implementation to testing and commissioning. Some of the most relevant aspects were:

- Development of the *MuonAlignment* package designed to manage the application of alignment corrections into the reconstruction and to generate muon misalignment scenarios. New functionalities were added to this package to allow out-of-the-hierarchy misalignments such as sector misalignments or global misalignments of the muon systems with respect to the central silicon tracker.

- Population of geometries into the CMS official database. Testing and commissioning of the drop-box mechanism responsible of the centralized treatment of alignment and calibration conditions in CMS.

- First testing and commissioning of the full software alignment chain with real data. During the Magnet Test and Cosmic Challenge, and for the first time, alignment constants were obtained, introduced into a standard CMSSW database, and used for a new reconstruction.

Development of misalignment scenarios for MonteCarlo simulation.
In order to study the impact of misalignments in the performance of the reconstruction of CMS, several fake misaligned geometries were deployed. Part of this thesis includes the design, implementation and validation of these geometries (usually called misalignment scenarios). The misalignment scenarios were uploaded into the official databases of CMS and were widely used by the collaboration in the major simulation and computing campaigns of CMS:

- Computing, Software and Analysis challenge in 2006 (CSA06). Three scenarios were produced: the *SurveyOnly*, *ShortTerm* and *LongTerm* scenarios. The first one assumed very poor alignment information, coming mainly from photogrammetry measurements. The second scenario incorporated the expected precision from very preliminary results from the optical system and track-based algorithms corresponding to the first data taking of the detector. Finally, the third scenario provided a picture of the alignment status of the muon spectrometer after long operation of the alignment systems.

- Computing, Software and Analysis challenge in 2007 (CSA07). Two scenarios were produced: the 10 pb^{-1} and the 100 pb^{-1} scenario. The former was based in the previous *SurveyOnly* although some improvements were included from the experience acquired during the Magnet Test and Cosmic Challenge. The latter scenario was based in the *ShortTerm* scenario, but taking into account the expected improvements that optical and track-based algorithms would produce during the first 10 pb^{-1} of data taking. Misalignments of sectors and a global misalignment of the muon system with respect to the tracker were accounted for.

- Computing, Software and Analysis challenge in 2008 (CSA08). Two scenarios were produced: the *Startup* scenario and the 10 pb^{-1} scenario. The former incorporated the most updated knowledge about the expected alignment status of the detector for the start up of the LHC machine. This included the information acquired during the global cosmic runs and magnet tests. The latter scenario, constituted an improvement of the former, because of the expected results from the alignment systems.

- These scenarios confirmed a good performance of the trigger system for the startup of the LHC, although refinements were still required for a correct reconstruction of very high momentum tracks.

Development of the Modified Blobel Alignment Algorithm.
A track-based alignment algorithm (Modified Blobel Alignment Algorithm, MBAA) based in the ideas of V. Blobel was developed taking into account the particular requirements of the muon system of CMS. Its working principle consists in the minimization of the track reconstruction residuals against both the alignment and track parameters. Two major improvements to the method were developed:

- The method was extended to incorporate more general "hits" including not only position coordinates but also direction, as needed for some of the implementations in the muon system of CMS. This included a more general parameterization of the residuals as a function of the alignment parameters.

- Track-based algorithms are affected by weak modes, specific configurations of misalignments that leave the residuals invariant (for instance a coordinate shift of all the subdetectors by the same quantity cannot be observed using track-based alignment algorithms). This problem has been widely discussed and two solutions were proposed: the usage of constraints and the fixation of the weak modes through eigenvalue analysis and pseudo-inverse matrix calculations. The algorithm was finally implemented in CMSSW for different applications.

Internal Alignment of the Drift Tube chambers.
The MBAA algorithm was implemented and adapted to align the internal structure of the drift tube chambers. Three sources of information were used for this alignment: cosmic tracks as main input for the MBAA algorithm, and constrains from the quality control measurements

of the layers (from the construction sites) and the photogrammetry of the superlayers (from the ISR calibrations).

- The alignment of the individual layers was validated by comparing the position of the hits with the reconstructed segments. The spread of the deviations was larger than 100 μm before the corrections were applied, and was reduced to a few microns, after their application.

- The relative alignment of the superlayers was validated by comparing the segments in each superlayer with the extrapolation of the segment in the previous superlayer. The spread in the δ_x parameter was reduced from 400 μm to 100 μm, while the spread in the δ_z parameter improved from 500 μm to 200 μm.

The calculated internal geometry was uploaded into the databases of CMS and was used by all the collaboration as the official geometry, producing an improved performance of the reconstruction process.

Positioning of the DT chambers in the CMS frame using photogrammetry measurements.
A mathematical model was developed in order to transform the position of the photogrammetry targets distributed over the structures of CMS, into alignment parameters of the chambers. The procedure was performed firstly for the photogrammetry information taken at the surface of point 5, and repeated with the measurements taken at the pit. The major conclusions and results are the following:

- The position and orientation of the chambers was calculated and introduced into standard CMS alignment databases. Validation results based in the propagation of cosmic muon tracks showed an improvement in the relative positioning of the chambers from 2.2 mm before the alignment to 1 mm after the alignment in the rϕ coordinate.

- The shape of the alignment parameters was studied, observing that the wheels suffered a gravitational sag up to 1.2 cm (see details for the different wheels in chapter 6). The shape of the wheels, initially circular, was deformed to an elliptical-like shape due to the weight of the iron. This was in good agreement with the expectations from numerical calculations.

- The comparison of the results at the surface and at the pit showed a very good reproducibility (at the level of the expected errors) indicating that the process of lowering down the wheels did not provoke large misalignments, and providing strong confidence in the stability of the obtained results.

The obtained constants were uploaded to the CMS production database and used as a starting geometry for further analysis. It is important to remark, that this level of precision was found to be enough for the correct functioning of the trigger system, and for the reconstruction of not very high momentum tracks.

The MBAA standalone alignment algorithm.
An implementation of the MBAA algorithm was developed to align the drift tube chambers of CMS, independently of the central silicon tracker. Due to the large correlation among the hits in a same chamber, the algorithm was adapted to use segments, considering the chambers as rigid bodies. The most important results obtained with this algorithm were the following:

- Alignment of the chambers in the Magnet Test and Cosmic Challenge. During the MTCC a simplified version of the algorithm, that only considered the rϕ coordinate, was applied. The distribution of residuals reduced from 1 mm to the 100 μm level.
- Alignment exercise in the Computing, Software and Analysis challenge of 2006 (CSA06). The same version of the algorithm was run over a sample of proton-proton simulated collisions, in which a Z^0 was produced and forced to decay to muon pairs. The Z^0 invariant mass was used as a measurement of the quality of the alignment. The degradation observed in the spread of the Z^0 peak when the misalignment scenario was used to reconstruct the tracks, disappeared once the corrected geometry was introduced.
- Alignment exercise in the Computing, Software and Analysis challenge of 2008 (CSA08). For this simulation campaign, the algorithm was prepared to measure three coordinates: the local x, local y and ϕ_y. The CSA08 exercise was more focused in the commissioning and testing of the alignment workflows than in the testing of the alignment and calibration algorithms themselves. The workflow associated to the MBAA was declared as a success, being the alignment constants calculated and uploaded to the databases in the expected time-scale.

Alignment of the chambers with respect to the central silicon tracker. The MBAA algorithm was adapted to align the muon chambers with respect to the central silicon tracker. This algorithm assumed that the track parameters were perfectly determined by the tracker, and therefore are removed from the MBAA fit. In practice, tracker tracks were extrapolated into the muon system, resulting in a relative alignment of the muon chambers with respect to the tracker. The most interesting results obtained with this procedure are the following:

- This algorithm was applied to the cosmic muon tracks taken at the Cosmic Run At Four Tesla in 2008 (CRAFT08). In order to estimate the intrinsic resolution of the algorithm, it was also applied to a Monte-Carlo sample of cosmic muons under ideal conditions (except for the muon geometry). The two most important alignment parameters δ_x and ϕ_y were measured with an intrinsic resolution of 500 μm and 400 μrad respectively. The constants calculated with the real data were introduced into standard CMSSW databases.
- The corrected geometry was validated using local propagation of tracks between chambers. The validation observables had a spread comparable to the intrinsic resolution of the validation method, setting an upper limit to the alignment precision of 700 μm and 1 mrad respectively for the δ_x and ϕ_y coordinates.
- A second validation was performed through the usage of split tracks (cosmic tracks that cross the whole detector, but are reconstructed as two, one in the upper part and in one in the lower). Split tracks provide two independent estimates of the momentum of the same particle, allowing to calculate its resolution. The MBAA geometry produced an impressive improvement of this momentum resolution (from 8.6% to 4.2%). It is interesting to remark that before the implementation of these corrections, the inclusion of the muon system did not improve the tracker-only resolution.

In the work presented in this thesis, several software tools and algorithms related to the alignment of the muon system, were developed and utilized along the different commissioning phases of CMS. Alignment results were produced

at different levels and using different sources of information. Validation procedures were performed over the calculated geometries, ensuring the improvement produced in the performance of the reconstruction. Finally, these geometries were accepted and introduced in the official databases of the CMS collaboration, helping CMS to achieve its physics goals.

Chapter 11

Resumen

11.1 El Gran Colisionador de Hadrones y el Solenoide Compacto de Muones

El Gran Colisionador de Hadrones (LHC), situado en el CERN, el Laboratorio Europeo para Física de Partículas, en las afueras de la ciudad de Ginebra, constituye una herramienta única para la investigación fundamental y es, de hecho, el acelerador de partículas más potente jamás construido. El LHC será capaz de producir dos haces de protones, cada uno con una energía de 7 TeV ($\sqrt{s}$ =14 TeV) y una luminosidad nominal de 10^{32} cm^{-2}s^{-1}. El LHC permitirá explorar una escala de energía sin precedentes, conocida normalmente como la escala del TeV, con el objetivo de poner a prueba el Modelo Estándar de las partículas, o alternativamente, la búsqueda de nueva física. En particular, el LHC permitirá entender el fenómeno de la ruptura espontánea de simetría, a través del descubrimiento del bosón de Higgs, tal y como predice el Modelo Estándar, a través de otros modelos como la Supersimetría, o el Tecnicolor, o incluso algún mecanismo aún desconocido.

El Solenoide Compacto de Muones (CMS), es uno de los detectores de propósito general instalados en el LHC. El programa de física de CMS se centra en el estudio del fenómeno de ruptura de simetría, la búsqueda de nueva física, como resonancias de nuevos bosones masivos, Cromodinámica Cuántica y física del top, y medidas de precisión de la matriz CKM. Con esta finalidad, CMS fue diseñado según los siguientes criterios: una buena identificación de muones sobre un amplio rango de momento, buena resolución y eficiencia de reconstrucción para partículas con carga, buena resolución de energía electromagnética, de energía perdida ("missing E_T"), y en la medida de la masa de di-jets.

Con el objetivo de cumplir estas especificaciones, CMS fue dotado de un imán superconductor de gran potencia, que es capaz de producir un campo magnético muy fuerte y muy homogéneo en la zona central del detector, donde el detector central de trazas y los calorímetros están instalados. Dichos componentes están rodeados por discos y ruedas de hierro que permiten el retorno del flujo magnético. Un sistema de detección de muones de gran precisión se encuentra instalado en el interior del hierro de retorno del flujo. El sistema magnético de CMS está compuesto por una masa de material superconductor insertada en el interior de un tanque de vacío y rodeado por el hierro de retorno. El cuerpo de material superconductor tiene 13 m de longitud y 6 m de diámetro, y es capaz de producir un campo magnético en la zona central del detector de 3.8 Tesla.

El detector central de trazas de CMS es un detector muy preciso construido íntegramente por silicio, y con una longitud de 5.8 m y 2.4 m de diámetro. Dado el gran número de partículas producido en cada colisión, el detector de trazas dispone de una gran granularidad, para garantizar la correcta identificación de las trayectorias. La región más próxima al tubo del haz está compuesta por detectores basados en ”pixels” de silicio, con una alta granularidad, permitiendo así una medida muy precisa del parámetro de impacto, lo que se traduce en una buena resolución en la medida de vértices secundarios. El sistema de ”pixels” está compuesto por una región cilíndrica alrededor del tubo del haz, y dos tapas en los laterales. El detector de tiras o ”strips” se encuentra instalado alrededor del sistema de ”pixels”, y está dividido en dos partes diferentes: el detector de tiras interior, en la zona más próxima al sistema de ”pixels” y el detector de tiras exterior. Ambos disponen de una parte cilíndrica en forma de barril alrededor del tubo (Barril Interior Detector de Trazas (TIB) y Barril Exterior Detector de Trazas (TOB)) y de dos tapas en los laterales (Discos Interiores Detectores de Trazas (TID) y Tapas del Detector de Trazas (TEC)).

El calorímetro electromagnético de CMS (ECAL) se caracteriza por su hermeticidad y homogeneidad. Está compuesto por cristales de plomo y tungsteno y se encuentra instalado alrededor del detector de trazas. Este calorímetro se divide también en una región cilíndrica en forma de barril y en dos tapas que le sirven de cierre. Su diseño está determinado por los siguientes requerimientos: una alta granularidad, una buena resolución energética con una elevada velocidad de respuesta y alta resistencia a la radiación.

El calorímetro hadrónico de CMS (HCAL) se encuentra instalado alrededor del ECAL y está compuesto por capas de cobre intercaladas con material centelleador. Su estructura está dotada de una parte cilíndrica en forma de barril cerrada por dos tapas. El diseño del HCAL requiere alta hermiticidad y granularidad, una moderada resolución en la medida de la energía, y una profundidad suficiente para recoger las cascadas hadrónicas.

Los procesos físicos con desintegraciones leptónicas son normalmente muy limpios y por lo tanto muy útiles para identificar y reconocer un gran número de sucesos muy interesantes. Por esta razón, CMS fue dotado de un sistema de muones de gran precisión. Este sistema de muones se encuentra instalado en el interior del hierro de retorno magnético y se divide en un barril cilíndrico con dos tapas en los laterales. La zona barril contiene cámaras de deriva (DT), mientras que las tapas están instrumentadas con cámaras de tiras (CSC). Ambos subsistemas contienen también cáamaras de resistividad (RPC) con la finalidad de producir una respuesta muy rápida útil para el sistema de trigger de eventos. El sistema de muones tiene fundamentalmente tres objetivos: identificación de muones, medida de su momento y función como trigger.

El barril del sistema de muones de CMS está formado por 4 estaciones, dispuestas en cilindros concénctricos alrededor del tubo del haz, y divididos en 5 ruedas en la dirección del mismo. Las 3 primeras estaciones están compuestas por 60 cámaras de deriva, 12 por rueda, y distribuidas en sectores cubriendo todo el rango de ϕ. La estación 4, sin embargo, está formada por 70 cámaras, 14 por rueda, distribuidas igualmente en sectores cubriendo todo el rango de ϕ.

Las cámaras de deriva son detectores complejos, formados por varias capas de hilos. Estas capas se agrupan en bloques de 4, dando lugar a una supercapa. En las 3 primeras estaciones, existen 3 supercapas, las de los extremos tienen sus hilos paralelos al haz y están diseñadas para producir medidas en el plano rϕ. La supercapa del medio tiene sus hilos perpendiculares al haz, y está dedicada a la medida de la coordenada z. Las cámaras de deriva en la estación 4, sólo disponen 2 supercapas del tipo rϕ.

Cada uno de los hilos se encuentra en el interior de una célula de deriva, en el seno de una mezcla gaseosa. Aquellos muones que atraviesas la célula provocan una ionización del gas, y como consecuencia una corriente de electrones fluye hacia el hilo. El tiempo de deriva se mide como la diferencia entre el paso del muon (dado por el tiempo en que se produjo la colisión) y el tiempo de llegada de la señal al hilo. El gas utilizado tiene la propiedad de tener una velocidad de deriva constante, de tal manera que el tiempo de deriva puede convertirse fácilmente en información espacial. La resolución de una cámara de deriva, combinando todas las capas, es del orden de 100 micras para la proyección rϕ y 150 micras para la proyección z.

Las tapas del sistema de muones de CMS forman 4 discos, con varios anillos de cámaras de tiras cubriendo por completo el rango en ϕ y superpuestas las unas a las otras. Cada cámara se compone de 6 planos de hilos intercalados entre 7 paneles catodizados. Una avalancha producida en un hilo induce en los planos una distribución de carga cuya forma es bien conocida. Las cámaras están segmentadas de tal manera que permiten la medida de dos coordenadas por cada plano individual.

Las cámaras de resistividad están instaladas en ambas regiones del sistema de muones. Estas cámaras son detectores de gas y placas paralelas, que combinan una resolución espacial moderada con una resolución temporal comparable a los centelleadores. Están especialmente diseñadas para dar una respuesta muy rápida en sistemas de detección de trazas, sirviendo así como un trigger específico para el sistema de muones, complementando la alta precisión espacial dada por las cámaras DT y CSCs.

El LHC produce colisiones protón-protón con una elevada frecuencia. Aproximadamente 20 colisiones protón-protón tienen lugar por cada cruce de paquetes, que tiene lugar cada 25 ns. La gran cantidad de datos asociada con el alto número de eventos producidos no puede ser procesada y almacenada, siendo necesaria una reducción drástica. Esta tarea la realiza el sistema trigger, que es el comienzo de la selección de eventos de interés físico. El sistema trigger realiza su selección en dos pasos diferenciados, el sistema L1 basado en electrónica especialmente diseñada a tal efecto, y el sistema trigger de alto nivel (HLT) basado en software ejecutado sobre CPUs convencionales. Los factores de reducción son 10^6 and 10^2 respectivamente.

La transferencia, almacenamiento y procesado de los datos seleccionados están gestionado por la infraestructura de computación de CMS, que debe proporcionar: un "framework" de software, un sistema de bases de datos distribuido, un conjunto de servicios de computación con herramientas capaces de transferir, localizar y procesar grandes cantidades de datos, una serie de servicios Grid capaces de acceder a recursos de computación distribuidos, y finalmente acceso local a sistemas de almacenamiento y procesado de datos. CMS es capaz de satisfacer estos requerimientos a través de una estructura jerárquica de centros agrupados. Los datos recogidos por el detector son transferidos al Tier-0, encargado de realizar el primer procesado y de exportar la información a los centros Tier-1. Un segundo procesado tiene lugar en el

Tier-1, siendo el resultado enviado a los centros Tier-2, donde los usuarios pueden ejecutar sus propios análisis. Un ”framework” de software conocido como CMSSW se ha desarrollado para cubrir todos los aspectos del procesado, y una serie de herramientas Grid fueron también desarrolladas para permitir a los usuarios ejecutar sus análisis de forma distribuida.

Toda la estrategia de análisis de CMS se basa en la reconstrucción de objetos físicos de alto nivel, que se corresponden con partículas propagándose a través del detector. Los diferentes componentes de CMS registran las señales de una partícula mientras atraviesa el material del detector, y dichas señales son reconstruidas como puntos individuales en el espacio, conocidos como ”Rechits” o ”hits”. Para reconstruir completamente una partícula, los ”Rechits” se asocian para determinar puntos de su trayectoria. Las características de dicha trayectoria son utilizadas para definir su momento, carga y para su identificación.

La reconstrucción de muones se basa en una parametrización de tipo hélice conocida como parametrización de perigeo. Este proceso puede realizarse utilizando información únicamente procedente del sistema de muones o combinando información del sistema de muones y del detector de trazas (reconstrucción global). Con el objetivo de tener en cuenta las heterogeneidades del campo magnético, los parámetros de la traza se calculan en una serie de superficies de referencia. Para calcular el proceso de propagación de las partículas a través del detector, se hace uso de propagadores, capaces de tener en cuenta las interacciones de la partícula con el material. El algoritmo de reconstrucción usa una técnica estadística conocida como filtro de Kalman, y en general se divide en cuatro fases: búsqueda de semillas que sirven como posibles estados iniciales, la construcción de trayectorias candidatas, seguido de un proceso de limpieza en el que se eliminan las posibles ambiguedades entre candidatas, y finalmente un proceso de suavizado, en el que el filtro Kalman se aplica en dirección inversa para añadir robustez a todo el proceso.

Cada una de las cámaras de deriva es capaz de realizar una reconstrucción local de la traza. Dado que el campo magnético no es tan intenso en el interior de las cámaras, y puesto que el gas del interior no afecta sustancialmente a la trayectoria de la partícula, las trazas de muones se reconstruyen como líneas rectas. Los ”hits” registrados en los layers se ajustan a una recta para cada una de las proyecciones rϕ y z, dando lugar a dos segmentos *2DSegments*. Finalmente ambos segmentos se combinan para producir un *4DSegment* que contiene la posición y la dirección de la traza en ambas proyecciones.

11.2 Alineamiento del sistema de muones de CMS

Para un funcionamiento óptimo del espectrómetro de muones de CMS a lo largo de todo el rango de momento, hasta valores del orden del TeV, las cámaras de muones deben alinearse entre sí y en relación al sistema de trazas central con una precisión de unos pocos cientos de micras en el plano rϕ.

Las cámaras del espectrómetro de muones pueden sufrir desalineamientos por diferentes motivos, desde que son construidas hasta que se encuentran en funcionamiento en el espectrómetro. Entre estas causas pueden encontrarse las tolerancias de construcción, las tolerancias de ensamblaje y cerrado del detector, efectos provocados por el campo magnético, y otros efectos de carácter menos permanente, como efectos de humedad o de dilatación térmica.

La precisión de alineamiento requerida para las cámaras CSC es del orden de 75-200 μm, mientras que para el barril, la precisión oscila entre 200 μm para las cámaras de la primera estación y unas 400 μm para la estación exterior. Con el objeto de conseguir estas precisiones, CMS combina medidas de fotogrametría de precisión, medidas de un sistema opto-mecánico, y los resultados de algoritmos de alineamiento basados en trazas de muones (tanto de muones cósmicos como de muones provenientes de colisiones pp) registradas en el detector. Además de todos los métodos y técnicas utilizadas para medir la posición de las cámaras, se ha desarrollado una infraestructura de software que permite el correcto almacenamiento y manipulación de las correcciones de alineamiento, permitiendo su aplicación a los algorithmos de reconstrucción. En esta tesis se presentan contribuciones relacionadas con las técnicas de fotogrametría y alineamiento basado en trazas, así como de desarrollo de la infraestructura de software.

La primera de las técnicas de alineamiento usada por el sistema de muones de CMS es el sistema de alineamiento óptico. Dicho sistema está formado por tres componentes bien diferenciados: el sistema de alineamiento del barril, que se encarga del alienamiento de las cámaras de deriva, el sistema de alineamiento de las tapas, que alinea las cámaras de tiras entre sí, y el sistema "link" que se encarga de conectar el barril con las tapas, y a su vez con el detector central de trazas.

El sistema óptico está compuesto por un conjunto de líneas laser, detectores ópticos, inclinómetros y distanciómetros, distribuidos de forma redundante, y que permiten el cálculo de la posición de los objetos. El sistema de alineamiento óptico genera 6 planos activos, paralelos al haz y distribuidos uniformemente en ϕ. En el barril se dispone de líneas laser capaces de conectar diferentes planos y diferentes ruedas. El sistema de las tapas, utiliza líneas laser que cruzan el diámetro de los discos, y líneas paralelas al haz, capaces de conectar los diferentes discos, y cada una de las tapas. Por su parte, el sistema link establece un sistema de líneas laser que parten de una estructura adherida a los laterales del detector central de trazas, y alcanzan otra estructura adherida al primer disco de las tapas. Esas mismas líneas son reflejadas hacia las caras externas de las ruedas exteriores, conectando así con el sistema del barril. El sistema *link* se encarga también de monitorizar las cámaras del anillo interior del primer disco de las tapas.

Los tres subsistemas ópticos de alineamiento comparten un mismo software de reconstrucción, conocido con el nombre de COCOA. Este algoritmo establece un modelo jerárquico de las componentes del sistema de alineamiento y minimiza el χ^2 asociado para encontrar las posiciones de los componentes que mejor se ajustan a las medidas.

La segunda técnica, ampliamente utilizada en CMS es la fotogrametría: varios puntos de control se distribuyen sobre los diferentes componentes del detector, y posteriormente son fotografiados desde diferentes ángulos y distancias, permitiendo el cálculo de sus posiciones a través de algorithmos de triangularización. La fotogrametría se usa normalmente para proveer de una geometría inicial al sistema de alineamiento óptico, o como una primera geometría aproximada, previa a las geometrías producidas por el sistema óptico o por los algoritmos de trazas, y en general válida para garantizar un correcto funcionamiento del sistema de trigger.

Finalmente, la última técnica utilizada en CMS es el alineamiento con trazas, que aprovecha la redundancia en la determinación de las trazas para extraer información de alineamiento.

Existen varios algoritmos de trazas como por ejemplo los algoritmos HIP, Millepede o el algoritmo de alineamiento con filtros de Kalman, aunque todos ellos se basan en el cálculo de una magnitud conocida como residuo. El residuo es la diferencia entre la verdadera posición de la partícula medida en un determinado detector, y la posición esperada en base a una geometría conocida.

Los residuos están relacionados con los parámetros de alineamiento a través de una relación puramente geométrica. En esta tesis, esta relación se ha obtenido para detectores capaces de medir no solo la posición sino también la dirección de la trazas, como es el caso de las cámaras de deriva (ver 3.23). Dicha relación es sólo válida para el caso de desalineamientos muy pequeños.

Una vez obtenida la relación entre residuos y parámetros de alineamiento, el algoritmo conocido como Millepede (desarrollado por V. Blobel) fue reimplementado para adaptarlo a las características del barril del sistema de muones (algoritmo MBAA). El principio de funcionamiento de este algoritmo consiste en la minimización de los residuos frente a los parámetros de alineamiento y de traza en un mismo ajuste conjunto. La posición medida de una partícula en un plano detector dado puede expresarse como una expansión de Taylor dependiendo de ambos conjuntos de parámetros 3.24.

Resulta posible definir un χ^2 de la forma dada en 3.27, cuya minimización dé lugar a los parámetros de traza y de alineamiento que mejor se ajustan a los datos. La dimensión del sistema lineal asociado a esta minimización depende del número de trazas consideradas. Con el fin de reducirla, es posible aplicar algunas manipulaciones matemáticas, que dan lugar a un sistema de ecuaciones cuya dimensión es igual al número de parámetros de alineamiento, 3.33.

Este sistema de ecuaciones es intrínsicamente no invertible debido a las llamadas invarianzas del sistema. Estas invarianzas son configuraciones de desalineamiento específicas que no alteran las distribuciones de residuos. Existen invarianzas, llamadas intrínsecas, producidas por configuraciones de desalineamiento que son absorbidas por los parámetros de traza. Por ejemplo, un desplazamiento coordinado y constante de todos los subdetectores es indistinguible de una traza que sencillamente está desplazada con respecto a su posición real. Las invarianzas pueden ser también producidas por una topología muy particular de las trazas entrantes (por ejemplo si todas las trazas son perpendiculares, no se podrá observar un desalineamiento en la dirección perpendicular). Por último, aunque no son propiamente invarianzas del sistema, se suele considerar como tales a aquellas configuraciones de alineamiento que se miden muy pobremente debido a la falta de estadística.

Con el objetivo de resolver el sistema matricial expresado arriba las invarianzas se extraen a través del cálculo de una matriz pseudoinversa (3.37), o se añaden ligaduras, típicamente basadas en información externa. Estas ligaduras añaden nuevos términos al χ^2 (3.38) y pueden ser en general de dos tipos: medidas externas, o ligaduras físicas. En el primer caso los términos se añaden al χ^2, pesados por sus correspondientes errores, sin introducir nuevos parámetros en el ajuste. El segundo tipo de ligadura se usa para fijar limitaciones físicas del sistema. Por ejemplo, en un caso en el que sólo la posición relativa de los detectores es de interés, la posición global de la estructura completa puede ser fijada a un valor determinado. Para realizar esta tarea se utilizan multiplicadores de Lagrange, que introducen nuevos parámetros en el ajuste.

Por otra parte los algorítmos de alineamiento con trazas están afectados por todos aquellos errores sistemáticos propios del proceso de reconstrucción, ya que dichos errores alteran el valor de los residuos. Una mala calibración de los detectores, una mala estimación del campo magnético, sesgos en la descripción del material, o un modelado erróneo de las interacciones de las partículas con el material, como la pérdida de energía, la difusión de Coulomb, o la difusión múltiple de Coulomb son causas típicas de error en los procedimientos de alineamiento con trazas.

Además de una serie de medidas acerca de la posición real de los detectores, es preciso contar con una infraestructura de software que permita implementar correctamente las correcciones de alineamiento en la reconstrucción de CMS. Esta infraestructura es conocida como el ”framework” de alineamiento de CMS, y se encarga de las siguientes tareas: almacenamiento y administración de las constantes de alineamiento, aplicación de las constantes a la reconstrucción, y establecimiento de una serie de métodos y herramientas comunes a todos los diferentes algoritmos de alineamiento con trazas. La mayor parte de estos servicios se encuentran codificados en el paquete *Alignment* perteneciente a CMSSW. Durante el desarrollo de esta tesis, se han realizado varias contribuciones al diseño, implementación y testado de este ”framework”. En particular, como parte del trabajo realizado en este tesis, la cadena completa de alineamiento fue culminada con éxito por primera vez con datos reales.

11.3 Escenarios de alineamiento del sistema de muones para simulaciones de Monte Carlo

Toda la maquinaria de software, reconstrucción y análisis de CMS fue exhaustivamente testada, en paralelo con la construcción y puesta a punto del detector. El software de CMS fue utilizado para generar muestras de Monte Carlo, emulando la respuesta electrónica del detector. Estas muestras fueron reconstruidas usando los procedimientos estándar y se realizaron varios análisis de física especialmente relevantes.

Con el objeto de entender y estudiar el impacto de los desalineamientos y de las malas calibraciones en las diferentes fases de la cadena de reconstrucción y análisis, se puso especial énfasis en preparar y simular las condiciones del comienzo del LHC. Por esta razón, varios conjuntos de geometrías y calibraciones realistas fueron diseñados e insertados en las bases de datos oficiales de CMS.

En particular, en el sistema de muones, varias geometrías simuladas, conocidas como escenarios de alineamiento, fueron producidas para recrear las condiciones de alineamiento esperadas en el sistema de muones. Puesto que los procedimientos de alineamiento fueron evolucionando en paralelo con el desarrollo del detector, la corrección y el realismo de dichos escenarios fue también evolucionando y mejorando con el tiempo.

El ”framework” usado para producir geometrías corregidas puede usarse también para generar escenarios de alineamiento falsos. En este caso, el punto de partida es la geometría nominal, que es modificada de acuerdo con la definición del escenario. Esta tarea se encuentra implementada en el paquete *MuonAlignment*, en una clase llamada *MuonScenarioBuilder*, que es capaz de leer los archivos de configuración de los escenarios, aplicar los desalineamientos especificados a la jerarquía de objetos *Alignable*, y almacenarlos en una base de datos. Un archivo de configuración de un escenario es un archivo en formato PYTHON, que contiene varios bloques anidados haciendo referencia a la jerarquía de objetos *Alignable*. En cada bloque una distribución estadística es seleccionada (normalmente gausiana) y la dispersión de la distribución es especificada para cada parámetro de alineamiento. El software es capaz de producir un número aleatorio en base a la distribución y dispersión dadas, y usarlo como desalineamiento para el *Alignable* considerado. En el caso de objetos compuestos, los desalineamientos son siempre propagados a las subestructuras.

Además del testado y administración del paquete, varios desarrollos fueron realizados en el paquete *MuonAlignment*. Los más importantes estuvieron relacionados con la inclusión de dos nuevas configuraciones de desalineamiento: movimiento global de todo el sistema de muones con respecto al detector de trazas central, y desalineamientos de los sectores en ϕ. Estas configuraciones fueron de gran importancia para estudiar el impacto de los desalineamientos entre el detector central de trazas y el sistema de muones en la reconstrucción global, y para entrenar a los algoritmos de trazas, ya que en general los desalineamientos de sectores suelen ser invarianzas del sistema.

Todas estas herramientas fueron utilizadas para generar escenarios de alineamiento para las tres grandes campañas de simulación de CMS: los ejercicios de computación, software y análisis de 2006, 2007 y 2008 (CSA06, CSA07 y CAS08).

Para el ejercicio CSA06 se desarrollaron tres escenarios de alineamiento: el *Survey Only*, el *Short Term* y el *Long Term*. El escenario *Survey Only* tenía como finalidad reproducir las condiciones de alineamiento del sistema de muones cuando ninguno de los sistemas de alienamiento hubiera empezado a funcionar. El escenario *Short Term* tiene en cuenta los primeros resultados producidas principalmente por el sistema óptico, ya que los algoritmos de trazas requieren un tiempo de acumulación de estadística. Finalmente el escenario *Long Term* describía la situación del detector una vez ambos sistemas habían sido utilizados ampliamente. La configuración de los escenarios es muy parecida en los tres casos, consistiendo en una parte de desalineamientos de grandes estructuras como ruedas y discos, y una parte de desalineamiento de las cámaras individualmente. La magnitud de los desalineamientos oscila entre las tolerancias de cierre del detector y la precisión de fotogrametría de las cámaras, 2.5 mm y 1 mm respectivamente (en el escenario *Survey Only*, y las 200 μm conseguidas con las técnicas de alineamiento (escenario *Long Term*). En el escenario intermedio, *Short Term*, se produce una gran mejora del alineamiento de grandes estructuras, debido al sistema óptico, pero no de las cámaras individuales. Una descripción detallada de estos escenarios puede encontrarse en las tablas 4.1, 4.2 y 4.3.

Los 3 escenarios fueron introducidos en las bases de datos oficiales de CMS y usados por toda la colaboración para los diferentes análisis llevados a cabo en el ejercicio CSA06. Estudios específicos para ver el impacto de dichos escenarios fueron llevados a cabo, en particular estudiando el pico de masa del bosón Z^0 (ver 4.4) y también a través de estudios de eficiencia y resolución. En general se observaron degradaciones de la eficiencia y la resolución, relativamente acusadas en el escenario *Short Term*, con respecto a la geometría nominal, y siendo recuperadas por el escenario *Long Term* tal y como cabía esperar (ver 4.5).

Nuevos escenarios fueron diseñados para el ejercicio CSA07: el escenario $10\,pb^{-1}$ y el escenario $100\,pb^{-1}$. Puesto que la calidad del alineamiento es una función del tiempo y de la luminosidad (para acumular un número suficiente de trazas de alto momento), se crearon estos 2 escenarios, intentando recrear el estado del alineamiento tras los primeros 10 pb^{-1} y 100 pb^{-1} de toma de datos. Ambos fueron desarrollados sobre la base de que, conservadoramente, el sistema de alineamiento óptico y los algoritmos de trazas no producirían una mejora considerable en el alineamiento durante la primera toma de datos del detector. Ambos escenarios están inspirados en los dos escenarios utilizados para la CSA06 *Survey Only* y *Short Term*.

El escenario $10\,pb^{-1}$ se basó en el escenario *Survey Only*, aunque algunas correcciones se hicieron, para incorporar parte de la experiencia adquirida durante el MTCC, en donde se vió que el alineamiento relativo de las cámaras individuales podía mejorarse, y donde el sistema de alineamiento óptico fue capaz de hacer una primera estimación de la compresión magnética de los discos. Por estos motivos, el alineamiento individual de las cámaras se mejoró un factor 2, y los desplazamientos de los discos de las tapas fueron también ligeramente reducidos. Una descripción detallada del escenario puede encontrarse en la tabla 4.4.

El escenario $100\,pb^{-1}$ está basado en el escenario *Short Term*. Fundamentalmente se redujo la magnitud de los desalineamientos, tanto individuales como de discos y ruedas, debido a los primeros resultados (aún preliminares) de los sistemas de alineamiento. De forma adicional, se añadió un desalineamiento de todo el sistema de muones con respecto al detector central de trazas, para permitir estudiar el impacto de este tipo de desalineamientos. La descripción del escenario se encuentra en la tabla 4.5.

Antes de la inclusión de los escenarios en las bases de datos oficiales de CMS, una pequeña muestra de muones de p_T = 100 GeV fue producida con el objetivo de testar el escenario. Las figuras 4.6(a) y 4.6(b) muestran estudios de eficiencia y resolución llevados a cabo sobre ambos escenarios. En general se observa una degradación de ambas magnitudes, que es especialmente acusada en la zona de las tapas, a valores altos de la pseudorapidez, en dónde la trayectoria de las partículas en el plano $\mathrm{r}\phi$ es muy corta.

Ambos escenarios fueron exportados a las bases de datos oficiales de CMS y utilizados para la producción de muestras en el ejercicio CSA07. Durante los análisis posteriores, el grupo de estudio de las resonancias de bosones Z' encontró inconsistencias entre ambos escenarios para muones de muy alto momento ($\tilde{1}$ TeV). En particular, la resolución en el momento, de la reconstrucción global de muones parecía ser mejor en el escenario de $10\,pb^{-1}$ que en el escenario de $100\,pb^{-1}$ (ver figura 4.8). El problema fue identificado y aislado como un efecto derivado de la inclusión del movimiento global del sistema de muones con respecto al detector central de trazas, incluido en el segundo de los escenarios pero no en el primero. Este estudio hizo patente la importancia de un buen alineamiento relativo entre ambos subsistemas, lo que dio pie posteriormente al desarrollo de algoritmos de trazas que garantizasen dicho alineamiento.

Finalmente, durante el ejercicio CSA08 se crearon dos nuevos escenarios. El primero de ellos fue llamado *Startup* o $1\,pb^{-1}$, y pretendía recrear las condiciones de alineamiento del sistema de muones en el start-up del LHC, y el escenario $10\,pb^{-1}$, dedicado a las condiciones de alineamiento tras los primeros 10 pb^{-1} de datos.

El primero de estos escenarios se construyó sobre la base de las medidas de fotogrametría, asumiendo que poca información podría utilizarse del sistema de alineamiento óptico o de los algoritmos de trazas. El algoritmo para el nuevo escenario de $10\,pb^{-1}$ asumió que el sistema de alineamiento óptico sería capaz de medir los movimientos de grandes estructuras hasta reducirlos un factor 2 con respecto al escenario previo. La medida de las cámaras individuales, se mejoró también, fundamentalmente debido a los algoritmos de trazas. La descripción detallada de ambos algoritmos se encuentra en las tablas 4.6 y 4.7.

Durante el ejercicio CSA08 se produjeron muestras utilizando ambos escenarios como geometrías. Los propios algoritmos de trazas fueron ejecutados sobre estos escenarios de alineamiento para intentar recuperar su geometría (ver capítulo 7 para más información).

11.4 Alineamiento interno de las cámaras de deriva

Las cámaras de deriva son detectores complejos formados por varias capas de hilos. Un buen alineamiento de sus estructuras internas es necesario para garantizar la calidad de los procesos de reconstrucción local y global. Para ello, existen varias fuentes de información relativas al posicionamiento de las capas y supercapas de las cámaras: las medidas de los controles de calidad, las medidas de fotogrametría y las trazas de muones.

Las medidas de control de calidad fueron realizadas en los centros de producción, cuando las cámaras estaban siendo construidas. El objetivo de estas medidas es el de garantizar que no se han excedido las tolerancias de construcción. Desde el punto de vista del alineamiento, varias medidas fueron realizadas, como por ejemplo la medida de la posición de los hilos con respecto a una posición fija en la mesa de calibración. Estos valores fueron promediados para cada capa, dando lugar a una medida del desalineamiento de cada una de ellas.

Las medidas de fotogrametría se realizaron en los ISR, una vez las cámaras habían sido ensambladas. En concreto, varios objetivos de fotogrametría fueron adheridos a las esquinas de las cámaras y las distancias y rotaciones relativas entre supercapas fueron registradas.

Finalmente, desde las primeras fases, las cámaras fueron expuestas a trazas de muones cósmicos. Estas trazas otorgaron la posibilidad de aplicar un algoritmo de trazas a la estructura interna de la cámara.

Las medidas de control de calidad y de fotogrametría fueron publicados en las páginas web de los centros de producción, y de los grupos de calibración. El formato, las unidades y la estructura de estas medidas era heterogéneo y una serie de programas fueron desarrollados con el objetivo de extraer la información de las respectivas páginas de una forma rápida y automática.

Un primer análisis de las medidas de control de calidad reveló unas correcciones en la coordenada rϕ, centradas en 0 y con una desviación estándar de aproximadamente 100 μm, con errores del orden de 40 μm. La dispersión asociada a las medidas de fotogrametría era del orden de 200 μm para la dirección rϕ y z, 150 μrad para las rotaciones, y 1.5 mm para el desplazamiento radial entre supercapas. Esto era debido a la distancia extra añadida por el pegamento utilizado para ensamblar la cámara.

El algoritmo MBAA fue aplicado a la estructura interna de las cámaras de deriva, usando la capa como la unidad mínima de alineamiento. Cada una de las capas es capaz únicamente de dar información acerca de la posición en la dirección perpendicular a los hilos, así que el único residuo considerado fue el asociado a Δx. Por otra parte, las trazas dentro de las cámaras fueron modeladas como líneas rectas tal y como se hace en el proceso de reconstrucción local. Este sistema se ve afectado por dos tipos de invarianzas: la invarianza de tipo flotante (un desplazamiento constante e igual para todas las capas) que es absorbida por el término independiente del ajuste, y la de tipo radial (un desplazamiento de las capas proporcional a su posición radial) que es absorbida por la pendiente de la recta. Estas invarianzas se fijaron a cero para resolver el sistema de ecuaciones asociado a MBAA (ver figuras 5.5(a) y 5.5(b)).

Resulta importante destacar que ninguno de los conjuntos de medidas disponibles tenía la capacidad de producir un alineamiento completo de las cámaras de deriva. Las medidas del control de calidad solo daban información relativa entre la posición de las capas dentro de una misma supercapa. Las medidas de fotogrametría, por el contrario solo daban cuenta de los desalineamientos relativos entre supercapas, y finalmente el algoritmo de trazas estaba afectado por sus invarianzas. A pesar de esto los tres conjuntos de medida tenían una zona del espacio de desalineamientos en común. Esta redundancia fue utilizada para comprobar la compatibilidad entre las medidas, concluyéndose que las medidas eran compatibles dentro de sus correspondientes errores.

Una vez se comprobó la consistencia de todos los conjuntos de medidas, las medidas del control de calidad y las medidas de fotogrametría se utilizaron como ligaduras del algoritmo de trazas. Además, un conjunto de multiplicadores de Lagrange fue también introducido para fijar la invarianza de tipo flotante a 0, de tal manera que la cámara no sufriese ningún desalineamiento global.

El desplazamiento radial δz entre superlayers no fue incluido en los cálculos previos, ya que fue estimado con un error del orden de los 1-2 mm. Esto fue debido fundamentalmente a la gran verticalidad de las trazas, y al hecho de que la medida de fotogrametría no fue usada, ya que no existía una explicación plausible que justificase unos valores tan sumamente grandes en esta coordenada. Un nuevo algoritmo de alineamiento fue diseñado con el objetivo de medir la distancia entre las supercapas. El algoritmo es un caso particular, del algoritmo MBAA: en lugar de realizar un ajuste de los residuos en función de los parámetros de traza y de alineamiento, sólo estos últimos son usados. Los parámetros de traza se calculan usando cada una de las supercapas rϕ, de tal manera que la parte dependiente de ellos en la ecuación 5.7 desaparece.

Una vez la traza es reconstruida en una de las supercapas, es extrapolada a la siguiente tal y como se ilustra en la figure 5.9. Los residuos, definidos como la diferencia entre el propio segmento de la supercapa y el segmento extrapolado de la capa previa, se minimiza en función del parámetro δ_z y de los parámetros δ_x y ϕ_y, que tienen correlación con este primero. Resulta importante remarcar, que este método no se ve afectado por invarianzas, ya que los parámetros de trazas quedan perfectamente fijados, y no existe ningún posible solapamiento con los parámetros de alineamiento. Por otra parte, los desalineamientos individuales de las capas, son una fuente de error sistemático, ya que la distorsión que provocan es automáticamente propagada a la siguiente supercapa.

Los resultados producidos por el algoritmo mostraron un desalineamiento en δ_z del orden de 1 mm para las cámaras en las estaciones 2, 3 y 4, y cercano a los 2 mm para la estación 1. El acuerdo entre las medidas de fotogrametría y los resultados del algoritmo de trazas fue de unas 600 μm 5.11(a).

Las geometrías obtenidas fueron exhaustivamente validadas después de la aplicación de los algoritmos. En primer lugar el alineamiento relativo de las capas fue estudiado a través de las distribuciones de residuos, definidos como la diferencia entre los hits y las intersecciones del segmento con las superficies de las capas. La figura 5.12 muestra como estas distribuciones pasan de tener una RMS cercana a las 100 μm para la geometría no corregida, a una RMS de pocas μm para la geometría corregida.

En segundo lugar, los residuos supercapa a supercapa fueron estudiados para comprobar el parámetro δ_z entre supercapas. Un desalineamiento en esta coordenada produce una correlación entre el residuo y el ángulo de la trazas (ver 5.13). Se realizó un ajuste lineal sobre esta correlación y los parámetros de ajuste fueron comparados antes y después del ajuste. Las tablas 5.1 y 5.2 muestran unas dispersiones en estos parámetros que van desde las 400 μm antes de las correcciones a las 100 μm después para la ordenada en el origen, y desde las 500 μm a las 200 μm para la pendiente de la correlación.

11.5 Posicionamiento de las cámaras DT en el sistema de CMS: fotogrametría

Después de la instalación de las cámaras de deriva en las ruedas de CMS, fueron sometidas a medidas de fotogrametría. En particular, al menos 3 puntos de control fueron colocados en las esquinas de cada cámara y sus posiciones fueron calculadas con una precisión de 300 μm. Estas medidas se realizaron primero cuando el detector se encontraba en la superficie del punto 5, y fueron repetidas una vez el detector fue instalado en la caverna. En ambos casos, se llevó a cabo un procesado de las medidas para convertir las posiciones de los puntos de control, en parámetros de alineamiento de las cámaras.

Para llevar a cabo esta conversión se desarrolló un modelo matemático, basado en la rigidez de las cámaras. En este sentido, la posición real de cada punto individual de fotogrametría podía ser descrita como una rotación y un desplazamiento (el mismo para todos los puntos dentro de la misma cáamara) aplicados sobre su posición nominal.

Si el vector, $\vec{x} = (x, y, z)$, denota la posición de cada punto de fotogrametría, y $\vec{x}^0 = (x^0, y^0, z^0)$ denota su posición nominal, la rigidez de las cámaras implica la relación 6.1, en donde $\mathbf{R}$ y $\vec{\delta}$ son una matriz de rotación y un desplazamiento que transforman el punto nominal en el real. Esta relación debe ser cierta para todos los puntos. Por lo tanto, para calcular la rotación y el desplazamiento que se ajusta mejor a las medidas reales de define el χ^2 6.2 y se busca su mínimo.

El código que lleva a cabo esta minimización se encuentra en el paquete de software *Alignment/SurveyAnalysis*. Este software es capaz de leer las medidas de fotogrametría de un archivo de texto, minimizar el χ^2 para cada cámara y almacenar las constantes de alineamiento obtenidas. Las medidas de fotogrametría se encuentran dadas en el sistema de referencia asociado a la rueda, que es paralelo al sistema global de coordenadas de CMS, pero centrado en la cara negativa de la rueda, en lugar de en el punto de interacción. Una vez que el software lee las medidas de fotogrametría, se encarga de añadir el desplazamiento en z que la convierte al sistema global de CMS, y desde ahí se pasa al sistema local de cada cámara, en el que la minimización tiene lugar.

Este algoritmo se aplicó en primer lugar a las medidas de fotogrametría tomadas en la superficie del punto 5, para las ruedas YB0, YB+1 e YB+2. Un primer vistazo a los resultados mostró que todas las ruedas se comportaban de una manera muy similar. Los parámetros de alineamiento δ_x, δ_z y ϕ_y mostraron una correlación clara con el número de sector mientras que el resto de parámetros mostraron en general desalineamientos menores y sin ningún tipo de correlación (ver 6.3, 6.4).

La correlación encontrada era consistente con una caída gravitacional de las ruedas. Cada una de las ruedas se deforma de tal manera que verticalmente se produce una compresión, mientras que horizontalmente se produce una expansión, adoptando así una forma elipsoidal. En efecto, el parámetro radial δ_x mostró como la distancia entre los sectores 1 y 7 aumentó, mientras que la distancia entre los sectores 4 y 10 disminuyó. Desde el punto de vista del parámetro δ_x se observa un desalineamiento despreciable para los sectores 4 y 10, y un desalineamiento grande para los sectores 1 y 7, en donde la dirección δ_x coincide con la vertical. Finalmente las cámaras en los sectores intermedios sufrieron sobre todo una rotación debida al achatamiento y a la forma elipsoide adquirida. La magnitud de este achatamiento, medido a través del promedio de la compresión vertical entre los sectores 4 y 10, fue de 1.6 cm, 0.9 cm y 1.0 cm respectivamente para YB0, YB+1 e YB+2.

La distribución del χ^2 normalizado se estudió con el objetivo de entender la calidad de la estimación de los errores. La medida de esta distribución estaba desplazada de la unidad (ver 6.6) indicando que los errores usados estaban subestimados por un factor 3 aproximadamente. Alternativamente, esto pudo deberse a deformaciones y efectos no contemplados en el modelo de cuerpo-rígido utilizado en este caso.

El algoritmo fue aplicado de nuevo sobre los nuevos datos de fotogrametría tomados en la caverna del punto 5, esta vez para las 5 ruedas. Los resultados fueron similares a los obtenidos en la superficie (ver 6.7, 6.8 y 6.9). La compresión media en los sectores 4 y 10 fue de 1.0 cm, 1.0 cm, 1.5 cm, 0.8 cm and 0.9 cm, respectivamente para las ruedas YB-2, YB-1, YB0, YB+1 e YB+2. El análisis de los errores arrojó la misma conclusión que en el caso anterior.

Una comparación entre las constantes de alineamiento en la superficie y en la caverna fue realizada, mostrando un acuerdo de 500 μm, 1.3 mm y 1 mm respectivamente para las posiciones y del orden de 300-400 μrad para los ángulos. Teniendo en cuenta las consideraciones hechas anteriormente acerca de los errores, es posible afirmar que el proceso de transporte de las ruedas a la caverna no provocó grandes desalineamientos en las cámaras. En cualquier caso, las nuevas constantes fueron introducidas en la base de datos oficial de CMS.

La nueva geometría fue validada a través de dos métodos diferentes: una herramienta de validación específicamente desarrollada a tal efecto, y a través de algunos análisis de CMS especialmente sensibles al alineamiento, y en los que la mejora de las nuevas geometrías se hizo patente.

La herramienta de validación a la que se hace referencia es conocida como la extrapolación segmento a segmento. Se trata de un test local que permite evaluar el alineamiento relativo de cámaras en un mismo sector y diferente estación. El método define un residuo como la diferencia entre el segmento de una cámara y la extrapolación del segmento de la cámara anterior. Los valores medios de las distribuciones de residuos se comparan entre las geometrías alineadas y no alineadas. Las RMS de los promedios pueden encontrarse en la tabla 6.2. En general, la coordenada espacial x pasa desde una RMS de unos 2 mm a una RMS de 1.0 mm, mientras que la coorenada angular ϕ_y pasa desde 1.3 mrad, hasta 1.1 mrad.

11.6 Alineamiento con trazas del sistema de muones aislado

Durante las primeras campañas de testado de CMS, el espectrómetro de muones estuvo listo para operar (al menos parcialmente). El detector central de trazas por el contrario no estaba listo para operar globalmente con el resto de subdetectores hasta finales del año 2008. Por esta razón, un algoritmo de trazas fue desarrollado usando exclusivamente información del sistema de muones, junto con ligaduras externas obtenidas de las medidas de fotogrametría.

Este algoritmo estaba basado en el algoritmo MBAA descrito anteriormente, aunque se adaptó a las características especiales de las cámaras de deriva. Con el objetivo de eliminar la gran correlación presente entre los hits de una misma cámara, la cámara fue considerada la unidad mínima de alineamiento, y tratada como un cuerpo rígido. Los hits de cada cámara fueron reconstruidos localmente para producir segmentos con un total de 4 residuos: ($\Delta\ x$, $\Delta\ \frac{dx}{dz}$, $\Delta\ y$, $\Delta\ \frac{dy}{dz}$), correspondientes a la posición y dirección en las dos proyecciones. La parametrización de la traza se basó en la parametrización de tipo perigeo, estándar en CMSSW. Las derivadas de los residuos con respecto a los parámetros de alineamiento fue obtenida de la relación 3.33, mientras que las derivadas de los parámetros de traza fueron calculadas numéricamente.

El algoritmo recibe como datos de entrada, las trazas reconstruidas únicamente en el sistema de muones, los segmentos asociados a cada cámara y las medidas de fotogrametría. El esquema lógico de funcionamiento se divide en tres partes: el cálculo de residuos, el cálculo de las derivadas con respecto a los parámetros de traza y de alineamiento y la aplicación de las ligaduras de fotogrametría, junto con la minimización del χ^2.

Los residuos son calculados como la diferencia entre el segmento y la extrapolación del estado más interno de la traza, hasta la superficie en la que está contenido el segmento. Las derivadas con respecto a los parámetros de traza se calculan variando simétricamente en torno a su valor inicial, los parámetros del estado mas interno de la traza, extrapolando hasta la superficie del segmento, y calculando la derivada numérica de segundo orden (7.2).

Este algorithmo fue implementado en CMSSW en el paquete de software llamado *MuonStandaloneAlignment*. El flujo del programa comienza con un algoritmo de búsqueda, capaz de asociar a cada traza sus correspondientes segmentos. Una vez dado este paso, comienza el cálculo de residuos, derivadas y otra información relevante, que es almacenada en objetos de tipo *TrackForAlignment*, y enviada de vuelta al *Event*. Estos objetos se leen de nuevo para producir las matrices parciales asociadas al algoritmo, que son a su vez almacenadas en archivos de tipo ROOT. Después de este procesado, otro programa se encarga de leer todas las submatrices, de los diferentes archivos ROOT, reordenarlas en una única matriz, aplicar las ligaduras de fotogrametría y producir finalmente la inversión de la matriz global. Las constantes de alineamiento resultantes se almacenan en los correspondientes registros de alineamiento, y son exportadas a las bases de datos oficiales una vez han sido convenientemente validadas.

La primera campaña en la que este algoritmo fue testado fue el MTCC, durante el año 2006. Para este ejercicio, únicamente 3 sectores del barril fueron instrumentados: los sectores 10 y 11 de la rueda YB+2 y el sector 10 de la rueda YB+1. Para reducir la complejidad del algoritmo únicamente el parámetro de alineamiento más importante δ_x fue considerado. Un estimador de alineamiento basado en la ecuación 3.37 fue definido y aplicado para 3 casos diferentes: la geometría nominal, la geometría corregida por fotogrametría, y finalmente la geometría con las correcciones de trazas a la geometría de fotogrametría. En general, el algoritmo midió desplazamientos del orden de 1 mm para la geometría nominal. Estos desplazamientos se redujeron a 200 μm con la geometría de fotogrametría y finalmente una vez se implementaron las medidas del propio algoritmo, por debajo de las 100 μm (ver 7.1).

El algoritmo fue entonces aplicado a una campaña de simulación conocida como CSA06, en la que se simularon fundamentalmente 2 millones de colisiones protón-protón con producción de un Z^0. De nuevo, se usó una versión simplificada del algoritmo, en la que solamente se tuvo en cuenta el parámetro de alineamiento más relevante δ_x. Un conjunto de medidas de fotogrametría fueron también simuladas para ejercitar en la simulación el uso de ligaduras.

Varias simulaciones de Monte-Carlo fueron realizadas, con el objeto de cuantificar el impacto de las ligaduras en el algoritmo. En estos estudios, el algoritmo fue ejecutado varias veces sobre el mismo conjunto de trazas y sobre el mismo escenario de alineamiento (el escenario Short Term), utilizando diferentes escenarios de medidas de fotogrametría. La calidad del alineamiento conseguido se mide a través de la dispersión de la geometría con respecto a la geometría nominal, mientras que los escenarios de fotogrametría se caracterizan por la precisión con la que vienen dados. En la figura 7.5 se muestra cómo el escenario Short Term tiene una dispersión de unos 2 mm, y que el algoritmo de trazas, sin utilizar información externa lo rebaja a unos 1.6 mm. La precisión obtenida es sin embargo mucho mejor, una vez se combinan las medidas de fotogrametría con las trazas. Incluso con un escenario de fotogrametría con precisiones superiores al milímetro, se consiguen alineamientos submilimétricos.

Finalmente, se escogió un escenario de fotogrametría realista (en función de los resultados del capítulo 6) y se calcularon unas constantes de alineamiento que fueron exportadas a una base de datos, y distribuida para su validación. Puesto que la muestra utilizada en este ejercicio contenía esencialmente partículas del tipo Z^0, la calidad del alineamiento se estudió a través de su impacto en el pico de masa de la misma. Estos resultados se muestran en la figura 7.6, en la que se observa como el escenario de desalineamiento degrada la resolución del pico desde los 20.51 GeV hasta los 22.8 GeV, y que tras la aplicación de las correcciones de alineamiento, la resolución del pico vuelve a 20.59 GeV.

En el año 2008, el algoritmo fue de nuevo testado dentro del ejercicio de simulación CSA08. Este ejercicio, tenía como objeto simular los primeros días de toma de datos del detector, y en general el objetivo perseguido no era tanto probar la efectividad de los algoritmos, sino la capacidad de toda la infraestructura de software asociada a los mismos. El ejercicio se dividio en dos ciclos, llamados S43 y S156, atendiendo a la luminosidad simulada, y se produjeron fundamentalmente sucesos de *minimum bias*. Este tipo de sucesos dan lugar a muones de muy bajo momento, que en general son incapaces de atravesar todo el sistema de muones. Por esta razón, el número de trazas en condiciones de ser usadas por el algoritmo era muy reducido (puede verse un desglose detallado en la tabla 7.2). Esta falta de estadística dio lugar a un cálculo bastante impreciso de las constantes de alineamiento (dentro de lo esperado). Para el ejercicio S43, el número de trazas por cámara era tan limitado que los errores asociados a las constantes eran del orden de varios milímetros. Para el ejercicio S156, con un factor 10 de aumento en la estadistica, y teniendo en cuenta solamente aquellas camaras con mayor estadística, se encontró un acuerdo de unas 700 μm entre las constantes calculadas y las constantes del escenario. Desde el punto de vista computacional el algoritmo fue un éxito, produciendo las primeras constantes en pocas horas después de la llegada de las muestras al centro de análisis en el CERN.

11.7 Alineamiento de las cámaras DT con respecto al detector de trazas

La reconstrucción estándar de CMS (reconstrución global) combina información del sistema de muones y del detector central de trazas. Esta es la base de un algoritmo de alineamiento alternativo al presentado anteriormente, que es capaz de alinear las cámaras de muones utilizando el detector de trazas como referencia. En este caso, además de un alineamiento relativo de las cámaras, se consigue alinear las cámaras con respecto al propio detector de trazas. Esto resulta de gran interés, ya que los desalineamientos relativos entre el sistema de muones y el detector de trazas producen una fuerte degradación en la resolución del momento.

Este nuevo algoritmo es un caso particular del algoritmo MBAA explicado en las secciones previas. La diferencia entre ambos reside en el hecho de que este último incluye en su ajuste de residuos los parámetros de traza, mientras que la nueva adaptación, fija los parámetros de traza a la estimación dada por el detector central de trazas, asumiendo además, que esta estimación es perfecta. El χ^2 asociado a este algoritmo es de la forma 8.1.

La primera consecuencia derivada de esta simplificación tiene que ver con el hecho de que las invarianzas intrínsecas del sistema desaparecen. Al fijar los parámetros de traza con el detector de trazas, se resuelve la ambiguedad entre estos y los parámetros de alineamiento. El sistema de ecuaciones asociado es por tanto regular, y puede resolverse con una simple inversión de su matriz asociada 8.2. Por otra parte, aunque el algoritmo no se ve afectado por invarianzas, al asumir que la traza del detector central de trazas es perfecta, cualquier error en la estimación de ésta es automáticamente extrapolado (y amplificado) al sistema de muones.

La segunda consecuencia está relacionada con la dimensión del problema de alineamiento. En el algoritmo MBAA implementado en el capítulo 6, la inclusión de los parámetros de la traza en el ajuste, introducía correlaciones entre las diferentes cámaras, dando lugar a un único sistema de ecuaciones de gran dimesión. En el algoritmo presentado aquí, el detector de trazas se usa como referencia, y las correlaciones entre cámaras desaparecen, de tal manera que el problema puede ser factorizado y resuelto para cada cámara individualmente.

Este algoritmo fue utilizado para alinear las cámaras de deriva con respecto al detector de trazas. Con el objeto de eliminar la correlación existente entre los hits dentro de una misma cámara, se realizó un ajuste lineal sobre ellos dando lugar a segmentos como los del capítulo 6. Los residuos se definieron como la diferencia entre el segmento de la cámara, y la extrapolación de la traza proveniente del detector central de trazas. La matriz de covarianza del segmento se calculó a traves de sus contribuciones: los errores de ajuste del segmento, y los errores de extrapolación. Se realizó un ajuste a una función de tipo Lorentz sobre los residuos, definiendo un rango de aceptancia en función de la anchura de la curva de Lorentz. Los residuos fuera del rango fueron rechazados, por pertenecer a colas no modelizadas por el algoritmo.

Desde el punto de vista del software, el algoritmo se desarrolló con total integración en el sistema general de alineamiento software de CMS, recibiendo como entrada para los cálculos colecciones de trazas y trayectorias, previamente calculadas por un módulo llamado *TrackRefitter*. Dicho módulo se encarga de rehacer el ajuste a las trazas globales. En esta aplicación los errores de alineamiento en las cámaras de muones fueron fijados a un valor muy alto, de manera que su contribución al ajuste de la traza fuese nula. De esta manera, las trazas resultantes se construyen haciendo uso únicamente de la información del detector central de trazas. A partir de estas trazas se obtienen los hits, se generan los segmentos y se calculan los residuos y las matrices de covarianza. Esta información se almacena en archivos de tipo ROOT, ya que esta parte del algoritmo es la que más tiempo de CPU requiere y suele dividirse en diferentes trabajos, ejecutándose en distintas máquinas.

En una segunda fase, el algoritmo es capaz de leer los archivos ROOT generados previamente, y lleva a cabo la selección de trazas y la posterior solución del sistema. Como resultado se tiene una nueva geometría que es almacenada.

Este algoritmo fue utilizado por primera vez, en una versión simplificada, sobre una muestra de datos de Monte Carlo, siendo los resultados publicados en el *Physics Technical Design Report* del experimento. Una versión completa del algoritmo se usó en la toma de datos de muones cósmicos que tuvo lugar en septiembre-octubre de 2008, y conocida como CRAFT08. Debido a las características topólogicas de los muones cósmicos (distribuidos principalmente alrededor de la vertical) las ruedas externas YB-2, YB+2 y los sectores horizontales 1 y 7 no pudieron ser alineados, al no haber suficiente estadística.

Un primer estudio de las distribuciones de residuos del algoritmo, mostró una fuerte dependencia de éstos con q/p_T (del orden de 1 cm para trazas de bajo momento). Este análisis fue uno de los primeros que detectaron la presencia de un gran sesgo en la determinación del campo magnético en el sistema de muones. Con objeto de limitar el impacto de esta fuente de error sistemático, el algoritmo fue ejecutado en diferentes intervalos de q/p_T, para interpolar el valor correspondiente a $q/p_T = 0$. Una vez CMS dispuso de una mejor estimación del campo magnético, esta protección se retiró, y se limitó simplemente a la selección de muones de alto momento. El algoritmo siempre fue ejecutado sobre las últimas versiones de alineamiento y calibración del detector central de trazas y del alineamiento interno de las cámaras de deriva.

Puesto que el algoritmo usa como referencia las trazas del detector central de trazas, se aplicaron sobre éstas varios criterios de calidad. En particular, se exigió un mínimo de 15 hits por traza, con un $\chi 2/ndof < 10$. Aquellas trazas con hits en el TEC o en el TID fueron rechazadas, debido a que dichos subdetectores no se encontraban alineados en el momento de la ejecución del algoritmo. Finalmente, sólo trazas en el rango de momento 100 GeV < p_T < 200 GeV, fueron utilizadas para reducir problemas relacionados con el campo magnético y con los procesos de difusión.

Antes de aplicarlo sobre datos reales, el algoritmo fue testado con una muestra de muones cósmicos de Monte-Carlo, usando exactamente la misma configuración descrita anteriormente. En este caso, el algoritmo se ejecutó sobre un escenario de desalineamiento con valores típicos de 4-5 mm y 4-5 mrad. Para el resto de condiciones de CMS tales como el campo magnético, la geometría del detector de trazas, o el alineamiento interno de las cámaras, se usaron los valores nominales.

La resolución alcanzada por el algoritmo en este caso se muestra en la tabla 8.1, y fue de 500 μm y 400 μrad en los parámetros de alineamiento maas importantes (δ_x y ϕ_y). La resolución en δ_y, y en los ángulos ϕ_x y ϕ_z fue de 1.1 mm, 0.8 y 0.7 mrad respectivamente. El parámetro radial δ_z fue el que obtuvo una peor resolución, 2.8 mm. Este parámetro se mide fundamentalmente a través del ensanchamiento que produce en la distribución de residuos Δx. Si el rango de aceptancia de residuos se mantiene muy grande, la medida de este parámetro mejora, pero da lugar a la entrada de colas en el ajuste que degradan la medida de δ_x. En general es preferible garantizar la medida de δ_x que la de δ_z, cuyo impacto en la reconstrucción es mucho más pequeño.

Finalmente, el algoritmo fue aplicado sobre datos reales, produciéndose una nueva geometría. Esta nueva geometría fue distribuida y sometida a dos procesos de validación independientes. El primero de ellos es el método de extrapolación segmento a segmento, utilizado ya en el capítulo 6. La tabla 8.2 contiene las RMS de las distribuciones de las medidas de los residuos. En general, la mejora en la coordenada x va desde los 2.1 mm para la geometría no alineada, hasta los 0.8 mm para la alineada, y para la coordenada angular, desde los 1.7 mrad a los 0.8 mrad. Puesto que la resolución del método oscila entre las 700-800 μm para la posición, y 1 mrad para los ángulos, se puede afirmar que la precisión conseguida en el alineamiento tiene como cota superior estos valores, quedando por tanto garantizado un alineamiento, al menos, a este nivel.

El segundo método está basado en los estudios de resolución del momento a través de "trazas separadas". Los muones cósmicos suelen atravesar CMS en dos mitades, permitiendo que una sola partícula sea reconstruida como dos diferentes, una en la parte superior y otra en la parte inferior del detector. Puesto que se trata de la misma partícula, y una vez tenidos en cuenta las interacciones con el material, el momento de ambas ha de ser el mismo, de manera que puede usarse una de ellas como referencia para calcular la resolución en el momento. Esta resolución fue estudiada para la geometría nominal y también para la geometría corregida. Los resultados se muestran en la tabla 8.3. Antes del alineamiento la distribución de la resolución estaba centrada en -2.5%±0.6%, con una anchura de 8.6%±0.5%. Estos valores pasan a ser respectivamente -0.9%±0.2% y 4.2%±0.2% para la geometría alineada. Por vez primera se consiguió que la resolución de la reconstrucción utilizando el sistema de muones, fuese ligeramente mejor o al menos, comparable, a la resolución del detector central de trazas.

11.8 Geometrías completas del sistema de muones

El fin último de los sistemas de alineamiento de CMS consiste en proporcionar una geometría corregida a través de los correspondientes registros de bases de datos (*DTAlignmentRcd* y *CSCAlignmentRcd*, en el caso del sistema de muones), para que sean usados por los algoritmos de reconstrucción. A lo largo de este trabajo se han presentado diferentes alineamientos atendiendo a su entorno de aplicación y a las técnicas y algoritmos utilizados para conseguirlo, sin prestar atención a las conexiones entre ellos. Estas conexiones resultan de especial relevancia a la hora de crear geometrías completas, ya que en muchos casos es preciso mezclar y combinar los diferentes resultados. Durante el desarrollo de esta tesis doctoral, se realizó la gestió de las geometrías del sistema de muones (para el barril y las tapas) contenidas en las bases de datos oficiales de CMS. Esto incluyó la creación de las geometrías, su exportación a las bases de datos y la producción y mantenimiento de documentación para el uso del resto de usuarios de CMS.

La primera consideración a la hora de crear una geometría completa del barril del sistema de muones, fue la combinación de la geometría interna de las cámaras (capítulo 5), con la geometría global (capítulos 6, 7 y 8). Con esta finalidad, el software descrito en el capítulo 3, fue desarrollado para ser capaz de manipular convenientemente el registro de geometría *DTAlignmentRcd* de tal manera que el alineamiento interno, modificase únicamente la posición de capas y supercapas, sin alterar la posición de las cámaras. De la misma forma, el mismo software se encargaba de propagar a las estructuras internas cualquier movimiento global de las cámaras. Además, para evitar toda correlación, el alineamiento interno fue desarrollado de tal manera que el movimiento global de todas las capas y supercapas fuese siempre igual a 0 (usando para ello, multiplicadores de Lagrange). Con estas consideraciones, el procedimiento de creación de bases de datos completas estaba dividido en dos fases: en primer lugar se cargaba la geometría interna de cada cámara, y en una segunda fase, cada cámara se colocaba en su lugar correspondiente. Esta división resulta especialmente importante para los algoritmos de trazas (globales), ya que sus resultados son dependientes de la geometría interna, y siempre han de ejecutarse sobre la geometría interna que le va a acompañar en la base de datos.

Todos los cálculos desarrollados en esta tesis doctoral sirvieron para crear tres bloques de geometrías del barril. Todos ellos, dieron lugar a geometrías completas, incluidas en las bases de datos de CMS, y usadas para los diferentes estudios llevados a cabo con los primeros datos recogidos por CMS. El primero de estos bloques, lo forman las geometrías de alineamiento interno, fotogrametría y trazas desarrolladas durante el MTCC, y que usaron los datos de los capítulos 5, 6 y 7. El segundo bloque estuvo compuesto por geometrías que combinaron el alineamiento intero y las medidas de fotogrametría una vez que CMS fue bajado a la caverna del punto 5. Finalmente, el último bloque incluyó geometrias que combinaban el alineamiento interno del capítulo 5, con el algoritmo de trazas del capítulo 8, en el contexto de la toma de datos conocida como CRAFT. El hecho de que las geometrías se dividan en bloques se debe al hecho de que varias versiones de cada una de ellas fueron incluidas en cada uno de los bloques.

Además de las diferencias en el entorno y objeto del alineamiento (por ejemplo diferencias entre alineamiento interno y global), existen diferencias debidas al hecho de la coexistencia de varios métodos que producen información acerca de lo mismo. Es el caso por ejemplo de los algoritmos de trazas, la fotogrametría y el alineamiento óptico.

A lo largo de la tesis se vio como las medidas de fotogrametría se integran en los algoritmos de trazas, combinando ambos métodos, y dando lugar a un alineamiento más completo, que el dado por cada uno de ellos por separado. Este mismo procedimiento puede ser utilizado también para incorporar la información del sistema óptico de alineamiento a los ajustes de los algoritmos de trazas. Alternativamente, los resultados de los algoritmos de trazas pueden también introducirse en los ajustes realizados por COCOA, para producir así una combinación de medidas. En muchas ocasiones, ocurrió que algunos de los parámetros de alineamiento estaban muy bien estimados por los algoritmos de trazas, mientras que otros lo estaban por el sistema óptico. En estos casos, se hicieron geometrías híbridas, en las que algunos parámetros de alineamiento estaban sacados de un sistema, y otros de otro sistema.

El último paso de los sistemas de alineamiento, una vez creadas las geometrías, es su exportación a las bases de datos oficiales, y la producción de documentación. En CMS existen dos métodos diferentes para llevar a cabo este proceso. El primero consiste en el uso de una interfaz, integrada en CMSSW, y que permite directamente escribir las constantes en las bases de datos correspondientes. El segundo método consiste en el uso de una serie de herramientas capaces de copiar bases de datos privadas (en formato MySQL) en los repositorios oficiales. El alineamiento de muones optó por esta segunda opción, que con el tiempo, y por motivos de seguridad, desembocó en el uso de un mecanismo conocido como "drop-box", en el que de forma central, las bases de datos propuestas por los responsables de cada subsistema eran insertadas en las bases de datos oficiales. La documentación de las constantes disponibles se hizo pública a través de páginas TWIKI disponibles para toda la colaboración.

11.9 Conclusiones

El trabajo presentado en esta tesis se enmarca dentro del contexto del experimento CMS (Solenoide Compacto de Muones) situado en el LHC (Gran Colisionador de hadrones). En particular, el trabajo está relacionado con el alineamiento del espectrómetro de muones de CMS, y de forma más específica, con el alineamiento de las cámaras de tubos de deriva, que componen el barril del sistema de muones. En esta sección se presenta una recopilación de los resultados más relevantes obtenidos a lo largo de la realización de la tesis.

Desarrollo y mantenimiento de la infraestructura de software de alineamiento del sistema de muones.
El alineamiento del sistema de muones requiere un software que permita el correcto almacenamiento y procesado de las constantes de alineamiento, para que sean correctamente usadas por los algoritmos de reconstrucción. Varias contribuciones fueron realizadas en el desarrollo de esta infraestructura, pasando desde la implementación de código, al testado y el comisionado. Algunos de los aspectos más relevantes se muestran a continuación:

- Desarrollo del paquete de software *MuonAlignment*, diseñado para gestionar la aplicación de correcciones de alineamiento a la reconstrucción y para la producción de escenarios de desalineamiento. El paquete fue extendido para permitir la inclusión de desalineamientos no pertenecientes a la jerarquía del sistema de muones, como el desalineamiento de sectores, o el desalineamiento de todo el sistema con respecto al detector central de trazas.

- Introducción de geometrías en las bases de datos oficiales de CMS y testado y comisionado del mecanismo drop-box, responsable del tratamiento centralizado de las constantes de alineamiento y calibración de CMS.

- Primer testado y comisionado de la cadena completa de alineamiento software con datos reales. Durante el "Magnet Test and Cosmic Challenge", y por primera vez, constantes de alineamiento fueron producidas, introducidas en las bases de datos estándar de CMS y usadas para realizar una nueva reconstrucción.

Desarrollo de escenarios de desalineamiento para simulaciones de Monte-Carlo.
Con el objeto de estudiar el impacto de los desalineamientos en la reconstrucción de CMS, varias geometrías desalineadas artificialmente fueron desarrolladas. Parte de esta tesis incluye el diseño, implementación y validación de estas geometrías (normalmente conocidas como escenarios de desalineamiento). Todos los escenarios fueron almacenados en las bases de datos oficiales de CMS, y se usaron de manera extensiva por toda la colaboración en las principales campañas de simulación del experimento.

- Computing, Software and Analysis challenge in 2006 (CSA06). Se produjeron un total de tres escenarios: *SurveyOnly*, *ShortTerm* y *LongTerm*. El primero partía de una información relativa al alineamiento aún muy pobre, principalmente proveniente de las medidas de fotogrametría. El segundo incorporaba algunos resultados aún muy preliminares de los sistemas de alineamiento, tras la primera toma de datos. Finalmente el tercero describe la situación del detector a largo plazo después de que los sistemas de alineamiento han operado de forma exhaustiva.

- Computing, Software and Analysis challenge in 2007 (CSA07). Se produjeron dos escenarios: el escenario 10 pb^{-1} y el escenario 100 pb^{-1}. El primero se basó en el escenario previo *SurveyOnly* aunque se incluyeron algunas mejoras provenientes de la experiencia adquirida durante el Magnet Test and Cosmic Challenge. El segundo escenario, estaba a su vez basado en el escenario *ShortTerm*, pero teniendo en cuenta las mejoras que se esperaban en el alineamiento debido a la operación de los sistemas durante los primeros 10 pb^{-1} de toma de datos. En este último, se añadieron desalineamientos de sectores, y del sistema de muones con respecto al detector central de trazas.

- Computing, Software and Analysis challenge in 2008 (CSA08). Se produjeron dos escenarios: el escenario *Startup* y el escenario 10 pb^{-1}. El primero incorporaba la información más realista de la que se disponía en relación al estado de alineamiento del detector durante el arranque del LHC. Esto incluía la información adquirida durante las tomas de datos de cósmicos y las pruebas del iman. El segundo escenario, constituía una mejora del primero, debido a los resultados que se esperaban de los sistemas de alineamiento.

- Estos escenarios confirmaron el correcto funcionamiento del sistema de trigger para el inicio del LHC, aunque se hizo patente la necesidad de varios refinamientos para una correcta reconstrucción de trazas de muy alto momento.

Desarrollo del Algoritmo de Alineamiento Modificado de Blobel.

Un algoritmo de alineamiento con trazas (el Algoritmo de Alineamiento Modificado de Blobel, MBAA) basado en las ideas de V. Blobel fue desarrollado teniendo en cuenta los requirimientos particulares del sistema de muones de CMS. Su principio de funcionamiento consiste en la minimización de los residuos de traza frente a los parámetros de traza y de alineamiento.

- El método fue extendido para incorporar "hits" más generales incluyendo no sólamente parámetros de posición, sino también de dirección, tal y como requieren algunas de las implementaciones para el sistema de muones de CMS. Esto incluyó una parametrización más general de los residuos en función de los parámetros de alineamiento.
- Los algoritmos de trazas están afectados por invarianzas, configuraciones particulares de desalineamientos que mantienen a los residuos inalterados (por ejemplo, un desplazamiento córdinado de todos los subdetectores, por la misma cantidad no puede ser observado por un algoritmo de trazas). Este problema es ampliamente discutido y dos soluciones son propuestas: el uso de ligaduras externas, y la fijación de las invarianzas a través del análisis de autovalores y del cálculo de matrices pseudo-inversas. El algoritmo fue finalmente implementado para las diferentes aplicaciones.

Alineamiento Intero de las Cámaras de Deriva.

El algoritmo MBAA fue implementado y adaptado para alinear la estructura interna de las cámaras de deriva. Tres fuentes de información fueron usados para este alineamiento: trazas de muones cósmicos para el algoritmo MBAA, y ligaduras provinientes del control de calidad de las capas, y de la fotogrametría de las supercapas.

- El alineamiento de las capas de forma individual fue validado, comparando la posición de sus respectivos hits con los segmentos reconstruidos a partir de ellos. La dispersión de las desviaciones encontradas estaba por encima de las 100 μm antes de que las correcciones se aplicaran, y se redujo hasta pocas micras, una vez fueron aplicadas.
- El alineamiento relativo de las supercapas fue validado comparando los segmentos en cada una de las supercapas, con la extrapolación del segmento, proviniente de la supercapa anterior. La dispersión in el parámetro δ_x se redujo desde las 400 μm hasta las 100 μm, mientras que la dispersión en δ_z mejoró desde las 500 μm a las 200 μm.

La geometría interna calculada en este proceso fue introducida en las bases de datos de CMS y fue usada por la colaboración como la geometría oficial, dando lugar a una significativa mejora en el proceso de reconstrucción.

Posicionamiento de las cámaras de deriva en el sistema de CMS usando medidas de fotogrametría.

Un modelo matemático fue desarrollado con el objetivo de transformar las posición de los puntos de control de fotogrametría distribuidos por las las estructuras de CMS, en parámetros de alineamiento de las cámaras. El procedimiento se realizó primero sobre las medidas tomadas en la superficie del punto 5, y fue luego repetido para las medidas tomadas en la caverna. Los resultados más importantes son los siguientes:

- La posición y orientación de las cámaras fue calculada e introducida en las bases de datos de CMS. Resultados de validación basados en la propagación local de trazas de muones cósmicos mostraron una mejora en la posición relativa de las cámaras que iba desde los 2.2 mm antes del alineamiento al nivel de 1 mm después del alineamiento y para la coordenada rϕ.
- La forma de los parámetros de alineamiento fue estudiado, observándose que las ruedas habían sufrido un achatamiento gravitacional de aproximadamente 1.2 cm (ver detalles para las diferentes ruedas en el capítulo 6). La forma de las ruedas, inicialmente circular, pasó a ser de tipo elíptica, debido al peso del hierro. Este resultado estaba en concordancia con las predicciones obtenidas a través de simulaciones numéricas.
- La comparación de resultados en la superficie y en la caverna, mostraron una buena reproductibilidad (al nivel de los errores) indicando que el proceso de descenso de las ruedas no provocó grandes desalineamientos, y dando una fuerte confianza en la relevancia de los resultados obtenidos.

Las constantes obtenidas fueron introducidas a la base de datos de CMS y usadas como una primera geometría inicial. Es importante remarcar que este nivel de precisión fue suficiente para permitir un correcto funcionamiento del sistema de trigger, y para la reconstrucción de trazas de no muy alto momento.

El algoritmo de alineamiento Standalone MBAA.
Una implementación del algoritmo MBAA fue desarrollada con el objetivo de alinear las cámaras de deriva, independientemente del detector central de trazas. Debido a la gran correlación entre los hits de una misma cámara, el algoritmo fue adaptado para usar segmentos, considerando a las cámaras como cuerpos rígidos. Los resultados más importantes obtenidos con este algoritmo son los siguientes:

- Alineamiento de las cámaras en el Magnet Test and Cosmic Challenge. Durante el MTCC una versión simplificada del algoritmo, que solo tenía en cuenta la coordenada rϕ, fue aplicada. La distribución de residuos se redujo desde 1 mm al nivel de las 100 μm.
- Ejercicio de alineamiento en el Computing, Software and Analysis challenge de 2006 (CSA06). La misma versión del algoritmo fue aplicada sobre una muestra de datos simulada de colisiones protón-protón, en las que un Z^0 fue producido y forzado a desintegrarse en pares de muones. La masa invariante del Z fue usada como medida de la calidad del alineamiento. La degradación observada en el pico de masa del Z cuando el escenario de desalineamiento fue introducido, se recuperó totalmente hasta los niveles de la geometría nominal, cuando la geometría corregida fue introducida.
- Ejercicio de alineamiento en el Computing, Software and Analysis challenge de 2008 (CSA08). Para esta campaña de simulación el algoritmo estaba preparado para medir tres coordenadas: la coordenada x local, y local y ϕ_y. El ejercicio CSA08 estaba más

centrado en el testado y comisionado de los circuitos de alineamiento, que en el testado de los algoritmos de alineamiento y calibración en sí mismos. El circuito asociado al algoritmo MBAA fue declarado un éxito, siendo las constantes de alineamiento calculadas e introducidas en las bases de datos dentro del plazo de tiempo correspondiente.

Alineamiento de las cámaras con respecto al detector central de trazas.

El algoritmo MBAA fue adaptado para alinear las cámras de muones con respecto al detector central de trazas. Este algoritmo asumió que los parámetros de traza estaban perfectamente determinados por el detector de trazas, y por lo tanto no se consideraron como parámetros libres en la minimización. En la práctica, las trazas del detector de trazas fueron extrapoladas hasta el sistema de muones, dando lugar a un alineamiento relativo de las cámaras de muones con respecto al detector central de trazas. Los resultados más interesantes en relación a este procedimiento se muestran a continuación:

- El algoritmo fue aplicado sobre una muestra de trazas de muones cósmicos tomada durante el Cosmic Run At Four Tesla en el año 2008 (CRAFT08). Con el objetivo de estimar la resolución intrínseca del algoritmo, también fue aplicado sobre una muestra de muones cósmicos de Monte-Carlo, usando condiciones ideales para el detector (excepto para la geometría del sistema de muones). Los parámetros de alineamiento más improtantes δ_x y ϕ_y se midieron con una resolución intrínseca de 500 μm y 400 μrad respectivamente. Las constantes calculadas con datos reales fueron introducidas en bases de datos estándar de CMSSW.

- La geometría corregida fue validada usando propagación local de trazas entre cámaras. Se observó que los observables de la validación tenían una dispersión comparable a la resolución del método, estableciendo un límite superior a la precision de alineamiento de 700 μm y 1 mrad respectivamente para las coordenadas δ_x y ϕ_y.

- Un segundo proceso de validación fue llevado a cabo haciendo uso de las "trazas separadas" (trazas de muones cósmicos que atraviesan todo el detector, pero son reconstruidas como dos trazas diferentes, una en la parte superior y otra en la parte inferior). Las "trazas separadas" proporcionan dos estimaciones independientes del momento de una misma partícula, permitiendo así el cálculo de su resolución. La geometría MBAA produjo una muy significativa mejora en la resolución del momento (desde 8.6% a 4.2%). Resulta interesante remarcar que antes de la implementación de estas correciones, la inclusión del sistema de muones no mejoraba la resolución del detector central de trazas en solitario.

En el trabajo presentado en esta tesis, varias herramientas de software y algoritmos relativos al alinemiento del sistema de muones han sido desarrollados, y utilizados en las diferentes fases de comisionado del detector CMS. Se produjeron resultados de alineamiento en diferentes niveles y utilizando diferentes tipos de medidas. Varios procesos de validación fueron aplicados sobre las geometrías calculadas, asegurando la mejora producida en el proceso de reconstrucción. Finalmente, estas geometrías fueron aceptadas e introducidas en las bases de datos oficiales de la colaboración, contribuyendo a que CMS alcance los objetivos de física para los que fue diseñado.

Appendix A

Skims for alignment and calibration (AlCaReco)

Alignment and calibration procedures are considered priority tasks, as all the components of CMS must be calibrated and aligned in order to produce a consistent, non-biassed response. For this reason, specific skims dedicated to alignment and calibration are centrally produced at the Tier-0, as soon as data reaches the offline farm. These samples are known in the CMS jargon as *AlCaReco*.

Each subsystem in CMS defines one or more *AlCaReco* depending on their needs. *AlCaReco* are a subset of the collections contained in the more general data formats of CMS: *RAW* (the raw information coming from the detector), *RECO* (the products of the reconstruction at the different stages, dropping most of the raw content) and *AOD* (subset of *RECO* containing high level reconstructed objects). Most of the *AlCaReco* consist in a selection of the *RECO* content, although some of them (there are different and specific *AlCaReco* for each subdetector) include as well information from the *RAW* information. The latter are known as type-II *AlCaReco*.

AlCaReco samples are produced through a series of CMSSW filter modules that are able to select the interesting events, based in the trigger bits, or in other physical or topological properties of the event. In addition these filters have the capability to select the collection content in the sample. Most of the collections are dropped, and only those interesting for the task the *AlCaReco* is intended for are left into the sample.

Table A.1 shows the *AlCaReco* samples defined for the alignment of the muon system. The muon alignment workflow that uses each sample has been specified. Reference [76] contains a more detailed description of the structure and definition of each *AlCaReco*.

Name	Type	Basic properties	Basic Content	Purpose
'MuAlCalIsolatedMu'	II	DT muon $P_t > 10$ GeV	DT Digis DT 1Dhits DT 4DSegments DT 4DSegments	Drift tube internal alignment Drift tube calibration
'MuAlStandAloneCosmics'	I	Standalone muon $P_t > 10$ GeV	1Dhits DT 4DSegments CSC 2DSegments Standalone tracks	Drift tube standalone alignment
'MuAlGlobalCosmics'	I	Globalmuon $P_t > 10$ GeV	1Dhits Global tracks	Tracker to muon alignment
'MuAlOverlaps'	I	CSC muon $P_t > 3$ GeV	CSC 1Dhits	Alignment of endcap rings
'MuAlZMuMu'	I	2 Standalone muons Lower $P_t > 10$ GeV	Standalone tracks	Alignment validation of the muon system

Table A.1: *AlCaRecos* defined for the muon system. Only the most important contents and physical properties are explicitly written.

Appendix B

CMS computing and commissioning campaigns

B.1 Introduction

Since the year 2006 CMS has been instrumented and commissioned in different campaigns using cosmic muons for testing the detector response and data taking and producing the first calibrations of the detector. Additionally the computing and software infrastructure of CMS has been tested in large simulation exercises involving all the stages of the computing challenge, ranging from the reconstruction process to the high level physics analysis. Figure B.1 shows the timeline of the major commissioning phases of CMS. Muon alignment worflows were tested in most of these stages and up to the level of development achieved at the moment of the campaign.

From the point of view of the detector commissioning, the first large-scale campaign was the Magnet Test and Cosmic Challenge (MTCC), that took place in the year 2006 when the detector was still installed at the surface of P5. After the MTCC, CMS was lowered to the cavern, and fully instrumented again. In the beginning of 2008 the first global commissioning runs were produced under the so called Global RUn in Middle-March (GRUMM) [77] of 2008. After GRUMM, the Cosmic RUn at Zero Tesla (CRUZET [78]) took place until the end of August, in a series of time-separated cosmic runs. At this point the detector was prepared for the first collision data during September 2008. Cosmic commissioning runs continued from October to the end of November in the so called Cosmic Run At Four Tesla in 2008 (CRAFT08), and during most of the first half of 2009 in the Middle Week Global Runs (MWGR [79]), and the Cosmic Run At Four Tesla in 2009 (CRAFT09) until the first collisions occurred in November 2009.

Several computing exercises were carried out in parallel with the commissioning of the detector. During the years 2006, 2007 and 2008 three exercises called Computing, Software and Analysis challenge (CSA06, CSA07 and CSA08) took place testing the response of the computing infrastructure at different scenarios of data taking rates. An analysis-oriented exercise was carried out as well in October 2009, and called the October Exercise [80] in preparation for the imminent collision data.

Most of the developments and results presented in this thesis constituted the basic input

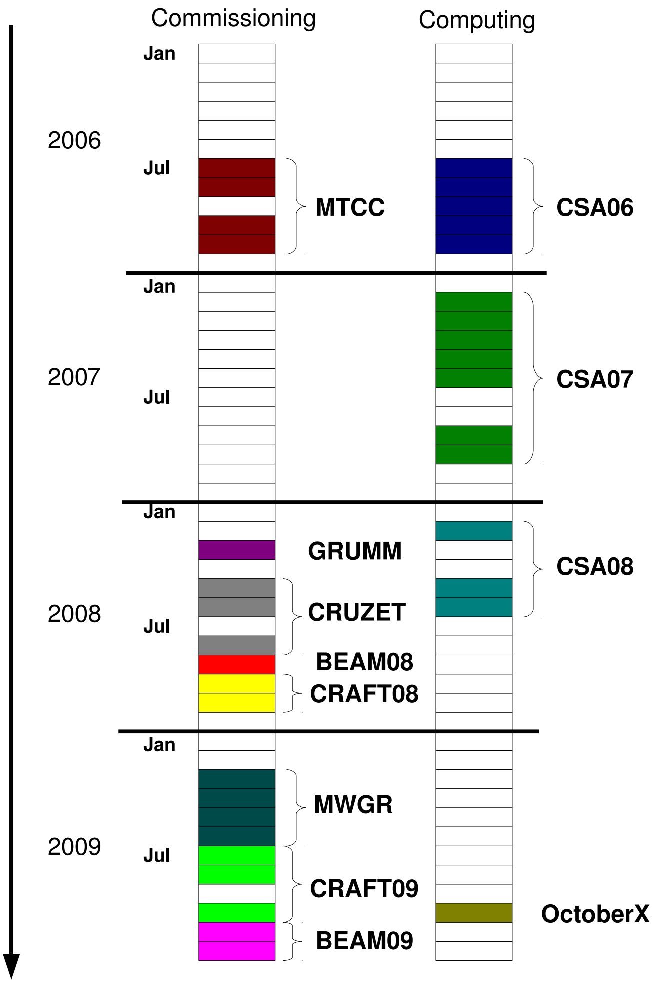

Figure B.1: Time distribution of the commissioning phases and computing exercises in the last years.

for the alignment of the barrel muon system and the muon alignment workflows focused in the drift tube system. In this appendix a brief description of those campaigns these workflows were involved is provided.

B.2 The Magnet Test and Cosmic Challenge

Before lowering the detector elements, several major tests were performed on the surface during the second half of 2006. On the one hand, they concerned the commissioning of the superconducting coil, hence the name Magnet Test. On the other hand the CMS collaboration set the goal to operate roughly $1/20^{th}$ of the CMS sub-detectors integrated with all central services and the Trigger and Data Acquisition Systems, using cosmic muons as a particle source. This major effort was named the Cosmic Challenge [74]. The participating sub-detectors included a 60 sector of the Cathode Strip Chamber and Resistive Plate Chamber Muon Systems in one end-cap, a 60 sector and a 30 sector of the Drift Tube and Resistive Plate

Chamber Muon Systems in two adjacent wheels of the barrel, two 80 sectors of the Barrel Hadronic Calorimeter, a 30 Sector of the Endcap Hadronic Calorimeter, two 20 modules of the Barrel Electromagnetic Calorimeter and a small setup of the Silicon Tracker containing parts of four barrel layers and one end-cap disk. Figure B.2 shows the layout of instrumented chambers in the muon system for this MTCC exercise.

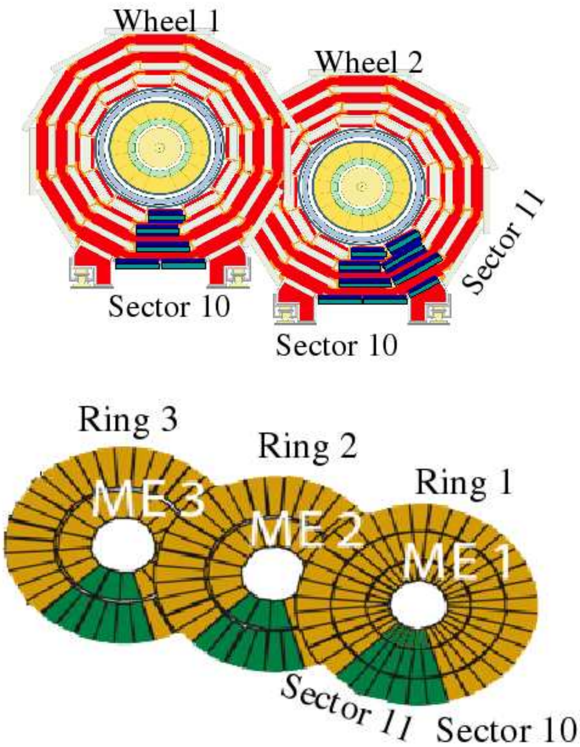

Figure B.2: MTCC layout of instrumented chambers in the muon system.

The MTCC was divided in two different phases. The first one was preceded by the commissioning of the magnet. The magnet was first cooled down to operating temperature in a very smooth operation during February 2006, taking care to keep temperature gradients small. After closing and interlocking the eleven detector elements, the magnet was powered with increasingly higher currents. After periods of constant magnetic field, the magnet was powered down using either the slow discharge method during which the solenoid stays at operating temperature or the fast discharge method during which superconductivity is lost and temperature increases by about 70 K. The nominal field strength of 4 T was reached at a current of 19.2 kA on August 22, 2006, setting a new world record for energy stored in a magnet of 2.5 GJ.

During the following days, known as the Cosmic Challenge phase 1, about 15 million cosmic events were taken with parts of all three Muon Systems, both Calorimeters and the Tracker at a field strength of 3.8 T.

After this first phase, the detector was opened, the two innermost sub-detectors, the Tracker and the Electromagnetic Calorimeter, were removed and a field mapping device was installed in their place. The detector was then closed and the field in the inner detector volume was mapped at field strengths of 0 T, 2.5 T, 3.5 T, 3.8 T and 4 T. In parallel to the field mapping, cosmic data taking continued with the muon systems and the hadronic calorimeter in the so called Cosmic Challenge Phase 2.

B.3 The Computing, Software and Analysis challenge of 2006

The combined Computing, Software, and Analysis challenge of 2006 [72] was an O(50) million event exercise to test the workflow and dataflow associated with the data handling model of CMS. It was designed to be a 25% capacity test of what was expected for operations in 2008. The main goals of this exercise were: the preparation of large simulated datasets (some with High Level Trigger tags), the prompt reconstruction at the Tier-0, the distribution of all the data all participating Tier-1s (as well as to some Tier-2s), the calibration jobs at Tier-1, Tier-2 and CAF, re-reconstructions performed at Tier-1 sites, skim jobs at some Tier-1s with data propagated to Tier-2s, and finally physics analysis jobs at Tier-2s. Most of these tasks were divided in several sub-tasks, in particular for the reconstruction step four issues were specially addressed: the reconstruction at 40 Hz using CMSSW, application of calibration constants from the offline database (ORCOFF), generation of skims and splitting of an HLT-tagged sample into O(10) streams.

B.4 The Computing, Software and Analysis challenge of 2007

The Computing Software and Analysis Challenge 2007 (CSA07) [73] was an opportunity to exercise as many elements as possible of the CMS Computing and Analysis models simultaneously at a defined scale. In particular CSA07 was intended to emulate the 50% of the computing load expected for the data taking. The exercise was focused in the use of computing and offline tools with a diverse and active user community, using similar data streams as the expected from the data taking, and focusing in the balance of the simulation and analysis activities. The total number of generated events was O(130 MEvents).

One of the improvements in CSA08 was the inclusion of HLT bits in the samples at the Tier-0 level. On the other hand, data transfers from Tier-0, Tier-1s and Tier-2s were extensively commissioned through load tests.

B.5 The Computing, Software and Analysis challenge of 2008

The goal of the CMS Computing Software and Analysis challenge (CSA08)[76] has been to test the full scope of offline data handling and analysis activities which will be needed for the CMS data-taking during the LHC operations in 2008. It constitutes the first full-scale challenge with large statistics under the conditions expected at LHC startup: initial mis-alignments and mis-calibrations as expected before collisions, and event signatures and rates typical for low instantaneous luminosity. The focus for this exercise is on the offline detector commissioning, with calibration and alignment constituting the central components.

The scope of the prompt alignment and calibration activities conducted during CSA08 is to demonstrate the complete workflow in as realistic a manner as possible. This includes the reconstruction of the data at the Tier-0, performing the skims selecting the information for the alignment and calibration algorithms on the basis of HLT bits, including necessary background rejection, and running these algorithms at the CAF with a low turn-around latency in the generation of new constants. The scope includes monitoring of all these steps wherever possible. The full complexity of almost 20 calibration and alignment workflows intended for startup were run concurrently, with interdependencies taken into account. The schedule was matched to the pace of the reconstruction, and alignment and calibration were performed in real-time, with resulting constants used to re-reconstruct the data. All exercises are technically conducted as prompt calibration and alignment workflows, though some of them, for example muon system alignment with high p_T muons, require data-sample sizes that in reality will, at least initially, require several weeks or months to collect.

The main goals of the physics activities are the demonstration of near real-time feedback on the quality of the reconstruction of physics objects and the carrying out of four detailed physics analysis intended for early data, based on both the prompt and re-reconstructed data.

Two representative operations scenarios were chosen for the purposes of CSA08: the 43 configuration with a luminosity of $L = 2\times 10^{30}cm^2s^{-1}$ and the 156 configuration with a luminosity of $L = 2\times 10^{31}cm^2s^{-1}$. Data samples for the challenge were created for both scenarios: the sample called S43 for the first scenario and the sample called S156 for the second. It takes 6 days at 100% efficiency to accumulate 1 pb^{-1} at $L = 2\times10^{30}cm^2s^{-1}$ and 10 pb^{-1} at $L = 2\times 10^{31}cm^2s^{-1}$ (or a month at 20% duty cycle). This may be more than the actual time available to accumulate data at these configurations, but the scenarios are meant to represent the average over several machine configurations.

B.6 Cosmic Run At Four Tesla 2008

After the short period of beam operation the CMS Collaboration conducted a month-long data-taking exercise known as the Cosmic Run At Four Tesla (CRAFT) [81]. In addition to commissioning the experiment operationally for an extended period, the cosmic muon dataset collected during CRAFT has proven to be extremely useful for understanding the performance of the CMS experiment as a whole.

The objectives of the CRAFT exercise were the following:

- Test the solenoid magnet at its operating field (3.8 T), with the CMS experiment in its final configuration underground.
- Gain experience operating CMS continuously for one month.
- Collect approximately 300 million cosmic triggers for performance studies of the CMS subdetectors.

The detector was fully instrumented and all the sub-systems were involved in the data taking. The magnet was commissioned again during this period in its final configuration at the UX5 cavern, giving the opportunity to measure the momentum of the cosmic muons. One of the drawbacks of the previous global runs GRUMM and CRUZET was due to the fact that no momentum measurement was possible because the magnet was not connected. This is important, as many calibration workflows have a strong dependency on the momentum of the muons.

Although the CRAFT exercise took place from October 13 until November 11, 2008, the analysis of CRAFT data extended during the following months, being extremely useful from the point of view of the calibration and alignment procedures of all the subsystems.

Appendix C

Crosschecks of different sets of measurements in the internal alignment

The different sets of measurements available for the internal alignments are not able to provide a full description of the internal geometry of the chambers. Nevertheless, these sets of measurements are not in general orthogonal because there is partially redundant information. The identification and comparison of this common information is very useful to crosscheck the compatibility of these measurements.

For this analysis, the formalism explained in chapter 2 will be used. Each configuration of misalignments in the 8 ϕ layers of the drift tubes, can be expressed with a vector of 8 components (per alignment parameter). In addition, it is possible to define a basis of misalignment vectors able to describe completely every possible misalignment. For instance, the δ_x alignment parameter can be described as

$$\vec{\delta_x} = \sum_i a_i \vec{e_i} \tag{C.1}$$

where $\vec{e_i}$ are the vectors of the basis. The simplest selection of this basis is the canonical one, in which every vector in the base describes uniquely the misalignment in a given chamber.

Within this formalism, the fact that the different sets of measurements are not able to fully describe the internal geometry, can be interpreted as the incapability of these measurements to cover the full vectorial subspace of misalignments. For instance, quality control measurements were taken before the assembly of the superlayers, and hence do not contain information about the alignment of the layers in one superlayer with respect to layers in the other. In addition, these measurements were referred to an external point fixed in the assembly table. This reference was lost as long as the superlayer was retired from the table.

In algebraic terms, these restrictions can be expressed as vectorial subspaces within the full vectorial space that are not accessible for the QC measurements. In particular, there are two vectors which generate this not accessible subspace: the relative alignment of the superlayers, and the averaged alignment of all the layers in one superlayer (which is not known given the fact that the reference is lost after the assembly of the chamber). The expression of these two vectors in term of the canonical basis is the following.

$$\vec{e_{SL}} = \frac{1}{\sqrt{8}}(\sum_{i=5}^{i=8}\vec{e_i} - \sum_{i=1}^{i=4}\vec{e_i}) \tag{C.2}$$

$$\vec{e_{layer}} = \frac{1}{2}(\sum_{i=5}^{i=8}\vec{e_i}) \tag{C.3}$$

Figures C.1(a) and C.1(b) show schematically these vectors. It is important to remark that the partner vector for the first superlayer is not included because it is a linear combination of the other two.

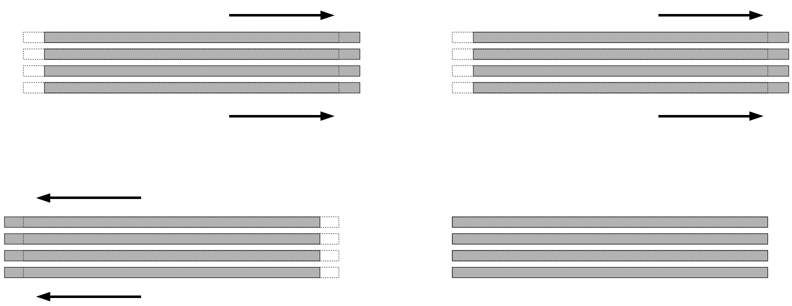

(a) (b)

Figure C.1: The vectorial subspace generated by these two configurations is not accessible by the QC measurements

Survey measurements, on the contrary, do not have any information about the individual position of the layers inside the superlayers. The reference of these measurements is always the first superlayer, and therefore only the vector related to the relative alignment of the two superlayers $\vec{e_{SL}}$ participates in these measurements.

In the case of the track-based alignment, the non accessible vectorial subspace is generated by those eigenvectors with a null associated eigenvalue. These eigenvectors are by definition the weak modes exposed in chapter 5, and constitute the kernel of the matrices associated to the residual minimization, typical of the track-based alignment algorithms.

QC and survey measurements are completely orthogonal. There is no overlap region in the vectorial subspaces generated by these type of measurements, so they can be combined. The redundant part of the measurements is therefore the intersection between the vectorial spaces accessible by the QC and survey, and the vectorial subspace accessible with tracks. Provided that the solution given by the track-based alignment procedure contains only, by construction, information from the non-vanishing eigenvectors, it is possible to get the redundant part in the QC and survey measurements by projecting them into the space of the non-vanishing eigenvectors.

$$\vec{\delta_x}^{qc+survey} = \sum_i (\vec{\delta_x}^{qc+survey}\vec{v_i})\vec{v_i} \tag{C.4}$$

where i is running over the non zero eigenvalues, and $\vec{v_i}$ denotes the associated eigenvectors. This quantity can be directly compared with the solution obtained using track-based alignment as it was shown in chapter 5.

Appendix D

Complete set of alignment parameters: photogrammetry measurements

A complete set of plots describing the photogrammetry alignment parameters and including all the wheels can be found below. In this polar representation the angular coordinate is the real angular position of the sectors, while the radius is the magnitude of the alignment parameter.

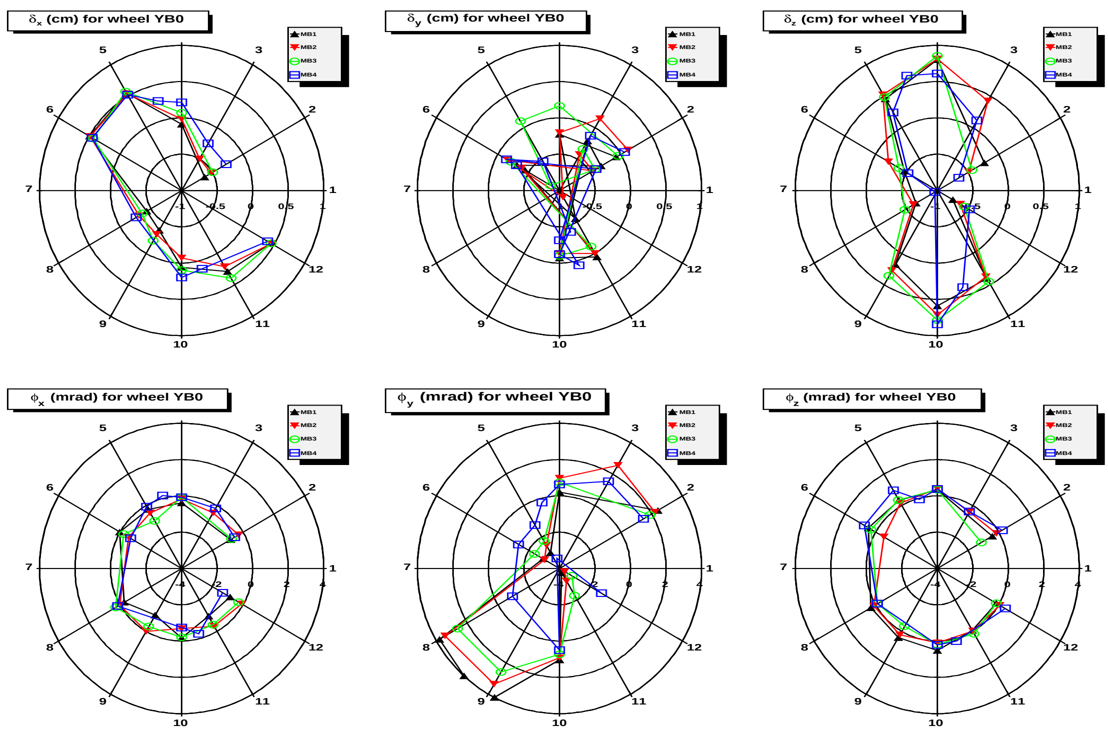

Figure D.1: From top-left to bottom-right, δ_x, δ_y, δ_z, ϕ_x, ϕ_y and ϕ_z alignment parameters for wheel 0 at the surface. The radius of these plots, represents the values of the plot 6.3, while the sector number is represented in the polar coordinate, mimicking their real position if the wheel is observed from the +Z side. It is important to remark that the 0 corresponds to the second inner circle.

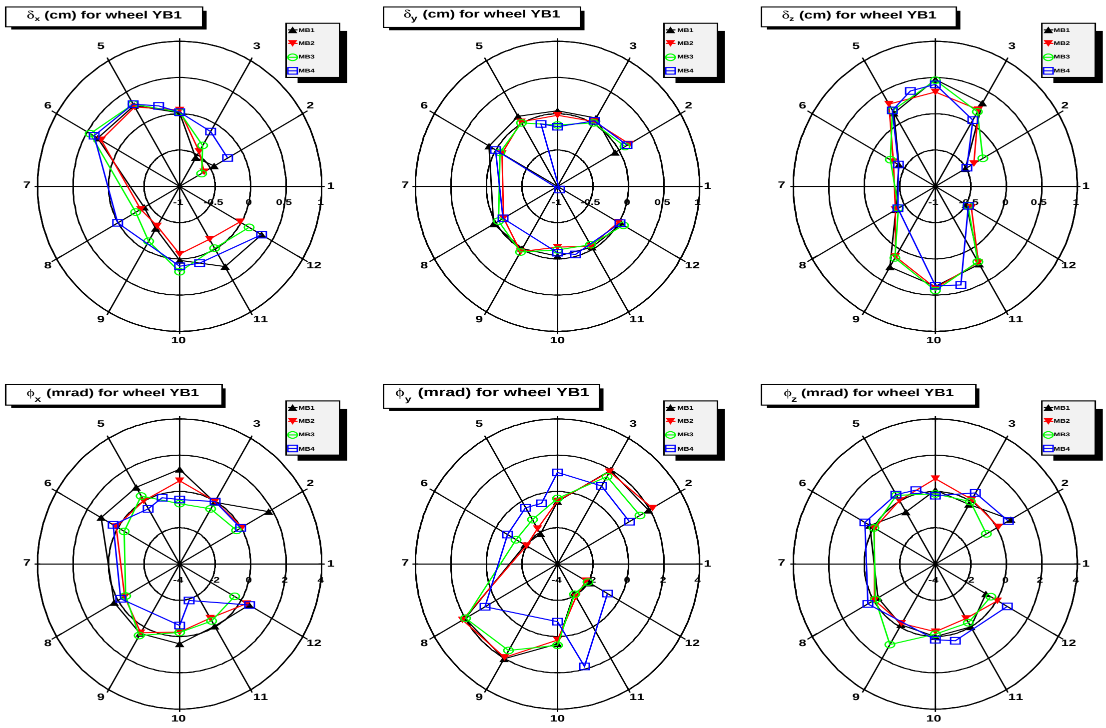

Figure D.2: From top-left to bottom-right, δ_x, δ_y, δ_z, ϕ_x, ϕ_y and ϕ_z alignment parameters for wheel 1 at the surface. The radius of these plots, represents the values of the plot 6.3, while the sector number is represented in the polar coordinate, mimicking their real position if the wheel is observed from the +Z side. It is important to remark that the 0 corresponds to the second inner circle.

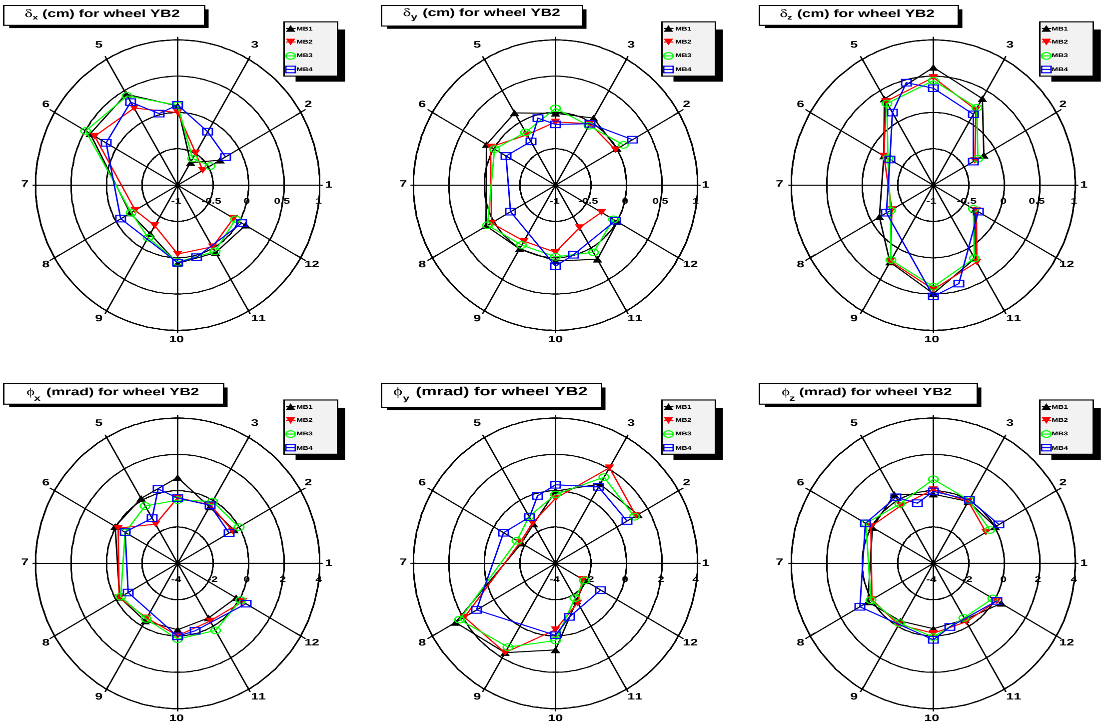

Figure D.3: From top-left to bottom-right, δ_x, δ_y, δ_z, ϕ_x, ϕ_y and ϕ_z alignment parameters for wheel 2 at the surface. The radius of these plots, represents the values of the plot 6.3, while the sector number is represented in the polar coordinate, mimicking their real position if the wheel is observed from the +Z side. It is important to remark that the 0 corresponds to the second inner circle.

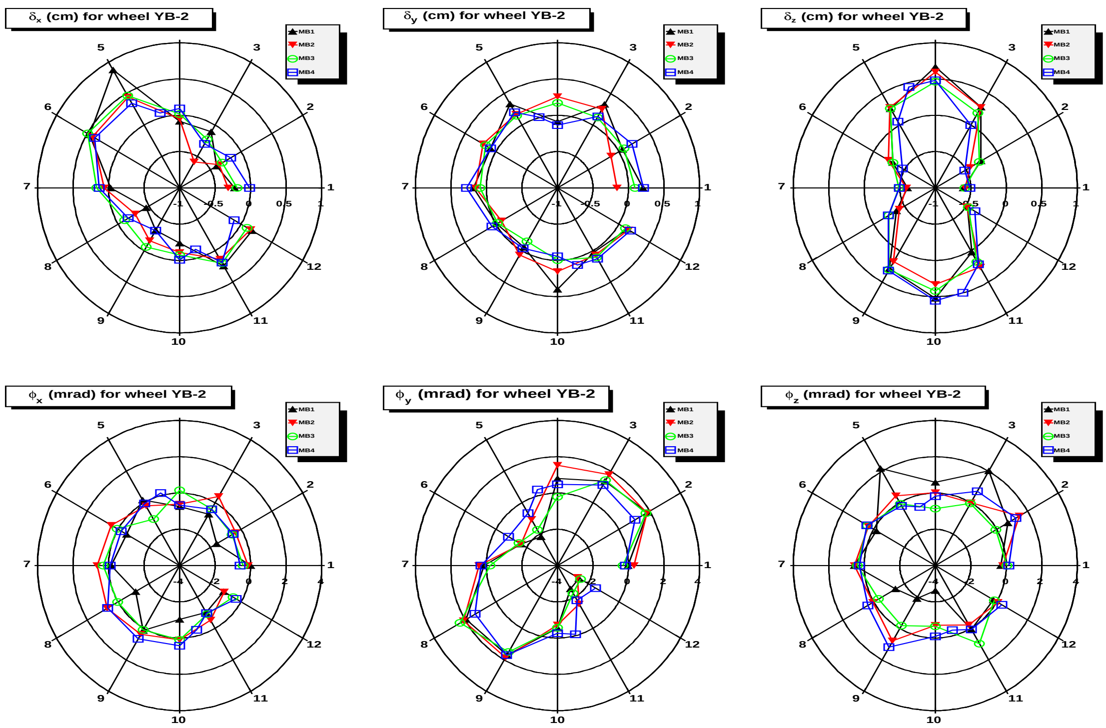

Figure D.4: From top-left to bottom-right, δ_x, δ_y, δ_z, ϕ_x, ϕ_y and ϕ_z alignment parameters for wheel -2 at the pit. The radius of these plots, represents the values of the plot 6.3, while the sector number is represented in the polar coordinate, mimicking their real position if the wheel is observed from the +Z side. It is important to remark that the 0 corresponds to the second inner circle.

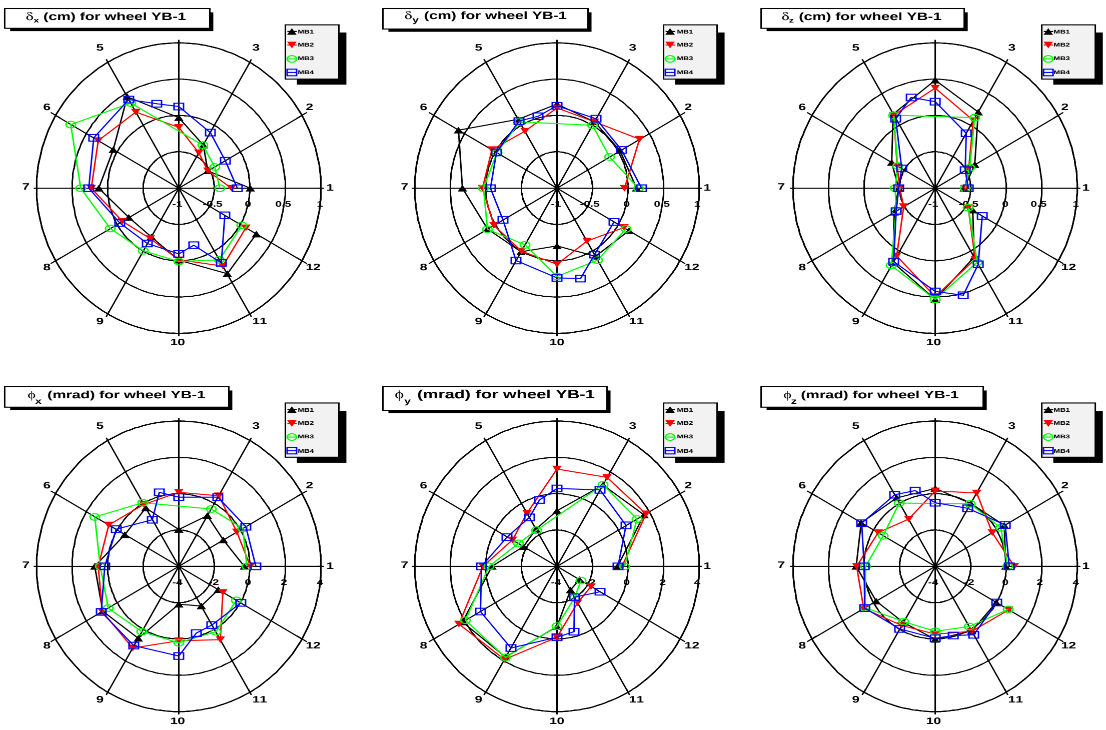

Figure D.5: From top-left to bottom-right, δ_x, δ_y, δ_z, ϕ_x, ϕ_y and ϕ_z alignment parameters for wheel -1 at the pit. The radius of these plots, represents the values of the plot 6.3, while the sector number is represented in the polar coordinate, mimicking their real position if the wheel is observed from the +Z side. It is important to remark that the 0 corresponds to the second inner circle.

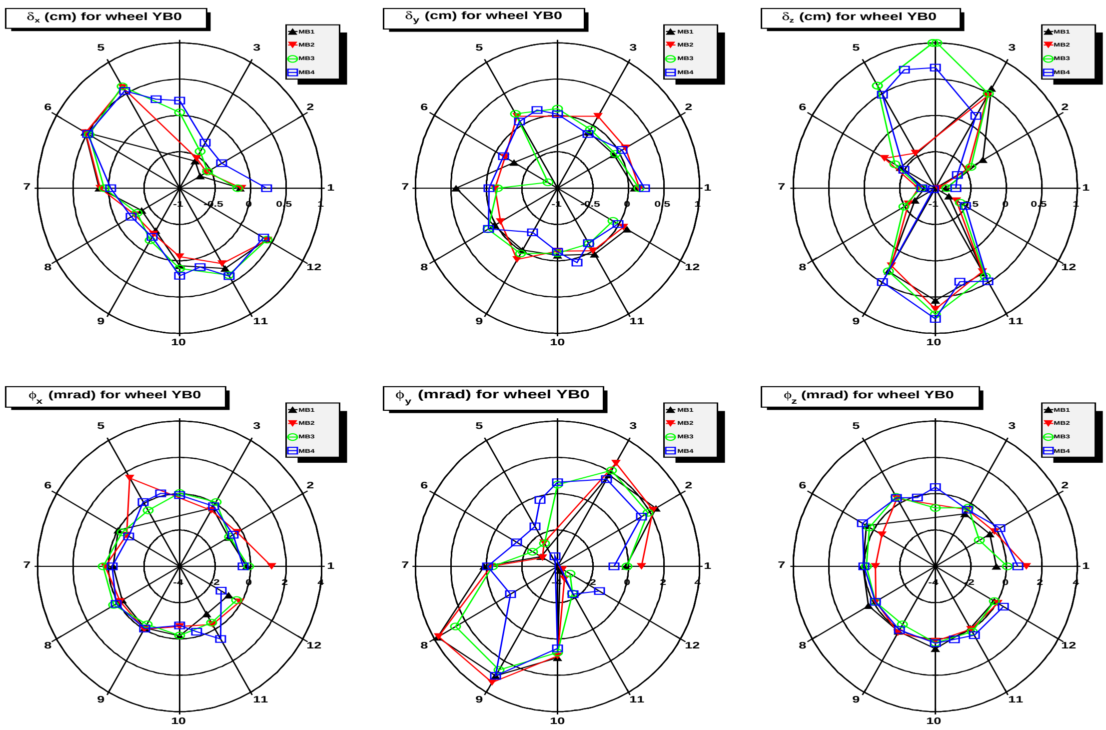

Figure D.6: From top-left to bottom-right, δ_x, δ_y, δ_z, ϕ_x, ϕ_y and ϕ_z alignment parameters for wheel 0 at the pit. The radius of these plots, represents the values of the plot 6.3, while the sector number is represented in the polar coordinate, mimicking their real position if the wheel is observed from the +Z side. It is important to remark that the 0 corresponds to the second inner circle.

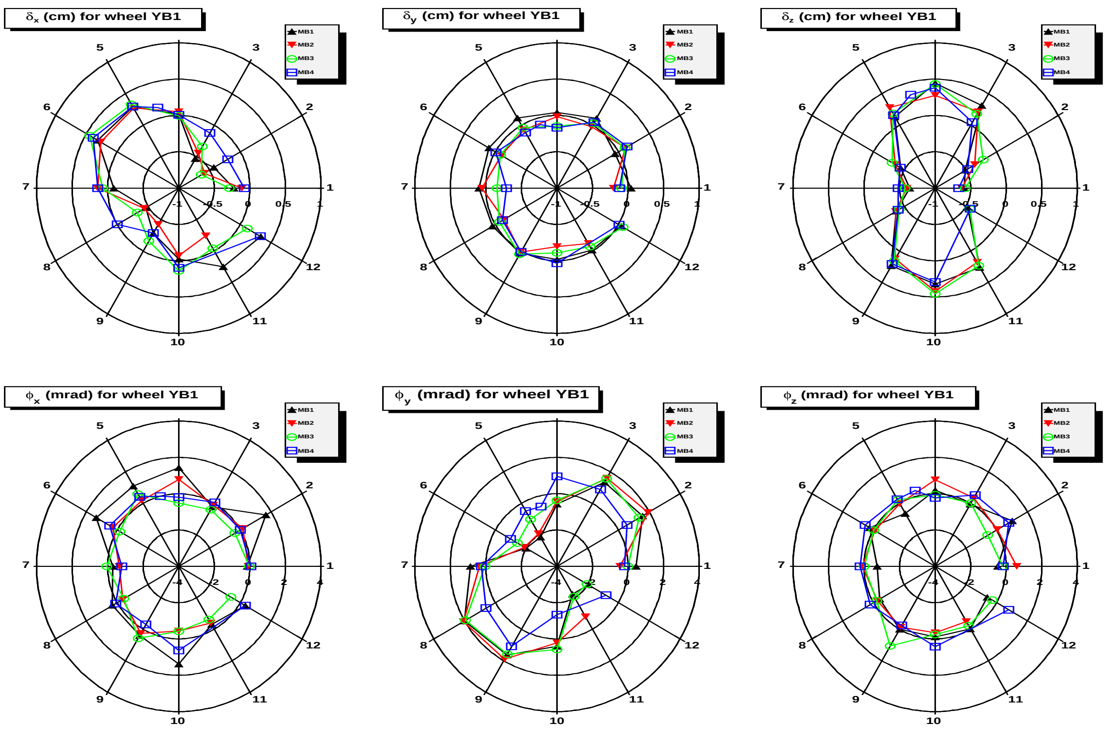

Figure D.7: From top-left to bottom-right, δ_x, δ_y, δ_z, ϕ_x, ϕ_y and ϕ_z alignment parameters for wheel 1 at the pit. The radius of these plots, represents the values of the plot 6.3, while the sector number is represented in the polar coordinate, mimicking their real position if the wheel is observed from the +Z side. It is important to remark that the 0 corresponds to the second inner circle.

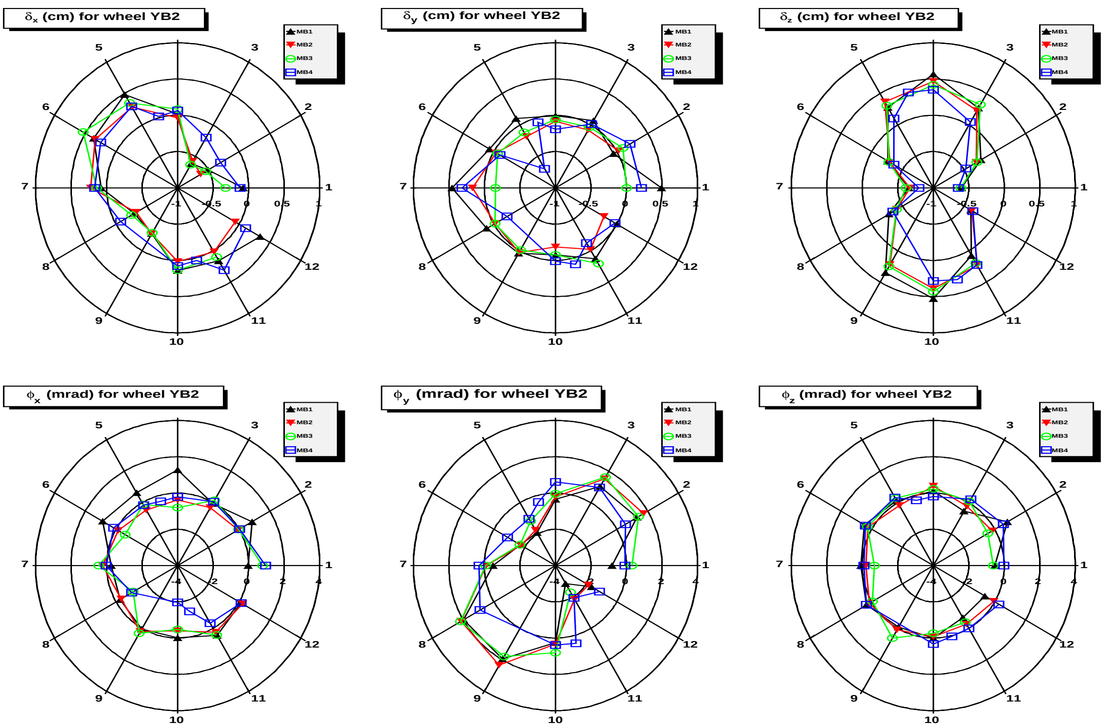

Figure D.8: From top-left to bottom-right, δ_x, δ_y, δ_z, ϕ_x, ϕ_y and ϕ_z alignment parameters for wheel 2 at the pit. The radius of these plots, represents the values of the plot 6.3, while the sector number is represented in the polar coordinate, mimicking their real position if the wheel is observed from the +Z side. It is important to remark that the 0 corresponds to the second inner circle.

Appendix E

Aligned chambers for the photogrammetry and global MBAA campaigns

E.1 Aligned chambers in the photogrammetry campaign

Not all the drift tube chambers could be aligned using photogrammetry information because of two reasons: the chamber was not measured by the photogrammetry team, or it was measured but the number of good points was not enough to make a total reconstruction. In many cases this was provoked because the chamber was not installed yet at the moment of the photogrammetry process, or sometimes because the accessibility of the chamber did not allow a correct measurement. Figures E.1 and E.2 show which chambers were aligned for both the surface and pit photogrammetry campaigns.

E.2 Aligned chambers in the global MBAA campaign

The global MBAA algorithm used global muons as input for its calculations. Since the algorithm was first applied to cosmic muons, not all the chambers could be aligned. The direction of the cosmic muons is very close to the vertical, and therefore there are very few cosmic tracks crossing at the same time the external wheels of the barrel and the tracker. This problem affects as well and for the same reason to the vertical sectors 1 and 7. Figures E.3 show the chambers were the number of tracks allowed to perform an alignment with the global MBAA algorithm. It is observed that mainly wheels +2 and -2, and sectors 1 and 7 were exclude from the analysis.

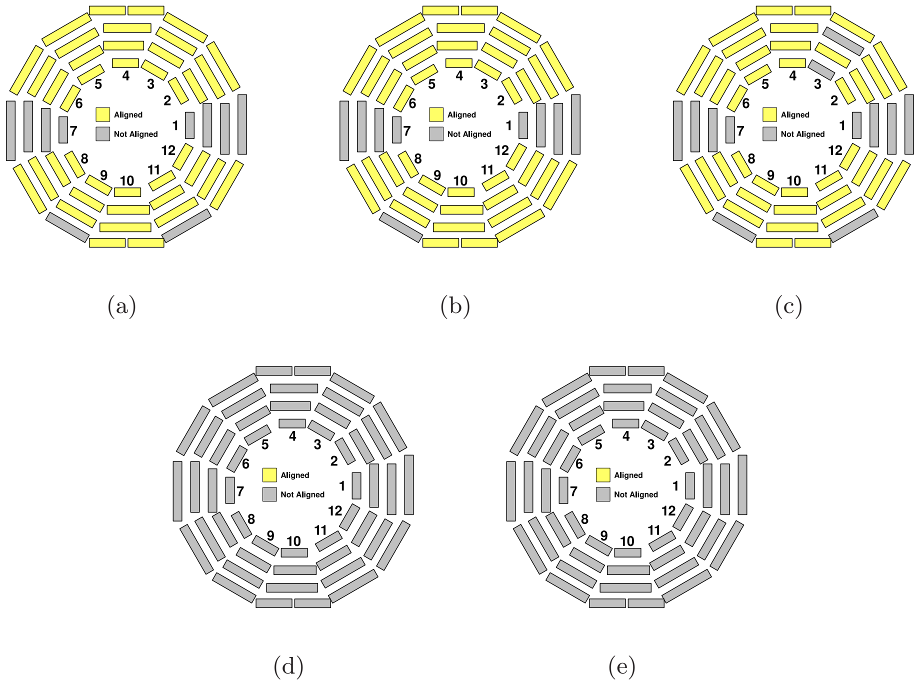

(a) (b) (c)

(d) (e)

Figure E.1: Schematic view showing in yellow the aligned chambers, and in grey the non-aligned chambers, for wheels -2 (a) to 2 (e), using the photogrammetry measurements at the surface.

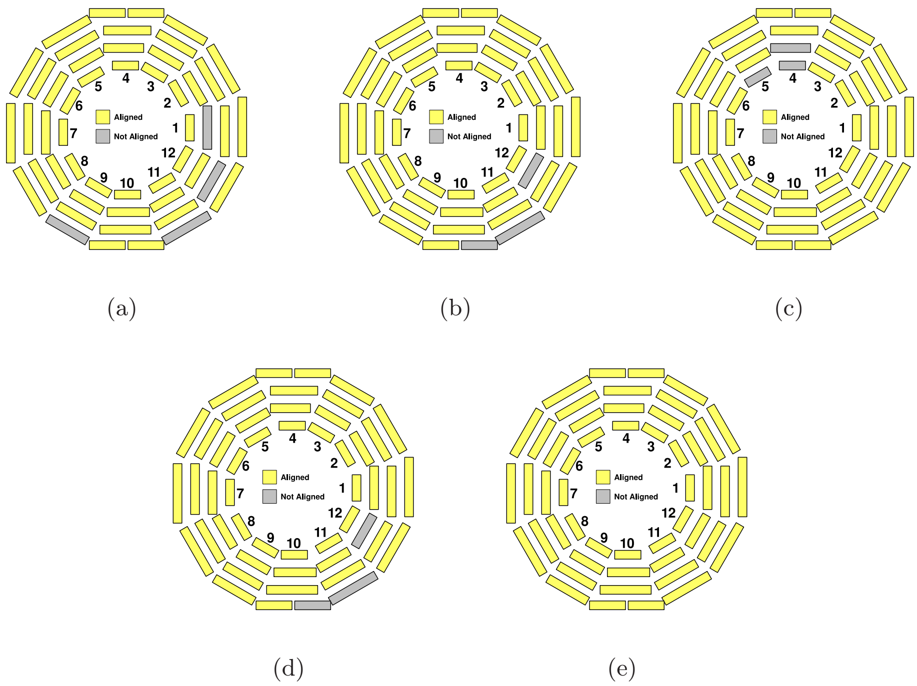

(a) (b) (c)

(d) (e)

Figure E.2: Schematic view showing in yellow the aligned chambers, and in grey the non-aligned chambers, for wheels -2 (a) to 2 (e), using the photogrammetry measurements at the pit.

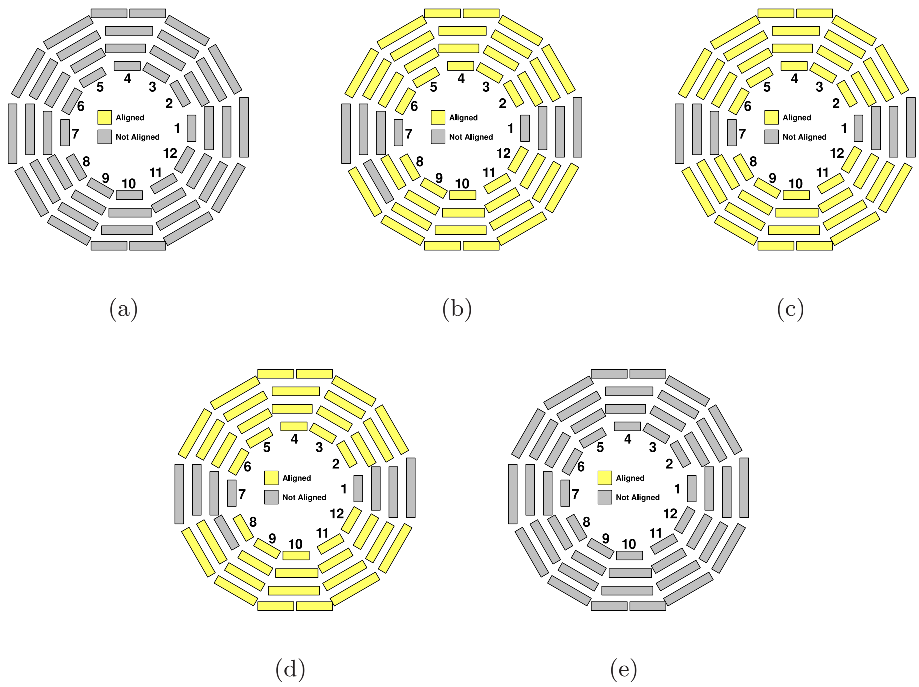

Figure E.3: Schematic view showing in yellow the aligned chambers, and in grey the non-aligned chambers, for wheels -2 (a) to 2 (e), using the global MBAA algorithm.

Appendix F

Calculation of MAB position using photogrammetry information

Photogrammetry measurements are frequently used to provide a first initial location of the components of the optical alignment system. This results in a faster convergence of the reconstruction algorithm (COCOA) and provides robustness against local minima of the system.

It was shown in chapter 6 how the photogrammetry of the DT chambers was processed in order to get the real position of the chamber. A similar technique was applied as well to the position of the MABs (see next section), with the aim of setting their initial position in the configuration file that the link system was using in COCOA.

F.1 Modules for Alignment of the Barrel (MABs)

Modules for Alignment of the Barrel, MABs, are carbon fiber structures (see figure F.1) attached to the faces of the barrel wheels of CMS. They are instrumented with several components of the optical alignment system such as light detectors, lasers, distance-meters, etc. There are two types of MABs: MABs between wheels, which only contain instrumentation for the barrel optical alignment system, and MABs in the external faces of wheels YB-2 and YB+2, which combine instrumentation for the barrel optical alignment system and for the link system.

Concerning the link alignment system, MABs contain the carriers for the two silicon optical detectors (ASPDs), the distance-meter (OMROM) and the laser, distributed as shown in figure F.1. The ASPDs, cross the laser line coming from the link disk attached to the endcap disk. The OMROM is an optical distance-meter located at the MAB and in charge of measuring the radial distance between the MAB and the ME1/1 chamber in the endcap. The laser hits the ASPDs and arrives to the transfer plate attached as well to the ME1/1.

F.2 Photogrammetry information and mathematical processing

Photogrammetry was performed over the different components of the MABs in different systems of reference. For instance the MABs were measured once they were installed in the wheels, using the reference system associated to the wheel described in chapter 5. On the

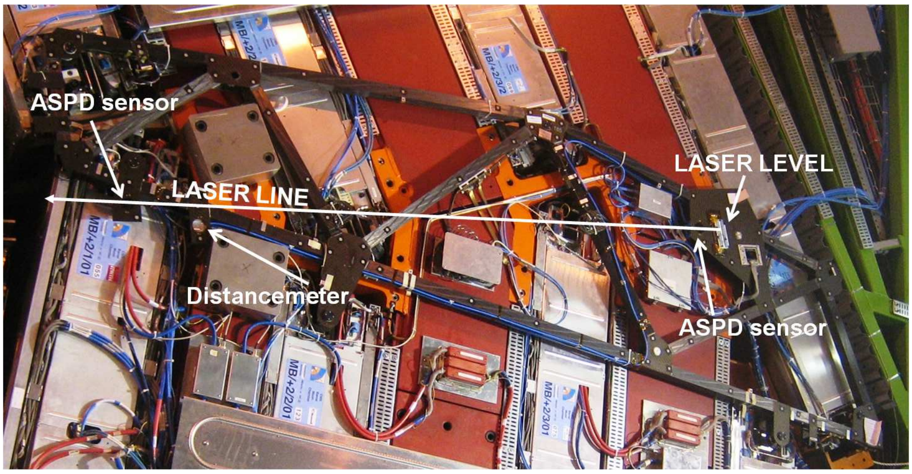

Figure F.1: Module for Alignment of the Barrel (MAB) attached to the face of the wheel. The MAB is the carrier of the instrumentation of the optical alignment system.

other hand, photogrammetry of other elements was performed in a calibration bench installed at the ISR facilities at CERN. In addition to photogrammetry, precision measurements were performed using a contact-3D machine at IFCA (Instituto de Fisica de Cantabria). At the end, the following sets of measurements were available:

- The 5 photogrammetry targets attached to the MABs, measured in two situations: once they were installed in the wheel, and using the system of coordinates of the wheel, and measured at the calibration bench at the ISR, using the reference system of the bench.
- The 3 photogrammetry targets inserted in the supporting structures of the ASPDs, for both top and bottom, and in the reference system fixed to the bench of the ISR, and in the reference system defined by the contact-3D machine.
- Measurement of the center of the ALMY in the reference system defined for the contact-3D machine.
- The 3 photogrammetry targets inserted in the carrier of the distance-meter, using the ISR system, and using the reference system of the contact-3D machine.
- Measurements of the center of the distance-meter in the system of reference defined for the contact-3D machine.
- The 4 photogrammetry targets inserted in the carrier of the laser, using the ISR system and the system defined by the contact-3D machine.
- Measurements of the center of the distance-meter in the reference system defined by the contact-3D machine.

COCOA utilizes a model in which geometrical structures are hierarchically organized as parent and child nodes. The position and orientation of a child is always provided in the reference system of the parent. In order to create a description file for the current case, the MAB must be described in the system of reference of the wheel, the supporters of the ALMYs, the distance-meter and the laser in the system of the MAB; and their detecting centers, in their own system of reference.

The conversions between the different systems of coordinates are not explicitly known, making impossible to build the hierarchy. For instance, when the MAB is placed in the wheel, not only its position must be provided, but also its orientation. This assigns a new direction for the coordinated axis which define the system of coordinates of the children objects. If afterwards, some of the child structures have to be located in that system of reference, and their measurements are given in the ISR frame, it is necessary to know how both system of coordinates are related.

A conversion between two systems of reference is defined by a vector $\vec{a}$ and a rotation matrix $\mathbf{R}$, in such a way that every point in both systems, parent and child, holds the following relation:

$$\vec{x}_i^{child} = \mathbf{R}\vec{x}_i^{parent} + \vec{a} \tag{F.1}$$

In the current case, it is necessary to calculate $\vec{a}$ and $\mathbf{R}$ for each of the transformations. As the photogrammetry measurements provide the position of several points in both reference systems, it is possible to calculate the conversion parameters by minimizing a χ^2, as it was done in chapter 6. In this case, the expression of the χ^2 is as follows:

$$\chi^2 = \sum_i (\vec{x}_i^{child} - \mathbf{R}\vec{x}_i^{parent} - \vec{a})^T \mathbf{E_i} (\vec{x}_i^{child} - \mathbf{R}\vec{x}_i^{parent} - \vec{a}) \tag{F.2}$$

where $\mathbf{E_i}$ is the covariance matrix, which is in fact a multiple of the unit matrix, provided the error of all the photogrammetry measurements is the same. It is important to remark that in this case the rotation matrix is not linear, as the rotations between frames could be large. In order to solve the system a non-linear minimization is performed using MATLAB [105]. The Euler angles extracted from the resulting rotation matrix, are the angles used to define the new direction of the object in COCOA.

F.3 Application to the MABs in YB+2

The procedure explained above was applied in order to calculate the COCOA description file for the ALMYs, the distance-meter and the laser of the three MABs instrumented for the MTCC (see appendix B). The laser required two calculations in order to convert the MAB system into the ISR, and the ISR into the system of the laser supporter. The ALMYs and the distance-meter only required one calculation, from the MAB to the ISR system. The measurements from the contact-3D machine were not used, because the differences with respect to the nominal positions were very small compared to the misalignments of the whole MAB structure. The photogrammetry information was collected from document [106] for the position of the mabs with respect to YB+2, and in [107], [108] and [109] for the components of the mabs in the ISR.

Tables F.1, F.2 and F.3 show the results of the algorithm applied over the three MABs. The COCOA description files generated with this information achieved a better χ^2 since the first iteration, and were used in order to perform the reconstruction for the MTCC geometry described in [66]. The procedure developed in this appendix was used to recalculate the initial position of the MABs once CMS was installed at the pit.

Obj.	Obj.	Obj.	Obj.	x/cm	y/cm	z/cm	ϕ_x/deg	ϕ_y/deg	ϕ_z/deg
mab				81.542	441.528	0.136	90.99	0.06	-105.74
	Laser. C.			-259.319	0.312	-28.600	88.54	0.85	-0.18
		Coll.		0	-4.35	0	0	0	0
			Laser	0.343	0.757	4.426	0.745	89.08	-0.75
	T. almy C.			-246.83	-6.453	-29.003	60.82	91.65	60.95
		T. almy		3.14	2.45	0	0	0	0
	B. almy C.			6.975	-6.450	-32.395	-117.32	88.46	-117.25
		B. almy		3.14	2.45	0	0	0	0
	Omrom C.			-23.296	-11.044	-43.631	2.40	-60.69	178.05
		Omrom		0.403	-0.94	-0.825	0	90.0	0

Table F.1: Calculated position of the instruments for the mab in YB+2 and line 75 deg.

Obj.	Obj.	Obj.	Obj.	x/cm	y/cm	z/cm	ϕ_x/deg	ϕ_y/deg	ϕ_z/deg
mab				-79.743	-448.629	0.84	91.46	-0.17	74.32
	Laser. C.			-253.704	0.267	-32.581	88.79	0.68	0.19
		Coll.		0	-4.35	0	0	0	0
			Laser	0.343	0.777	4.375	0.7	88.84	-0.7
	T. almy C.			-241.216	-6.508	-32.968	66.88	91.25	66.85
		T. almy		3.14	2.45	0	0	0	0
	B. almy C.			12.659	-0.655	-36.355	-119.32	88.35	-119.23
		B. almy		3.14	2.45	0	0	0	0
	Omrom C.			-17.369	-1.255	-47.607	178.36	-180.77	-180.00
		Omrom		0.403	-0.94	-0.825	0	90.0	0

Table F.2: Calculated position of the instruments for the mab in YB+2 and line 255 deg

Obj.	Obj.	Obj.	Obj.	x/cm	y/cm	z/cm	ϕ_x/deg	ϕ_y/deg	ϕ_z/deg
mab				348.732	-293.631	0.277	91.13	0.10	134.26
	Laser. C.			-254.076	0.009	-32.301	88.80	0.69	-0.29
		Coll.		0	-4.35	0	0	0	0
			Laser	0.343	0.775	4.287	-0.03	90.18	0.03
	T. almy C.			-241.601	-6.772	-32.712	58.92	91.18	58.82
		T. almy		3.14	2.45	0	0	0	0
	B. almy C.			12.297	-6.37	-36.050	48.57	91.08	48.91
		B. almy		3.14	2.45	0	0	0	0
	Omrom C.			-17.767	-1.140	-47.337	179.13	-180.46	-179.73
		Omrom		0.403	-0.94	-0.825	0	90.0	0

Table F.3: Calculated position of the instruments for the mab in YB+2 and line 315 deg

Agradecimientos

En primer lugar, me gustaría agradecer al grupo de Altas Energías del Instituto de Física de Cantabria, por la oportunidad que me brindaron para realizar esta tesis doctoral. Aunque en ciertos momentos el trabajo se hizo bastante duro, el apoyo, el ambiente y el espíritu con que me he encontrado en este grupo ha sido inmejorable.

En este sentido, quisiera mostrar todo mi agradecimiento a mi director de tesis y amigo Francisco Matorras Weinig. En estos cuatro años, he aprendido de él a pensar verdaderamente como un físico. En todas esas horas de pizarra, modelos aproximados y Mathcad que hemos pasado juntos, he aprendido bastante más que en el mejor de los libros o el mejor de los cursos. Ni que decir tiene también que con su buen humor y disposición ha conseguido siempre que venir a trabajar sea algo agradable y divertido. Se me ocurre ahora mismo, que nos quedó por resolver el problema de la deriva de los tiltmeters con el campo magnético. Y eso que aquella solución con el modelo magneto-hidrodinámico, de O(10) páginas tenía -buena- pinta.

También quiero expresar toda mi gratitud y admiración a Teresa Rodrigo Anoro. Bajo su tutela en el CERN, he aprendido lo que es la dedicación y el rigor en la física. Su inagotable capacidad para enfocar y resolver problemas han sido para mí todo un ejemplo a seguir. Adicionalmente, agradezco su preocupación e interés por todos los aspectos de la vida en Ginebra, en los que siempre me mostró su apoyo y ayuda.

Igualmente agradezco a Gervasio Gómez y a Luca Scodellaro, compañeros de fondues y de tantos momentos de risa y diversión. Creo que sobra que diga cualquier otra cosa, porque vosotros ya lo sabéis: muchas gracias por vuestra amistad. También esto lo digo por Alicia Calderón y Mar Sobrón, que habéis pasado por el alineamiento antes que yo, y me habéis ayudado y apoyado siempre en todo.

Mis agradecimientos van mucho más allá entre los componentes del grupo: a Rebeca González, compañera de despacho por una temporada, y con la que he me reído muchísimo (el CERN sin ti no hubiera sido lo mismo). También a Isidro González, fuente siempre de buen rollo y siempre capaz de darte un buen consejo. A Javier Fernández, que tan bien supo siempre esquivar los "besitos" (él seguramente sabe a lo que me refiero), y con el que trabajar fue un auténtico lujo. A Celso Martínez Rivero, con el que di los primeros pasos por el código de CMS. A Marcos Fernández, salsa-man, y en general a todas las personas con las que he trabajado, y con las que siempre he tenido buenos momentos y experiencias: Rocío, Javier, Ibán, Pablo, Álvaro, Luis, Clara, Rafa, Jesús, Amparo, Alberto, Iván, Irma, María, Lara, Dani, Luis Ángel ... espero no dejarme a nadie.

Me gustaría también mencionar a otras personas a las que he conocido a lo largo del desarrollo de esta tesis y que siempre me han ayudado y apoyado. Entre ellas destaco a Mary-Cruz Fouz, Begoña de la Cruz, Pablo García, Ugo Gasparini, Anna Menneguzzo, Kerstin Hoepfner, Gyorgy Bencze, Zoltan Szillasi, Luca Malgeri, Marco Dallavalle,.... Todos ellos siempre depositaron una gran confianza en mí, y eso es siempre de agradecer. Tampoco quiero olvidarme de gente como Alex, Ricci, María, o el cártel de ninjas colombianos.

Cambiando un poco el alcance y los ámbitos, sin duda merecen ser mencionados en estos agradecimientos todos mis amigos que llevan acompañándome y sufriéndome desde hace mucho tiempo. Empiezo por Ignacio Coterillo, y continuo por Miguel Expósito. La verdad es que no tengo palabras por su amistad incondicional. Empezamos hace años una campaña para equilibrar el stock de cerveza mundial, y a día de hoy, todavía no ha habido ninguna acumulación importante en ninguna región del planeta. También me gustaría mencionar a Bruno Casal, a Héctor Otí, a Carlos Díez, a Arturo Medela, a Javier Alonso, a Miguel Martínez, a Manuel del Jesus, a Carlos Barquín, a Enrique de la Puente Campano y a Marina Pelayo (Marini, eres la mejor). Todos ellos saben, así que no hace falta que sea muy explícito.

También quiero agradecer a Lola Saiz Santos el apoyo que me brindó durante el desarrollo de la tesis. Ella es, sin duda, quien más la sufrió (o me sufrió), y aunque al final las cosas no fueron demasiado bien, quiero que sepa que le agradezco todo el apoyo y los momentos que vivimos. Fueron geniales. Y esto va también por Lola Santos, que siempre me mostró todo su cariñño y Ramón Saiz Santos, con el que tengo aún unos pokers pendientes.

Las últimas palabras están dirigidas a mi familia. Para empezar, mis padres Yolanda Ruiz del Árbol, y José Antonio Martínez, que durante toda mi vida han sido sencillamente perfectos, y a los que admiro terriblemente por encima de todo. A mi hermana María Martínez a la que veo más guapa cada día. Y a mi tío Paco Ruiz del Árbol "Tito", y mi abuela Araceli Andérez "Ali", que me dieron una educación, y moldearon lo que soy ahora. Esta tesis está dedicada a vosotros. Por supuesto que también menciono a mi abuela Fany, Jesús, Alicia, Juan e Ignacio, a las "titas" y a mis primos. La lista de nombres es gigantesca, y siempre me dejaré a alguien olvidado, aunque debe saber que también va por ellos.

Muchas gracias.

Bibliography

[1] S.L. Glashow, Nucl. Phys. 22 (1961) 579

[2] A. Salam, J.C. Ward, Phys. Rev. Lett. 13 (1964) 168

[3] S. Weinberg, Phys., Phys. Rev. D 19 (1967) 1264

[4] S.L. Glashow, J. Iliopoulos y L. Maiani, Phys. Rev. D 2 (1970) 1285

[5] P. Anderson, Phys. Rev, Phys. Rev. Lett. 130 (1963) 439

[6] P.W. Higgs, Phys. Rev. Lett. 12 (1964) 132

[7] P.W. Higgs, Phys. Rev. Lett. 13 (1964) 508

[8] P.W. Higgs, Phys. Rev. 145 (1966) 1156

[9] F. Englert y R. Brout, Phys. Rev. Lett. 13 (1964) 321

[10] G.S. Guralnik, C.R. Hagen y T.W.B. Kibble, Phys. Rev. Lett. 13 (1964) 585

[11] T.W.B. Kibble, Phys. Rev. 155 (1967) 1554

[12] Lyndon Evans and Philip Bryant (Editors), The LHC Machine, 2008 JINST 3 S080001

[13] Stephen P. Martin, A Supersymmetry Primer, arXiv:hep-ph/9709356v5, 2008

[14] K. Lane, Technicolor and Precision Tests of the Electroweak Interactions, Proc. of the 27th International Conference on High Energy Physics, Glasgow, 1994

[15] The CMS Collaboration, The CMS experiment at the CERN LHC, 2008 JINST 3 S08004

[16] The ALICE Collaboration, The Alice experiment at the CERN LHC, 2008 JINST 3 S08002

[17] The LHC-b Collaboration, The LHC-b experiment at the CERN LHC, 2008 JINST 3 S08005

[18] The ATLAS Collaboration, The ATLAS experiment at the CERN LHC, 2008 JINST 3 S08003

[19] Rizzo, Thomas G., Probes of universal extra dimensions at colliders, Phys. Rev. D 64: 095010, doi:10.1103/PhysRevD.64.095010, 2001

[20] M. Kobayashi, T. Maskawa, CP-Violation in the Renormalizable Theory of Weak Interaction, Progress of Theoretical Physics 49 (2): 652-657, doi:10.1143/PTP.49.652, 1973

[21] The CMS Collaboration, The Physics Technical Design Report, CERN/LHCC 2005-023 2005

[22] ALEPH, DELPHI, OPAL, SLD, LEP Collaborations, Precision electroweak measurements on the Z resonance., Phys. Rept. 427:257, 2006

[23] ALEPH, DELPHI, L3 and OPAL Collaboration, Search for the Standard Model Higgs boson at LEP, Phys. Lett., Phys. Rev. Lett. 565 (2003) 61

[24] The CDF and D0 Collaborations, Combined CDF and D0 Upper Limits on Standard Model Higgs-Boson Production with 2.1 - 5.4 fb-1 of Data, HCP 2009 conference, Evian, France, arXiv:0911.3930v1, 2009

[25] F. Abe et al., The CDF detector: an overview Export, Nuc. Ins. Met. A, Vol. 271, No. 3. pp. 387-403, 1988

[26] The D0 Collaboration, The Upgrated D0 detector, Nuc. Ins. Met. A, Vol. 565, pp. 463-537, arXiv:physics/0507191v1, 2006

[27] The CMS Collaboration, The Magnet Technical Design Report, CERN/LHCC 97-10 1997

[28] The CMS Collaboration, The Tracker Technical Design Report, CERN/LHCC 98-6 1998

[29] The CMS Collaboration, The ECAL Technical Design Report, CERN/LHCC 97-33 1997

[30] The CMS Collaboration, The HCAL Technical Design Report, CERN/LHCC 97-31 1997

[31] The CMS Collaboration, The Muon Technical Design Report, CERN/LHCC 97-32, 1997

[32] The CMS Collaboration, The Trigger Technical Design Report, CERN/LHCC 2000-38 2000

[33] The CMS Collaboration, The Computing Technical Design Report, CERN/LHCC 2005-023 2005

[34] The CMS Collaboration, The CMS software page; `http://cms-cpt-software.web.cern.ch/cms-cpt-software/General/`

[35] M.De Gruttola et al., Persistent storage of non-event data in the CMS databases, CMS Note

[36] The Oracle corporation, `http://www.oracle.com`

[37] The Globus Project, `http:www.globus.org`

[38] G. Abbiendi et al., Muon Reconstruction in the CMS Detector, CMS AN-2008/097 2008

[39] The CMS Collaboration, Results On Local Muon Reconstruction in DT Chambers From Analysis of Cosmic Muon Data, submitted to JINST

[40] F. Matorras, A. Meneguzzo, Requirements on the alignment errors of MS based on muon PT resolutions CMS-TN 1995/069

[41] The CMS Collaboration, Alignment of the CMS Silicon Tracker during Commissioning with Cosmic Rays , sub. to JINST (2009)

[42] The CMS Collaboration, Alignment of the CMS Muon System with Tracks from Cosmic Ray and Beam-Halo Muons, submitted to JINST (2009).

[43] P. Arce and A. Lopez-Virto, CMS Object Oriented Code for Optical Alignment, CMS Note 2002/060 (2002)

[44] P. Arce, Object Oriented Software for Simulation and Reconstruction of Big Alignment Systems, Proc. of 7th International Workshop on Accelerator Alignment (IWAA), Spring-8, Japan (2002)

[45] P. Arce, Object Oriented Software for Simulation and Reconstruction of Big Alignment Systems, Proc. of 7th International Workshop on Accelerator Alignment (IWAA), Grenoble, France (1999)

[46] V. Karimaki, A. Heikkinen, T. Lampen, T. Linden, Sensor Alignment by Tracks, Proc. of 2003 Conference for Computing in High Energy and Nuclear Physics, La Jolla, California, eConf C0303241, TULT008, 6pp. (2003) [arXiv:physics/0306034]

[47] T. Lampen, V. Karimaki, S. Saarinen, O. Buchmuller, Alignment of the Cosmic Rack with the Hits and Impact Points Algorithm, CERN-CMS-NOTE-2006-006

[48] V. Karimaki, T. Lampen, F. Schilling, The HIP Algorithm for Track Based Alignment and its Application to the CMS Pixel Detector, CERN-CMS-NOTE-2006-018

[49] R. Fruhwirth et al, Estimation of detector alignment parameters using the Kalman filter with annealing", 2003 J. Phys. G: Nucl. Part. Phys. 29 561-574

[50] V. Blobel, Software alignment for tracking detectors, Nucl. Instrum. Meth. A566 (2006) doi:10.1016/j.nima.2006.05.157

[51] V. Blobel, C. Kleinwort, A new method for the high-precision alignment of track detectors, Proc. PHYSTAT2002, Durham [arXiv-hep-ex/0208021]

[52] V. Blobal, Millepede manual, `http://www.desy.de/~blobel/wwwmille.html`

[53] F. Matorras, Muon Station movements and coordinate measurement, CMS TN-1995/097

[54] The CMS Collaboration, Calibration of the barrel muon drift tubes of CMS, Nuc. Ins. and Met. A, doi:10.1016/j.physletb.2003.10.071

[55] K. Groupen, Particle Detectors, Cambridge University Press, ISBN 0 521 55216 8, (1996)

[56] The SQLite web page, `http://www.sqlite.org/`

[57] G. Flucke, D. Futyand, R. Mankel, The CMS Framework for Alignment and Calibration, XII Advanced Computing and Analysis Techniques in Physics Research November 3-7, 2008 Erice, Italy

[58] The CMS Collaboration, From Detector to Analysis: CMS Data Processing Workflows During an Extended Cosmic Ray Run, submitted to JINST (2009)

[59] David Futyan, Commissioning of the CMS Alignment And Calibration Framework, proc. of Computing In High Energy Physics 2009, Prague, Czech Republic

[60] The CMS Collaboration, CAF twiki page, https://twiki.cern.ch/twiki/bin/view/CMS/CAF.

[61] Rene Brun and Fons Rademakers, ROOT - An Object Oriented Data Analysis Framework, Proceedings AIHENP96 Workshop, Lausanne, Sep. 1996, Nucl. Inst. Meth. in Phys. Res. A 389 (1997). http://root.cern.ch

[62] S. Kosyakov et al., FroNtier: High Performance Database Access using Standard Web Components in a Scalable Multi-Tier Architecture, proc. of Computing in High Energy Physics, Interlaken, Switzerland (2004)

[63] T. Sjstrand, P. Edn, C. Friberg, L. Lnnblad, G. Miu, S. Mrenna and E. Norrbin, Computer Phys. Commun. 135 (2001) 238 (LU TP 00-30, hep-ph/0010017)

[64] M.L. Mangano, M. Moretti, F. Piccinini, R. Pittau, A.D. Polosa, ALPGEN, a generator for hard multiparton processes in hadronic collisions, JHEP 0307 (2003) 001, arXiv:hep-ph/0206293v2

[65] J. Allison, Geant4 - A Simulation Toolkit, Nuclear Physics News, Volume 17 Issue 2, April 2007, doi:10.1080/10506890701404297

[66] A. Calderon et al., Motions of CMS detector structures due to the magnetic field forces as observed by the Link alignment system during the test of the 4 T magnet solenoid, Nuc. Ins. Met. A, Volume 606, Issue 3, 21 July 2009, Pages 344-361

[67] The ORCA web page, http://cmsdoc.cern.ch/cms/OO/Reconstruction/

[68] P. Martinez et al., Simulation of Misalignment Scenarios for CMS Tracking Devices, CMS NOTE-2006/008 (2006)

[69] P. Martinez et al., Influence of misalignment scenarios on muon reconstruction, CMS NOTE-2006/017 (2006)

[70] Python web page http://www.python.org/

[71] P. Martinez et al., A software and computing prototype for CMS muon system alignment, 2008 J. Phys.: Conf. Ser. 119 072008

[72] The CMS Collaboration, CMS Computing, Software and Analysis Challenge in 2006 (CSA06), CMS NOTE 2007-006 (2007)

[73] The CMS Collaboration, CMS Computing, Software and Analysis Challenge in 2007 (CSA07) https://twiki.cern.ch/twiki/bin/viewauth/CMS/CSA07

[74] The CMS Collaboration, The CMS Magnet Test and Cosmic Challenge (MTCC Phase I and II), CMS NOTE 2007-005 (2007)

[75] G. Abbendi et Al., Muon Reconstruction in the CMS Detector, CMS AN-2008/097

[76] R. Mankel, D. Futyand, Computing, Software and Analysis Challenge, Proc. of CHEP09, Prague, Czech Republic, (2009)

[77] The CMS Collaboration, GRUMM analysis page, https://twiki.cern.ch/twiki/bin/viewauth/CMS/GRUMMAnalysis

[78] The CMS Collaboration, CRUZET analysis page,
https://twiki.cern.ch/twiki/bin/viewauth/CMS/CRUZETAnalysis

[79] The CMS Collaboration, MWGR analysis page,
https://twiki.cern.ch/twiki/bin/viewauth/CMS/MWGRSummaries

[80] The CMS Collaboration, October Exercise,
https://twiki.cern.ch/twiki/bin/viewauth/CMS/OctoberX

[81] The CMS Collaboration, The CMS CRAFT Exercise, submitted to JINST (2009)

[82] Oana Vickey Boeriu, Searches for Supersymmetry in All-Hadronic and Lepton+Jets+MET Final States in CMS, CMS CR-2008/106, (2008)

[83] M. Cvetic y S. Godfrey, Discovery and identification of extra gauge bosons, Electroweak symmetry breaking and new physics at the TeV scale, pages 383-415, World Scientific, 1996, arXiv:hep-ph/9504216

[84] The CMS DT Chambers Collaboration Group, Drift Tubes Quality Control Manual and Procedures,
http://www.to.infn.it/activities/experiments/cms/QUALITY/QCMANUAL/qcqa.pdf, February (2002)

[85] M. C. Fouz, J. Puerta, Quality Control Procedures Applied to Test the Performance of the CMS Muon Drift Chambers Built at CIEMAT, CMS NOTE, NT-2004/012, (2004)

[86] Institute for Theoretical Physics RWTH Aachen, Germany,
http://wwwdbac.physic.rwth-aachen.de/

[87] Legnaro National Laboratories (INFN), Italy,
http://dbcms.pd.infn.it/db/

[88] Centro de Investigaciones Energeticas, Medioambientales y Tecnologicas (CIEMAT), Spain,
http://wwwae.ciemat.es/cms/ChamberConsDb/db.html

[89] INFN Sezione di Torino, Italy,
http://tok17w2.to.infn.it/mb4adm/Chambers.php

[90] The CERN Drift Tube chamber database
http::/oraweb03.cern.ch:9000/pls/cms_mb_prod/chambers.main

[91] University of Debrecen, Institute of Experimental Physics, Hungary,
http://kismalac.phys.klte.hu/bnoemi/ch_indexpage.html

[92] The CERN Engineering and Equipment Data Management Service,
http://edms.cern.ch

[93] R. Goudard, et al., Photogrammetry of YB0 Muon Chambers on SX5, May, June and July 2006, edms: CMS-SG-UR-0056

[94] R. Goudard, et al., Photogrammetry of YB1 Muon Chambers on SX5, November 2005, edms: CMS-SY-UR-0024

[95] R. Goudard, et al., Photogrammetry of YB2 Muon Chambers on SX5, October 2005, edms: CMS-SY-UR-0019

[96] R. Goudard, et al., Photogrammetry of YB2 Muon Chambers on UX5, January-February 2007, edms: CMS-SG-UR-0074

[97] R. Goudard, et al., Photogrammetry of YB1 Muon Chambers on UX5, February 2007 and January 2008, edms: CMS-SG-UR-0112

[98] R. Goudard, et al., Photogrammetry of YB0 Muon Chambers on UX5, April 2007 and January 2008, edms: CMS-SG-UR-0078

[99] R. Goudard, et al., Photogrammetry of YB-1 Muon Chambers on UX5, November 2007 and March 2008, edms: CMS-SG-UR-0110

[100] R. Goudard, et al., Photogrammetry of YB-2 Muon Chambers on UX5, October-December 2007 and January 2008, edms: CMS-SG-UR-0109

[101] R. Goudard, et al., YB0 with respect to LHC beam axis on UX5, April-May 2008, edms: CMS-SG-UR-0114

[102] A. Calderon, Internal CMS meetings and private communications

[103] M. Aldaya, P. Garcia-Alba, Measurement of the Charge Ratio of Cosmic Muons using CMS Data, ICHEP08, Philadelphia, USA, July 2008, arXiv:0810.3515v1

[104] P. Spagnolo, et al., Internal CMS meetings and private communications

[105] The Mathworks company, MATLAB software, `http://www.mathworks.com`

[106] The CMS photogrammetry team, Position of the MABs 187, 188 and 191 with respect to YB+2, CMS-MA-UR-0059, edms:761853

[107] The CMS photogrammetry team, Photogrammetry of the MAB 187 at the calibration bench at the ISR, edms:473704

[108] The CMS photogrammetry team, Photogrammetry of the MAB 188 at the calibration bench at the ISR, edms:452754

[109] The CMS photogrammetry team, Photogrammetry of the MAB 191 at the calibration bench at the ISR, edms:457109

[110] The ROOT reference, `http://root.cern.ch/root/Dictionary.html`

[111] The CMS Collaboration, Magnetic Field studies, accepted JINST (2009)

[112] The CMS Collaboration, Performance of CMS Muon Reconstruction in Cosmic-Ray Events, submitted JINST (2009)

[113] The CMS alignment and calibration constants twiki page, `https://twiki.cern.ch/twiki/bin/view/CMS/SWGuideAlignmentConstants`

[114] The CMS muon alignment twiki page, `https://twiki.cern.ch/twiki/bin/view/CMS/MuonAlignment`